Active nematic films under confinement : harnessing topological defects, shaping active flows and designing autonomous microfluidic machines

Claire Doré

PSL UNIVERSITÉ PARIS

THÈSE DE DOCTORAT

DE L'UNIVERSITÉ PSL

Préparée à l'École Supérieure de Physique
et de Chimie Industrielles de la ville de Paris

Active nematic films under confinement: harnessing topological defects, shaping active flows and designing autonomous microfluidic machines

Films nématiques actifs en confinement : contrôle des défauts topologiques et des flux actifs et conception de machines microfluidiques autonomes

Soutenue par

Claire Doré

Le 15 décembre 2022

École doctorale n°564

Physique en Ile-de-France

Spécialité

Physique

Préparée au

Gulliver UMR7083

Composition du jury :

Olivia DU ROURE ESPCI Paris	*Présidente du jury* *Examinatrice*
Denis BARTOLO ENS de Lyon	*Rapporteur*
Jörn DUNKEL Massachusetts Institute of Technology	*Rapporteur*
Chantal VALERIANI Universidad Complutense de Madrid	*Examinatrice*
Juan DE PABLO University of Chicago	*Co-encadrant*
Teresa LÓPEZ-LEÓN ESPCI Paris	*Directrice de thèse*

ESPCI PARIS | PSL

Acknowledgements

I would like to express my gratitude to all the persons who contributed to this thesis in any way.

First and foremost, I would like to express my deepest appreciation to the members of the jury. Thank you to Olivia du Roure, Chantal Valeriani and Tyler Shendruk for examining this work. I am deeply indebted to Denis Bartolo and Jörn Dunkel for their careful revision of the manuscript as rapporteurs. I could not thank enough Tyler Shendruk who, as an invited member of the jury, helped me greatly to improve this manuscript.

I cannot begin to express my thanks to Teresa Lopez-Leon for being my supervisor all along the last three years. Thank you for welcoming me in your group first as an intern, then for supporting me to continue as a PhD student, helping me to find funding and making me work on the astonishing "active nematics". You put a lot of trust in me and gave me a lot of freedom, which was unsettling at first but necessary to make the project my own. All of this was possible thanks to your great patience, kindness and enthusiasm. In addition, you put a lot of time to teach me how to give a talk, write a paper or a proposal, both by providing direct advice and feedbacks and also by setting a great example. Thank you Teresa !

I would like to extend my deepest gratitude to the Professor Juan de Pablo for welcoming me in his group at the University of Chicago during the 3rd year of the PhD. I feel extremely lucky for this opportunity to go abroad and learn more about hydrodynamics and numerical simulations. Before this visit, I was missing mathematics and computer science. This experience was particularly enriching and I would like to thank Professor de Pablo for promoting such a good dynamics in his group, by encouraging autonomy, initiative and collaborative work between the group members. In addition, I very much appreciated and benefited from the wise feedbacks, directions and also encouragements you provided along the project.

I would like to thank André Estevez-Torres and Ken Sekimoto, for the feedback they provided twice as members of the thesis committee.

I must also thank Jordi Ignés-Mullol and Francesc Sagués for giving me the opportunity to

collaborate with them on active boundary layers. I sincerely enjoyed all the discussions we had together!

I would like to send special thanks to Justine Laurent, in particular for 3D-printing the grids. Without you none of the experiments would have been possible. You were also eager to help me with many other technical issues, all the time with good spirit! More generally, you are a key element for everybody in the lab. I really appreciated working with you!

In the very beginning of the PhD, I had the pleasure to work with Jérôme Hardoüin, who trained me and transferred to me his experience and knowledge about active nematics and PhD life in general. Thank you Jérôme, I very much benefited from your creativity, the ingenious suggestions, practical advice and also the moral support!

I also wish to thank Martina Clairand, my fellow PhD colleague for two years, also working on active nematics. Martina you were always ready to give me a hand with anything in the lab, we also shared many meetings and prepared a lot of samples together. Your constant good mood and optimism was trully inspirational, and sometimes I wish you were still around in the lab to speak your words of wisdom and remind us what really matters!

At the very end of the PhD, I had the pleasure to work with Zhengyang Liu. Zhengyang brought a fresh look at the project at the time I had my focus on nothing else but the manuscript.

I would like to send many thanks to Noe Atzin-Canas for the fantastic job. I really appreciated the time you devoted to me, no matter the day or the hour you were always making yourself available when I needed some help with the simulations, in exchange of a piece of chocolate. I must also thank Ali Mozaffari and Rui Zhang for the valuable advice they provided.

I thoroughly enjoyed being part of the Gulliver lab. I would like to extend my thanks to Olivier Dauchot, for fostering a terrific work environment and navigating us through covid times. I would like to address special thanks to Fée and Elisa, Hyo-Jin and Aurélie, for making administrative tasks smooth and easy for us. Thank you also to Paul and Jeremy for organizing the student seminar. As an experimentalist, I wish to thank everybody with whom I shared the lab facilities. In particular, thank you Mengshi for being so helpful with the microscope. More generally, I would like to thank everyone who gave a little bit of their time to comment on my research, whether it was during a meeting, after a talk or simply in the kitchen. In particular, I would like to acknowledge the insightful feedback of Vincent Démery.

In the de Pablo group, I very much appreciated the help of many group members. First, my thanks go to Viviana Palaccio-Betancur, for the numerous times you helped me with computer-related problems, with an infinite amount of patience. You made sure I did not feel homesick and that I kept a balanced diet by bringing baguettes, croissants, brioches... You were also a

great liquid crystal group organizer. I must also thank Pablo Zubieta for the great amount of assistance with the computer. Thank you to the early-eaters who made lunchtime enjoyable and entertaining with the sometimes heated discussions : Joshua, Ludwig, Artem & Heyi, Abhinendra, Abhishek, Fabian... Thank you Jonathan for the spontaneous social activities, and thank you Abhishek for making me discover India from Chicago, your open-mindedness and friendliness.

I would now like to extend my gratitude to all the people outside of the academic world, whose moral and emotional support helped me achieve this dissertation. In particular, I could not be more grateful to my close family, for the love and the support they have shown me since the beginning.

Résumé

Les systèmes vivants se composent d'un grand nombre d'unités convertissant l'énergie chimique environnante en mouvement. Les exemples s'étendent sur plusieurs échelles, allant du cytosquelette des cellules aux foules humaines. L'apport d'énergie permanent maintient ces systèmes actifs hors d'équilibre et entraîne l'émergence de structures auto-ordonnées et de mouvement collectif sur de grandes distances. Les modèles de physique statistique de l'équilibre en général peinent à expliquer ces phénomènes. Un défi central dans le domaine de la matière active est donc de développer une théorie universelle capable d'expliquer la diversité des comportements observés. Une autre ligne de recherche s'attache à utiliser la matière active pour alimenter en énergie des machines microscopiques programmables et reconfigurables. Dans cette thèse, nous étudions un matériau actif synthétique inventé par le groupe de Zvonimir Dogic, appelé "nématique actif", fait à partir de constituants du cytosquelette. L'unité active est un faisceau de microtubules, qui s'étire sous l'action des kinésines, moteurs moléculaires consommateurs d'adénosine triphosphate (ATP). Les faisceaux de microtubules s'auto-assemblent à l'interface d'une huile, où ils forment un film dense présentant un ordre nématique sur une distance bien plus grande que le faisceau de microtubules. A la différence des cristaux liquides à l'équilibre, l'ordre nématique est interrompu par la présence de défauts topologiques auto-propulsés, qui conduisent la dynamique vers un état de chaos spatio-temporel. Dans cette thèse, nous explorons l'émergence de structures spatio-temporelles ordonnées dans les systèmes nématiques actifs confinés latéralement. En nous appuyant à la fois sur des expériences et des simulations numériques, nous montrons que l'on peut utiliser les parois latérales pour contrôler les flux actifs.

Le chapitre 1 est une introduction aux concepts de matière active et de cristal liquide. De nombreux systèmes actifs ne développent pas d'ordre à longue portée, si bien qu'à grande échelle, les flux sont désordonnés et qualifiés de turbulence active. Cependant, les particules actives interagissent de façon non triviale avec les parois et les obstacles physiques qu'elles rencontrent. De nombreux exemples, déjà, ont montré que des parois géométriques peuvent être utilisées pour contrôler les flux actifs des systèmes bactériens, capturer et trier des bactéries selon différents critères. La nage des bactéries peut entraîner la rotation persistante d'un micro-engrenage, démontrant la possibilité d'extraire de l'énergie mécanique des systèmes actifs. Le fluide nématique actif à 2 dimensions dont il sera question dans cette thèse développe aussi un état de turbulence active en l'absence d'un confinement fort en deçà de la distance intrinsèque entre défauts topo-

logiques.

Dans le chapitre 2, nous présentons nos méthodes expérimentales et d'analyse d'image. Le gel actif est préparé à partir de microtubules courts et de kinésines, des moteurs moléculaires qui dans ce cas précis sont attachés en grappe afin d'induire le mouvement relatif de deux microtubules. De l'ATP, ainsi qu'un système enzymatique permettant de regénérer l'ATP, fournit de l'énergie chimique aux moteurs moléculaires. Un agent déplétant est ajouté à la solution afin d'induire l'assemblage des microtubules en faisceaux. Cette solution active est isotrope. Nous la déposons au fond d'une chambre d'observation, au contact avec un substrat en verre ayant reçu un traitement hydrophile, et recouvrons la solution d'une huile de silicone afin de créer une interface plane entre l'huile et la phase active. Les microtubules s'assemblent de façon spontanée à l'interface avec l'huile, où ils forment un film nématique à 2 dimensions. Pour introduire des parois latérales dans le système, nous utilisons une technique microfluidique de surface, qui consiste à placer au niveau de l'interface une plaque en résine de quelques millimètres de côté. La plaque est ajourée, et le film nématique actif se retrouve confiné latéralement dans les ouvertures.

Dans le chapitre 3, nous présentons le modèle théorique et la méthode numérique employée pour effectuer les simulations. Nous choisissons un modèle continu, dans lequel l'ordre nématique est représenté par le tenseur $\boldsymbol{Q}$. Les équations d'évolution des champs orientationnels et de vitesse du cristal liquide sont les équations de Beris–Edwards. Les forces actives produites par l'activité du système sont introduites à travers un tenseur de contrainte proportionnel à $\boldsymbol{Q}$. Ces équations étant hautement non-linéaires, pour les résoudre numériquement nous avons recours à une méthode hybride, dans laquelle l'équation d'évolution de $\boldsymbol{Q}$ est résolue par un schéma numérique de différences finies, et les équations de Navier-Stokes pour la vitesse par la méthode de Boltzmann sur réseau.

Dans le chapitre 4, nous étudions le nématique actif au bord d'une paroi. Nous montrons l'existence d'une "couche limite active" (CLA) polarisée au bord de la paroi. En effet, la CLA n'est habitée que par des défauts topologiques de charge négative $-\frac{1}{2}$, qui présentent des propriétés exotiques en comparaison des défauts du bulk. Ces défauts $-\frac{1}{2}$ proviennent de la nucléation d'une paire $-\frac{1}{2}/+\frac{1}{2}$ à la paroi. Le défaut $+\frac{1}{2}$ quitte le mur pour rejoindre le bulk, tandis que le défaut $-\frac{1}{2}$, qui a une symétrie polaire due à la présence de la paroi au lieu de la symétrie triple du bulk, reste à la paroi. Il n'y a souvent aucun filament entre le coeur du défaut et la paroi, aussi, pour définir la charge topologique nous avons recours à une formule généralisée aux défauts de bords. La symétrie polaire des forces actives produit une force nette qui pousse le défaut contre le mur, l'empêchant de s'en écarter. En revanche, ces défauts sont capables de se déplacer le long de la paroi, en raison d'une asymétrie latérale des forces actives et de la condition de glissement au bord. De ce fait, les défauts négatifs au sein de la CLA finissent par se rapprocher et se combiner avec leur voisin. Lorsque leurs coeurs respectifs se combinent, ils forment un défaut transitoire de charge -1 qui est immédiatement combiné avec un défaut $+\frac{1}{2}$ venu du bulk. Cet événement de recombination entre 3 défauts consomme un défaut négatif

de bord et conserve la charge topologique totale. Nous qualifions la couche limite d'active en référence au comportement dynamique des défauts, qui nucléent, se déplacent et se recombinent continuellement. Dans une deuxième partie, nous montrons qu'il est possible de contrôler les défauts topologiques au voisinage de la paroi en lui donnant des contours géométriques. Nous avons testé des motifs périodiques, tels que des contours triangulaires, des contours courbes et des contours en "ratchet" (*i.e.* dents de scie). Ces motifs séparent les défauts topologiques selon le signe de leur charge : les charges positives migrent vers les régions concaves de la paroi, tandis que les charges négatives se localisent au niveau des contours convexes, et sont épinglées à la pointe des triangles, générant un flux orthogonal au mur. Les parois en dents de scie génèrent un flux net le long du mur, et imposent un ancrage incliné effectif au lieu de planaire vis-à-vis de la paroi.

Dans le chapitre 5, nous étudions expérimentalement le nématique actif confiné dans de longs canaux étroits dont les deux extrémités débouchent sur le reste du matériau non confiné qui joue le rôle d'un thermostat. Dans les canaux aux murs droits (sans motifs géométriques) nous observons l'émergence d'écoulements spontanés dans l'une ou l'autre des directions du canal. Cette direction est sélectionnée par brisure de symétrie spontanée. Pour certaines géométries, l'écoulement est instable et la direction peut s'inverser. L'amplitude de l'écoulement est bien définie et fluctue autour d'une valeur moyenne ϕ_0 qui dépend de la géométrie du canal. L'amplitude de l'écoulement augmente avec la largeur du canal du fait de la moindre résistance visqueuse, jusqu'à une largeur critique à partir de laquelle l'ordre induit par les deux parois est perdu. La stabilité de l'écoulement augmente avec la longueur du canal. Dans les canaux avec des murs en ratchet orientés dans la même direction, le fluide s'écoule dans la direction des ratchets. Ce type de canal en ratchet, qui génère un flux dans une des directions seulement, sans appliquer une force extérieure, constitue une diode microfluidique. Si les murs en ratchet ont des orientations opposées, le fluide ne s'écoule pas. Les écoulements le long du canal sont associés à la propagation d'une onde dans le champ des vitesses, et à l'ordre orientationnel des défauts $+\frac{1}{2}$. Le long de la ligne centrale du canal, ceux-ci s'orientent dans la direction du flux, tandis que près des parois, ils s'orientent dans le sens opposé. Cet ordre orientationnel est renforcé et s'accompagne d'un ordre positionnel dans les canaux dont les ratchets ont la même direction. Enfin, nous proposons un modèle minimal pour décrire les fluctuations de l'écoulement dans les canaux dont les parois sont dépourvues de ratchet. Bien que le système soit actif, nous proposons de le modéliser par une dynamique de l'équilibre, la dynamique de Langevin dans un potentiel à double puits. Si ce modèle est satisfaisant au premier ordre, il sera intéressant de tester des modèles plus complexes prochainement. Les écoulements que nous décrivons, qui comportent des défauts topologiques, n'ont pas encore été expliqués par les modèles théoriques des matériaux actifs nématiques.

Dans le chapitre 6, nous faisons des simulations numériques d'un fluide nématique actif confiné dans un canal rectangulaire avec des conditions périodiques aux deux extrémités. Pour les canaux aux parois droites, un régime d'écoulement incorporant des défauts topologiques s'établit lorsque le système est initialisé avec un flux dans l'une des directions, tandis que sans vitesse initiale le système converge vers des attracteurs sans écoulement net : selon le cas, il

s'agit du régime chaotique ou du régime où les défauts positifs suivent des trajectoires faisant penser au Ceilidh, une danse écossaise traditionnelle. Dans les simulations où les parois du canal suivent des contours en ratchet, même sans vitesse initiale un écoulement dirigé s'établit. Les défauts présentent le même ordre orientationnel et spatial que dans les expériences. Le rapport d'aspect des dents de scie peut-être ajusté afin de générer des modes d'écoulement différents : écoulement laminaire sans défauts, écoulement où les défauts réalisent la danse écossaise, et écoulement où les défauts suivent des trajectoires en forme d'épi de blé. Le mouvement collectif des défauts génère de l'advection chaotique, ainsi de tels systèmes sont intéressants pour réaliser un mélange efficace à l'échelle de la microfluidique.

Dans le chapitre 7, nous étudions expérimentalement le comportement du fluide actif lorsqu'il est confiné dans des réseaux de topologies et de géométries différentes. Tout d'abord, nous fabriquons un réseau élémentaire, où trois canaux A, B, C de longueurs et largeurs identiques sont connectés en une jonction centrale pour former une bifurcation de symétrie d'ordre trois. Nous mesurons les valeurs des écoulements ϕ_A, ϕ_B, ϕ_C dans les trois canaux. Pour une telle configuration, les écoulements sont instables quoique légèrement polarisés : l'écoulement est le plus souvent important dans deux des canaux et faible dans le troisième, mais les transitions entre ces états polarisés sont fréquentes. Dans un deuxième temps, nous construisons la bifurcation asymétrique suivante, où la branche C est plus courte que les branches A et B de longueurs égales, et où une diode est ajoutée sur la branche A (les parois de A comportent quelques dents de scies afin d'empêcher un flux sortant). Dans ce cas, l'état de flux est polarisé et l'écoulement entrant par le canal A ressort le long du canal B qui est le plus long. Ces comportements sont en accord avec des travaux théoriques modélisant les réseaux de fluides actifs à partir desquels des designs de portes logiques ont été proposés. Dans un troisième temps, nous concevons un circuit microfluidique qui a pour fonction d'effectuer les opérations logiques ET et OU à partir des valeurs de deux flux entrants X et Y. L'absence de flux entrant code pour 0 tandis que la présence d'un flux entrant code pour 1. Le circuit est une jonction en forme de H, assemblée à partir de 7 canaux élémentaires. Des diodes sont placées au niveau des entrées et des sorties. Le design du circuit logique repose sur les principes suivants : des configurations de flux polaires émergent, et les écoulements suivent le parcours le plus long possible. Ainsi, la porte de sortie OU est placée au bout de la branche la plus longue de la jonction H, et la porte de sortie ET au bout de la branche la plus courte, afin qu'elle ne reçoive un flux que lorsque les deux entrées valent $+1$. Les résultats expérimentaux que nous obtenons sont conformes aux prédictions, cependant ils pourraient être améliorés en modifiant légèrement la géométrie du circuit. Dans le futur, il faudra mettre au point une technique expérimentale permettant de contrôler la valeur des entrées X et Y, afin d'évaluer le temps de réponse du circuit. Une voie prometteuse est l'utilisation de moteurs moléculaires sensibles à la lumière qui ne s'activent que sous lumière ultra-violette. Le niveau des entrées à $+1$ ou 0 sera modulé par l'application d'un masque. L'avantage d'une telle méthode est d'être non invasive et surtout reconfigurable.

Cette thèse a donc permis le développement d'un ensemble de composants microfluidiques capables de contrôler les flux actifs. Nous avons apporté une preuve de concept pour la lo-

gique des fluides actifs. Plus généralement, nos résultats montrent que géométrie et topologie permettent de contrôler les flux actifs et de générer des états d'écoulement polarisés dans les réseaux microfluidiques.

Abstract

Living systems rely on a large number of agents converting local chemical energy into motion. Examples can be found across scales, from the cell cytoskeleton to a human crowd. The constant energy input holds these active systems out-of-equilibrium and is responsible for the emergence of a myriad of self-organized hierarchical structures and large-scale collective motion, which equilibrium statistical physics is unable to explain. A main challenge in the field of active matter is thus to develop a universal theory accounting for all the variety of observed behaviors. Another axe of research has its focus on the use of active matter to engineer and power autonomous micro-machines that can be programmable and reconfigurable.

In this thesis, we study a model synthetic active material created by the group of Zvonimir Dogic using cytoskeleton elements, which is typically referred to as « active nematic ». Here, the active unit is an extensile bundle of microtubules driven by kinesin clusters fueled by adenosine triphosphate. At an oil interface, the bundles self-assemble into a dense film that displays nematic order on a scale much larger than the microtubule or the bundle itself. However, unlike passive liquid crystals, here nematic order is disrupted by the presence of motile topological defects that drive the system dynamics into spatio-temporal chaos. In this thesis, we investigate the emergence of ordered spatio-temporal patterns in laterally confined active nematics using both experiments and numerical simulations, and we show that lateral boundaries can be used to control active flows.

First, we experimentally study semi-confined active nematics in the vicinity of a lateral boundary. While positive and negative 1/2 defects equally populate the bulk, we find that the lateral wall is exclusively populated by negative defects, which exhibit exotic structure and dynamics. Despite being like-charged, they attract each other and eventually fuse together while conserving the total topological charge of the system. We show that geometrical patterning of the lateral boundary can allow for control over defect nucleation and induce directional flows.

Then, we confine the active nematic to individual, narrow, open channels, and observe the emergence of directional flows along one direction, selected by spontaneous symmetry breaking. When fluctuations are important, the system can reverse the flow direction. We show that the flow amplitude and its stability can be geometrically controlled. For instance, we are able to effectively enforce either shear or directed flow states by shaping the confining wall with a ratchet pattern. Geometrical patterning of the channel wall induces spatial and orientational ordering of the motile topological defects. We perform numerical simulations using nematodynamics equa-

tions and a hybrid Lattice Boltzmann method, capturing some main features of our experimental results.

Finally, we experimentally build active nematic flow networks where we test a previously published theoretical model. We start with a simple configuration of three channels connected in a bifurcation, and we conclude with the realization of an AND/OR logical gate, demonstrating the potential of active nematics to power autonomous microfluidic networks.

Preface

This thesis is the result of the three years I spent as a PhD student, from October 2019 to December 2022, in the framework of a collaboration program between CNRS and the University of Chicago. From October 2019 to September 2021, I conducted experiments with a biomimetic active nematic material at Ecole Supérieure de Physique et de Chimie Industrielles de la Ville de Paris, under the supervision of Dr. Teresa Lopez-Leon. From September 2021 to June 2022, I carried out numerical simulations of the same system at Pritzker School of Molecular Engineering, under the supervision of Prof. Juan de Pablo. This preface announces the outline of the thesis and acknowledges the collaborators involved in each part of the project.

In the **first chapter**, we introduce the scientific context of this work. First, we present the topic of active matter together with the issues and challenges related to the field. Then, we focus on active nematics, a class of materials at the crossroad of active fluids and liquid crystals. We give a succinct state-of-the-art specific to active nematic systems. Finally, we expose the scientific objectives of this thesis.

In the **second chapter**, we describe the experimental methods that we developed to study active nematics in situation of lateral confinement. We detail the protocol that we followed to prepare the active material. The two main proteins constitutive of the active nematic were produced outside of our laboratory : the kinesins motors were provided by the BioNMR group at the University of Barcelona, and the tubulin monomers were obtained from the Biological Materials Facility of Brandeis University. The method used to laterally confine the active nematic film consists in placing a thin micro-printed polymer grid at the interface where the active nematic forms. The grids were printed using a 2-photon Nanoscribe printer by Justine Laurent, a research engineer at ESPCI. The images of the active nematic, obtained by confocal fluorescence microscopy, are processed using the ImageJ software and analyzed with various matlab routines.

The **third chapter** describes the theoretical model and the numerical methods used to complement the experimental results. We used a hydrodynamic model, namely, the Beris–Edwards equations, a set of partial differential equations dynamically coupling the $\boldsymbol{Q}$-tensor field -encoding the orientationnal order- and the velocity field. The Beris-Edwards equations were generalized to active nematics by the addition of an active stress tensor. To solve numerically the equations,

we used a hybrid lattice Boltzmann method, which offers a good accuracy and has the advantage to be easily parallelizable. The code was developed by the de Pablo group at the University of Chicago.

In **chapter four**, we present the experimental results concerning the behavior of active nematics in the vicinity of the boundary. This part of the project was done in collaboration with Jérôme Hardoüin, who was at the time a PhD student at the University of Barcelona under the supervision of Jordi Ignés-Mullol and Francesc Sagués. We investigate how the geometrical patterning of the wall affects the dynamics of topological defects and exert some control over the active flows.

In **chapter five**, we experimentally study the building blocks of our future autonomous microfluidic devices : the active nematic channels. More specifically, the active nematic is confined to straight microfluidic channels with open ends connected to a chaotic external bath. We assess the robustness of the flow state that spontaneously emerges in any of the two directions with equal probability, and investigate how the geometry of the channel or the patterning of the boundaries controls the flow state.

Chapter six presents the results of the numerical simulations carried out in the de Pablo group, under the guidance of Noe Atzin Canas, Ali Mozaffari and Rui Zhang. We simulate channels of active nematics with periodic boundary conditions, and explore the dynamics obtained for various initial configurations, boundary conditions and shapes of the boundaries.

In **chapter seven**, we report the conception of active nematic flow networks. We first use elementary bifurcations to probe the principles governing the flow dynamics in topologically frustrated network configurations. We finally make a logical circuit performing the AND and OR logical operations upon two input flows. The results obtained so far are still preliminary and more configurations and experimental developments are still to be explored. This project will be followed up by Zhengyang Liu and Antonio Tavera-Vazquez.

This work was funded by CNRS as part of a international collaboration with the University of Chicago.

Table des matières

List of movies

Movies are accessible by clicking here or by scanning the following QR code :

Chapter 1

1. **Unconfined active nematic :** 2D active nematic layer filmed with confocal fluoresence microscopy. Access here.

Chapter 2

1. **Grid placement :** a polymeric grid embedding a bifurcation network is lowered is placed at the water/oil interface. Access here.

Chapter 4

1. **Disk spiral :** active nematic confined in a disk of radius $R =$ displaying the spiralling dynamics. Access here.
2. **Disk jet :** active nematic confined in a disk of radius $R =$ displaying the oscillating jet dynamics, with a persistent wall defect. Movie made by Jérôme Hardoüin. Access here.
3. **Straight wall :** the active nematic is filmed next to a straight wall. Access here.
4. **Slip condition at the wall :** high magnification (x60) movie next to a straight wall. The active nematic is sliding along the wall. Access here.
5. **Topological transformation at the wall :** high magnification movies (x60) next to a straight wall showing the defects events at the wall : **A)** nucleation ; **B)** annihilation ; **C)** defect merging. Access here.
6. **Defect pinning at a protrusion :** a negative defect is pinned at the tip of a triangular protrusion of height h =200 µm and wavelength λ =400 µm. Access here.
7. **Ratchet wall :** active nematic filmed next to a ratchet wall of amplitude h =100 µm and wavelength λ =200 µm. Access here.

Chapter 5

1. **Straight channels 1 :** the active nematic flows in straight channels of width w =50 µm and w =100 µm. Movie has been sped up 5 times. Access here.

2. **Straight channels 2 :** the active nematic flows in straight channels of width w =150 µm and w =200 µm. Movie has been sped up 5 times. Access here.
3. **Ratchet channel :** the active nematic flows in the ratchet channel. Movie has been sped up 5 times. Access here.

Chapter 6

1. **Dancing disclinations :** Simulation of the active nematic in a straight channel, following a static initial state, with activity $\zeta = 0.005$. The movie shows the director field, in which blue stains indicate topological defects. The dynamics reaches the dancing disclination state. Access movie here.
2. **Simulation straight channel drifting state :** Simulation of the active nematic in a straight channel, initialized with a net current, with activity $\zeta = 0.013$. The system reaches a net-flow state embedding topological defects. The movie shows the director field, with blue stain indicating topological defects. Access movie here
3. **Simulation ratchet channel :** Simulation of the active nematic in a straight channel, with activity $\zeta = 0.014$.The movie shows the director field, with blue stain indicating topological defects. Access movie here

Chapter 7

1. **Symmetric bifurcation M1 :** the active nematic is confined to a symmetric bifurcation. Movie has been sped up 5 times. Access here.
2. **Symmetric bifurcation M2 :** the active nematic is confined to a symmetric bifurcation. Movie has been sped up 5 times. Access here.
3. **Symmetric bifurcation M3 :** the active nematic is confined to a symmetric bifurcation. Movie has been sped up 5 times. Access here.
4. **Asymmetric bifurcation M1 :** the active nematic is confined to the asymmetric bifurcation (branch B is twice longer than branch C). Movie has been sped up 5 times. Access here.
5. **Asymmetric bifurcation M2 :** the active nematic is confined to the asymmetric bifurcation (branch B is twice longer than branch C). After depletion of ATP, PEP was added and activity is recovered in branch C while branch B is still partially inactive. Movie has been sped up 5 times. Access here.
6. **Asymmetric bifurcation M3 :** the active nematic is confined to the asymmetric bifurcation (branch B is twice longer than branch C). After depletion of ATP, PEP was added and as the activity fully comes back to normal, the flow sets in branch B again. Movie has been sped up 5 times. Access here.
7. **Logical gate grid tour :** the active nematic is confined to the grid embedding four AND/OR logical circuits, corresponding to the four input configurations. Access here.

List of figures

Acronymes

ABL Active Boundary Layer
AFN Active Flow Network
AG Active Gel
AN Active Nematic
ITO Indium Tin Oxide
LBM Lattice Boltzmann Method
LC Liquid Crystal
MT Microtubule
NOA Nordland Optical Adhesive

Chapter 1

Introduction

The research that we report in this thesis aims at exploring, understanding and controlling the spatio-temporal dynamics of an active fluid termed active nematic, which combines the properties of liquid crystals and active matter. In this chapter, we provide an introduction to the field of active matter in general, then we develop in more detail the subcategory of active nematics, and finally we present the scientific objectives of this thesis.

1 Active matter

Active matter systems, by definition, are composed of a large number of units converting ambient energy into motion. Most active systems belong to the living world. At the nanoscale, molecular motors are proteins which convert chemical energy into mechanical work, and ensure, for instance, intracellular transport of vesicles. At the microscale, the cell cytoskeleton — a network of filamentous polymers (microtubules, actin filaments, intermediate filaments), crosslinked and strained by the molecular motors — is responsible for the cell motility, response to external stimuli, and mitosis. Biological microswimmers, such as sperm and *Escherichia coli*, are also active micrometer-scale structures that self-propel by beating or rotating their flagella or cilia. When a large number of these units are incorporated in a liquid, they constitute an active fluid displaying spontaneous turbulent flows. At the millimeter scale, biological tissues, which are ensembles of connected cells, behave collectively in order to flow, deform, reorganize or heal. In the animal realm, aggregates of ants, school of fish, flocks of birds, mammals herds and human crowds are also considered active matter systems, able to collectively move on large distances and collaborate to perform specific tasks, such as lifting a load, or protecting themselves against predators. How do living systems organize themselves without a central nervous system or a leader ? Answering this question is fundamental to understanding biological processes such as morphogenesis, wound healing, cancer spreading, or to prevent catastrophes like crowd collapses and crushes. However, living active systems are very complex, their basic components can be capable of creating chemical feedbacks and decision making. This is why, over the last decades, researchers have developed minimal active matter models, both theoretical (Vicsek model, model

of active Brownian particles...) and experimental (synthetic active particles, genetically modified biological swimmers, etc) systems allowing them to study active matter in a controllable and reproducible manner, and identify which ingredients (symmetry, interaction...) are at the origin of the striking features observed in nature.

1.1 Examples of active matter systems

In this Section, we present a few synthetic active materials that have been classified according to the basic active units that compose them.

Self-propelled colloids. Micro-meter beads can acquire motility via different mechanisms. For instance, Quincke colloidal rollers are dielectric colloids dispersed in a conductive fluid, which spontaneously sediment on a bottom substrate [1]. When an orthogonal electric field is applied, spontaneous symmetry breaking of the charge distribution at the surface of the Quincke roller puts the bead in rotation about a random direction orthogonal to the applied electric field. As a result, the bead self-propels on the 2D surface, at a speed that can reach a few mm/sec. As the density of Quincke rollers is increased, the beads align their velocity. This aligning interaction results at moderate density in the emergence of polar bands and at even higher density, in the formation of a dense, homogeneous, polar phase where the particles move coherently in the same direction (Figure 1.1 a-e). The self-propulsion of Janus particles [2] comes from their inherent broken symmetry : they are composed of two hemispheres with distinct surface properties (for instance, one in silicium, the other in titanium). Placed in an oscillating electric field, Janus particles acquire their motility and form patterns and phases controlled by the frequency of the electric oscillation and the density of particle : homogeneous gas, clusters, chains, or a polar phase associated to the collective motion of the colloids [3] (Figure 1.1 f-i). Swimming droplets can be prepared by immersing droplets of an active fluid in a second fluid with anisotropic properties [4], or by exploiting Marangoni forces [5, 6].

Self-propelled bio-polymers. This synthetic active system is inspired from motility assays, where protein filaments are propelled by molecular motors attached to a substrate, in order to measure the velocity of isolated pairs motor/filaments. By increasing the density of actin filaments lying on a carpet of myosin molecular motors, Bausch et at [7] observed the transition towards collective motion. Above a critical density, filaments self-organize into polar clusters moving independently. At higher density, the filaments move in bands, and spiralling structures are also observed. The addition of a depletion agent, such as PEG (see Chapter 2), leads to new patterns [8]. For instance polar filaments can assemble into high-density nematic lanes forming a large-scale network (Figure 1.2 a-c).

Active nematics. As they are central to this thesis, we will provide a thorough description of active nematics in the next section. In contrast with the systems described above, whose basic active unit itself can display directed motion due to spontaneous or inherent symmetry breaking, and develop collectively polar order by aligning their velocity, active nematics are composed of

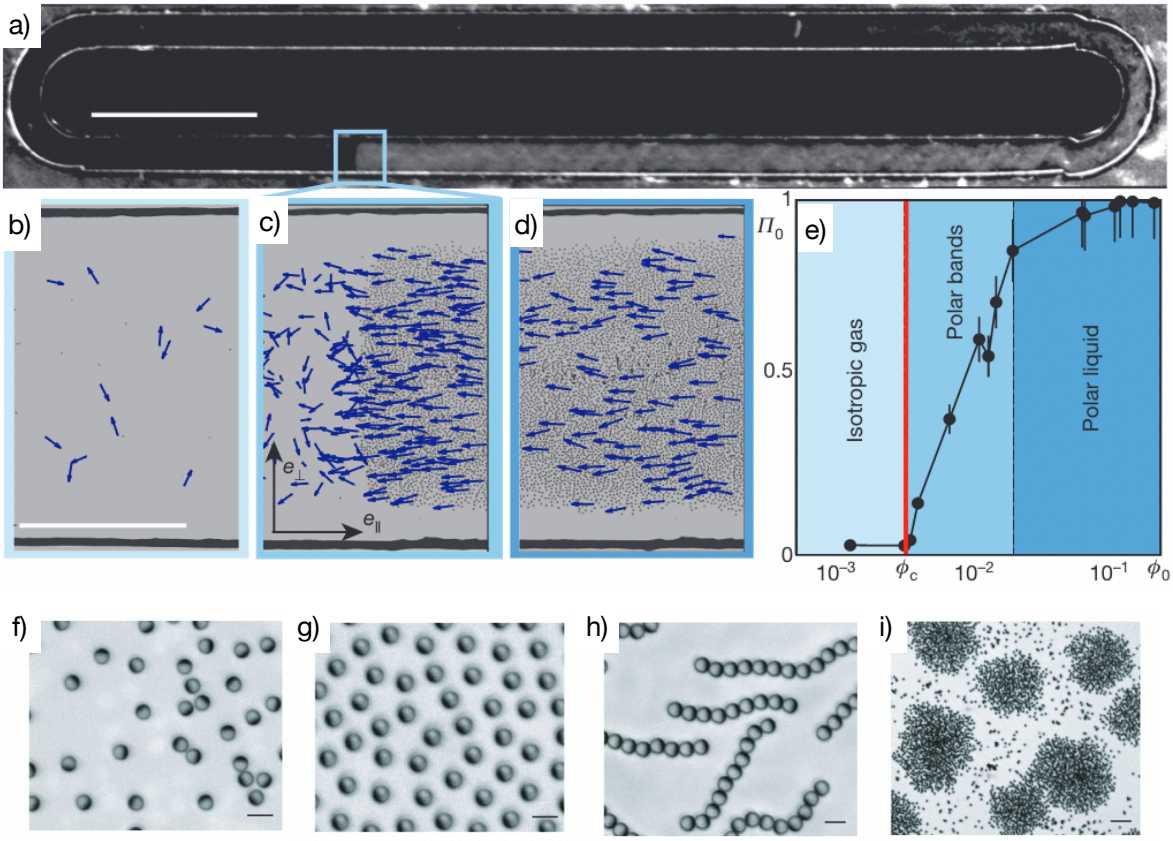

FIGURE 1.1 – **Polar fluids made of motile colloids. a-e)** Quincke rollers, adapted from [1]. a) Quincke rollers are confined inside a racetrack and collective motion gradually emerges as the density is increased ; b) gas phase at low concentration ; c) polar bands propagating ; d) homogeneous polar fluid ; e) phase diagram showing the polarisation versus the density. **f-i)** systems made of Janus particles, adapted from [3] ; f) gas phase ; g) swarms ; h) chains ; i) clusters.

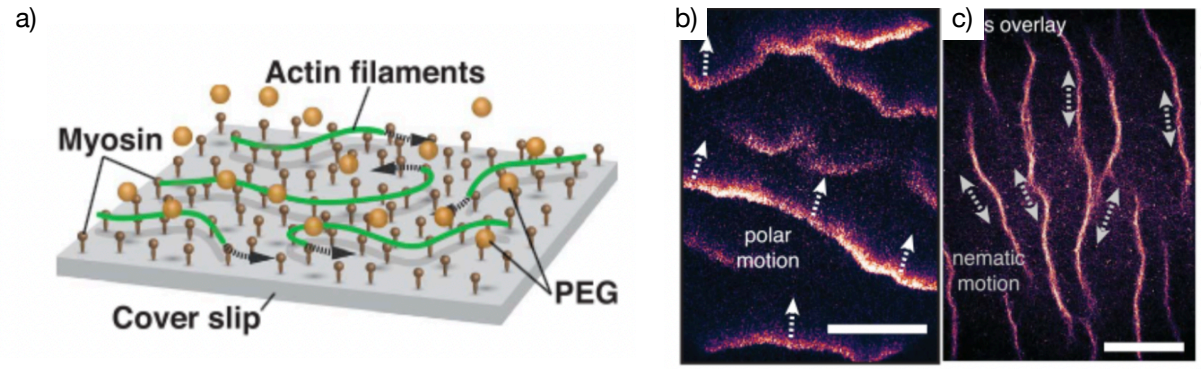

FIGURE 1.2 – **Driven polar filaments.** Adapted from [8] **a)** actin/myosin motility assay in presence of a depletion agent (PEG) **b)** at low PEG concentration, filaments form polar bands moving collectively ; **c)** at high PEG concentration, polar actin filaments form a network of high-density lanes with nematic order.

elongated units with head-tail (nematic) symmetry. An isolated unit extends in the direction of its long axis while its center of mass does not move. Such extensile units can be prepared using cytoskeletal filaments (microtubules, actin), which are bundled together by a depletion agent, and strained by clusters of molecular motors (kinesin, myosin), which are in turn fueled by ATP (Figure 1.3 a and b). When active bundles are densely packed, for instance by dispersing them in a passive liquid crystal [9] (Figure 1.3 e and f) or depleting them at an oil-water interface [10] (Figure 1.3 c and d), they form a nematic phase. However, the nematic order is not long-range, but only mesoscale, at it is disrupted by topological defects on a typical length scale decreasing with the ATP concentration. Topological defects nucleate and annihilate persistently and the particular force distribution around them generates local flows. There are no coherent flows at the macroscale (the system scale) since flows are chaotic. This is in stark contrast with the colloidal polar fluids described above, for which polar order and collective motion is long-range and extends to the whole system.

Others. Synthetic active solids can be prepared by motorizing the nodes of an elastic network with robots [12]. At a bigger scale, vibrated disks with asymmetric legs also acquire self-propulsion, and align their velocities with their neighbours via steric interactions [13]. Assemblies of robots interacting via simple and local rules can also be considered active matter systems and

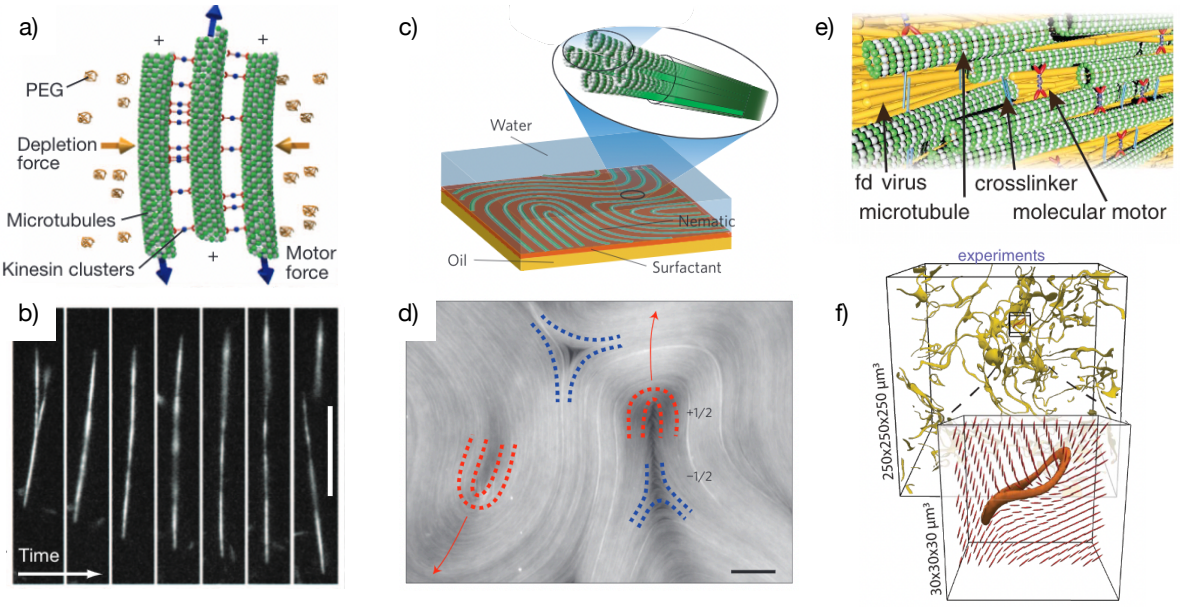

FIGURE 1.3 – **Synthetic active nematics made of mcirotubules. a and b)** Adapted from [10]. a) preparation of extensile active nematic units with microtubules and kinesin clusters b) time sequence showing the extension of an isolated active unit, scale bar 15 µm. **c and d)** 2D active nematic, adapted from [11] c) the 2D active nematic forms at the interface between water and oil ; d) 2-dimension active nematic displays point-like topological defects of charge $\pm\frac{1}{2}$. Scale bar 50 µm ; **e and f)** a 3-dimensional active nematic system, adapted from [9] ; e) active units are dispersed in a passive liquid crystal phase of filamentous virus ; f) In 3-dimensions, the active nematic displays disclination loops.

can be programmed to display specific collective behaviors [14].

1.2 Some hallmarks of active matter.

Active systems, in which energy is injected at the scale of their constituents, are inherently out-of-equilibrium. Therefore, they display remarkable behaviors that are not accessible to passive systems.

Active clustering and phase separation. Active particles can self-assemble into ordered structures because of their activity. In passive systems, self-organization is the result of the minimization of the free energy (for instance, ferromagnetic order in a system of spins or crystallization in a colloidal system). This is not the case in active systems, where crystallization, for example, can be driven by activity, as shown by Palacci et al [15] using light-activated particles. Under light activation, particles acquire self-propulsion, and clusterize together to form a "living crystal" : within the cluster, particles have a high degree of positional order like in a classic crystal, however the structure is not static but dynamic, it forms, breaks and reforms. When light is turned off, passive diffusion destroy the clusters. In this particular case, the authors showed that phoretic motion (motion directed by a chemical gradient) is responsible for the clustering. For other systems, clustering is induced by the motility of the particles : when velocity is coupled to density, particles tend to accumulate in those regions where they move more slowly (in the cluster). This phenomenon is known as "motility-induced phase separation" (MIPS).

Spontaneous flows. Active fluids have the ability to dissipate the local energy input by flowing. If some develop macroscopic flows that are coherent over the whole system (this is the case of colloidal rollers, Janus particles, etc), others display chaotic flow states with a highly disordered distribution of vortices, a state referred to as *active turbulence*, or meso-scale turbulence, or even low-Reynolds-number turbulence (Figure 1.4 a and b). Active turbulence is distinct from classic turbulence, which originates from the inertial term in the Navier-Stokes equation and emerges at high Reynolds number ($Re \geq 10^3$) in 3 dimensions only. There is no intrinsic length-scale in the eddies distribution for inertial turbulence characterized by the energy cascade from the largest eddies to the smallest ones. In contrast, meso-scale turbulence emerges at low Reynolds number ($Re \leq 1$) and, as its name suggests, is characterized by a typical vortex size called active length-scale. It can appear in 2-dimensions and is observed in many biological systems, including bacterial suspensions [16, 17, 18, 19], cell mono-layers [20, 21] and filament/motor mixtures [10, 22]. As for the transition towards inertial turbulence, the transition towards active turbulence is an active topic of research [23, 24, 25]. In living organisms, active turbulence is a mean to realize fluid mixing and transport of molecules much more efficiently than via passive diffusion.

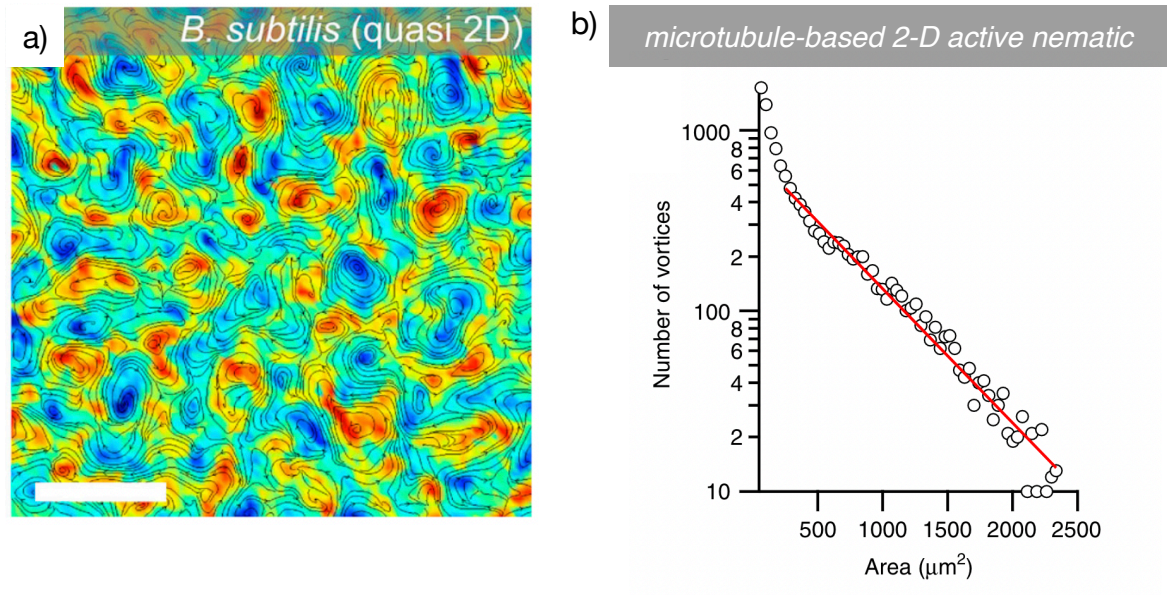

FIGURE 1.4 – **Active turbulence. a)** vorticity field of a quasi 2D suspension of *Bacillus Subtilis*, adapted from [25] **b)** Distribution of the vortex area for the 2D microtubule-based active nematic. The linear decay in the log-scale graph reveals the existence of a typical vortex area. Adapted from [26].

Wet or dry active matter ? This is an important question that one has to ask when modelling active fluids [27]. Dry systems refers to systems dominated by friction with a substrate with which they exchange momentum. Therefore, momentum is not conserved and hydrodynamic variables for them are the density and the polarity. With wet systems, on the other hand, we refer to active particles dispersed in a solvent, transferring their momentum via hydrodynamic interactions to their neighbours. We consider that momentum is conserved in such systems, and momentum is therefore a hydrodynamic variable in the descriptive equations. Nonetheless, the wet and dry limits are the idealized ends of a spectrum, in practice, active fluids are lying somewhere in between. The environment embedding the active particles indeed greatly affects the resulting dynamics.

1.3 Challenges for active matter physicists

The field of active matter presents many challenges for physicists, both from fundamental and applied perspectives [28].

Theoretical challenges. Due to the energy consumption at the constituent scale, active systems are inherently out-of-equilibrium. They can break time reversal symmetry and detail balance. Therefore, tools and laws from equilibrium statistical physics are in principle not applicable to active systems, such as the notion of free energy. One challenge is to develop methods to identify processes resulting from non equilibrium activity, that can look very similar to thermally agitated equilibrium-processes [29]. Indeed, detailed balance, broken at the micro-scale for active

systems, can re-emerge at the macro-scale [30]. This implies that equilibrium-like descriptions can apply to active matter systems at larger scale, but to what extent ? At the moment, most models have been developed in order to describe specific active matter systems. Can we set universal statistical principles for active matter ? And produce models that are general enough to derive some principles, lower and higher bounds, applicable to all active systems ? Can we identify universality classes among active particles ? And, in addition to deriving predictions from theoretical models, can we find ways to determine the necessary rules leading to a target behavior ?

Control of active matter. The other challenge is more applied in nature and aims at controlling active materials. Only considering the case of bacteria, for instance, controlling their motion in microfluidic devices would help in many industrial and healthcare related applications [31]. Bacteria are crucial to the pharmaceutical industry, where they are used to express proteins and drugs, such as insulin and cancer drugs. Such processes involve the manipulation of bacteria in microfluidic devices, careful mixing of micro-reactors and high-throughput screening and sorting of bacteria. Bacteria can also serve as drug-delivery vectors thanks to their ability to navigate through the micro-vasculature and porous tissues. More obviously perhaps, researchers are looking for ingenuous methods to prevent bacteria accumulation near surfaces, where they form biofilms costing billions in healthcare each year.

In addition, harnessing the chaotic flows of active fluids would make possible to use them to power micro-scale machines. Di Leonardo et al showed that a bacterial suspension of *Escherichia coli* is able to put in rotation an immersed microscopic gear [32] (Figure 1.5 a). Bacteria can also power the transport of a boomerang-shaped particle whose orientation is controlled with an external magnetic field [33]. The optimal transport speed is obtained when the density of bacteria is high enough to develop active turbulence. The bacteria inside the cusp of the carrier are protected from the outside fluctuations (Figure 1.5 b). Conceptual works modelled the flow of an active fluid within the channels of a network and proposed to design autonomous microfluidic devices able to perform specific tasks - such as logical operations - in response to external stimuli [34, 35]. Additionally, mixing at the microscopic scale is a difficult task, as flows are usually laminar at this scale. Active turbulence could be exploited to perform chaotic mixing at the microscale.

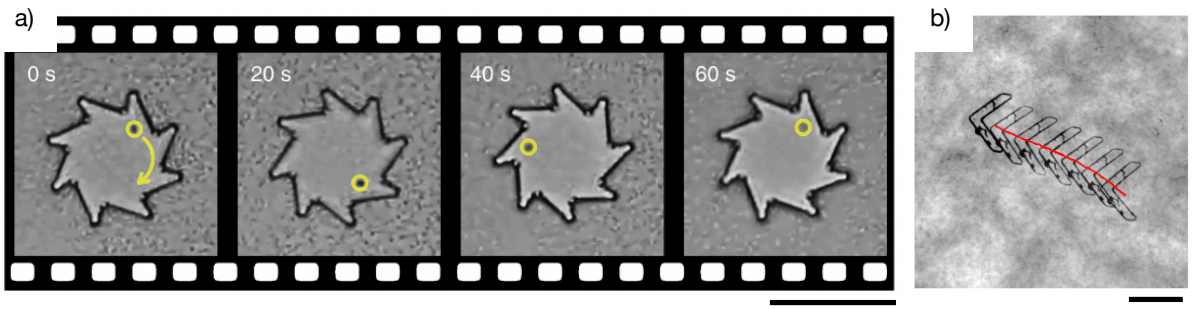

FIGURE 1.5 – **Bacterial micro-machines. a)** time sequence showing the rotation of a micro-gear immersed in a bacterial bath of *Escherichia coli*. Adapted from [32]. Scale bar = 50 µm ; **b)** Superposition of a time-sequence of images, showing a boomerang-shaped particle, orientated with a magnetic field and immersed in a bacterial bath of *Bacillus Subtilis*. In the active turbulence regime, the boomerang carrier displays directed motion. Adapted from [33]. Scale bar = 200 µm.

1.4 Active systems and boundaries

It is not enough to study infinite or large active systems. Most living systems are indeed confined and this can drastically affect their dynamics. The cytoplasmic membrane confines the cytoskeleton within the cell, cells in turn are compartmentalized with organelles. Microswimmers and cells move through porous media and channels, let's take for instance the example of sperm navigating along the female oviduct, or cancer cells collectively migrating in the stoma, organs' supportive tissue [36]. The question of the interaction between active particles and boundaries is therefore crucial in our understanding of living matter and the development of potential applications [37].

Quite many works have already focused on active matter and boundaries. The non-equilibrium behavior of active particles lead to unusual effects, forbidden to passive systems, when they enter in contact with a wall. Particles interact with walls via hydrodynamic and steric interactions. When a microswimmer, such as a ciliated of flagellated bacteria, encounters a wall, it does not bounce back like a passive particles but keep pushing against it for a while. Therefore, active particles tend to accumulate at the walls, creating non uniform pressure around the walls of the container if they are geometrically patterned (pressure is not a state function for active matter systems) [38]. This active phenomenon offers many possibilities to use boundaries to control active particles.

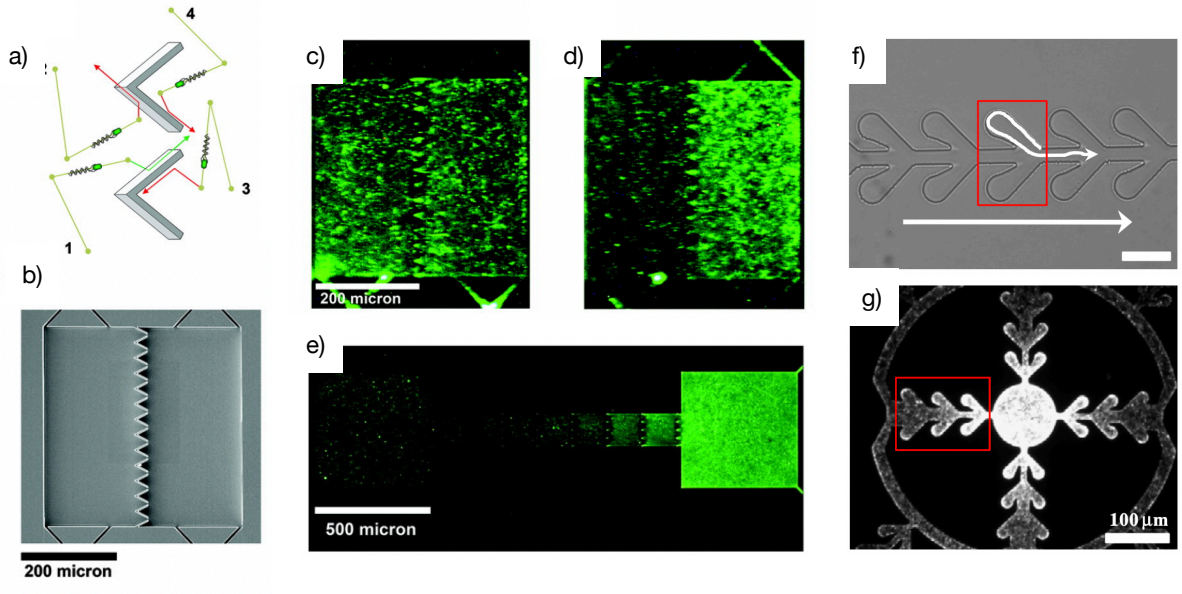

FIGURE 1.6 – **Ratchet effect in bacterial systems. a-e)** *Escherichia coli* interacting with a funnel array, adapted from [39]. a) bacteria coming from the right are trapped in the cusp of the funnel, while bacteria coming from the left are directed towards the openings of the funnel arrays ; b) the observation chamber is divided in two compartments by a funnel array ; c) fluorescence image of the initial state, bacteria fill the two compartments equally ; d) after 80 minutes, a rectification effect has occurred and bacteria concentration is higher in the right compartment ; e) several funnel arrays are associated in series to form a bacteria pumping device ; **f and g)** *Escherichia coli* in microfabricated ratchet channels, adapted from [40] f) bacteria swimming towards the left are re-oriented towards the right by the channel walls ; g) fluorescence image of the bacteria inside a microfabricated concentrator.

For instance, Galajda et al placed a bacterial bath of *Escherichia coli* inside a container divided into two compartments by an array of funnels that was placed in the middle of the container [39] (Figure 1.6 a and b). Once the system had reached a stationnary state, they observed a higher concentration of bacteria in one of the two compartments, an effect called rectification (Figure 1.6 c-e). Passive particles instead would fill the volume homogeneously. Numerical studies found that the amount of rectification depends on a few swimming parameters, such as the length of the mean free path, and were able to sort two species of active particles with differing swimming properties by adjusting the shape of the funnel array [41]. The rectification caused by the asymmetric funnel array is an instance of active ratchet effects [42]. Thermally agitated passive particles living on an asymmetric substrate or potential landscape do not spontaneously drift in one direction in the absence of an external force, they need at least an external periodic driving force with appropriate frequency in order to create a continuous drift of particles, known as ratchet effect [43]. However, active particles can spontaneously drift continuously. Many experimental realizations have been done, mostly with micro-swimmers. For instance, Kim et al designed microfluidic channels with ratchet-like patterns able to guide *Escherichia coli* motion, and create spatial patterning in the density of the motile cells [40] (Figure 1.6 f and g).

2 Active nematic liquid crystals

The experimental system studied in this thesis belongs to the class of active nematic materials. Its constitutive units develop nematic order, therefore it is considered to be an active liquid crystal. We first present passive liquid crystals (LC) in order to introduce some important notions associated to these anisotropic systems.

2.1 Passive Liquid Crystals

Liquid crystals are materials that exhibit phases between the crystalline and the isotropic phase. Their anisotropic constitutive molecules (often, elongated molecules with head-tail symmetry similar to a tiny rod), called *mesogens*, display some degree of order, the type of order defining the mesophase.

Mesophases. In the *isotropic phase*, rods residing within a mesoscopic volume can be found with equal probability at any orientation (Figure 1.7 a). In the *nematic phase*, rods tend to align along an average direction parallel to the unit vector $\boldsymbol{n}$, called the director (Figure 1.7 b). The strength of the alignment along the director $\boldsymbol{n}$ is measured by a nematic order parameter S which is 0 in the isotropic phase and 1 for the perfectly aligned system. The distribution of the centers of mass of the mesogens though, is isotropic. In the *smectic phase*, in addition to the nematic orientational order, the mesogens acquire positional order along one of the three spatial dimensions. They tend to align side by side forming layers (Figure 1.7 c) . Within the plane of the layer, the position of the mesogens is isotropic. Therefore, smectic phases are less ordered than crystals. Chirality in the mesogens, or the addition of a chiral dopant, results in new twisted phases, such as cholesteric phases, or blue phases.

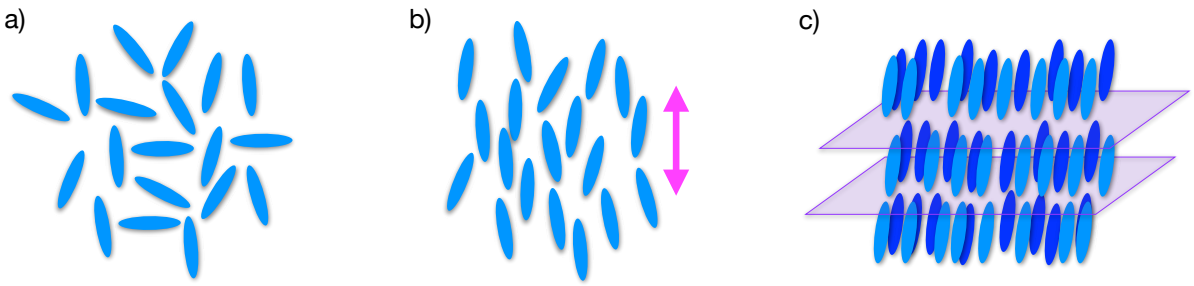

FIGURE 1.7 – **Mesophases.** a) isotropic phase b) nematic phase c) smectic phase

Phase transition. Thermotropic liquid crystals transition from the isotropic phase to the nematic phase as the temperature is lowered below a critical temperature T_c. Famous examples of thermotropic liquid crystal are 4′-pentyl-4-cyanobiphenyl (5CB) and 4′-octyl-4-cyanobiphenyl (8CB). The temperature above which they become isotropic is respectively 35 °C and 40.4 °C. Lyotropic liquid crystals are two-component systems, in which the mesogens are dispersed in a solvent. Here, both mesogen concentration and temperature control the type of phase exhibited

by the liquid crystal. For instance, the nematic phase appears above a critical concentration that depends on temperature. Biopolymers such as DNA or cellulose belong to the lyotropic family.

Liquids with elasticity. The orientational order of the mesogens in the nematic phase has a consequence at the macroscale : liquid crystals react elastically to orientational distortions. This means that any deformation of the director field $\boldsymbol{n}$ is penalized by an elastic energy, which is commonly described by the Frank-Oseen free energy density f_{FO} with

$$f_{\mathrm{FO}} = \frac{1}{2}K_1(\boldsymbol{\nabla}\cdot\boldsymbol{n})^2 + \frac{1}{2}K_2(\boldsymbol{n}\cdot(\boldsymbol{\nabla}\times\boldsymbol{n}))^2 + \frac{1}{2}K_3(\boldsymbol{n}\times(\boldsymbol{\nabla}\times\boldsymbol{n}))^2, \tag{1.1}$$

where $\boldsymbol{\nabla} = \begin{pmatrix}\partial_x\\ \partial_y\\ \partial_z\end{pmatrix}$.

Equation 1.1 decomposes any deformation of the director $\boldsymbol{n}$ into three (main) fundamental modes (splay, twist and bend), with their respective elastic constant (K_1, K_2, K_3). In Figure 1.8, we represent the three elastic modes of deformation. In a classic liquid crystal, elastic constants are of the order of a few pN.

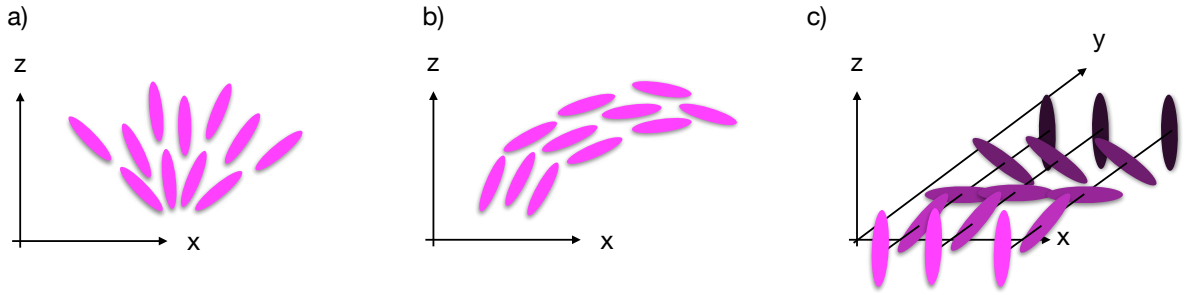

FIGURE 1.8 – **Elastic modes of deformation** a) splay b) bend c) twist

Anchoring. At boundaries, mesogens often adopt a specific orientation θ_0 that is energetically favored, a phenomenon called anchoring. The preferred orientation is transmitted from the surface to the mesogens in the bulk in order to minimize elastic deformations, and therefore, boundary conditions can drastically affect and control the director field in the bulk. In the case of homeotropic anchoring, mesogens are oriented perpendicularly to the interface (θ_0 =90°). For planar anchoring, mesogens lie in the plane of the interface (θ_0 =0°). If the anchoring is planar degenerate, any orientation within the interface plane is equivalent. If it is planar non-degenerate, a fixed direction within the interfacial plane is favored. Finally, intermediate between hometropic and planar anchoring, conic anchoring favors out-of-planed orientations making an angle between 0° and 90° with the interface. The anchoring boundary condition is associated to a surface free energy term, a common expression of it is the Rapini-Papoular anchoring potential (Equation 1.2)

$$f_S = W(\sin\theta - \theta_0)^2. \tag{1.2}$$

The anchoring coefficient W measures the strength of the anchoring. For strong anchoring (W is greater than the bulk elastic constant), anchoring enslaves the bulk director field by imposing the orientation θ_0. For weak anchoring, (W is smaller than the bulk elastic constant), the system minimizes the distortion in the bulk by adopting an orientation at the interface $\theta_0' \neq \theta_0$, which means anchoring violation. In practice, for passive liquid crystals, the type of anchoring can be controlled by adding surfactant molecules that orient the mesogens via physico-chemical interactions, in case fluid interfaces, or by surface patterning, in case of solid substrates.

Topological constraints Resulting from their inherent orientational order and their sensitivity to boundary conditions, passive liquid crystals respond strongly to the topology of the space in which they live. Topology is a branch of mathematics interested in the properties of an object that are unaffected by continuous transformations : such properties are called topological invariants. The Gauss-Bonnet theorem states that the integral of the Gaussian curvature (product of the two principal curvatures κ_1 and κ_2) of a surface is a topological invariant. It writes

$$\int_S \kappa_1 \kappa_2 dS = 2\pi\chi, \tag{1.3}$$

where the topological invariant χ is the Euler characteristic of the surface. By looking at a surface, χ can be determined from the genus number g which counts the number of *holes* (handles) of the surface, and the number of *boundaries* h [44],

$$\chi = 2(1-g) - h. \tag{1.4}$$

A sphere has no hole and no boundary, therefore its Euler characteristic is $\chi = 2$. The surface of a donut, or of a coffee mug, has one hole ($g = 1$) and no boundary, therefore the Euler characteristic is $\chi = 0$. A disk or a square has no hole ($g = 0$) and one boundary ($h = 1$), so $\chi = 1$. A Möbius strip has two boundaries and no hole, therefore $\chi = 0$.

The Poincaré-Hopf theorem states that a director field lying on a surface with non-zero Euler characteristic must host an irreductible number of point-like singularities, called topological defects, and that the sum of their individual topological charges s_i must equate the Euler characteristic

$$\chi = \sum_i s_i. \tag{1.5}$$

The topological charge s is defined as the *winding number* of the director $\boldsymbol{n}$ along a counterclockwise (CCW) loop $\mathcal{C}$ defined by the infinitesimal loop segment $\boldsymbol{dl}$ encircling the defect, *i.e.*, the signed number of 2π rotations around the defect. The topological charge s therefore writes as

$$s = \frac{1}{2\pi} \int_{\mathcal{C}} \boldsymbol{dl} \cdot \boldsymbol{\nabla}\theta. \tag{1.6}$$

If the director rotates CCW as we move around the CCW loop $\mathcal{C}$, the topological charge is positive, and if it rotates clockwise (CW), the topological charge is negative.

In a nematic liquid crystal, the defect core is a singular spot where the order parameter

S is close to zero (isotropic phase). Around the defect core, the director field rotates by a multiple of π (due to the nematic symmetry), therefore, topological charges are half-integers. The microtubule-based active nematic forms exclusively $+\frac{1}{2}$ and $-\frac{1}{2}$ topological defects, because of energetic reasons. We show a $+\frac{1}{2}$ defect in Figure 1.9 a, and a $-\frac{1}{2}$ defect in Figure 1.9 b. Note that fluorescent images of the active nematic allow us to directly visualize the lines of the director field, and that in this particular case, the core of the defect is not an isotropic phase but a space totally devoid of filaments.

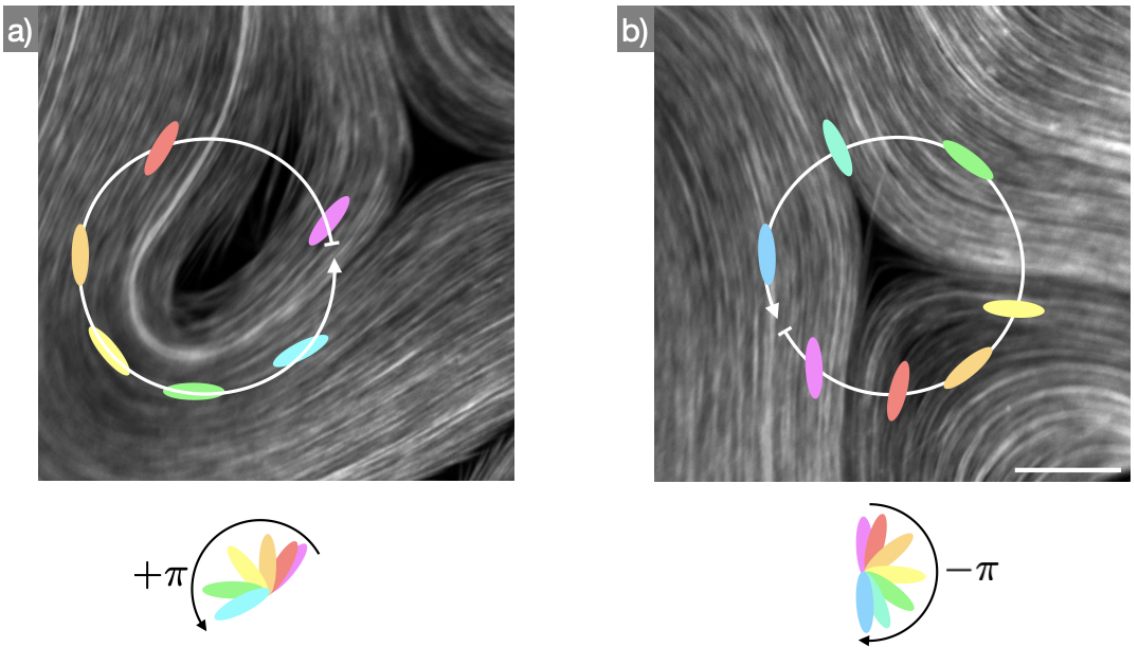

FIGURE 1.9 – **Winding number of AN defects. a)** Rotation of the director field around the core of the $+\frac{1}{2}$ defect. **b)** Rotation of the director field around the core of the a $-\frac{1}{2}$ defect. Scale bar for a, b 20 µm. We use x60 magnification images of the AN.

2.2 Active nematics, out-of-equilibrium liquid crystals

Active nematics (AN) are active materials composed of elongated units which acquire nematic order at high concentrations [45]. Experimental realizations so far are mostly 2D, they can be contractile or extensile, but most experimental systems made with cytoskeletal elements are extensile, such as the microtubule-kinesin 2D active nematic studied in this thesis, on which is based the description that follows. As mentioned above, this system is prepared by depleting extensile bundles of microtubules at an interface between water and oil. It was created by the group of Zvonimir Dogic almost ten years ago [10] and since then it has served as a model system of active nematics.

Active nematics do not minimize their elastic free energy since they are maintained out-of-equilibrium by a constant energy input. Instead, if the energy input is above a critical level, that is, if the concentrations of motors and ATP are high enough, bend distortions in the nematic field are amplified, as active forces overcome the elastic forces. This is a mechanism of *bend*

instability, and it selects a specific length scale intrinsic to the system, the so called active length scale $L_\zeta = \sqrt{\frac{K}{\zeta}}$, with K the bend elastic constant and ζ the activity, scaling as the logarithm of the ATP concentration [46]. Bend instability leads to the *nucleation* of a pair of $\pm\frac{1}{2}$ topological defects, a time sequence of the nucleation mechanism in shown in Figure 1.10 b. In contrast with a passive liquid crystal which has reached its equilibrium state, active nematic defects are not static, but move across the sample (Movie accessible here). Indeed, molecular motors generate forces that add up around such distorted nematic structures. Forces around $+\frac{1}{2}$ defects, which have a comet-like polar shape (Figure 1.9 a), result in a net propulsive force that propels the defect in the direction of the head of the comet. The threefold symmetry of $-\frac{1}{2}$ defects results in a zero average net active force on the negative defect, therefore negative defects are not considered to be self-propelled but have a diffusive motion, as they are advected by the chaotic flows. The persistent creation of pairs of topological defects is balanced by pair *annihilation*, a time sequence is shown in Figure 1.10 b.

Therefore, in the absence of strong confinement, the bulk of the active nematic is populated by many topological effects spaced in average by a distance L_ζ (Figure 1.10 a). Defects are in excess with respect to the minimal number that is topologically required. That is why it is said that active nematics are not strongly impacted by the topology of the space in which they live, unless the system size is similar to the active length scale. Then, the number of defects and their charges are controlled by topology, and the otherwise chaotic flows get organized.

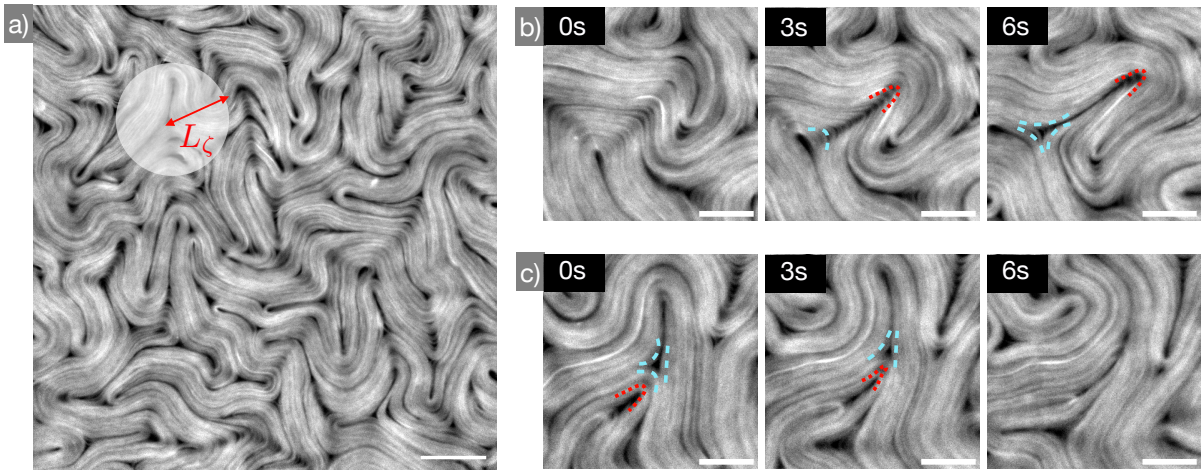

FIGURE 1.10 – **Nucleation and annihilation of AN topological defects. a)** Fluorescence image of the MT-kinesin system depleted at an interface between water and oil, scale bar 100 µm. A movie is accessible here. **b)** Time sequence showing the nucleation of a pair of $\pm\frac{1}{2}$ defects. **c)** Time sequence showing the annihilation of a pair of $\pm\frac{1}{2}$ defects. Scale bar for b and c 50 µm.

2.3 Confined active nematics.

The microtubule-based active nematic has been studied in various confined geometries and topologies. We first report the different types of confinement that have been imposed to the 2D system. The system was first confined to the surface of a lipid vesicle of about 30 µm in radius (below the active length scale) [47] (Figure 1.11 a and b). Such active nematic vesicle

only features four $+\frac{1}{2}$ moving periodically around the sphere. Then, the AN was confined to the surface of a toroidal droplet and the migration of topological charges towards regions of like-sign Gaussian curvature was reported [48] : $+\frac{1}{2}$ migrated at the outer side of the torus, where the Gaussian curvature is positive, while $-\frac{1}{2}$ migrated at the inner side of the torus, where the Gaussian curvature is negative (Figure 1.11 c). More recently, the effect of curvature gradients was probed by coating an ellipsoidal smectic droplet with the active nematic, and it revealed the existence of two different dynamic states, with bipolar and quadrupolar symmetry respectively, both displaying an oscillatory dynamics in which the active nematic periodically switches between a rotational and a translational regime [49] (Figure 1.11 d and e).

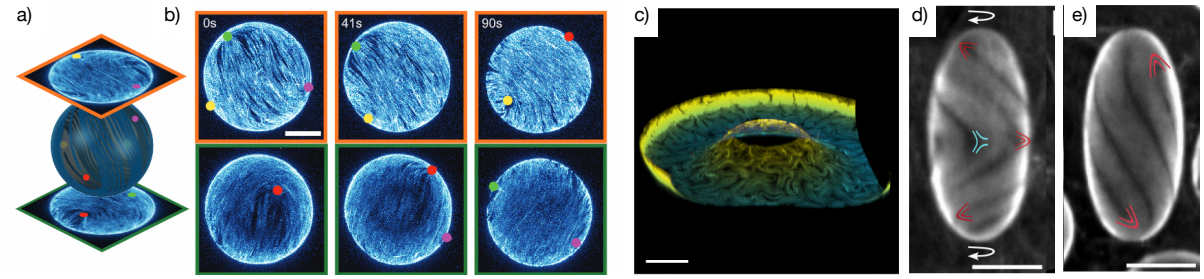

FIGURE 1.11 – **AN confined on curved surfaces. a,b)** AN vesicles, adapted from [47]. a) The vesicle is imaged with confocal microscopy and the two hemispheres are reconstituted by stacking the confocal images. b) Time sequence showing the dynamics in the two hemispheres, there are strictly four $+\frac{1}{2}$ defects at all time. **c)** Image showing the bottom half of an AN toroid, the color indicate the z-coordinate. Adapted from [48]. **d,e)** AN ellipsoids, adapted from the work of Martina Clairand [49]. d) In the quadrupolar state, there are more positive defects than topologically required. e) In the dipolar state, there are exactly four $+\frac{1}{2}$ defects whose dynamics is affected by the anisotropic curvature of the ellipsoid.

Planar films of active nematic have also been laterally confined using circular boundaries [50]. In small disks, the system featured a periodic, organized spatio-temporal dynamics. Two central $+\frac{1}{2}$ defects co-rotate and generate coherent circular flows in the whole disk, until one of the central defect is periodically replaced by the nucleation of a new positive defect at the wall. Spontaneous net flows have also been reported in annular channels, and chiral notches were able to control the flow handedness [50, 51]. Three annular channels were connected into a genus-three handlebody platform. When the annuli strongly overlaps, this leads to a frustrated flow state where only two of the annuli display a circulation of the AN texture with opposite handedness, that is, there are anti-synchronized, while there is no net circulation in the third annulus[51]. In closed, rectangular channels, the system adopted a periodic dynamic alternating between a defect-free shear-flow state and a vortex lattice triggered by the nucleation of pairs of topological defects at the wall [52].

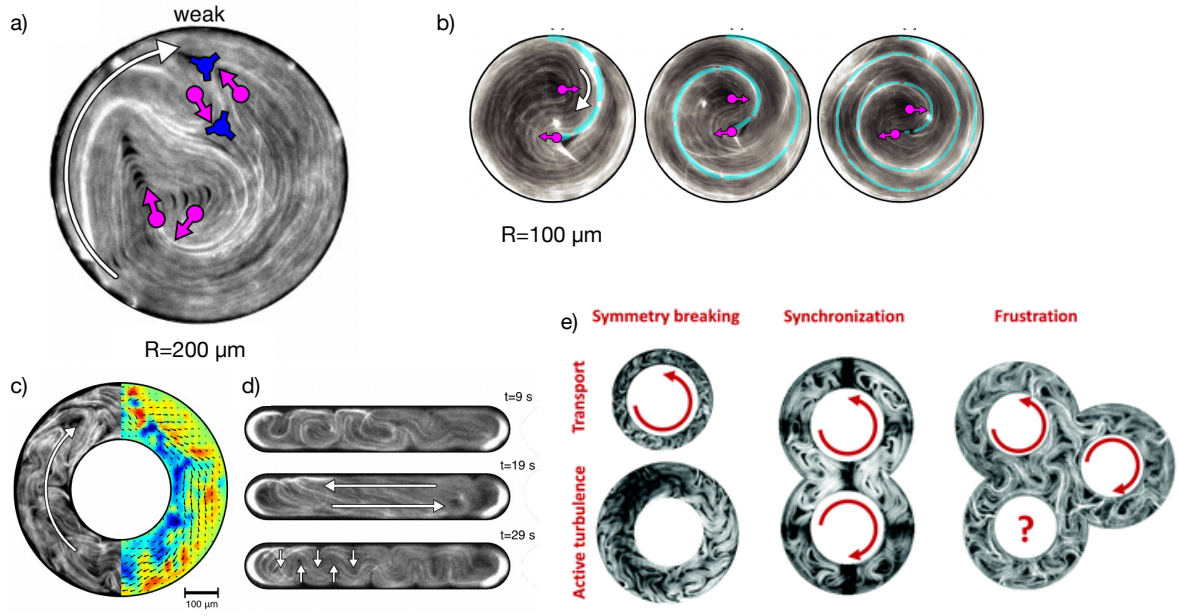

FIGURE 1.12 – **Control of the AN with lateral boundaries. a-d)** Adapted from [50]. **a)** In situation of weak confinement (the disk radius is 200 µm, the AN develops four $+\frac{1}{2}$ defects and two $-\frac{1}{2}$ defects. The total topological charge equates the Euler characteristic of the disk $\chi = 1$ with an excessive number of topological defects. **b)** Time sequence of the AN in a smaller disk, most of the time there are only two $+\frac{1}{2}$ defects, the minimal number required to satisfy the Poincaré-Hopf theorem. These two defects co-rotates in the center and drive circular flow patterns. **c)** AN confined in a 150 µm-wide annuli develops spontaneously a net flow although many defects disorganize the system. **d)** AN confined in closed channels alternates between a quasi-aligned nematic field associated to bidirectional flows and a state where defects nucleate at the walls and cross laterally the channel. **e)** AN confined in handle-bodies of different Euler characteristics. Topology does not control well the defects but strongly constraints the flows. Adapted from [51].

An alternative method of control, that does not require lateral boundaries or closed surfaces, is to used patterned interfaces. One possibility is to interface the active nematic with an oil of anisotropic viscosity, such as a smectic passive LC, where the easy flow direction is parallel to the smectic layers [26, 22]. When the smectic is bounded by a water phase (imposing planar anchoring) and air (imposing homeotropic anchoring), it spontaneously forms toroidal focal conic domains. The AN defects rotate below the circular domains created by the smectic at the water interface, following the easy-flow direction set by the smectic layers. The layers of the passive smectic LC can be oriented along one specific direction by applying a magnetic field. In this case, the AN organizes its flows in lanes of opposite flow direction, parallel to the smectic layers. A second alternative to create frictional patterns is to use submersed micropatterned structures below the flat active nematic film [53]. A third method consists in applying patterns of light to an actin-myosin system whose myosin motors are activated under UV illumination. Using this method, defects can be effectively trapped in areas of high activity [54].

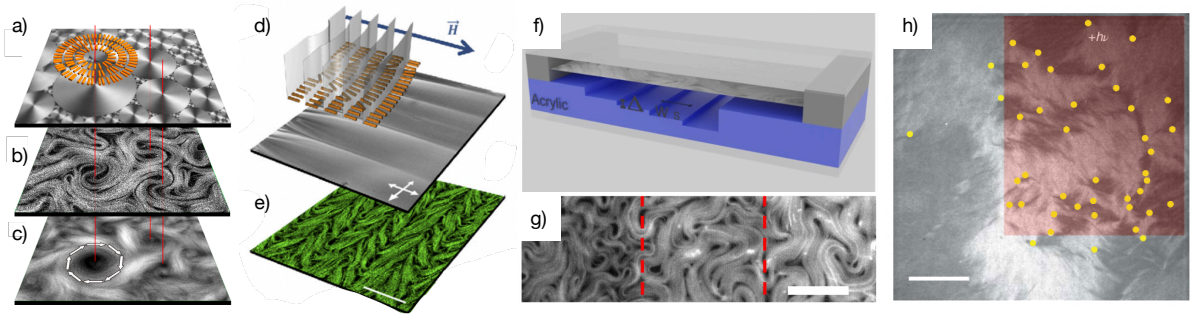

FIGURE 1.13 – **Control of the AN with patterns of friction and light. a-c)** AN interfaced with a smectic oil developing focal conic domains, adapted from [26]. **a)** Polarized image showing the structure of the smectic oil. **b)** Fluorescence image of the AN at the interface. **c)** The temporal average of the AN texture shows that circular patterns are persistent. **d, e)** The smectic oil is aligned with a magnetic field $\vec{H}$, adapted from [22]. **d)** Structure of the smectic oil. **e)** Fluorescence image of the AN layer that develop bidirectional flows orthogonal to the magnetic field. **f, g)** the AN layer forms above the micro-patterns of different heights. The heterogeneous depth of the oil phase below the AN layer creates heterogeneous friction. Adapted from [53]. **g)** Fluorescence image of the AN. **h)** Polarized image of actin-myosin AN controlled by patterns of light, adapted from [54].

From all these experiments, a few observations can be made. The topology of the confinement affects the number and the nature of topological defects only if the system is confined at scales comparable to the active length scale (case of the vesicle and the small disk). In large systems, although the sum of topological charges equates the Euler characteristics, there are an excessive number of defects in comparison with the minimal number required by topology. However, flows can still display organized spatio-temporal patterns (circulation, periodic dynamics...) despite the lack of control over topological defects.

2.4 Active nematics in the living world

Active nematics are present in many living organisms. Some types of bacterial colonies (Figure 1.14 a) and cells, such as fibroblasts, melanocytes, lipocytes, amoebid cells, and neurons can develop nematic order. Tissues resulting from their assembly display topological defects, and it was shown that those defects were associated to morphological changes and biological function such as visual development ([55, 56, 57]. $+\frac{1}{2}$ defects are correlated to events of apoptosis, where a dying cell is extruded from the tissue, and attract neighbouring cells, while $-\frac{1}{2}$ deplete cells [58, 21] (Figure 1.14 b-d). The organism hydra, that has the ability to self-regenerate from an excised fragment, was shown to develop features (tentacles, mouth, foot) at the defect sites formed by the actin fibers during the regeneration process [59] (Figure 1.14 e and f). However, although models of active nematics are relevant to describe such biological systems like cell tissue, bacteria colonies, cytoskeletal fibers, they differ from the microtubule-based active nematic in several ways : they are often dominated by friction with a substrate (dry active matter), elastic forces are more predominant which is why they can be found in frozen states more often, and they feature splay rather than bend deformations.

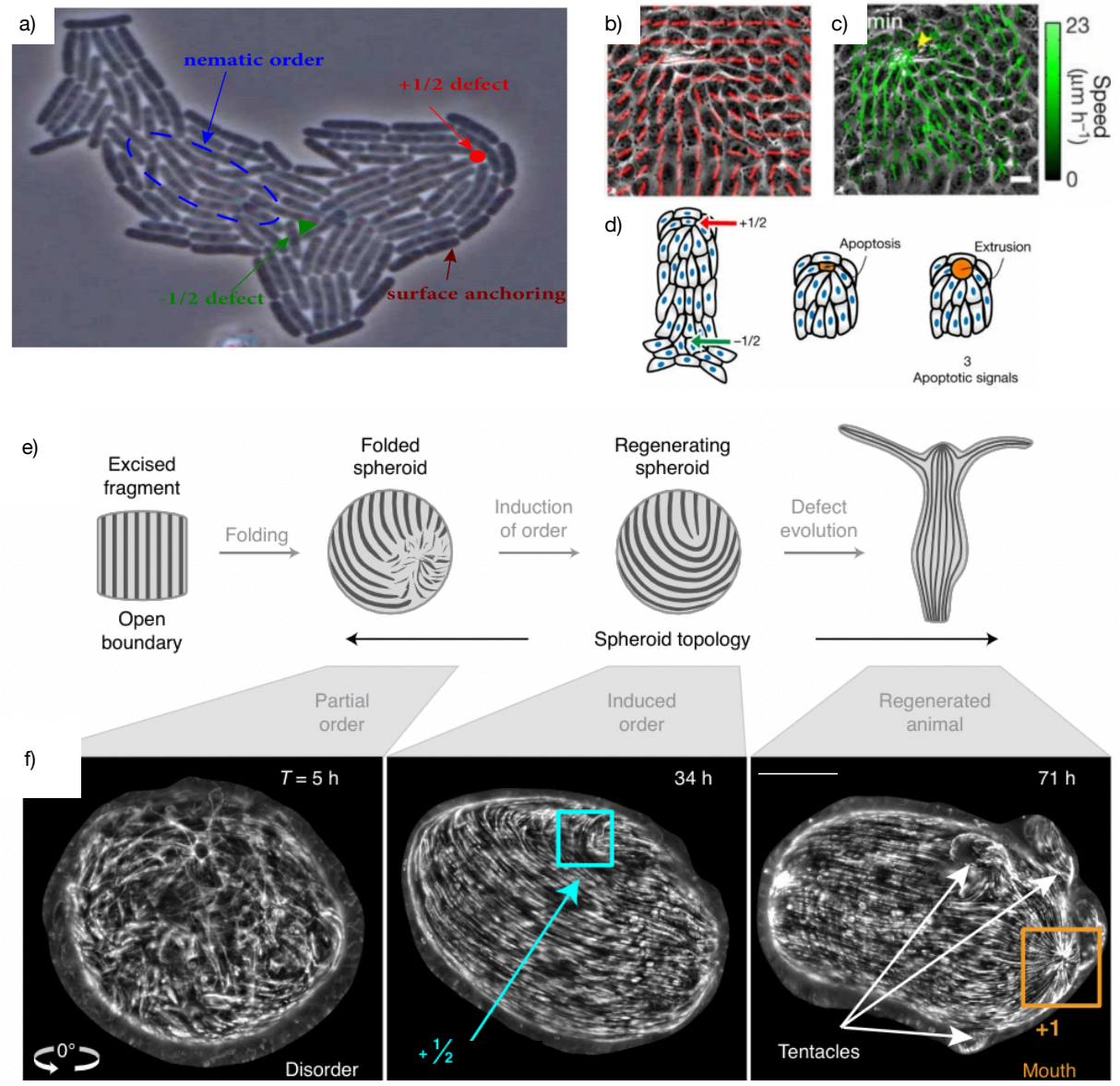

FIGURE 1.14 – **Living active nematics.** **a)** A growing colony of *Escherichia coli* displays nematic order and topological defects of charge $+\frac{1}{2}$ (in red) and $-\frac{1}{2}$ (in green). Adapted from [60]. **b-d)** Monolayer of Madin Darby canine kidney cells, adapted from [58]. **b)** The nematic orientation of each cell is overlaid in red, a $+\frac{1}{2}$ defect is present in the image ; **c)** the velocity field shows that cells move towards the defect, the yellow arrow indicates the position of the extrusion site, scale bar 10 µm ; **d)** sketch illustrating how the cell located at the defect site is extruded out-of the monolayer. **e,f)**Sketch and 2D projection of the 3D stack of confocal images showing the self-regeneration process of *Hydra*, adapted from [59]. Scale bar 100 µm.

3 Objective of this thesis

The primary objective of this thesis is to study how *lateral confinement* transforms the chaotic flows of the 2D active nematic into more organised flow patterns. The effect of lateral confinement can be studied at different scales. At the level of the active length scale first, we aim

at answering the following questions : how do topological defects interact with lateral boundaries, and how do they respond to geometrical patterns ? What type of order, if any, the topological defect landscape can acquire in confined configurations ? At larger scales, we will put the focus on the macroscopic flows emerging under lateral confinement. Even if topology does not exert a strong control over the defect dynamics in large systems, to what extent does the topology of the confining space constrain the emergent active flows ? Can we coarse-grain the dynamics and describe it with an equilibrium-like model ?

A second objective of this thesis is to develop a toolbox of elementary compounds able to exert some control over the active nematic defects and flows. We will demonstrate that we can assemble these compounds into functional autonomous microfluidic devices.

To address these questions, we combine experiments and numerical simulations, and adopt a bottom-up approach structured around three main topics :

Active nematics near a wall. First, we examine how the active nematic interacts with a boundary. This is done experimentally by observing the system next to the rim of a polymeric platform, placed at the interface. Previous studies have pointed out the particular behavior of defects near walls. The role of the boundary is characterized in terms of slip and planar-anchoring boundary conditions. We identify three types of topological events happening at the walls, namely defect nucleation, annihilation and recombination. We investigate how geometrically-patterned walls can be designed in order to manipulate topological defects and shape the near-wall flows.

Active nematics in channels. Next, we study the transition from chaos to directional flow in active nematic films confined to channels. Experimentally, we study the coherent flows emerging in long and narrow channels whose extremities are open and connected to an external active nematic bath. We show how the flow can be controlled by the channel geometry and wall patterning. We propose a simple equilibrium-like model to describe the fluctuations of the macroscopic net flow that emerges. We complement the experiments with numerical simulation of channels with periodic boundary conditions, which capture most of the experimental findings.

Active nematic flow networks. We experimentally study the interplay between active flows and topology by confining the active nematic to microfluidic networks. We use bifurcations as an elementary building block of the network to probe the rules governing network dynamics and compare our results to theoretical predictions. Finally, we demonstrate the possibility to create functional microfluidic networks powered by the active nematic fluid by making an AND/OR logical gate.

Chapter 2

Experimental materials and methods

In this chapter, we provide some explanations about the protocols used to prepare the active nematic liquid crystal, imaging the nematic layer, imposing lateral confinement and analyzing the recorded images to extract the nematic field and the velocity field.

1 Active gel preparation

The active gel under study has been developped by the group of Zvonimir Dogic. It was presented in their seminal 2012 paper [10]. It is an isotropic mixture composed by three main building blocks : short microtubules (MT), a depletion agent and clusters of kinesin. We first provide a general description of microtubules and kinesins, then the protocols used for protein purification and preparation of the active mixture.

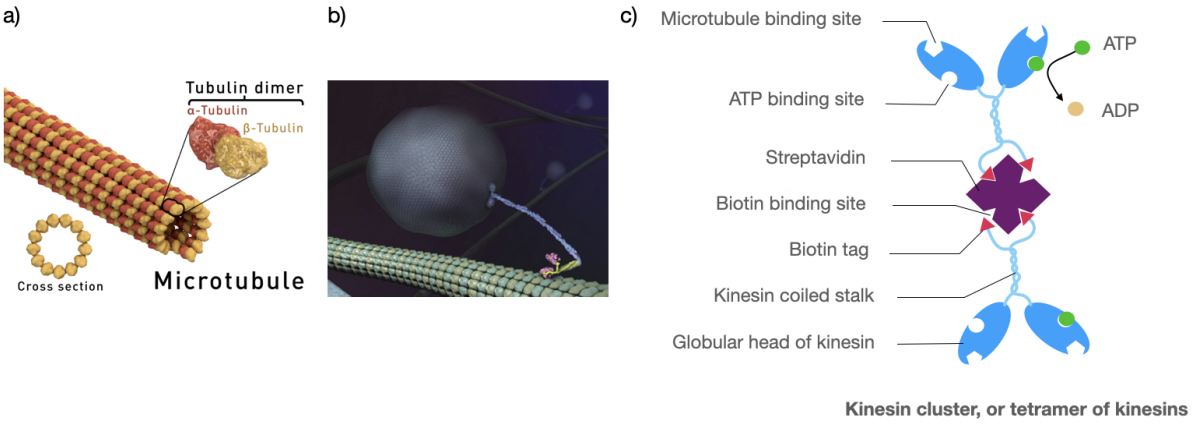

FIGURE 2.1 – **Microtubule and kinesins. a)** Illustration of a microtubule by Thomas Splettstoesser (Creative Commons Attribution-Share Alike 4.0 International). **b)** Illustration of a kinesin dimer transporting a vesicule along a microtubule, by the Vale lab (https ://valelab.ucsf.edu). **c)** Sketch representing the tetrameric kinesin cluster, assembled with a molecule of streptavidin that binds to the biotin tags of two of kinesin dimers.

1.1 Generalities

Microtubules are polymers of the α/β-tubulin heterodimer [61]. Tubulin dimers polymerize end-to-end to form a protofilament. As they grow, protofilaments associate laterally to form a hollow tube : the microtubule (Figure 2.1 a). Typically, a microtubule is the lateral association of 13 protofilaments, which gives to the microtubule an outer diameter of 24 nm. It is a stiff filament due to lateral interaction between the protofilaments : the persistence length has been measured to be 5 mm [62]. Microtubules are also polar filaments : because the β-subunit of the tubulin dimers binds with the α-subunit of the next dimer, a protofilament has an end where an α-subunit is exposed (the (-) end) and an end where the β-subunit is exposed (the (+) end). The protofilaments associate laterally with the same polarity. Therefore, the microtubule itself has an (-) end with only α-subunits and a (+) end with only β-subunits.

Kinesins are a huge protein family of molecular motors associated to microtubules, they convert into mechanical work the chemical energy released by the hydrolysis of adenosine triphosphate (ATP) into adenosine diphosphate (ADP). The monomer's heavy chain is composed of a globular part, the motor domain, attached to a coiled stalk. Two kinesin monomers spontaneously form a dimer by getting their stalks entertwined. Kinesin dimers strikingly resemble a pair of legs with two enormous feet, as they often walk along the microtubule in a well-defined direction, most of them towards the (+) end (Figure 2.1 b). When one of the globular head binds a molecule of ATP and hydrolyzes it into ADP, the kinesin changes its conformation and take a 8 nm step along the microtubule. The two heads cooperate to repeat this process in alternance, in a walking fashion. Single kinesin velocity along the microtubules highly depends on the environement, the ATP concentration, whether the kinesin moves freely or carries a cargo, but can reach $50\,\mathrm{nm}\cdot\mathrm{s}^{-1}$ [63].

In eukaryotic cells, microtubules and kinesins play many roles : spindle formation during mitosis, intracellular transport, moving cilia and flagella, and cell morphology and mechanical resistance.

1.2 Protein purification

Kinesin expression and purification is carried out in the labs of the BioNMR group at the insitute of bioengineering of Catalunya (IBEC). The idea is to tag the stalk of each kinesin monomer with a biotin carboxyl protein, so that they will later be able to bind to one of the four biotin binding sites of a streptavidin tetramer (Figure 2.1 c). Drosophila melanogaster heavy-chain kinesin-1 K401-BCCP-6His (which means that the kinesin chain is truncated at residue 401, fused to biotin carboxyl carrier protein (BCCP), and labeled with six histidine tags for purification purposes) is expressed in *Escherichia coli* using the plasmid WC2 from the Gelles Laboratory (Brandeis University) and purified with a nickel column. After dialysis against 500 mM imidazole aqueous buffer, kinesin concentration is estimated by absorption spectroscopy. The protein is stored in a $0.07\,\mathrm{mg}\cdot\mathrm{mL}^{-1}$ aqueous sucrose solution at $-80\,^{\circ}\mathrm{C}$ for future use.

Tubulin purification was carried out by Dr. S Dalal at Brandeis Materials Research Science and Engineering Center. It was extracted and purified from bovine brain via two cycles of polymerization-depolymerization in a high molarity Pipes buffer. They also provided us with tubulin labelled with Alexa-647, a far red fluorophore excitable at 647 nm and emitting at 665 nm.

Polymerization of short and stable microtubules In vivo, the polymerization of microtubules requires that α/β-tubulin dimers bind 2 molecules of guanosine-5'-triphosphate (GTP). GTP can be hydrolyzed after assembly, transforming into guanosine-5'-diphosphate (GDP). When the terminal tubulin is bound to a GTP, the protofilament is stable. But as soon as the terminal GTP is hydrolized into GDP, the microtubule depolymerizes rapidly. This dynamic instability is useful in vivo for cell motility, but undesirable to prepare active nematics. To produce stable microtubules, we replace GTP with a quasi non hydrolysable analogue [64] : guanosine 5'-(α/β-methylenetriphosphate) (GMPCCP), from Jena Biosciences. The energy barrier of the nucleation of the microtubule is shorter in presence of GMPCPP than GTP, therefore GMPCPP-stabilized microtubules are shorter. In vivo, microtubules are often 100 µm long. In our system, long microtubules have a tendency to crosslink, leading to elastic forces that cannot be overcome by molecular motors. The elastic gel formed by long microtubule would stay close to equilibrium . Thus, short microtubules are essential to obtain an active system. We manage to produce 2 µm-long microtubules by polymerizing tubulin at high concentration, $8\,\mathrm{mg}\cdot\mathrm{mL}^{-1}$. Tubulin, 3% of which is labelled with Alexa-647, is incubated for 30 minutes at 37 °C at a concentration of $8\,\mathrm{mg}\cdot\mathrm{mL}^{-1}$ in a M2B aqueous buffer in the presence of 6 mM of GMPCPP and 1 mM of dithiothreitol (DTT). M2B buffer consists of 80 mM of PIPES (Sigma, P1851) ; 1 mM of EGTA (Sigma, E3889) ; 2 mM of $MgCl_2$. After incubation, the final solution is kept at room temperature for 5 hours, then frozen in liquid nitrogen and stored at −80 °C for future use.

1.3 Active gel recipe

Depletion forces induce bundle formation. To make the microtubules form bundles, we add a depletion agent : polyethylene-glycol of 20 kDa (PEG, Sigma 95172). PEG is non-adsorbing and creates an attractive interaction of entropic origin between MT filaments causing them to align and associate into bundles. PEG molecules are far more numerous than the filaments in the solution, so, to maximize the entropy, PEG molecules need to occupy as much space as possible. A microtubule filament is surrounded by a cylindrical volume, called excluded volume, that cannot be accessed by the center of mass of PEG molecules. However, if the filaments aggregate laterally, their excluded volumes overlap, which increases the volume accessible to PEG molecules (Figure 2.2 a).

Bundle dynamics. Consider an isolated bundle of two MT filaments, which are aligned (thanks to the depleting agent), with the *same polarity* (Figure 2.2 b) . Each kinesin of the cluster will walk towards the (+) end of the filament it is attached to, that is to say, in the same direction. Thus, the cluster will simply translocate between the two filaments, not exerting any force, not providing any mechanical work to the MTs. If, on the contrary, the two filaments are

aligned with *opposite polarity* (Figure 2.2 c), the two pairs of kinesin walk in opposite direction, and because the cluster cannot stretch, it will cause the filaments to slide with respect to each other. In this configuration, the cluster of molecular motors provide the MTs with mechanical work. Depending on the starting configuration of the MTs and the kinesins, the length of the bundle may start decreasing. Yet, the bundle will always end up extending if the motors walk for long enough time. Thus, the motor clusters induce overall *bundle extension*. The average time that a motor walks on a microtubule before detaching is called processivity and it is an important characterisation parameter of the motor. Using clusters of kinesins (tetramers), as well as the bundle configuration, improves the processivity. Kinesins, which are subject to thermal fluctuations, have a probability to detach from the MT at each time step, but it is very unlikely to see all the kinesins of a cluster detached at the same time. So, if a kinesin unbinds, the cluster will stay attached to the bundle thanks to the other kinesins. The unbinded kinesin will have a great probability to reattach to the multiple binding sites offered by the bundle configuration.

Consider now a bundle composed of many microtubules of random polarity and including kinesin clusters. In the end of the process, the bundle will be polarity sorted : strands with a given polarity will be gathered at one end of the bundle and strands with the opposite polarity at the other end. The system has reached a static state : kinesin clusters will be able to walk only between polarity sorted MTs, not producing any motion. Yet, this static state induced by polarity sorting is not reached in the active gel, where bundles are not isolated. In the 3D gel, each bundle is connected to others, so that the extension of a bundle is hindered. Hence, while extending, the bundle buckles, until it fractures. The typical length scale at which it fractures is 100 µm. Then, the fragments are incorporated with a random orientation in neighbouring bundles. The recombined bundle, extends, buckles and fractures again. The system is constantly remodeling, so that the gel never reaches the polarity sorted state.

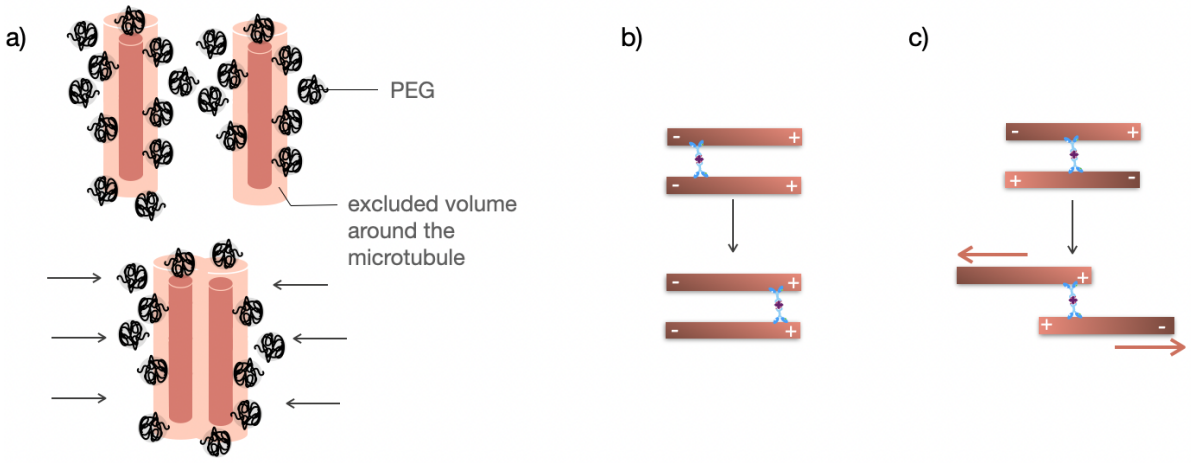

FIGURE 2.2 – **Microtubule bundles induced by depletion. a)** Bundling of two microtubules induced by the depletion agent PEG. When the two excluded volume overlap, the total excluded volume is reduced. **b)** Kinesin cluster translocates along two parallel microtubules. **c)** Kinesin cluster shear 2 anti-parallel microtubules.

Active gel protocole The active gel we use is composed of 0.5 µL of the microtubule solution and 2.5 µL of the so-called "active solution" (AS) containing all the other compounds and prepared separately as follows. Biotinylated kinesin motor proteins and tetrameric streptavidin (Invitrogen ; 43-4301) are mixed at the stoichiometric ratio 2 :1 in M2B buffer in presence of 0.2 mM of DTT and incubated on ice for 30 min to obtain kinesin–streptavidin motor clusters. Clusterized kinesins are then mixed with ATP (Sigma ; A2383) and an enzymatic ATP-regenerator system in order to maintain a constant concentration of ATP during the experiments. The ATP-regenerator system consists of phosphoenolpyruvate (PEP) (Sigma ; P7127) and the enzymes pyruvate kinase/lactate dehydrogenase (PK/LDH) (Sigma ; P0294). Pyruvate kinase is an enzyme that cuts the phosphate group from the PEP, then the free phosphate group spontaneously reacts with ADP to produce ATP. The AS also contains the depletion agent polyethylene glycol (PEG, 20 kDa ; Sigma ; 95172), and pluronic F-127 (Sigma ; P-2443), a PEG-based triblock copolymer surfactant. Several antioxidant components are also included in the solution to avoid protein denaturation, and to minimize photobleaching, including Trolox (Sigma, 238813) and two antioxidant solutions AO1 and AO2. AO1 contains 15 $\mathrm{mg \cdot mL^{-1}}$ of glucose (Sigma ; G8270) and 2.5 M of DTT ; AO2 contains 10 $\mathrm{mg \cdot mL^{-1}}$ of glucose oxidase (Sigma G2133) and 1.75 $\mathrm{mg \cdot mL^{-1}}$ of catalase (Sigma, C40). A high-salt M2B solution is used to raise the $MgCl_2$ concentration in the AS. Buffer for stock solutions of PEP, DTT, ATP, PEG and Streptavidin are M2B, and we add 20 mM of K_2HPO_4 to the buffer of catalase, glucose, glucose oxidase and Trolox. A typical recipe is summarized in 2.1. The active solution is stored in small aliquots of 2.5 µL at −20 °C for up to one month. The active gel (AG) is prepared just before the experiment by mixing 2.5 µL of AS with 0.5 µL of the microtubule solution.

Compound	Stock solution	Final volume fraction
PEG	0.12 $\mathrm{g \cdot mL^{-1}}$	0.139
PEP	200 mM	0.139
Mix	69 mM of $MgCl_2$ in M2B	0.05
Trolox	20 mM	0.104
ATP	50 mM	0.03
Catalase	3.5 $\mathrm{mg \cdot mL^{-1}}$	0.012
Glucose	300 $\mathrm{mg \cdot mL^{-1}}$	0.012
Glucose oxidase	20 $\mathrm{mg \cdot mL^{-1}}$	0.012
PK/LDH	600-1000 units.$\mathrm{mL^{-1}}$	0.03
DTT	0.5 M	0.012
Streptavidin	0.352 $\mathrm{mg \cdot mL^{-1}}$	0.023
Kinesin	0.07 $\mathrm{mg \cdot mL^{-1}}$	0.234
Microtubules	8 $\mathrm{mg \cdot mL^{-1}}$	0.2
Pluronic	0.17 $\mathrm{g \cdot mL^{-1}}$	0.027

Table 2.1 – Active gel composition

2 Active Nematic assembly, lateral confinement and imaging technique

In the active gel, bundle orientation is isotropic. To obtain a nematic phase, one has to increase the concentration of nematogens. This can be achieved by adding filamentous passive viruses to produce a 3-dimensional active nematic phase [9], or by interfacing the active gel with an oil [10]. The interface is stabilized with Pluronic F-127, which is a PEG-based triblock copolymer surfactant. Over time, bundles of microtubules adsorb onto the PEG brush formed by the surfactant molecules at the interface, forming a dense quasi-2D layer of active nematic liquid crystal. In this thesis we use the second strategy.

2.1 Creating a flat interface between water and oil

To create a flat interface between water and oil, we assemble a chamber made of a coated glass slide on which we place a plastic container.

Acrylamide coating of glass slides To prevent non specific adsorption of proteins on the glass slide surface, we coat the glass with a polyacrylamide brush. This also creates a hydrophilic surface, which helps to obtain a flat interface between the aqueous phase and the oil phase. First, the glass slides are thoroughly cleaned by being sonicated for 5 minutes in three successive solutions : first in a a solution with 1% of Hellmanex detergent, second in ethanol, and finally in 1 M of NaOH solution. Once the glass slides are cleaned, they are immersed for 13 minutes in a mixture of 98.5% ethanol, 1% acetic acid, and 0.5% of the silane-bonding agent 3-(Trimethoxysilyl)propylmethacrylate. This process, called silanization, creates covalent bonds between the silane agent and the glass. Next, the glass slides are immersed in a aqueous solution of 2% acrylamide monomer solution, with 0.35 ‰of TEMED, and $0.7\,\mathrm{g}\cdot\mathrm{L}^{-1}$ of ammonium persulfate as polymerization initiators. Glass slides are immersed in the acrylamide solution for at least 3 hours. Before use, the coated glass slides are rinsed with DI water and dried with compressed air. They can be stored in the acrylamide solution for 1 month.

Observation chamber. We stick on the glass slide a cylindrical container molded in Polydimethylsiloxane (PDMS) using a curable glue (Norland Optical Adhesive) and a UV lamp. The bottom surface of the PDMS is intentionally ribbed by the mould which favors the infiltration of the glue by capillarity between the PDMS and the glass slide and ensures a good sealing (Figure 2.3 a). Then, we place 2.5 µL of the active gel directly on the glass slide at the bottom of the chamber, we cover it immediately with 200 µL of silicone oil of $20\,\mathrm{mPa}\cdot\mathrm{s}$ viscosity. The addition of the oil makes the water phase spread over the hydrophilic glass surface. The bundles of microtubules, initially in the bulk of the water phase, spontaneously adsorb at the interface with oil, and a dense nematic layer is formed within usually 1 hour (Figure 2.3 b).

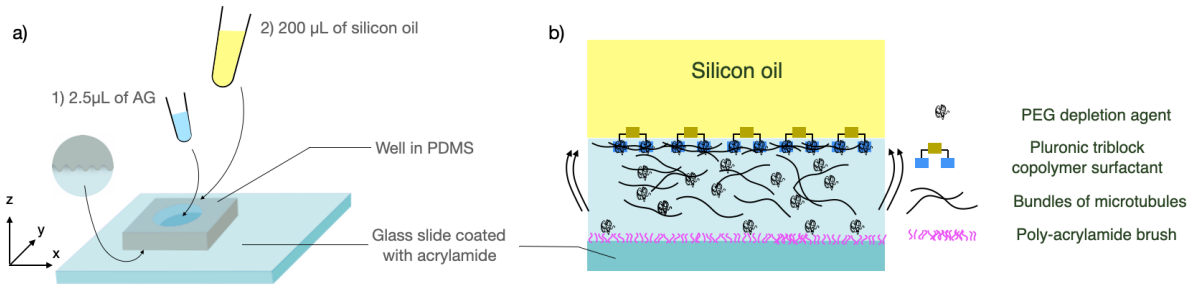

FIGURE 2.3 – **Assembly of the observation chamber. a)** A PDMS circular well is bound on the glass slide, filled with the active mixture and then covered with oil. **b)** MT bundles, initially in suspension in the water phase, self-assemble at the surfactant-stabilized oil interface within 1 hour.

2.2 Imposing lateral confinement with micro-printed grids

Grids manufacturing. To create lateral boundaries in the system, we create millimeter-sized platforms in photoresist encompassing the enclosures in which the AN will be trapped (Figure 2.4). Grids are 3-D printed with a two-photon polymerization printer, a Nanoscribe GT Photonic Professional device, with a negative-tone photoresist IP-S (Nanoscribe GmbH, Germany) and a 25x objective. Two-photon polymerization lithography prints 3-dimensional structures by polymerizing the photoresist point by point in space with a focused laser beam. The grids are directly printed on silicon substrates without any preparation to avoid adhesion of the resist to the substrate (plasma cleaner of the substrate, for example, would increase the adhesion). After developing 30 minutes in Propylene Glycol Monomethyl Ether Acetate (PGMEA 99.5%, Sigma Aldrich) and 5 minutes in isopropanol (Technical, VWR), a batch polymerization is performed with UV exposure (5 min at 80% of light power). The pattern resolution achieved is about 50 nm. The grid thickness is 100 µm, to ensure a good resistance during manipulation. Most of the time, the grid is made of various parts that need to be hold together with bridges spanning over the enclosure. Grid are designed with the software Inventor Professional.

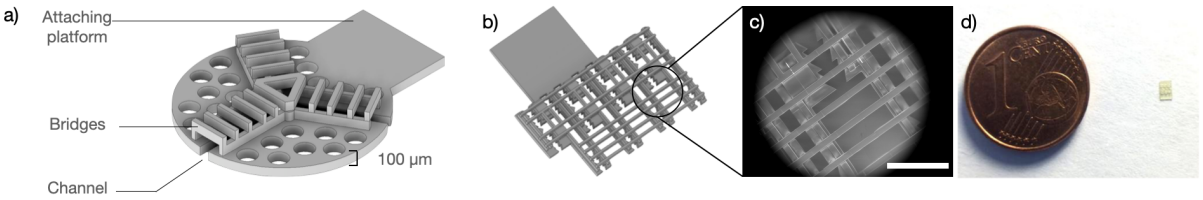

FIGURE 2.4 – **Grids. a)** Grids are 100 µm-thick platforms embedding several channels, the different parts being hold together by 200 µm-high bridges. Circular holes are often extruded to reduce the printing time. **b)** Grid embedding four AND/OR logical circuits, and **c)** Scanning Electron Microscopy image of a part of it, scale bar 500 µm. **d)** A grid next to a 1-cent coin.

Placing the grid at the interface. Grids are detached from the wafer after being immersed for 30 s in a propanol bath and moved to a PDMS cushion. Then grids are air-dried and attached

to the end of a capillary with UV-curable glue. The capillary is attached to a micromanipulator fixed to the microscope stage. Once the AN is well assembled, we can proceed to insert the grid at the interface. We first place the grid above the center of the observation chamber, and then we lower the grid slowly inside the oil phase until it reaches the interface (Figure 2.5 a, d, e, and a movie is accessible here). The moment at which the grid touches the interface is immediately noticeable on the camera, because capillary forces disturb greatly the nematic layer and microtubule bundles immediately react (Figure 2.5 e and f). After a few minutes, the bundles of microtubules below the platform have reorganized and found a place in the grid openings, where a water/oil interface still exist (Figure 2.5 b, c, g). This step requires dexterity, and a bit of luck. If the grid is placed too low, the interface might attach to the bridges used to hold the different parts of the grid together. Often an experiment is failed because of the interface placement : if too high, bridges will exert friction, if too curved, the dynamics can be altered and focus cannot be made on the whole film. The grid is hydrophilic.

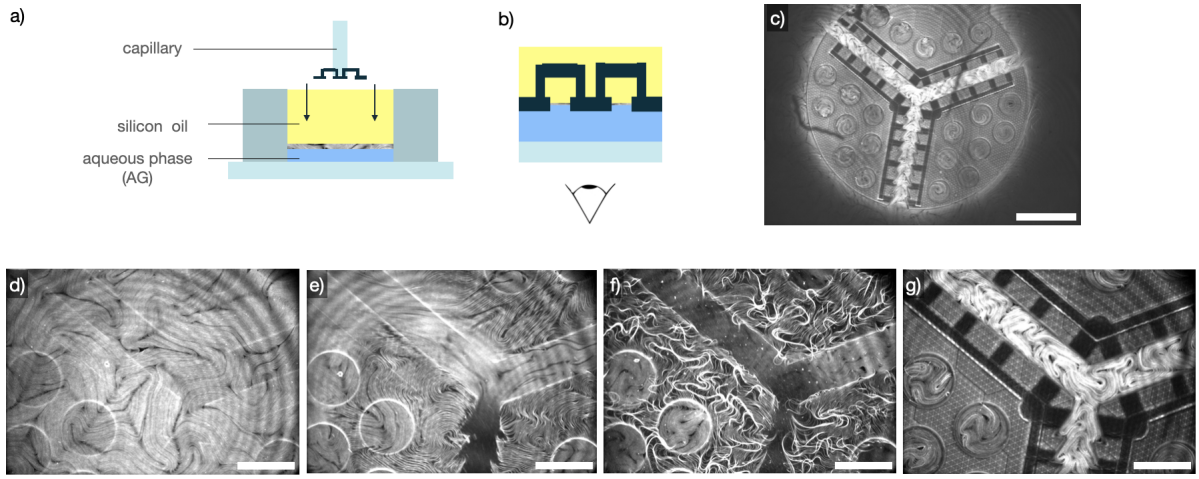

FIGURE 2.5 – **Placing the grid at the interface. a, b)** Side view of the system. **a)** The grid is bound to a capillary and lowered into the oil phase with a micromanipulator. **b)** The active nematic is trapped in the enclosures of grid placed at the interface. **c)** A large confocal image of a grid where the active nematic is confined in three connected channels. **d-g)** A time sequence during grid placement ; **d)** the grid is still above the AN layer ; **e)** the grid hits the AN, creating strong flows ; **f)** bundles under the grid detach ; **g)** 3 minutes later the AN is well confined within the channels. A movie of the full process is accessible here.

2.3 Confocal fluorescence microscopy

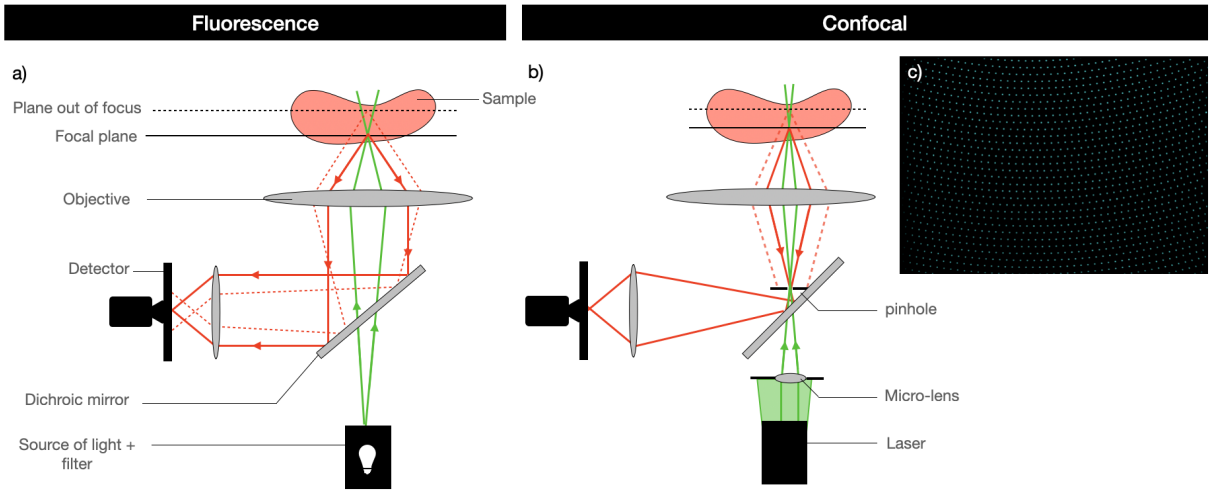

FIGURE 2.6 – **Principle of classic fluorescence microscopy and confocal fluorescence microscopy. a)** In classic fluorescence microscopy, the whole sample is illuminated and out of focus fluorophores contribute to the image that forms on the detector. **b)** Confocal microscopes illuminate a small region in the sample with a focused laser beam and cut the light emitted by out-of-focus fluorophores with pairs of co-aligned microlens and pinholes. **c)** The pinhole array of the spinning disk can be visualized on the detector by stopping the rotation of the disk.

In classic fluorescence microscopy, some components of interest in the sample are tagged with a fluorophore, that is a molecule that emit light at a specific wavelength upon light excitation at a shorter wavelength. The microscope is set-up in order to record the light emitted by the molecules (Figure 2.6 a). Since the emitted light is much less intense than the excitation light, the excitation light, reflected or transmitted by the sample, must be filtered out before reaching the detector. To separate the two colors, a semi-reflective mirror, called dichroic mirror, is placed on the observation path. It transmits selectively colors belonging to a narrow waveband, that we choose centered around the excitation light, and reflect all the other colors. This microscopy technique allows for high speed imaging and it is adapted to thin samples. However, it is does not offer the best resolution, in particular when the sample is thick. First, a point-like source in the sample, even in the focal plane, will project a small patch on the detector, because of diffraction through the objective aperture for instance (the so-called Airy disk) and optical aberrations. The size of a pixel is limited to the size of the patch, which limits the image resolution. In addition, point-like sources out of the focal plane will also contribute to the image, by illuminating an even larger region. Instead of a black background with neat bright spots corresponding to the fluorophores, the fluorescence micrograph is blurry because of out-of-focus light (Figure 2.7 c, d).

Confocal fluorescence microscopy improves the image resolution by blocking out-of-focus light (Figure 2.6 b and Figure 2.7 a, b). First, in contrast with fluorescence microscopy, where

the whole sample is illuminated, confocal microscopy selectively excites a point in the sample : the source of light is replaced by a laser beam focused by a tiny lens and pinhole (about 50µm) towards a point (x,y,z) in the sample. Only the fluorophores in a small region around this point, very narrow in the (x,y) plane, can emit back light. Second, the emitted light pass through the pinhole which block out-of-focus light. As a result, the confocal image has an improved resolution, both the the (x,y) plane and in the z direction, but a very short depth of field. It images a thin slice in the sample. The downside of this technique is that the image needs to be acquired pixel by pixel by moving the pinhole over the whole region of interest, which limits the acquisition rate greatly unless we increase the intensity of the laser, causing rapid photo bleaching. Spinning disk confocal microscopes have been invented precisely to scan faster. The unique pair of microlens and pinhole described before is replace by a spinning disk embedding an array of pinholes. Multiple pixels are acquired in parallel, and the high speed rotation of the disk scan the pinholes over the whole region of interest. Acquisition rate can be as high as 2000 fps.

Our microscope set-up. We image the active nematic layer using a Nikon eclipse Ti-E inverted microscope, equipped with a confocal spinning disk CSU-X1 from the brand Yokogawa and a motorized stage Nikon Ti-S-EJOY. Images are captured with a x10 objective (Nikon) and a camera Hamamatsu Orca Flash4.0, and acquired with the software NiS-Elements. The sample is excited with a laser beam at 647 nm. Exposure is between 200-500 ms depending on the sample fluorescence, and the acquisition frame rate is 2 fps.

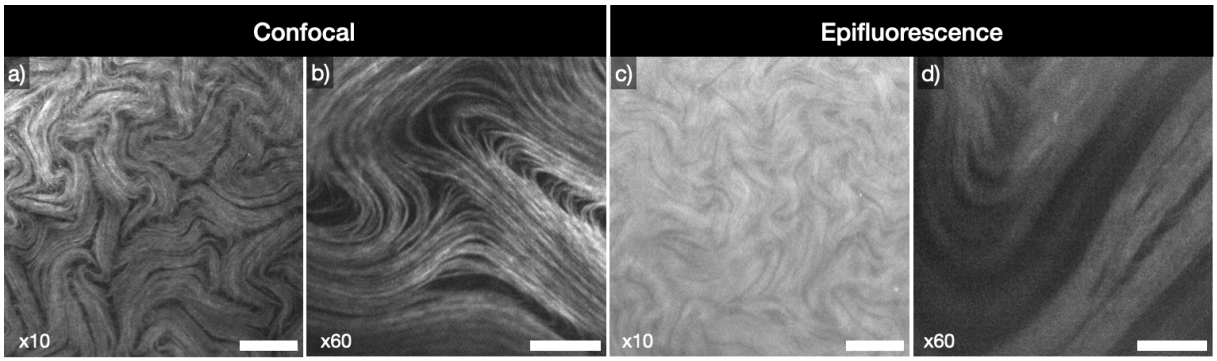

FIGURE 2.7 – **Confocal versus fluorescence microscopy.** Confocal images (**a, b**) of the AN layer are more defined than classic epifluorescence images (**c, d**), even though our system is a thin film. With an x10 objective (**a, c**), out-of-focus microtubules produce a bright background in c). At x60 magnification (**b, d**), mainly microtubules in the focal plane are responsible for the blurriness. Notice how bundles are sharp on the confocal image b), while they are more blurry in d). Scale bars for a, c : 100µm. Scale bars for b,d : 20µm.

3 Image analysis

3.1 Extracting the velocity field

To extract the velocity field from two consecutive images taken at time t and $t + \delta t$, I_1 and I_2, we use two different methods.

Particle Image Velocimetry (PIV) consists in seeding a fluid with light-scattering or fluorescent particles as tracer particles. The particle should be such that it can be assumed that they are purely advected by the fluid (matching density, small enough size...). I_1 is split into several interrogation windows W_{ij}^1, indexed by the horizontal coordinate i and the vertical coordinate j of its center. The interrogation window W_{ij}^1 from image I_1 is compared to all the windows of identical size in I_2 located within a larger search window with center i, j. The relative position of the window in I_2 for which the cross-correlation is maximum provides the vectorial displacement δ_{ij}^1 of the fluid contained in window W_{ij}^1 from time t and $t+\delta t$. By progressively decreasing the interrogation window size, a better PIV resolution can be achieved, but in the lower limit, this window should contain several tracers. We use a PIV cross-correlation ImageJ plugin [65] to extract velocity field from images. Sometimes, we seed the active nematic with fluorescent particles, but this prevent from acquiring at the same time the particle-free active nematic with the usual acquisition rate of 2fps. For this reason, we most often use the PIV method directly on the active nematic texture free of tracer particles. In such case, short scale density fluctuations (bundles of microtubules) as well as topological defects, replace the tracer particles. The resolution achieved is 10 µm. However, this method underestimates velocities parallel to the director field, where the density is more homogeneous (Figure 2.8 a).

Optical flow methods. When we want to infer the velocity field more precisely, we use an optical flow method developed by Sun et al [66] implemented in MATLAB. This method infers the velocity field $\boldsymbol{v}$ with pixel resolution, by minimizing a penalty function that trades off matching intensity levels in I_1 and I_2 and smoothness of $\boldsymbol{v}$. Velocity field are captured more precisely (Figure 2.8 b).

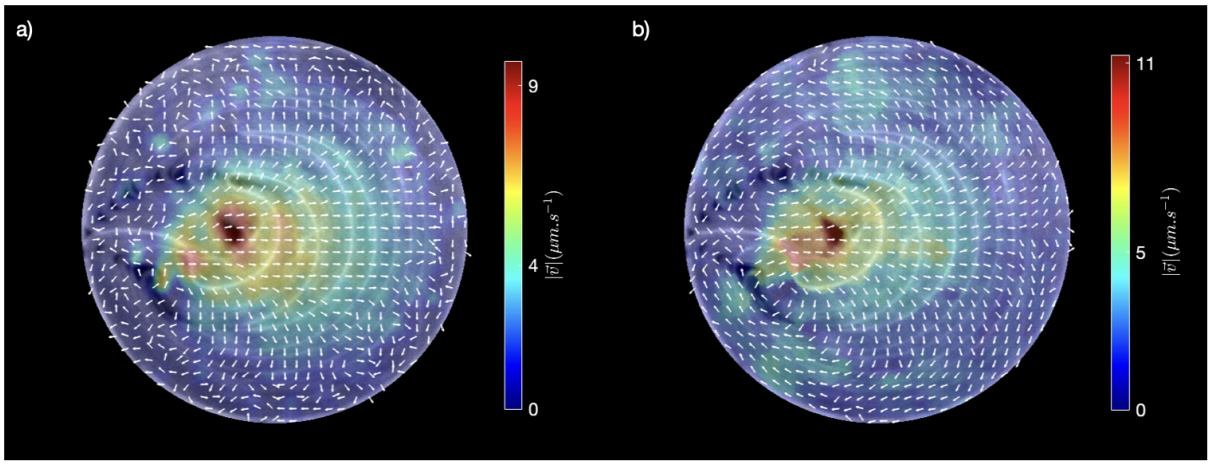

FIGURE 2.8 – **Velocity fields inferred from successive images. a)** Velocity field computed with a PIV cross-correlation algorithm, implemented in ImageJ. **b)** Velocity field computed with an optical flow method implemented in MATLAB. The vector field is normalized and quivered over the image, while the norm of the velocity is overlaid in color.

3.2 Detecting director field and topological defects

This method was developed by PW. Ellis during its PhD in the group of Alberto Fernandez-Nieves at Georgia Institute of Technology [67].

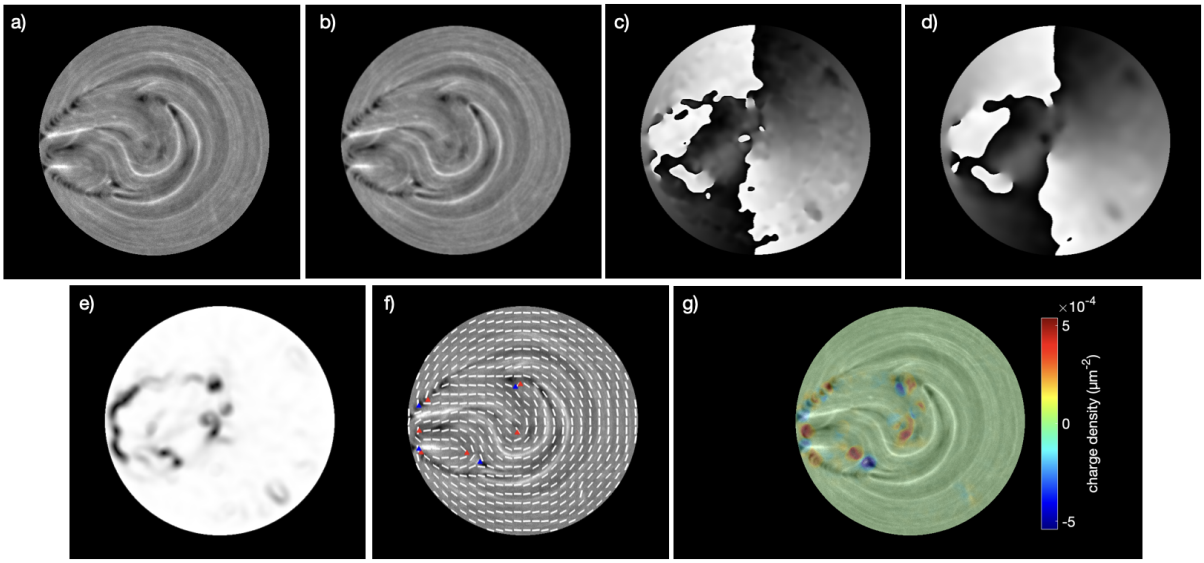

FIGURE 2.9 – **Step by step detection of director field and topological defects. a)** The raw image I ; **b)** the blurred image I after Gaussian filtering with $\sigma_1 = 1$; **c)** the angle of the eigenvector of the structure tensor with respect to the horizontal axis ; **d)** the angle of the eigenvector of the structure tensor after applying a Gaussian filter with $\sigma_2 = 7$; **e)** Gray scale image of the order parameter S. Black corresponds to $S = 0$, and white to $S = 1$. S is extracted from the $\boldsymbol{Q}$-tensor, estimated with a spatial average over a region of size β=16 pixels ; **f)** nematic director field, detected $+\frac{1}{2}$ defect (red triangles) and $-\frac{1}{2}$ defects (blue triangles) ; **g)** colormap of the diffuse charge density q.

Director field. The first step is to apply a Gaussian filter of standard deviation σ_1 to the initial image in gray scale $I(x, y)$ in order to remove part of the random noise (Figure 2.9 b). Then, the direction of the microtubules is extracted with a method called Coherence Enhanced Diffusion Filtering (CEDF) [68]. In brief, for each pixel of I, this method finds the direction in which the gray scale intensity varies the least. This direction is the eigenvector corresponding to the smallest eigenvalue of the structure tensor $\boldsymbol{\nabla} I(\boldsymbol{\nabla} I)^T$. A component-wise Gaussian filtering of standard deviation σ_2 is applied to the structure tensor before diagonalization. The orientation of the eigenvector with respect to the horizontal axis is given between $[0, \pi]$ and overlaid in gray scale in Figure 2.9 c. This provides us with the molecular director field $\boldsymbol{u}$ for each pixel that we use next to determine the nematic field $\boldsymbol{n}$ (Figure 2.9 f) .

$\boldsymbol{Q}$-tensor. In the next chapter, we will see that the right mathematical object to describe nematic order is not the vector field but a tensor field of order 2, i.e. a matrix, that we call the $\boldsymbol{Q}$-tensor. In the case of a 2D nematic, where the director field lays in a plane (x,y), a 2×2 matrix is enough to characterize nematic order. We compute the $\boldsymbol{Q}$-tensor with a spatial average involving the molecular field over a region of size β around each pixel :

$$\boldsymbol{Q} =< \boldsymbol{u} \otimes \boldsymbol{u} - \frac{1}{2}\boldsymbol{I_2} >_\beta, \tag{2.1}$$

where $\boldsymbol{I_2}$ is the 2×2 identity matrix. By virtue of the spectral theorem that applies to real symmetric matrices, $\boldsymbol{Q}$ can be diagonalized. The highest eigenvalue of $\boldsymbol{Q}$ is half the nematic order parameter S (Figure 2.9 e) and the associated eigenvector is the director field $\boldsymbol{n}$ (Figure 2.9 f) .

Topological defects and their topological charge. We decide that regions where the order parameter S is lower than a chosen threshold, usually $S < 0.1$, host a topological defect. The local minimum of this region is the core of the topological defect. The charge of the defect is determined by computing the winding number : the number of π-rotation of the nematic direction along a loop circling the defect.

Density of charge. When the nematic field is described by a $\boldsymbol{Q}$-tensor, topological defects are no longer singularities because the order parameter S becomes 0 at the defect. Hence, point-like defects do not make so much sense anymore. Instead, one can define a charge density field q from the gradients of the $\boldsymbol{Q}$-tensor [69] that is written

$$q = \frac{1}{\pi}(\partial_x Q_{x\alpha}\partial_y Q_{y\alpha} - \partial_x Q_{y\alpha}\partial_y Q_{x\alpha}). \tag{2.2}$$

The charge density is represented in Figure 2.9 g.

$+\frac{1}{2}$ defect orientation. $+\frac{1}{2}$ are polar and self-propelled in the direction of the comet head. The unit vector $\boldsymbol{p}$ representing their polarity can be defined as the resulting active force acting on the defect which is proportional to the divergence of the $\boldsymbol{Q}$-tensor, $-\boldsymbol{\nabla} \cdot \boldsymbol{Q}$ (Figure 2.10). We

average the divergence of the $\boldsymbol{Q}$-tensor on a loop $\mathcal{L}$ around the $+\frac{1}{2}$ defect and normalize it :

$$\boldsymbol{p} = -\frac{<\boldsymbol{\nabla}\cdot\boldsymbol{Q}>_{\mathcal{L}}}{|<\boldsymbol{\nabla}\cdot\boldsymbol{Q}>_{\mathcal{L}}|}. \tag{2.3}$$

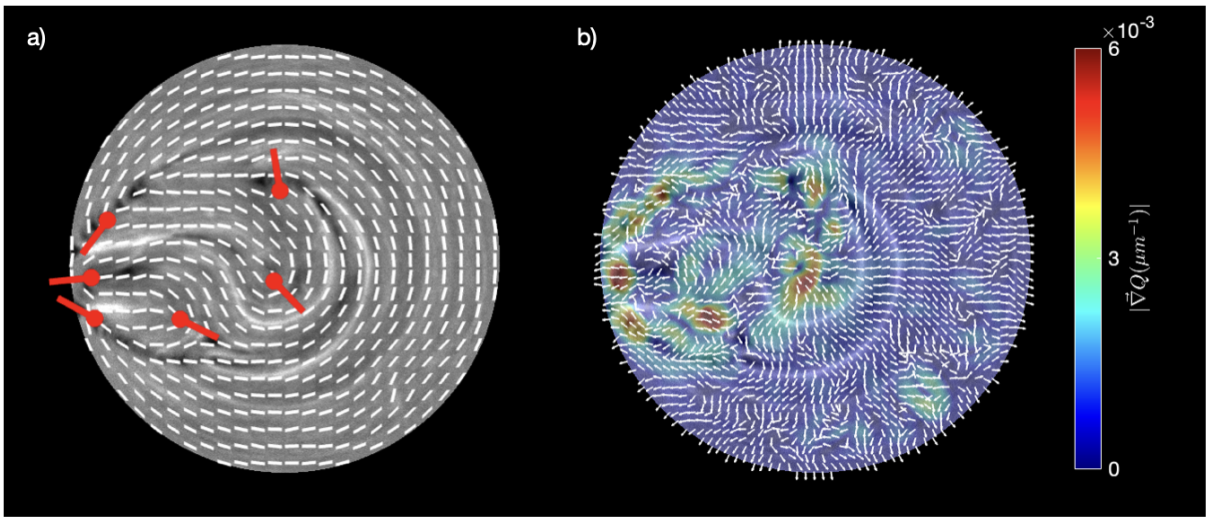

FIGURE 2.10 – $+\frac{1}{2}$ **defect orientation and active force field. a)** The core of $+\frac{1}{2}$ defects are marked with a red circle, and their orientation is represented with a rod pointing towards their head. **b)** The active force vector field $-\boldsymbol{\nabla}\cdot\mathbf{Q}$ is quivered in white and the colormap represents the force magnitude $|\boldsymbol{\nabla}\cdot\boldsymbol{Q}|$.

In practice, the three parameters σ_1, σ_2, β are optimized by eye on a small selection of frames from one experiment.

Defect tracking. To track negative and positive defects, we use a combinatorics-based particle tracking algorithm [70]. This algorithm identifies topological defects and track their positions across successive frames, which we use to reconstitute their trajectories.

Detection of topological defects in numerical simulations. Numerical simulations output directly the $\boldsymbol{Q}$-tensor, the order parameter S and the nematic director field $\boldsymbol{n}$. Detection of defects, their topological charge, orientation and tracking is achieved as described before from $\boldsymbol{Q}$.

Chapter 3

Theoretical model and numerical methods

In this chapter, we present the mathematical model used to describe the active nematic dynamics and the numerical method employed to carry out the simulations. In brief, we use a continuous hydrodynamic model for liquid crystals, namely the Beris–Edwards equations [71], supplemented with an active term accounting for the stretching action of the molecular motors. The equations of the model are highly non linear and thus require a robust numerical method to be solved. The method chosen is a hybrid lattice Boltzmann and finite difference method.

Remarks on notations. Unless stated otherwise, bold lowercase letters such as $\boldsymbol{a}$ represent column vectors, while bold uppercase letters such as $\boldsymbol{A}$ represent matrices. We call $\boldsymbol{e_1}$, $\boldsymbol{e_2}$, $\boldsymbol{e_3}$ the vector forming the basis of the cartesian coordinate system. We use Einstein summation convention, which means that we sum over indices that are repeated twice in a term. $\boldsymbol{AB}$ denotes the matrix product, *i.e.* $(\boldsymbol{AB})_{ij} = A_{ik}B_{kj}$. Similarly, $(\boldsymbol{A}^2)_{ij} = A_{ik}A_{kj}$ and $(\boldsymbol{A}^3)_{ij} = A_{ik}A_{kl}A_{lj}$. The trace of a matrix is written $\mathrm{Tr}(\boldsymbol{A}) = A_{ii}$. The tensorial product is denoted by $\otimes$, we have $(\boldsymbol{a} \otimes \boldsymbol{b})_{ij} = a_i b_j$ and $(\boldsymbol{A} \otimes \boldsymbol{b})_{ijk} = A_{ij} b_k$.

To take spatial derivatives, we use the operator "nabla", $\boldsymbol{\nabla} = \begin{pmatrix} \partial_x \\ \partial_y \\ \partial_z \end{pmatrix}$. The gradient of a vector is a second order tensor, $\boldsymbol{\nabla a} = \partial_k \boldsymbol{a} \otimes \boldsymbol{e_k}$, *i.e.* $(\boldsymbol{\nabla a})_{ij} = \partial_j a_i$. The gradient of a matrix is a third order tensor, $\boldsymbol{\nabla A} = \partial_k \boldsymbol{A} \otimes \boldsymbol{e_k}$, *i.e.* $(\boldsymbol{\nabla A})_{ijk} = \partial_k A_{ij}$. The divergence of a vector is the scalar $\boldsymbol{\nabla} \cdot \boldsymbol{a} = \partial_i a_i$; the divergence of a matrix is the vector $\boldsymbol{\nabla} \cdot \boldsymbol{A}$, with $(\boldsymbol{\nabla} \cdot \boldsymbol{A})_i = \partial_j A_{ji}$.

1 Passive liquid crystal

1.1 How can we mathematically describe nematic order ?

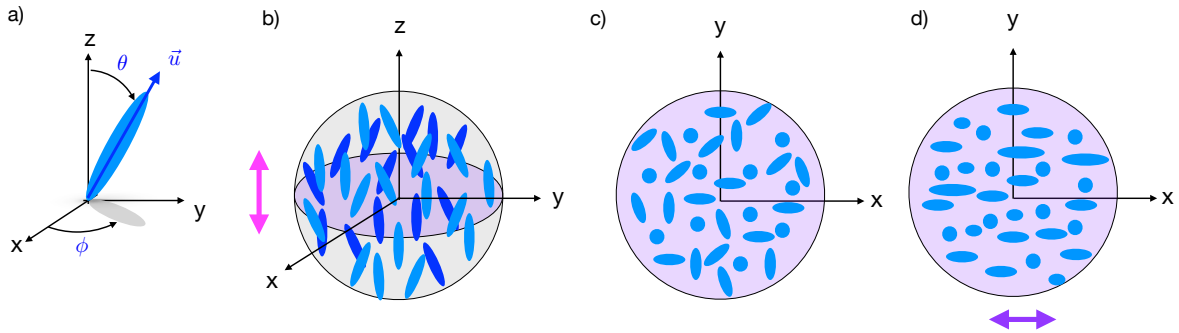

FIGURE 3.1 – **Mesogens distribution. a)** Spherical coordinates used to measure the mesogen orientation. **b)** The mesogens located inside the mesoscopic sphere have nematic order along $\boldsymbol{n} = \boldsymbol{e_z}$. **c, d)** View from the z-axis of the mesogens. **c)** For a uniaxial system, the orientation within the xy-plane is isotropic. **d)** For a biaxial system, the orientation within the xy plane is anisotropic. Here, the biaxial axis is $\boldsymbol{e_x}$.

The most convenient mathematical object to describe the orientation in a nematic phase is a tensor of rank 2, called the $\boldsymbol{Q}$-tensor. In 3-dimensions, this tensor is a 3×3 matrix. Let us consider a mesoscopic volume containing a large number of nematogens. Each nematogen within this volume can be represented by a unit vector $\boldsymbol{u}$ representing the molecular orientation (θ, ϕ) in the spherical coordinate system (Figure 3.1). The sign of $\boldsymbol{u}$ is arbitrary if the molecule has head-tail symmetry. The $\boldsymbol{Q}$-tensor is related to the second moment of the distribution of the molecular orientation $f(\theta, \phi)$:

$$\boldsymbol{Q} = < \boldsymbol{u} \otimes \boldsymbol{u} - \frac{1}{3}\boldsymbol{I} >_f . \tag{3.1}$$

By construction, $\boldsymbol{Q}$ is invariant under the transformation $\boldsymbol{u} \to \boldsymbol{u}$, and is symmetric and traceless. By virtue of the spectral theorem, the real symmetric matrix $\boldsymbol{Q}$ can be diagonalized in an orthonormal basis. Given its 3 eigenvalues $\lambda_1 \geq \lambda_2 \geq \lambda_3$ and their respective eigenvectors $\boldsymbol{m_1}$, $\boldsymbol{m_2}$ and $\boldsymbol{m_3}$, we can decompose $\boldsymbol{Q}$ in such a way :

$$\boldsymbol{Q} = \lambda_1 \boldsymbol{m_1} \otimes \boldsymbol{m_1} + \lambda_2 \boldsymbol{m_2} \otimes \boldsymbol{m_2} + \lambda_3 \boldsymbol{m_3} \otimes \boldsymbol{m_3}. \tag{3.2}$$

Now, $\boldsymbol{Q}$ is not any tensor, it is traceless and related to the orientation distribution $f(\theta, \phi)$ and this has some strong consequences on the eigenvalues :

$$\begin{aligned} \lambda_1 + \lambda_2 + \lambda_3 &= 0, \\ -\frac{1}{3} \leq \lambda_i &\leq \frac{2}{3}. \end{aligned} \tag{3.3}$$

We choose to express $\boldsymbol{Q}$ in a more meaningful way :

$$\boldsymbol{Q} = S(\boldsymbol{n} \otimes \boldsymbol{n} - \frac{1}{3}\boldsymbol{I}) + \frac{P}{2}(\boldsymbol{m_2} \otimes \boldsymbol{m_2} - \boldsymbol{m_3} \otimes \boldsymbol{m_3}), \tag{3.4}$$

with $\boldsymbol{n} = \boldsymbol{m_1}$, $S = \frac{3}{2}\lambda_1$ and $P = 2\lambda_2 + \lambda_1$. P and S must respect the following inequalities : $-\frac{1}{2} \leq S \leq 1$ and $-1 \leq P \leq 1$.

Interpretation of $\boldsymbol{Q}$ S is the order parameter associated to the main axis of order $\boldsymbol{n}$, and proportional to the highest eigenvalue of $\boldsymbol{Q}$. P is the biaxiality parameter associated to the second axis of order $\boldsymbol{m_1}$. When we look at the orientations of the mesogens within the mesoscopic volume through the main axis $\boldsymbol{n}$, if the orientations are isotropic around $\boldsymbol{n}$ (Figure 3.1 c), then the system is uniaxial, and since $\lambda_2 = \lambda_3$, $P = 0$. However, the distribution can be anisotropic around $\boldsymbol{n}$ and in this case P is non zero (Figure 3.1 d). The $\boldsymbol{Q}$ tensor has a physical meaning (represents the molecular orientation) if the eigenvalues respect the above-mentioned inequalities. In the isotropic state, $S = 0$ and $\boldsymbol{Q} = 0$.
Remarks : Being traceless and symmetric, for a 3D-system, $\boldsymbol{Q}$ has only 5 independent components that we note q_1, q_2, q_3, q_4, q_5. For uniaxial nematic order, the system is entirely characterized by S and $\boldsymbol{n}$, thus $\boldsymbol{Q}$ has only three independent components.

For passive liquid crystal that has reached equilibrium, the $\boldsymbol{Q}$-tensor field minimizes the total free energy of the system F_{tot}. For a system contained in the volume Ω bounded by the surface $\delta\Omega$, F_{tot} is the integral of the bulk free energy density, f_{bulk}, and the integral of the surface free energy density, f_{surf} :

$$F_{\text{tot}} = \int_{\Omega} f_{\text{bulk}} \mathrm{d}V + \int_{\partial\Omega} f_{\text{surf}} \mathrm{d}S. \tag{3.5}$$

The bulk free energy density takes often the form of the *Landau-de-Gennes free energy* density, which is composed of two terms : f_{phase} that accounts for the nematic to isotropic phase transition, and f_{elastic} that accounts for the orientational elasticity of the liquid crystal :$f_{\text{bulk}} = f_{\text{phase}} + f_{\text{elastic}}$. Their phenomenological expressions, that we will now explicit, has been determined by Taylor expansion of $\boldsymbol{Q}$ and $\boldsymbol{\nabla Q}$ around $\boldsymbol{Q} = 0$ and $\boldsymbol{\nabla Q} = 0$, and by taking into account all the transformations upon which the free energy must be invariant : $x \to -x$, $y \to -y$, $z \to -z$, any rotation of $\boldsymbol{Q}$...

1.2 The nematic-isotropic phase transition.

For a thermotropic liquid crystal, the first order (discontinuous) transition from the nematic state to the isotropic state as the temperature T is increased is captured by the phenomenological free energy derived with the Landau theory :

$$f_{\text{phase}} = \frac{A_0}{2}(1 - \frac{U}{3})\,\mathrm{Tr}(\boldsymbol{Q}^2) - \frac{A_0 U}{3}\,\mathrm{Tr}(\boldsymbol{Q}^3) + \frac{A_0 U}{4}(\mathrm{Tr}(\boldsymbol{Q}^2))^2, \tag{3.6}$$

where A_0 is a constant setting the scale of this energy, and U is a temperature-dependent parameter. Since, at equilibrium, the system adjusts the degree of order in order to minimize the free energy, U controls the value of S. Indeed, for uniaxial order along $\boldsymbol{e_x}$ and order parameter S, we can express the free energy as a function of S and the minimization of $f(S)$ leads to the following relationship linking the order parameter in the nematic phase S_0 to the parameter U : $S_0(U) = \frac{1}{4} + \frac{3}{4}\sqrt{1 - \frac{8}{3U}}$ for $U \geq \frac{8}{3}$ and $S(U) = 0$ for $U \leq \frac{8}{3}$. In Figure 3.2, we plot the shape of $f_{\text{phase}}(S)$ for different values of the parameter T (or U).

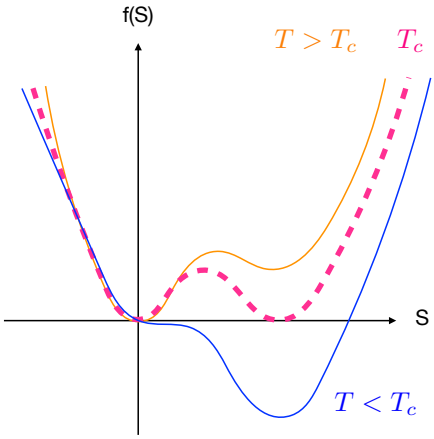

FIGURE 3.2 – **Nematic to isotropic phase transition.** f_{phase} is plotted versus the order parameter S. For $T > T_c$, the global minimum is $S = 0$. If a local minimum exists for $S > 0$, the nematic state is metastable. At $T = T_c$, the ground state is degenerate and the nematic and isotropic phases coexist. For $T < T_c$, the global minimum is $S > 0$ and the nematic phase is stable.

1.3 Elasticity

Now, let us introduce spatial deformations in the $\boldsymbol{Q}$-tensor field. The cost of the deformation is accounted by a bulk elastic free energy f_{elastic} depending on the gradients of $\boldsymbol{Q}$. Several expressions exist for f_{elastic}, here we chose the simplest form :

$$f_{\text{elastic}} = \frac{L}{2}(\boldsymbol{\nabla Q})^2 = \frac{L}{2}\partial_k Q_{ij}\partial_k Q_{ij}. \tag{3.7}$$

This is the one constant-approximation for the $\boldsymbol{Q}$-tensor representation, which means that splay, bend and twist distortions are equally penalized.

1.4 Surface anchoring

The system we consider, of volume Ω, is bounded by a boundary $\delta\Omega$. The anchoring of the liquid crystal at the interface $\delta\Omega$ is accounted for by a surface free energy term. To represent finite non-degenerate anchoring, we choose the surface energy :

$$f_{\text{surf}} = \frac{1}{2}W\,\text{Tr}[(\boldsymbol{Q} - \boldsymbol{Q_w})^2] \tag{3.8}$$

where $\boldsymbol{Q_w}$ is the tensor associated to the orientation favored at the surface of the system.

1.5 Energy minimization for equilibrium systems

The total free energy of the system F is thus the sum of the integral over the volume Ω of the bulk free energy, and the integral over the surface $\delta\Omega$ of the surface free energy :

$$F[\boldsymbol{Q}, \boldsymbol{\nabla Q}] = \int_\Omega f_{\text{bulk}}(\boldsymbol{Q}, \boldsymbol{\nabla Q}) \mathrm{d}V + \int_{\partial\Omega} f_{\text{surf}}(\boldsymbol{Q}) \mathrm{d}S. \tag{3.9}$$

The relaxation of a passive liquid crystal towards the equilibrium state is governed by the Ginzburg-Landau equation, which is the gradient descent of the total free energy. Each of the five independent components of $\boldsymbol{Q}$ evolves according to :

$$\begin{aligned} \partial_t Q_{ij} &= -\Gamma[\frac{\partial f_{\text{bulk}}}{\partial Q_{ij}} - \boldsymbol{\nabla} \cdot \frac{\partial f_{\text{bulk}}}{\partial \boldsymbol{\nabla} Q_{ij}}] \quad \forall \boldsymbol{r} \in \Omega \\ \text{and} \quad \partial_t Q_{ij} &= -\Gamma[\frac{\partial f_{\text{bulk}}}{\partial \boldsymbol{\nabla} Q_{ij}} \cdot \boldsymbol{\nu} + \frac{\partial f_{\text{surf}}}{\partial Q_{ij}}] \quad \forall \boldsymbol{r} \in \delta\Omega \end{aligned} \tag{3.10}$$

where $\boldsymbol{\nu}$ is the unit vector normal to the surface and Γ, called the rotational viscosity parameter, is the rate of the relaxation towards the equilibrium state. The terms on the right-hand side of the equations are gathered in the $\boldsymbol{H}$-tensor called the molecular field. The tensorial expression of the Ginzburg-Landau relaxation is written as

$$\partial_t \boldsymbol{Q} = \Gamma \boldsymbol{H}. \tag{3.11}$$

2 Active liquid crystals

Active liquid crystals spontaneously flow. Therefore, the nematic field $\boldsymbol{Q}$ and the flow field $\boldsymbol{v}$ are coupled. On the one hand, $\boldsymbol{Q}$ is advected, rotated by the fluid flow $\boldsymbol{v}$, on the other hand, the fluid is non Newtonian but viscoelastic, and $\boldsymbol{Q}$ is affecting the flow in return. A hydrodynamic theory can be derived using symmetry and conservations law. Hydrodynamics variables are $\boldsymbol{Q}$, the velocity field $\boldsymbol{v}$ and the density ρ. They follow a set of coupled, partial differential equations, called the *Beris-Edwards equations*, or the *nematodynamics equations*.

2.1 Evolution of the Q-tensor

In presence of a flow field $\boldsymbol{v}$, equation 3.11 needs to be modified. First, as any field, $\boldsymbol{Q}$ is advected by the flow, therefore $(\boldsymbol{v} \cdot \boldsymbol{\nabla})\boldsymbol{Q}$ must be added to the left-hand side. Moreover, since the $\boldsymbol{Q}$-tensor contains the orientation of the particle of liquid crystal, and the degree of ordering around this direction, $\boldsymbol{Q}$ is not simply transported by the velocity field but is also transformed by the velocity field. The velocity gradient matrix $(\boldsymbol{\nabla v})_{ij} = \partial_j v_i$ can be decomposed into a symmetric part, the strain rate tensor $\boldsymbol{D} = \frac{\boldsymbol{\nabla v} + \boldsymbol{\nabla v}^T}{2}$, and an asymmetric part, the spin tensor $\boldsymbol{\Omega} = \frac{\boldsymbol{\nabla v} - \boldsymbol{\nabla v}^T}{2}$. As the particle of fluid is rotated and sheared, the nematic direction $\boldsymbol{n}$ is rotated by

the spin tensor $\boldsymbol{\Omega}$, and the molecules are aligned by the strain tensor $\boldsymbol{D}$. In addition to this purely geometric considerations, the nematogens might have a physical response to the surrounding flow and react more to the strain rate or the spin rate tensors. The alignment parameter ξ accounts for this effect. Typically, for low ξ nematogens keep rotating (flow tumbling regime), while for high ξ nematogens align with the shear flow at an angle called the Leslie angle (flow alignment regime). This phenomenon is taken into account with a generalized advection term $\boldsymbol{S}$, also called co-rotation term, which takes the form

$$\boldsymbol{S} = (\xi\boldsymbol{D} + \boldsymbol{\Omega})(\boldsymbol{Q} + \frac{\boldsymbol{I}}{3}) + (\boldsymbol{Q} + \frac{\boldsymbol{I}}{3})(\xi\boldsymbol{D} - \boldsymbol{\Omega}) - 2\xi(\boldsymbol{Q} + \frac{\boldsymbol{I}}{3})\,\mathrm{Tr}(\boldsymbol{Q}\boldsymbol{\nabla}\boldsymbol{v}). \tag{3.12}$$

In the end, the equation for the $\boldsymbol{Q}$-tensor in presence of a flow field is

$$\partial_t\boldsymbol{Q} + (\boldsymbol{v}\cdot\boldsymbol{\nabla})\boldsymbol{Q} - \boldsymbol{S} = \Gamma\boldsymbol{H}. \tag{3.13}$$

2.2 Navier-Stokes equations

The generalized Navier-Stokes equations for the evolution of the velocity field are

$$\begin{aligned} \partial_t\rho + \boldsymbol{\nabla}\cdot(\rho\boldsymbol{v}) &= 0, \\ \rho[\partial_t\boldsymbol{v} + (\boldsymbol{v}\cdot\boldsymbol{\nabla})\boldsymbol{v}] &= \boldsymbol{\nabla}\cdot\boldsymbol{\Pi}_{\text{passive}} + \boldsymbol{\nabla}\cdot\boldsymbol{\Pi}_{\text{active}}, \end{aligned} \tag{3.14}$$

where $\boldsymbol{\Pi}_{\text{active}}$ is the active stress tensor, and $\boldsymbol{\Pi}_{\text{passive}}$ is the passive stress tensor. The passive stress tensor is composed of an isotropic contribution $\boldsymbol{\Pi}_{\text{iso}}$ and an anisotropic contribution coming from the viscoelastic nature of the liquid crystal $\boldsymbol{\Pi}_{\text{LC}}$. We have

$$\begin{aligned} &\boldsymbol{\Pi}_{\text{passive}} = \boldsymbol{\Pi}_{\text{iso}} + \boldsymbol{\Pi}_{\text{LC}}, \\ \text{with}\quad &\boldsymbol{\Pi}_{\text{iso}} = 2\eta\boldsymbol{D} - P_0\boldsymbol{I}, \\ \text{and}\quad &\boldsymbol{\Pi}_{\text{LC}} = 2\xi(\boldsymbol{Q} + \frac{\boldsymbol{I}}{3})\,\mathrm{Tr}(\boldsymbol{Q}\boldsymbol{H}) - \xi\boldsymbol{H}(\boldsymbol{Q} + \frac{\boldsymbol{I}}{3}) - \xi(\boldsymbol{Q} + \frac{\boldsymbol{I}}{3})\boldsymbol{H} - \boldsymbol{\nabla}\boldsymbol{Q} : \frac{\delta F}{\delta\boldsymbol{\nabla}\boldsymbol{Q}} + \boldsymbol{Q}\boldsymbol{H} - \boldsymbol{H}\boldsymbol{Q}. \end{aligned} \tag{3.15}$$

The equation above makes use of the special notation $(\boldsymbol{\nabla}\boldsymbol{Q} : \frac{\delta F}{\delta\boldsymbol{\nabla}\boldsymbol{Q}})_{ij} = \partial_j Q_{\alpha\beta}\frac{\delta F}{\delta\partial_i Q_{\alpha\beta}}$.

2.3 Active stress

The active stress, $\boldsymbol{\Pi}_{\text{active}}$, accounts for the active forces exerted by the motors. Motors are stretching microtubules bundles which can be viewed as extensile rods. Let us consider the α-th bundle with its center of mass located at $\boldsymbol{r_\alpha}$ and the molecular orientation $\boldsymbol{u_\alpha}$. We assume that it exerts a force dipole on the fluid, that is to say two point-like forces, one acting on the point $\boldsymbol{r_\alpha} + a\boldsymbol{u_\alpha}$ in direction of $+\boldsymbol{u_\alpha}$ with norm f, the other acting on the point $\boldsymbol{r_\alpha} - a\boldsymbol{u_\alpha}$ in direction of $-\boldsymbol{u_\alpha}$ with norm f. If $f > 0$, the force dipole is extensile. The force density exerted by this bundle is therefore

$$\begin{aligned}\boldsymbol{f_\alpha}(\boldsymbol{r}) &= f\boldsymbol{u_\alpha}\delta(\boldsymbol{r}-(\boldsymbol{r_\alpha}+a\boldsymbol{u_\alpha}))-f\boldsymbol{u_\alpha}\delta(\boldsymbol{r}-(\boldsymbol{r_\alpha}-a\boldsymbol{u_\alpha}))\\ &= -f\boldsymbol{u_\alpha}[\delta(\boldsymbol{r}-\boldsymbol{r_\alpha}+a\boldsymbol{u_\alpha})-\delta(\boldsymbol{r}-\boldsymbol{r_\alpha}-a\boldsymbol{u_\alpha})].\end{aligned} \tag{3.16}$$

We can expand the delta function around $\boldsymbol{r}-\boldsymbol{r_\alpha}$ at first order to express the force density as the divergence of a tensor :

$$\begin{aligned}\boldsymbol{f_\alpha}(\boldsymbol{r}) &= -f\boldsymbol{u_\alpha}[2a\boldsymbol{u_\alpha}\cdot\boldsymbol{\nabla}\delta(\boldsymbol{r}-\boldsymbol{r_\alpha})]\\ \boldsymbol{\nabla}\cdot\boldsymbol{\Pi_\alpha} &= -2af\boldsymbol{\nabla}\cdot[\boldsymbol{u_\alpha}\otimes\boldsymbol{u_\alpha}\delta(\boldsymbol{r}-\boldsymbol{r_\alpha})].\end{aligned} \tag{3.17}$$

By summing the contributions of all the bundles contained in the particle of fluid, we see that the total active stress tensor is proportional to the $\boldsymbol{Q}$-tensor :

$$\boldsymbol{\Pi}_{\text{active}} = -\zeta\boldsymbol{Q}. \tag{3.18}$$

The activity parameter ζ depends on the number of active units in the particle of fluid, the length of the active unit and the force f, and is positive in the case of extensile active nematics [72].

2.4 Active anchoring

For the microtubule-based active nematic system, we observe that the mesogens have a planar anchoring with interfaces and lateral boundaries. This effective planar anchoring does not originate from chemical interaction, but rather from hydrodynamic interactions. It is referred to as *active anchoring*. However, in our model we account for the anchoring just as for a passive liquid crystal with a surface energy term (equation 3.8).

3 Hybrid Lattice Boltzmann method

The equations for $\boldsymbol{Q}$-tensor and the velocity field $\boldsymbol{v}$ are both highly non-linear. In the Navier-Stokes equation, problematic terms are on the right-hand side, since at low Reynolds number we can neglect the advection term on the left-hand side. They need robust numerical methods to be solved. Several numerical methods can be used to solve the Beris-Edwards equations. One that is popular is the Lattice Boltzmann Method (LBM), that proved to be well-suited for simulations of complex fluids [73]. At first, a full LBM method was proposed to solve the equations for $\boldsymbol{Q}$-tensor and the velocity field $\boldsymbol{v}$ [74, 75], but, in 3D, this is very memory-demanding because many variables need to be stored and evolved. Thus, a hybrid method was proposed, where the $\boldsymbol{Q}$ is evolved with finite differences and the velocity field $\boldsymbol{v}$ is evolved with the LBM [76].

3.1 The Boltzmann equation

The LBM is based on the Boltzmann equation and kinetics theory, which describe the fluid at the mesoscale by the function $f(\boldsymbol{x},\boldsymbol{c},t)$ representing the mass density of particles located at $\boldsymbol{x}$

with velocity $\boldsymbol{c}$ at time t. We call $\boldsymbol{c}$ the microscopic velocity, it is not the velocity of a macroscopic volume of fluid, which is $\boldsymbol{v}(\boldsymbol{x},t)$. The distribution function is very rich in information. From its moments we can recover all the hydrodynamic fields, in particular the density ρ, the macroscopic velocity $\boldsymbol{v}$, the total energy density ρE :

$$\begin{aligned}\rho(\boldsymbol{x},t) &= \int f(\boldsymbol{x},\boldsymbol{c},t)d^3c \\ \rho(\boldsymbol{x},t)\boldsymbol{v}(\boldsymbol{x},t) &= \int \boldsymbol{c}f(\boldsymbol{x},\boldsymbol{c},t)d^3c \\ \rho(\boldsymbol{x},t)E(\boldsymbol{x},t) &= \frac{1}{2}\int |\boldsymbol{c}|^2 f(\boldsymbol{x},\boldsymbol{c},t)d^3c\end{aligned} \tag{3.19}$$

The Boltzmann equation describes how the distribution function $f(\boldsymbol{x},\boldsymbol{c},t)$ is transformed by *forces* applied on the particle as it is travelling freely and the collisions with other particles :

$$\frac{\partial f}{\partial t} + \boldsymbol{c}\cdot\frac{\partial f}{\partial \boldsymbol{x}} + \frac{\boldsymbol{F}}{\rho}\cdot\frac{\partial f}{\partial \boldsymbol{c}} = \Omega(f) \tag{3.20}$$

where the *vector* $\boldsymbol{F}$ is the density field of body forces (for instance, gravitational force) and Ω is the operator representing the effect of the collisions. In this description, viscous forces and pressure forces result from the collisions with other particles. The effect of the collisions is to bring the particle of fluid towards *local equilibrium*. Given the macroscopic velocity $\boldsymbol{v}$, collisions even out the distribution of the velocities around the $\boldsymbol{v}$ and relax $f(\boldsymbol{x},\boldsymbol{c},t)$ towards the equilibrium distribution function $f^{\mathrm{eq}}(\boldsymbol{x},\boldsymbol{c}-\boldsymbol{v},t)$. Several operators exist, but the most common and the one that we choose is the Bhatnagar, Gross, Krook (BGK) collision operator

$$\Omega_{BGK}(f) = -\frac{1}{\tau}(f - f^{eq}), \tag{3.21}$$

where τ is the relaxation time and control the value of the shear viscosity η. By construction, the collision operator conserves mass, momentum and energy, as it should for elastic collisions. The equilibrium distribution function is the Maxwell-Boltzmann distribution centered around the macroscopic velocity $\boldsymbol{v}$:

$$f^{\mathrm{eq}}(\boldsymbol{x},\boldsymbol{c}-\boldsymbol{v},t) = \rho\left[\frac{1}{2\pi RT}\right]^{\frac{3}{2}} e^{-|\boldsymbol{c}-\boldsymbol{v}|^2/(2RT)} \tag{3.22}$$

Because of the presence of $\boldsymbol{v}$ in $f^{\mathrm{eq}}(\boldsymbol{x},\boldsymbol{c},t)$, the collision term depends in a non-linear way on $f(\boldsymbol{x},\boldsymbol{c},t)$.

3.2 Discretization of the Boltzmann equation

The Lattice Boltzmann Method discretises space, time and the space of the microscopic velocities. In 3D, space is discretised by defining nodes on a cubic lattice of lattice size Δx (we will use $\Delta x = 1$). Time is discretised with regular time intervals Δt (we will use $\Delta t = 1$). Microscopic velocities are discretised with the D3Q15 velocity set composed of 15 velocities $\boldsymbol{c_i}$ (they are vectors) with associated weights w_i. The microscopic velocities are such that, a particle

located on a node $\boldsymbol{x}$ at time t with velocity $\boldsymbol{c_i}$ hopes exactly on one of the neighbouring nodes defined by the velocity set at time $t+\Delta t$. The D3Q15 velocity set is composed of the rest velocity $\boldsymbol{c_0} = (0,0,0)^T$, with associated weight $\frac{2}{9}$, the velocities pointing to the direct neighbours on the square lattice $\boldsymbol{c_1}$, $\boldsymbol{c_2}$, $\boldsymbol{c_3}$, $\boldsymbol{c_4}$, $\boldsymbol{c_5}$, $\boldsymbol{c_6}$ with associated weight $\frac{1}{9}$, and the velocities pointing to the diagonal corners of the cube $\boldsymbol{c_7}$, $\boldsymbol{c_8}$, ..., $\boldsymbol{c_{14}}$ with associated weight $\frac{1}{72}$. The D3Q15 velocity set is depicted in Figure 3.3.

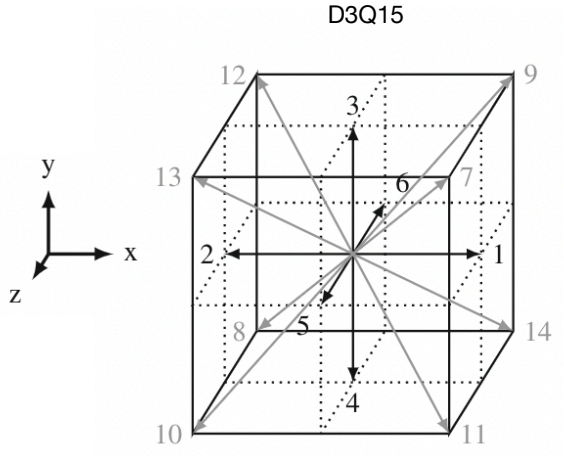

$$+ \quad \boldsymbol{c_0} = (0,0,0) \qquad w_0 = \frac{2}{9}, \quad w_{1,2,3,4,5,6} = \frac{1}{9}, \quad w_{7,8,9,10,11,12,13,14} = \frac{1}{72}$$

FIGURE 3.3 – **The D3Q15 velocity set.** The velocity set is composed of 15 velocities $\boldsymbol{c_i}$. The 0-velocity vector, the velocities pointing to the centers of the 6 faces of the cube, and the velocities pointing to the 8 diagonal corners. The velocity set also includes the weights w_i associated to $\boldsymbol{c_i}$. Adapted from [73].

Remarks : in all this section about the Lattice Boltzmann method latin indices, such as i, refer to Lattice Boltzmann directions. Therefore, $\boldsymbol{c_i}$ is a vector. Greek indices, such as α, refer to the spatial coordinates x, y, z. Therefore, $c_{i\alpha}$ refers to the α-coordinate of velocity $\boldsymbol{c_i}$. We apply Einstein summation rule only to Greek indices.

The continuous distribution function $f(\boldsymbol{x}, \boldsymbol{c}, t)$ is replaced by the discrete distribution $f_i(\boldsymbol{x}, t)$ representing the mass density of particles located at $\boldsymbol{x}$ with velocity $\boldsymbol{c_i}$ at time t. The *discrete velocity Boltzmann equations* are derived from the Boltzmann equation by discretizing the velocity space only, while space and time are still continuous. With Einstein summation rule applied to Greek indices only, it is written as

$$\partial_t f_i + c_{i\alpha}\partial_\alpha f_i = \Omega_i(\boldsymbol{x}, t) + F_i(\boldsymbol{x}, t). \tag{3.23}$$

This equation describes how discrete distributions $f_i(\boldsymbol{x}, t)$ are transformed via advection (left-hand side), collisions with other particles of fluid (encompassed by the scalar quantity Ω_i) and body forces applied on the particle (encompassed by the scalar quantity F_i). The discretized quantities f_i, Ω_i, and F_i are obtained through Hermite expansion and Gauss quadrature. The discretization of space and time by integrating equation 3.23 between t and $t + \Delta t$ then leads

to the *Lattice Boltzmann Equations* (LBE). Below we show a first order approximation :

$$f_i(\boldsymbol{x} + \boldsymbol{c_i}\Delta t, t + \Delta t) = f_i(\boldsymbol{x}, t) + \Delta t(\Omega_i + F_i). \tag{3.24}$$

3.3 Recovering hydrodynamic fields

Hydrodynamic fields can be recovered from the populations f_i on the lattice nodes $\boldsymbol{x}$:

$$\begin{aligned} \rho(\boldsymbol{x}, t) &= \sum_i f_i(\boldsymbol{x}, t), \\ \rho(\boldsymbol{x}, t)\boldsymbol{v}(\boldsymbol{x}, t) &= \sum_i \boldsymbol{c_i} f_i(\boldsymbol{x}, t). \end{aligned} \tag{3.25}$$

3.4 Collision operator

The discrete versions of the BGK collision operator Ω_i and the equilibrium distribution function f_i^{eq} are

$$\begin{aligned} \Omega_i &= -\frac{f_i - f_i^{eq}}{\tau}, \\ \text{and} \quad f_i^{\text{eq}} &= w_i \rho \left[1 + \frac{\boldsymbol{v} \cdot \boldsymbol{c_i}}{c_s^2} + \frac{(\boldsymbol{v} \cdot \boldsymbol{c_i})^2}{2c_s^4} - \frac{\boldsymbol{v} \cdot \boldsymbol{v}}{2c_s^2} \right], \\ \text{with} \quad c_s^2 &= \frac{1}{3}. \end{aligned} \tag{3.26}$$

Remark : if $\tau = 1$, the distribution has fully relaxed towards the equilibrium distribution in one time-step.

3.5 Force term

The discrete version of the force term $-\frac{\boldsymbol{F}}{\rho} \cdot \frac{\partial f}{\partial \boldsymbol{c}}$ is the set of scalar quantities F_i which are written as

$$F_i = w_i \left[\frac{c_{i\alpha}}{c_s^2} + \frac{(c_{i\alpha}c_{i\beta} - c_s^2\delta_{\alpha\beta})v_\beta}{c_S^4} \right] F_\alpha. \tag{3.27}$$

Here, F_α is the α-coordinate of the body force $\boldsymbol{F} = \boldsymbol{\nabla} \cdot \boldsymbol{\Pi}_{\text{LC}} + \boldsymbol{\nabla} \cdot \boldsymbol{\Pi}_{\text{active}}$.

3.6 Propagation/collision

All numerical schemes of the lattice Boltzmann equation evolves the distribution f_i from time t to time $t + \Delta t$ through steps of *propagation* and steps of *collision*. Here, we present a first order scheme for the force-free case $\boldsymbol{F} = 0$ in order to introduce the technique in a simple way, illustrated in Figure 3.4. Starting from the initial distributions t $f_i(\boldsymbol{x}, t)$ at time, we compute the macroscopic quantities $\boldsymbol{v}(\boldsymbol{x}, t)$ and $\rho(\boldsymbol{x}, t)$ in order to compute the value of $f_i^{\text{eq}}(\boldsymbol{x}, t)$ and $\Omega_i(\boldsymbol{x}, t)$. We apply a step of collision that transforms *locally* $f_i(\boldsymbol{x}, t) \to f_i^\star(\boldsymbol{x}, t) = f_i(\boldsymbol{x}, t)(1 - \frac{1}{\tau}) + f_i^{\text{eq}}(\boldsymbol{x}, t)\frac{1}{\tau}$. We have to create a new variable $f_i^\star(\boldsymbol{x}, t)$ and keep in memory $f_i(\boldsymbol{x}, t)$ as we compute the populations after collisions. Then, we apply a step of propagation :

the population $f_i^\star(\boldsymbol{x}, t)$ is advected to the neighbouring node $\boldsymbol{x} + \boldsymbol{c_i}$: $f_i(\boldsymbol{x} + \boldsymbol{c_i}, t+1) = f_i^\star(\boldsymbol{x}, t)$. The new macroscopic quantities can be computed at time $t + 1$.

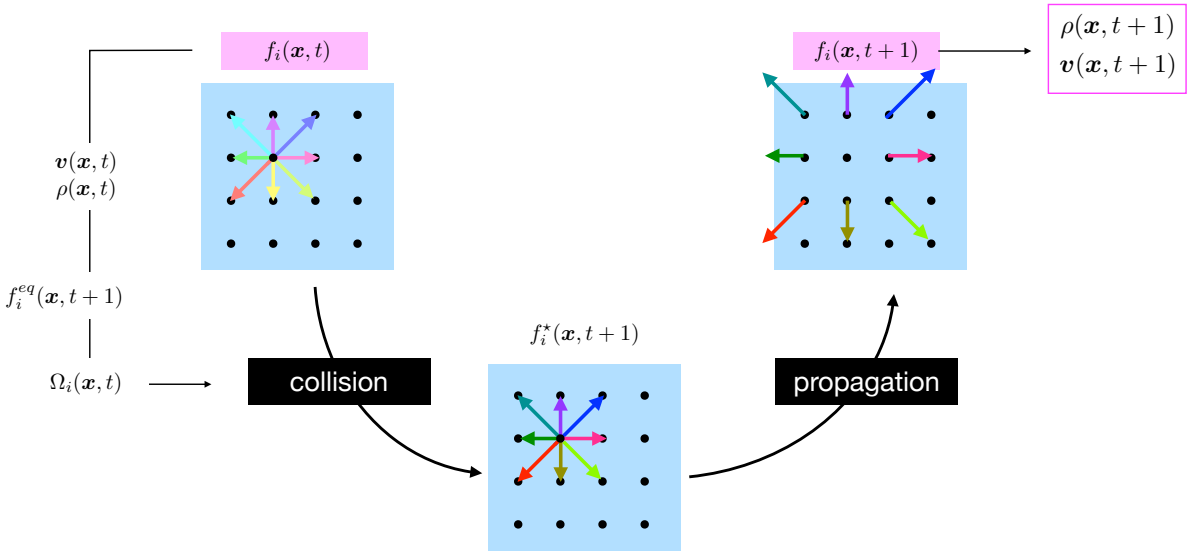

FIGURE 3.4 – **Collision-propagation scheme.** Illustration for the D2Q9 lattice. Arrows direction and length represent the microscopic velocity c_i, the color represents the population f_i. After the collision step, populations have changed locally : the color have changed but the arrow did not move. After the propagation step, populations are advected without being changed.

3.7 Boundary conditions

Boundary node. We consider a system delimited by walls. Boundary nodes are the nodes of the system that have at least one D3Q15 link connecting them to the solid node, and one D3Q15 link connecting them to the fluid node. If the boundary is placed exactly *on* the boundary node, the boundary conditions are referred to as *wet* or *on-grid*. If the boundary between the solid and the fluid lies in between the nodes of the lattice, they are referred to as *midway*, *mid-drid*, or *halfway*. Such configurations are shown in Figure 3.5 a. We use mid-grid boundary conditions in the numerical simulations. When a particle hits the boundary of the system, its microscopic velocity $\boldsymbol{c_i}$ is changed differently whether the wall enforces no slip of free slip boundary conditions.

No-slip with mid-grid bounce-back. If the wall imposes no slip, a possible way to encode that in the LBM is to use the *mid-grid bounce-back* boundary condition (Figure 3.5 d). When a particle with an incident velocity $\boldsymbol{c_i}$ hits the wall, its new velocity has the opposite direction ${\boldsymbol{c_i}}^S = -\boldsymbol{c_i}$. At the end of the propagation step, the populations are still located on the same node but their velocities have been reversed. As a result, the macroscopic velocity at the boundary is zero.

Remark : the boundary conditions described above results in no-slip only if the initial velocity field $\boldsymbol{v}(\boldsymbol{x_b}, t)$ respects the boundary condition. In practice, the boundary condition is applied during the propagation step.

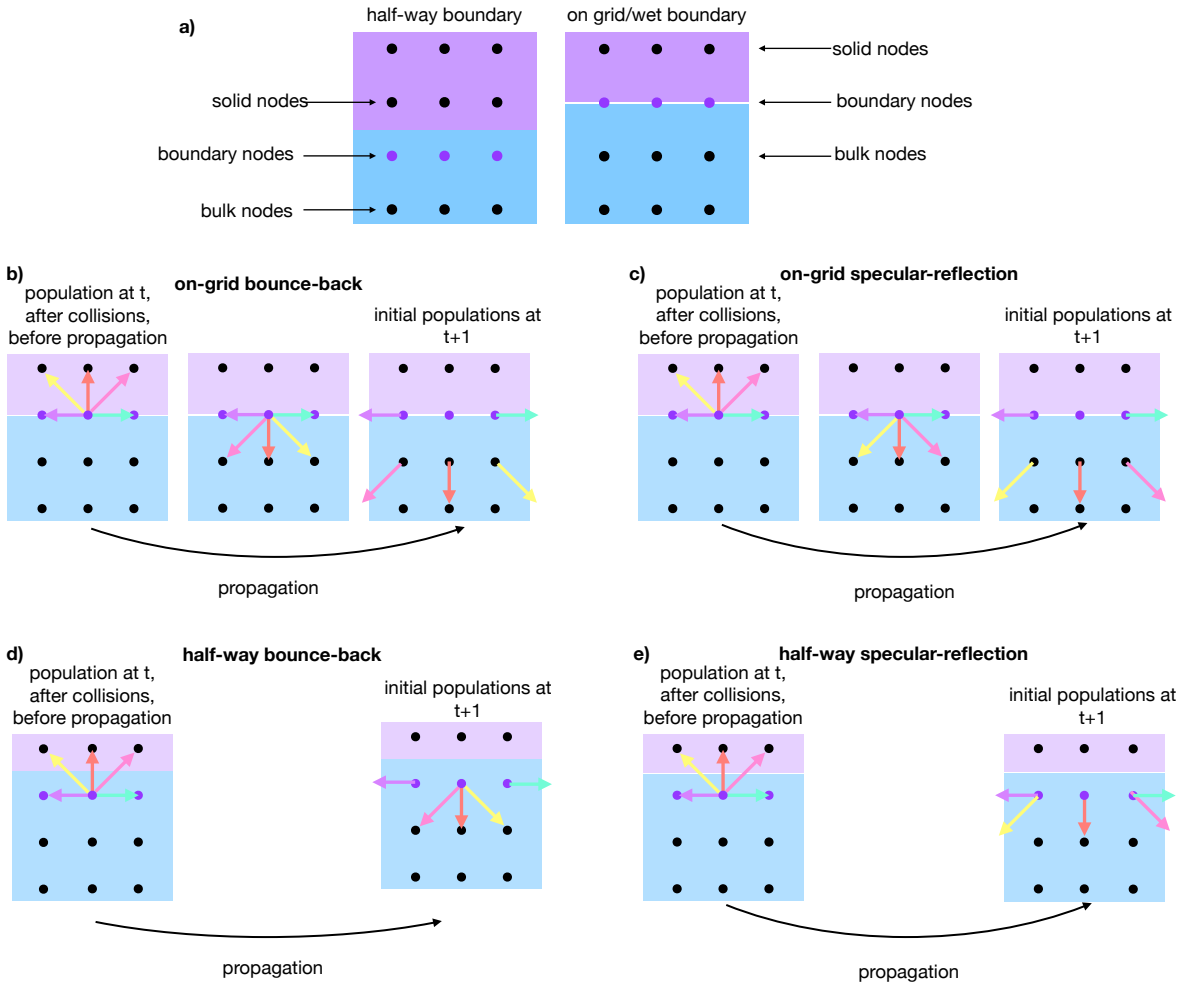

FIGURE 3.5 – **Boundary conditions. a)** Left : the wall is half-way between the lattice nodes. Right : the wall is exactly sitting at the lattice wall. **b)** Collision and propagation steps for on-grid bounce-back. **c)** Collision and propagation steps for on-grid specular reflection. **d)** Collision and propagation steps for mid-grid bounce-back. **e)** Collision and propagation steps for mid-grid specular reflection.

3.8 Initial conditions

Given the initial hydrodynamic velocity field $\boldsymbol{v}(\boldsymbol{x}, \boldsymbol{t = 0})$, the initial populations $f_i(\boldsymbol{x}, t = 0)$ are the local equilibium populations $f_i^{\text{eq}}(\boldsymbol{x}, \boldsymbol{v})$ (equation 3.26).

3.9 Numerical scheme for the velocity evolution

In this paragraph, we describe the numerical scheme with which we evolve the populations f_i from time t to time $t+1$. A numerical scheme (discrete space and time) is obtained by integrating

equation 3.23 between t and $t + \Delta t$:

$$\begin{aligned} \int_t^{t+\Delta t} (\partial_t f_i + c_{i\alpha}\partial_\alpha f_i) &= \int_t^{t+\Delta t} (\Omega_i + F_i) \\ f_i(\boldsymbol{x} + \boldsymbol{c_i}\Delta t, t + \Delta t) - f_i(\boldsymbol{x}, t) &= \int_t^{t+\Delta t} (\Omega_i + F_i) \end{aligned} \tag{3.28}$$

It means that we need to take into account all the collisions and body forces applied to the particle during the time interval. In equation 3.24, we did a first order integration by assessing the collision term and force term at the initial time t : $\int_t^{t+\Delta t} \Omega_i + F_i = (\Omega_i(\boldsymbol{x}, t) + F_i(\boldsymbol{x}, t))\Delta t$. Although this scheme is explicit, it does not have a good accuracy. Instead, we will use the trapezoidal rule :

$$\begin{aligned} \int_t^{t+\Delta t} \Omega_i &= \frac{\Omega_i(\boldsymbol{x}, t) + \Omega_i(\boldsymbol{x} + \boldsymbol{c_i}, t + \Delta t)}{2}\Delta t \\ \int_t^{t+\Delta t} F_i &= \frac{F_i(\boldsymbol{x}, t) + F_i(\boldsymbol{x} + \boldsymbol{c_i}, t + \Delta t)}{2}\Delta t \end{aligned} \tag{3.29}$$

However, the scheme becomes implicit because the collisions and forces now depend on the system state at time $t + \Delta t$. A change of variables $f_i \to \overline{f_i}$ produces an explicit scheme for $\overline{f_i}$. Let's use the variable :

$$\overline{f_i} = f_i - \frac{(\Omega_i + F_i)\Delta t}{2} \tag{3.30}$$

The second order Lattice Boltzmann equation with the trapezoidal rule and the change of variable writes

$$\overline{f_i}(\boldsymbol{x} + \boldsymbol{c_i}\Delta t, t + \Delta t) - \overline{f_i}(\boldsymbol{x}, t) = (\Omega_i + F_i)\Delta t. \tag{3.31}$$

Using the BGK operator for Ω_i, and using the change of variable in order to replace f_i with $\overline{f_i}$ leads to the following equation :

$$\begin{gathered} \overline{f_i}(\boldsymbol{x} + \boldsymbol{c_i}\Delta t, t + \Delta t) - \overline{f_i}(\boldsymbol{x}, t) = -\frac{\Delta t}{\overline{\tau}}(\overline{f_i} - f_i^{\mathrm{eq}}) + \left[1 - \frac{\Delta t}{2\overline{\tau}}\right] F_i \Delta t, \\ \text{with} \quad \overline{\tau} = \tau + \frac{\Delta t}{2}. \end{gathered} \tag{3.32}$$

The hydrodynamic fields are derived from the populations $\overline{f_i}$ as such :

$$\begin{aligned} \rho &= \sum_i f_i = \sum_i \overline{f_i} + \frac{\Delta t}{2}\sum_i F_i, \\ \rho\boldsymbol{v} &= \sum_i \boldsymbol{c_i} f_i = \sum_i \boldsymbol{c_i}\overline{f_i} + \frac{\Delta t}{2}\sum_i F_i \boldsymbol{c_i}. \end{aligned} \tag{3.33}$$

The hydrodynamic fields do not depend on the Ω_i because the collision operator conserves mass and momentum.

A sketch representing the implemented 2nd order forcing scheme is shown in Figure 3.6.

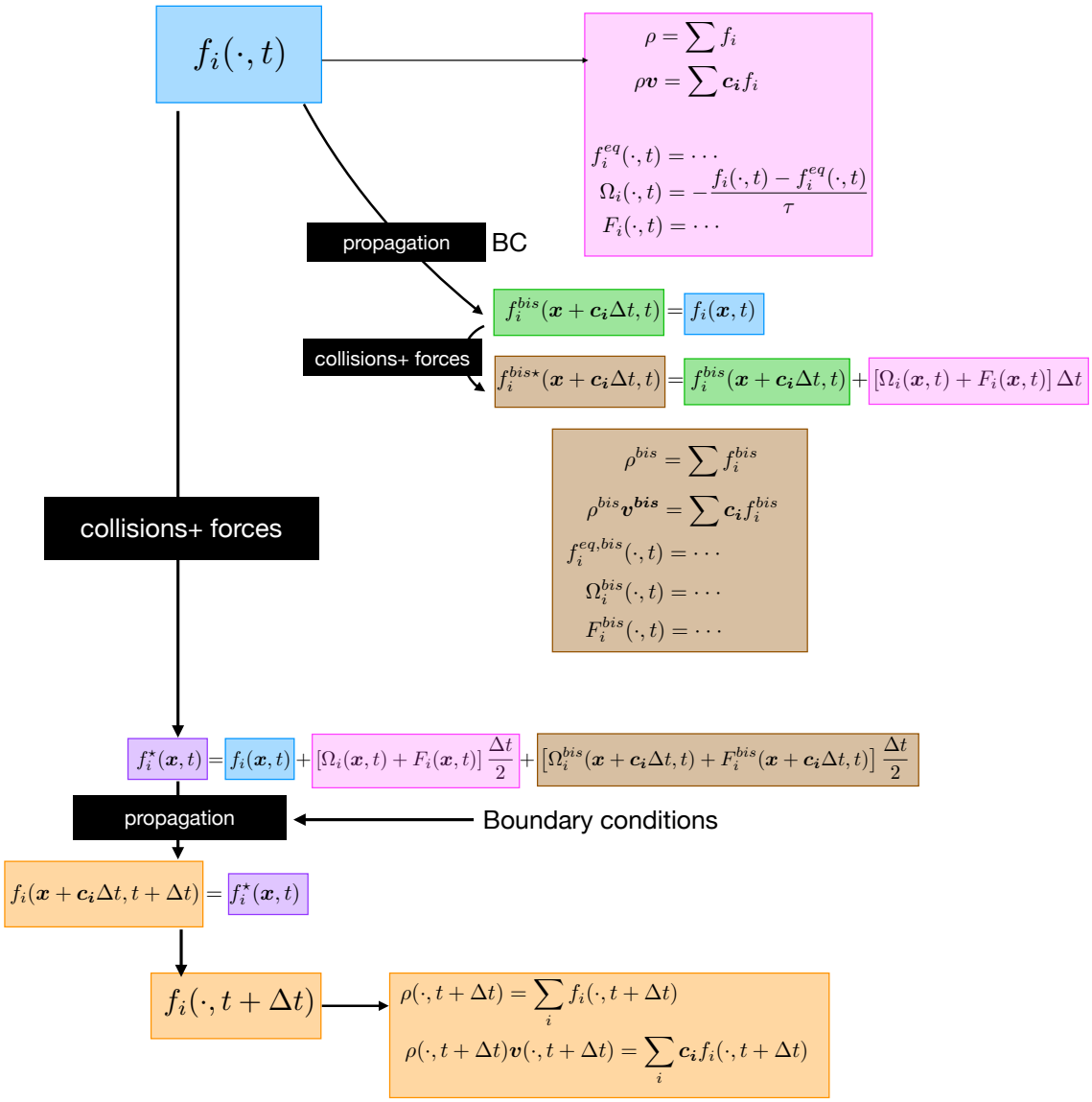

FIGURE 3.6 – **Implementation of the LBM.** This sketch represents one step of evolution of the populations $f_i(\cdot,t) \to f_i(\cdot,t+\Delta t)$. Boundary conditions (periodic, no-slip) are implemented during propagation steps.

3.10 Hybrid implementation

We now explain the full hybrid LBM numerical scheme, by which we evolve $\boldsymbol{Q}$-tensor and $\boldsymbol{v}$. At each time step of the simulation, the orientation $\boldsymbol{Q}$ is updated with a finite difference method. Time integration is executed with an Euler forward-scheme, and spatial derivatives are expressed with second order central differences. Then, the evolution of the velocity field is performed with the LBM described before, using the new values of $\boldsymbol{Q}$ to compute the force term. The LBM is more accurate than a finite difference method applied to the Navier-Stokes equations. Both the finite difference method and LBM are parallelizable. We use the library Open MPI to update in

parallel different subparts of the system. The code is implemented in C and was developped by several current members and alumni of the group of the professor Juan de Pablo. The version I used was handed to me by the professor Rui Zhang [77, 78, 54]. The simulations results are visualized with the software Paraview and analyzed with matlab.

3.11 Embedded particles to create geometrical boundaries

One of the addition I brought to the existing code is the incorporation of triangular solid particles in the fluid. Such particles are right-angle triangles, and the sides adjacent to the 90°angle are parallel to x and y directions (Figure 3.7). The particle position and shape are encoded by the coordinates (x_c, y_c) of the 90°corner, and the algebraic lengths L_x and L_y of the triangle legs. All the nodes that are strictly outside of the triangle defined by the three points $\{(x_c, y_c); (x_c + L_x, y_c); (x_c, y_c + L_y)\}$ are fluid nodes (boundary or bulk). The other nodes are solid nodes belonging to the solid. There are two sets of boundary nodes. The boundary nodes for the evolution of the $\boldsymbol{Q}$-tensor are those having at least one link of the *cubic* lattice connecting them to a solid node and one link of the *cubic* lattice connecting them to a fluid node (Figure 3.7 a). The boundary nodes for the evolution of $\boldsymbol{v}$ are nodes having at least one link of the *D3Q15 velocity lattice* connecting them to a solid node and one link of the *D3Q15 velocity lattice* connecting them to a fluid node (Figure 3.7 b). The system being discretised on a lattice, the slope of the triangle is not smooth but has a staircase shape. However, for the $\boldsymbol{Q}$-tensor, the normal to the solid particle is defined as the normal to the smooth boundary (orange arrows are orthogonal to the purple lines in Figure 3.7 a). This way, the anchoring along the slope is not affected by the staircase shape. The triangular shape of the particle creates many concave and convex corners. Boundary nodes located at corners have specific mid-grid bounce-back boundary conditions (Figure 3.7 c and d). Only the populations with a microscopic velocity $\boldsymbol{c_i}$ directed towards a solid node bounce back.

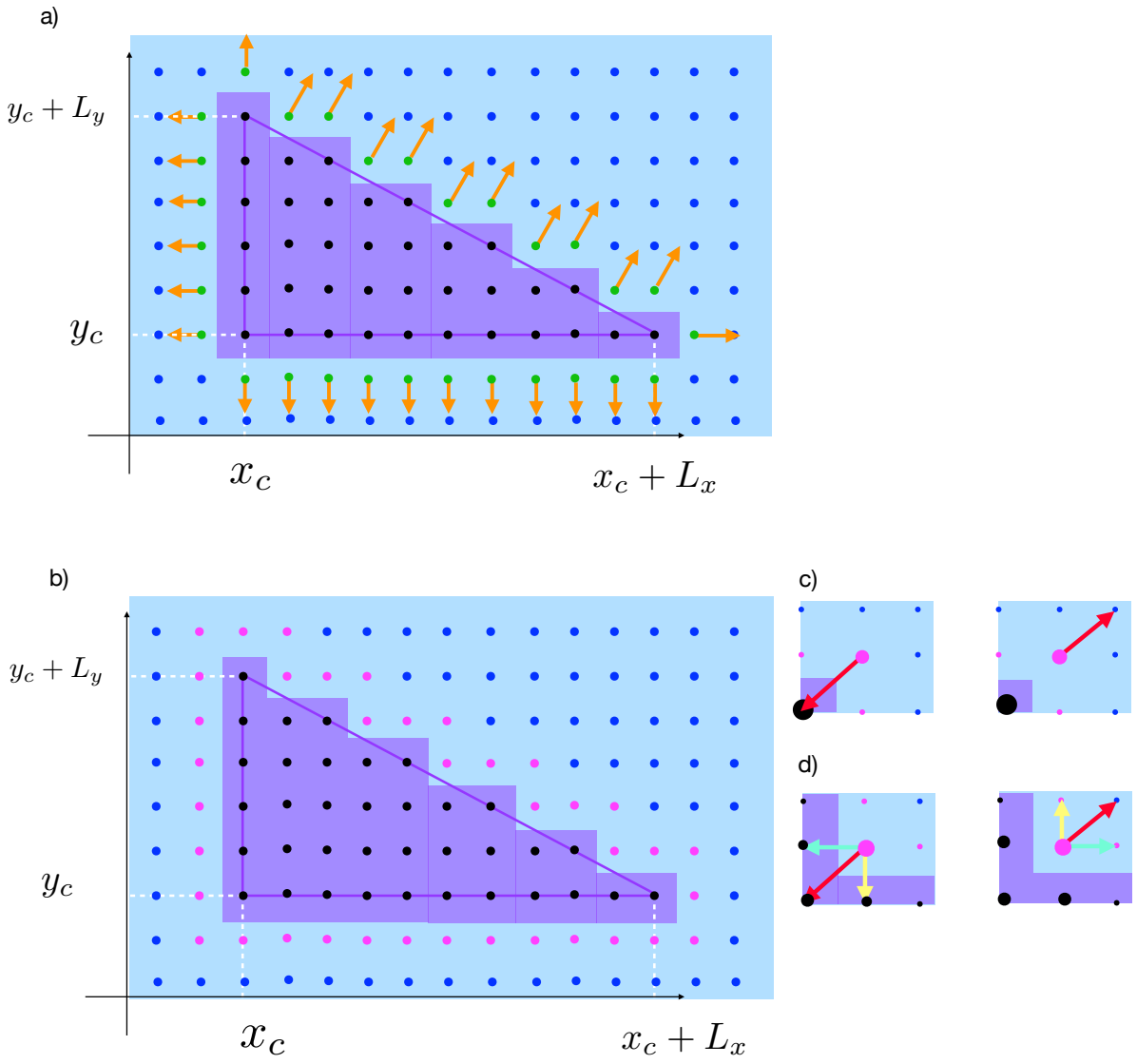

FIGURE 3.7 – **Triangular solid particles.** Black nodes belong to the solid. Blue nodes are bulk nodes belonging to the fluid. **a)** definition of the boundary nodes (in green) for the $\boldsymbol{Q}$-tensor evolution. The normal to the surface of the solid is represented by the orange arrows. **b)** definition of the boundary nodes (in pink) for the LBM evolving the velocities. **c)** mid-grid bounce-back for the boundary nodes at the convex corners. **d)** mid-grid bounce-back for the boundary nodes at the concave corners.

3.12 A 3D-model adapted to 2D system.

The mathematical model we use accounts for 3D active nematics, where the orientation and the velocities can, in principle, be out-of the xy plane. However, we adapt it to simulate 2D systems lying in the xy plane, with very few nodes in the z direction ($N_z = 6$) and periodic boundary conditions along z, by setting $Q_{xz} = Q_{yz} = 0$ and the z component of the body force $F_z = 0$ at all time. Therefore, the biaxiality P of such system is not 0. The system is initialized with a random director field $\vec{n}$ in the xy plane and relaxed partially towards static

equilibrium. When the Ginzburg-Landau relaxation stops, the system still has a few topological defects and the initial condition breaks the symmetry. From there, the simulation evolves the coupled Beris–Edwards equations as we described.

Chapter 4

Active nematics at the wall

Under strong lateral confinement, topological defects exclusively nucleate and annihilate on the confining walls. This has been reported for a disk geometry [50], where the co-rotation of two bulk $+\frac{1}{2}$ defects is periodically disrupted by the nucleation of a pair of $\pm\frac{1}{2}$ defects at the boundary (access movie showing the spiralling motion here). The $-\frac{1}{2}$ defect stays still at the wall and is quickly annihilated by one of the central defects, while the newly nucleated $+\frac{1}{2}$ defect is injected in the bulk to take part of the co-rotational motion at the center. Additionally, quasi-aligned director field configurations, observed under long and narrow rectangular confinement [52], are periodically disrupted by the nucleation of pairs of $\pm\frac{1}{2}$ defects at lateral walls. Negative defects stay at the wall, while positive ones cross the channel and annihilate with negative defects on the opposing wall. Controlling the dynamics of the AN under lateral confinement requires elucidating how the system interacts with the boundaries, and in particular, the behavior of topological defects near walls.

In this chapter, we consider semi-confined AN films in the vicinity of a boundary. This is experimentally realized by inserting a grid at the interface and observing the AN along the outer rim of the grid. For some particular experiments, to maximize the contour length of the boundary under observation, we confine the AN within annular enclosures of the grid, the width of the annular channel being large enough so that opposite walls do not influence each other. In the first part of the chapter, we characterize the behavior of the active nematic next to straight boundaries. These results were the subject of a publication [79]. In the second part, we shape the confining wall with geometrical patterns and characterize how this affects the AN in term of both topological defects dynamics and resulting active flows.

1 Active Boundary Layer next to a straight wall

We observe the AN in the vicinity of a straight wall. We report the formation of an "Active Boundary Layer" (ABL), hosting exclusively negative topological defects particularly motile and featuring exotic interactions.

1.1 Alignment at the wall and localized defects

The nematic director field $\boldsymbol{n}$ in the near-wall region is mostly parallel to the wall, except for some very localized regions hosting strong distortions (Figure 4.1 a, c, d). Noting $\boldsymbol{\nu}$ a unit vector tangential to the wall, we define the wall alignment parameter

$$P_w(y) =< 2(\boldsymbol{n} \cdot \boldsymbol{\nu})^2 - 1 >_{x,t}, \tag{4.1}$$

so that $P_w = 1$ if and only if the director is parallel to the wall everywhere, and $P_w = 0$ if the director has no preferential direction. The profile of P_w in the direction orthogonal to the wall is very close to 1 at the wall ($y = 0$) and decays on a length scale of 100 µm as we move towards the bulk (Figure 4.1 b). Surprisingly, away from the wall, for 100 µm $\leq y \leq$250 µm, P_w is not 0 but slightly negative, indicating a preferential direction orthogonal to the wall. This means that, at this distance from the wall, the AN is still impacted by the boundary.

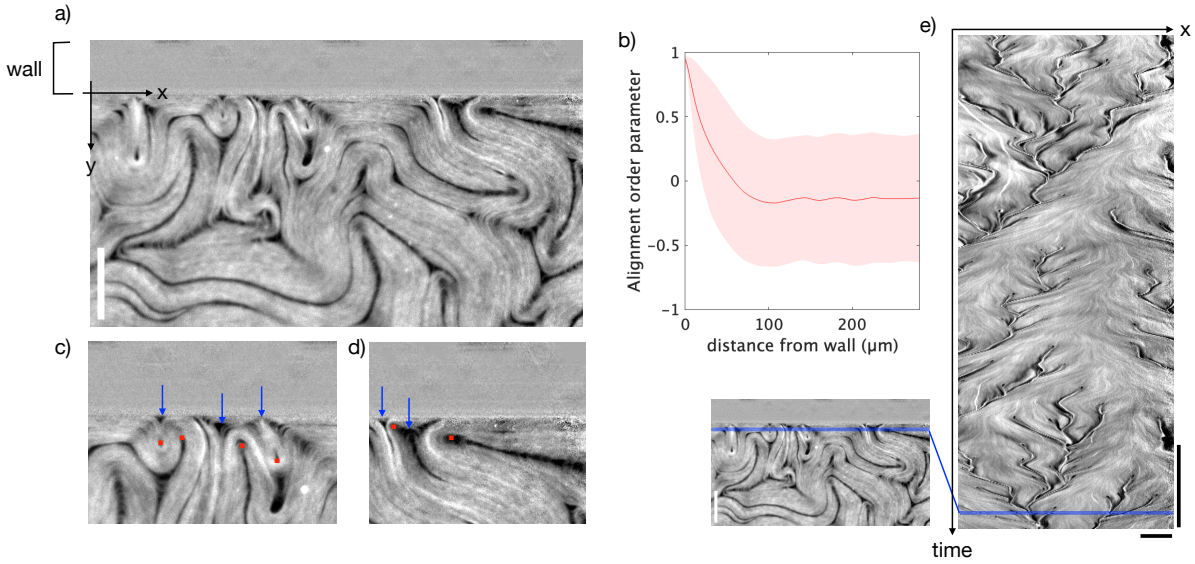

FIGURE 4.1 – **Wall alignment. a)** Fluorescence micrograph of AN semi-confined at $y = 0$ by a straight wall, scale bar = 100 µm. Access movie here. **b)** Lateral profile of the parameter measuring the alignment of the director with the wall (equation 4.1). **c and d)** Zoom on a group of defects near the wall : $+\frac{1}{2}$ defects are marked by red dots, $-\frac{1}{2}$ defects locations are pointed with a blue arrow. **e)** Kymograph of the AN along the wall : the dynamics of $-\frac{1}{2}$ defects at the wall results in a tree-like pattern. Horizontal scale bar = 100 µm, vertical scale bar = 60 s.

Along the wall, MT bundles are strongly aligned, and therefore prone to bend instability and the nucleation of pairs of $\pm\frac{1}{2}$ topological defects in the normal direction to the wall. When pairs unbind, negative defects remain at the boundary while their positive counter-parts migrate towards the bulk. This process results in the formation of a boundary layer, that has the size of a defect core, that hosts exclusively negative defects (Figure 4.1 c and d, and movie accessible here). Within the boundary layer, negative defects slide along the wall in an apparent diffusive motion. Eventually, they collide with a neighbour $-\frac{1}{2}$ defect, and the two recombine, leaving

a unique $-\frac{1}{2}$ at the wall, in a process that we will explicitly describe later. Thanks to this recombination event that consumes a negative defect, the number of negative defects residing at the wall is statistically constant, since creation and consumption events occur at similar rates. To visualize defect dynamics at the boundary layer, we built a kymograph by measuring the fluorescence intensity profile along the wall and by stacking vertically the resulting pixel lines obtained at increasing times (Figure 4.1 e). The cores of negative defects, devoid of fluorescent filaments, create on this space-time image tree-like patterns that illustrate the defect dynamics over time, from their nucleation to their annihilation. Trees are separated by regions of uniform intensity corresponding to places where the bundles are parallel to the boundary.

The fact that MT bundles align with the boundary and locally adopt an orthogonal direction around the defects is not surprising given that the AN system is not a traditional liquid crystal. No chemical interactions govern wall anchoring here, but rather hydrodynamics interactions with the wall, which induce the parallel alignment of the MT bundles, an effect called "active anchoring", as it was discussed in Chapter 3.

Next, we use high magnification fluorescence images of defects at the wall to elucidate their structure and explain the topological transformations taking place during the events of creation and consumption.

1.2 Defects nucleation, annihilation and recombination at the wall

Below we describe the different mechanisms giving rise to the creation or disappearance of topological defects at the wall. We find a single mechanism for defect creation (defect nucleation) and two different mechanisms leading to defect consumption (defect annihilation and recombination). The three mechanisms are shown on a movie accessible here.

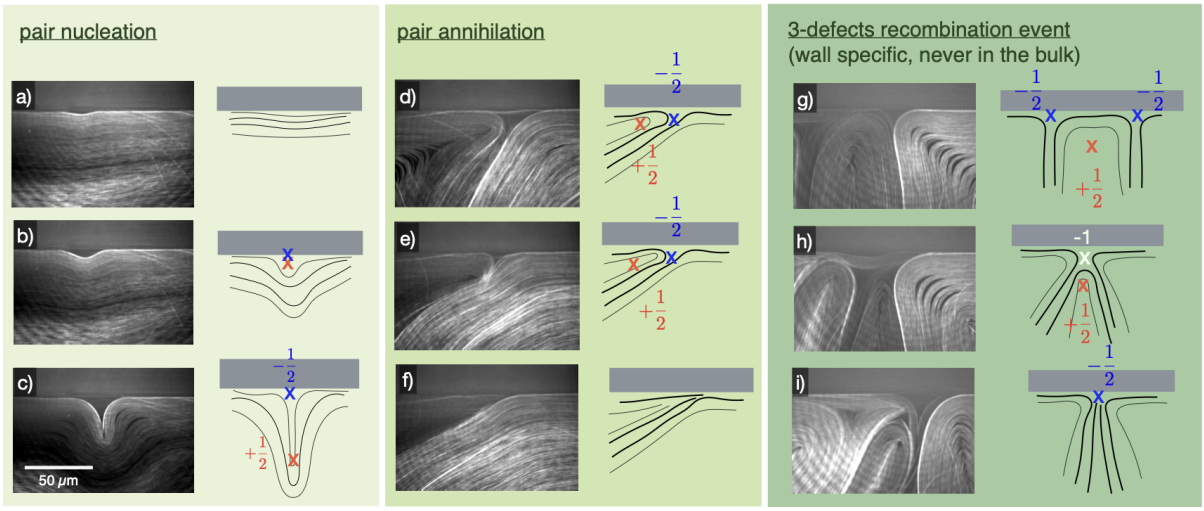

FIGURE 4.2 – **Defect events at the wall.** Fluorescence micrographs acquired with a x60 objective (scale bar 50 µm) and sketches illustrating the different mechanism. **a-c) Nucleation of a pair of $\pm\frac{1}{2}$ defects at the wall** : a,b) development of the bend instability ; c) unbound defect pair, note that there is no MT filaments between the wall and the core of the $-\frac{1}{2}$ defect. **d-f) Annihilation of a pair of $\pm\frac{1}{2}$ defects at the wall** : d) here, a very thin filament separate the core of the $-\frac{1}{2}$ defect and the wall, a $+\frac{1}{2}$ approach the negative defect from the left side ; e) filaments between the $-\frac{1}{2}$ and $+\frac{1}{2}$ defects cores start to fracture, the sudden darkening of the filaments on the left of the image might indicate that the AN film deforms in the third dimension ; f) point-like defects have disappeared, a disclination line has not healed yet. **g-i) 3-defect recombination event at the wall**, involving two $-\frac{1}{2}$ wall defects and a $+\frac{1}{2}$ bulk defect. g) Asymmetric forces around the left $-\frac{1}{2}$ wall defect induce the defect motion towards the right $-\frac{1}{2}$ wall defect. A $+\frac{1}{2}$ defect coming from the bulk is interposed. h) The two $-\frac{1}{2}$ defects are so close that their cores have merged, forming a transient -1 defect. The filaments between the $+\frac{1}{2}$ and -1 defects start to fracture from the strong bending. i) The $+\frac{1}{2}$ defect has merged with the transient -1 defect, leaving at the wall a unique $-\frac{1}{2}$ defect. A movie showing side by side the three defect events is accessible here.

Pair nucleation. Starting from MT bundles aligned with the wall (Figure 4.2 a), a bend perturbation germinates from the bundles closest to the wall, and the instability grows in the direction orthogonal to the wall (Figure 4.2 b). This leads to the creation of a recognizable $+\frac{1}{2}$ defect migrating towards the bulk, and leaves at the wall a defect to which we attribute $-\frac{1}{2}$ topological charge, so that the total topological charge is conserved in the process (Figure 4.2 c). In the example shown in Figure 4.2 a,b,c, the core of the $-\frac{1}{2}$ defect is directly in contact with the wall, there are no MT bundles in between. However, this is not always the case. For instance, in Figure 4.2 i and j, we see on the left a negative defect that is separated from the wall by MT bundles. It all depends whether the bend perturbation started exactly at the wall, bending all the MT bundles near the wall, or slightly away from the wall, letting behind a thin layer of aligned MT bundles. The newly formed $-\frac{1}{2}$ defect has a polar symmetry instead of the usual threefold symmetry of $-\frac{1}{2}$ bulk defects (Figure 4.3 a, b). The net active force acting on the $-\frac{1}{2}$ defect is non zero and pushes the defect against the wall, thus the defect is trapped in the boundary layer because of the polar symmetry imposed by the presence of the wall.

Pair annihilation. A typical event of defect annihilation at the wall is shown in Figure 4.2 d-f. Initially, a wall $-\frac{1}{2}$ defect is laterally approached by a $+\frac{1}{2}$ defect coming from the bulk (Figure 4.2 d). In case of slip boundary conditions with the wall, this asymmetric configuration generally leads to the pair of $\pm\frac{1}{2}$ defects simply sliding laterally along the boundary, and pair annihilation does not happen. If sliding along the boundary is impeded, we observe that the $+\frac{1}{2}$ defect gets close enough to the $-\pm\frac{1}{2}$ defect, the fibers separating the two cores then fracture (Figure 4.2 e) and the defect pair annihilates in a process similar to that observed in bulk (Figure 4.2 f), leaving no defects behind.

3-defect recombination event or defect "merging". A remarkable behavior of $-\frac{1}{2}$ defects residing at the wall is their tendency to drift towards each other (Figure 4.2 g), due to an imbalance in the surrounding active forces (Figure 4.3 c). This apparent attraction of like-sign defects is surprising, given that in the bulk like-sign defects repel each other. As negative defects get closer, the director field between them has to bend very strongly, thereby involving a $+\frac{1}{2}$ bulk defect in the process (Figure 4.2 h). The cores of the $-\frac{1}{2}$ eventually merge together, forming a transient single defect to which we attribute a -1 topological charge in order to conserve the total topological charge in the system. Fibers separating the -1 and the $+\frac{1}{2}$ defect cores break, and the two defects recombine to form a single $-\frac{1}{2}$ defect (Figure 4.2 i).

Both wall annihilation and defect merging consume a $-\frac{1}{2}$ wall defect while preserving the total topological charge in the system. In our experimental set-up, we observe predominantly the second mechanism (defect merging). We link this to the slip boundary condition often imposed by our polymeric grids that facilitates the drift of defects along the wall. However, we occasionally observe wall annihilation in certain grids imposing a no-slip boundary condition. Although all the grids that we use are produced in the same way, it seems that their surface properties could slightly vary from one batch to another or depend on the age of the grid. The boundary conditions for the velocity field, i.e. slip or no-slip, influence not only the defect dynamics at the wall, but also the whole system dynamics in situations of strong confinement. Indeed, in the experiments performed by Opathalage et al [50], where the AN is confined to a small disk and

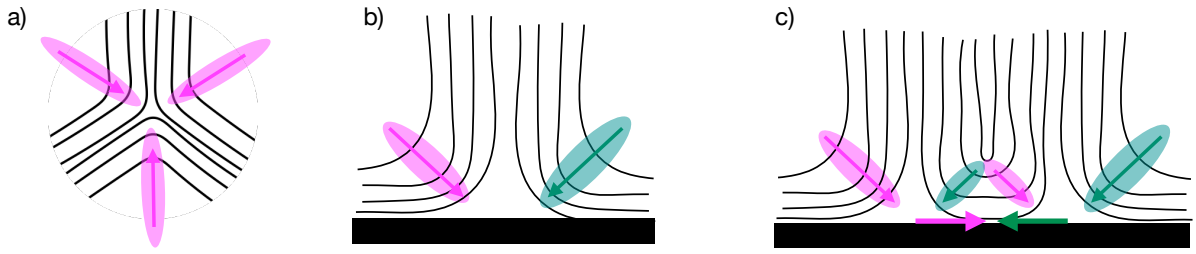

FIGURE 4.3 – **Forces acting on $-\frac{1}{2}$ defects. a)** the resulting active force acting on a bulk negative defect with three-fold symmetry is zero; **b)** the resulting active force acting on a isolated $-\frac{1}{2}$ wall defect with polar symmetry points towards the wall; **c)** active forces acting on two neighbouring $-\frac{1}{2}$ wall defects result in pair attraction.

two $+\frac{1}{2}$ defects co-rotate in the bulk, only wall annihilation occurs because there is a unique $-\frac{1}{2}$ wall defect at the wall. In contrast, in our experimental set-up, confining the AN inside a small disk generally leads to another kind of dynamics : a persistent $-\frac{1}{2}$ defect slides diffusely along the boundary and merge with transient $-\frac{1}{2}$ wall defects that nucleate near the main defect. A movie showing such dynamics, recorded by Jérôme Hardoüin, can be accessed here. In a minority of the experiments only, we observe the spiralling motion reported by Opathalage (a movie of ours showing this particular dynamics is accessible here). In this case, the $-\frac{1}{2}$ wall defect has little motility and a short life-time. We attribute the two different behaviors to no-slip boundary condition for the spiralling motion, and slip boundary condition for the long-lived defect.

1.3 Wall topological defects and their charge

We now justify why we attribute either $-\frac{1}{2}$ or -1 topological charge to wall defects. In the bulk, a topological defect is a localized singularity and its topological charge is the number of 2π rotations made by the director field along a loop surrounding the defect core. For the wall defects sitting exactly at the wall, the absence of filaments between the defect core and the wall makes it impossible to define the charge in such a way. Additionally, the charge can be in principle delocalized instead of point-like. We explain a method to compute the charge carried by boundaries [80]. Let's consider a 2D system enclosed inside a 1D boundary, and the local Frénet basis attached to the boundary : $\boldsymbol{e_n}$ the normal to the wall pointing towards the LC , and $\boldsymbol{e_t}$ the tangential vector such that $\boldsymbol{e_n} \times \boldsymbol{e_t}$ points towards us. We measure the angle α that the director $\boldsymbol{n}$ makes with respect to $\boldsymbol{e_t}$. The number of 2π-rotation of α is the charge associated to the boundary and is a positive or negative half-integer if the boundary is a loop. Now let's apply this method to a few examples.

First, a circular boundary enclosing a unique $s_b = +\frac{1}{2}$ defect (Figure 4.4 a). The anchoring at the wall is weak therefore the director field does not keep a constant orientation with the wall. As we follow along the boundary in the clockwise direction, the director field performs $+\pi$ rotation *with respect to the boundary*. Therefore, the topological charge associated to the boundary is $s_w = +\frac{1}{2}$. The bulk charge s_b and the boundary charge s_w sum up to give a total topological charge of $+1$, as the Poincaré-Hopf theorem requires for a disk. With this definition of edge charge, we see that boundaries can carry a delocalized topological charge even though the director field is well defined all along the wall.

Let's consider now the AN system next to a wall right after a pair nucleation event (Figure 4.4 b), the defect sitting at the wall has a dark core devoid of MT filaments, where the director field is undefined. Following the line along the wall, slightly detached from the wall so that it intersects MT filaments all along, the director field rotates abruptly by $-\pi$, therefore the wall defect topological charge is $-\frac{1}{2}$. Similarly, the transient defect formed by two $-\frac{1}{2}$ wall defects merging bears a -1 topological charge because the director field rotates by -2π (Figure 4.4 c). This is compatible with the conservation of the total topological charge upon the three kinds of defect events at the boundary.

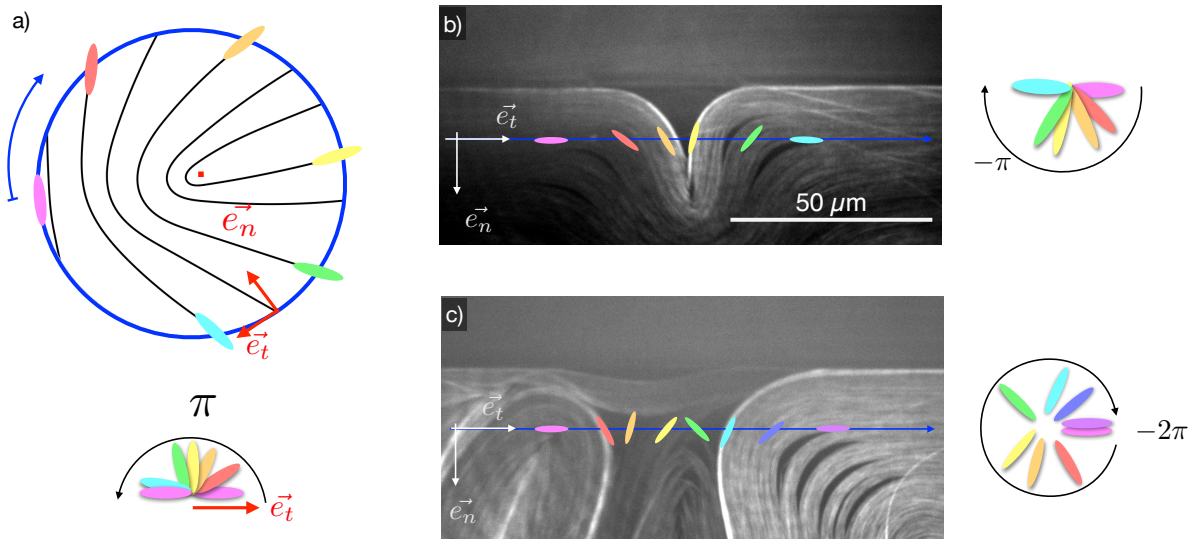

FIGURE 4.4 – **Topological charges at the wall. a)** We consider a circular boundary imposing no particular anchoring on the enclosed LC. A bulk $+\frac{1}{2}$ defects resides in the center of the disk. To fulfill Poincaré-Hopf theorem, stating that the total topological charge for a disk is $+1$, we have to take into account the charge carried by the boundary, even in the case where there is no singularity at the boundary. To do so, we follow the boundary in the CW direction and measure the angle α that the director field makes with the tangential vector $\vec{e_t}$ of the Frénet basis attached to the boundary. The number of 2π-rotations of α is the edge charge s_b. In this case, α rotates by $+pi$, therefore the boundary carries a $+\frac{1}{2}$ topological charge ; **b-c)** AN wall defects are singular : they have a core devoid of MT where $\vec{n}$ is undefined. Therefore, we draw a line separated from the wall by the size of the defect core, so that it crosses MT filaments all along ; **b)** the director field from left to right turns by $-\pi$, hence the $-\frac{1}{2}$ charge we attribute to the defect. **c)** For the transient defect resulting from the merging of two $-\frac{1}{2}$, the director field rotates by -2π, hence the associated topological charge is -1.

1.4 Dynamics and influence of the boundary layer

The mechanisms explained above result in the formation of an active boundary layer (ABL) near the wall populated by $-\frac{1}{2}$ defects, whose structures and dynamics are different from those of $-\frac{1}{2}$ bulk defects. In order to characterize the collective dynamics of these wall defects, we confined the AN to a large annular channel of width w=200 µm, inner radius R_i =150 µm and outer radius R_o =350 µm (Figure 4.5 a). This allowed us to maximize the length along which we observe the AN. The annulus is large enough so that the AN is in a chaotic state [51]. Another advantage of this fully confined geometry is that the oil-water interface is less curved, allowing the AN layer to be equally on focus near and far from the wall. We measure the distance with respect to the inner wall $r = R - R_i$ (Figure 4.5 a). This experiment was performed by Jérôme Hardoüin.

Similarly as in the case of a straight wall (Figure 4.1 e), we observe the formation of an active boundary layer at the inner and outer walls of the annulus (Figure 4.5 b for the outer wall and c for the inner wall), implying that ABLs are not impacted by moderate wall curvature in the range $[-\frac{1}{R_o}, +\frac{1}{R_i}]$. We analyze the collective dynamics of defects along the inner wall and build a kymograph at increasing distance r from the wall (Figure 4.5 c to f).

Close to the wall, the kymograph displays a clear tree pattern, where we can identify the three kind of defects events mentioned before (Figure 4.5 g). Defect nucleation corresponds to a leaf in the tree (orange diamond) : the core of the negative defects is quite large right after nucleation and shrink afterwards. Branches of the trees represent the space-time trajectory of a defect sliding along the wall. Bifurcation points between branches correspond to a defect merging event (green inverted triangle). Wall annihilation events are rare, and correspond to the extinction of a tree (white circle). This tree pattern is therefore a signature of the particular dynamics of topological defects within the ABL.

How far does the ABL dynamics penetrate in the bulk ? As we move away from the wall, the kymograph tree structure is gradually replaced by smaller and more isotropic patterns in the center of the channel (Figure 4.5 e and f). To capture this transformation, we compute the radial auto-correlation function of each kymograph (Figure 4.5 h). The typical size of the correlations decays with the distance from the wall, to stabilize around the bulk value at a distance of roughly 40 µm. In a nutshell, the thickness of the boundary layer, defined as the near-wall region exclusively populated by negative defects, has the size of the core of negative defects (10 $\sim$ 20 µm), but the ABL's region of influence extends to 40 µm.

1.5 Slip or no slip boundary condition at the wall ?

As we mentioned above, the dynamics of an ABL depends on the slip or no-slip condition imposed by the wall to the velocity field. In order to characterize our grids in these terms, we seed the fluid with fluorescent colloids emitting green light and use high magnification images near the wall. We film the boundary by acquiring alternating images of the AN layer and the colloids. The concentration of colloids was adapted to x10 magnification, but not high enough to infer the velocity field from x60 magnification images. Therefore we extract the velocity field from the

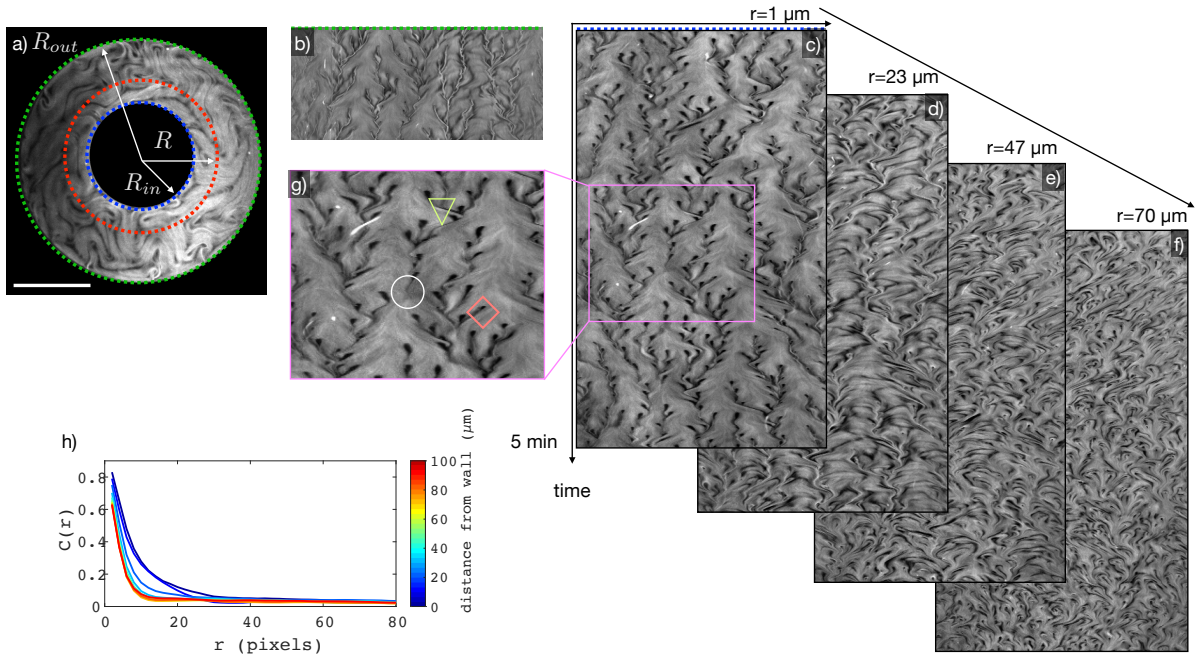

FIGURE 4.5 – **Dynamics of wall defects. a)** fluorescence micrograph of the AN confined in the annular channel, scale bar 200 µm. **b)** kymograph along the outer wall ; **c-f** kymograph at increasing distance $r = R - R_i$ from the inner wall ; **g)** zoom on a portion of the kymograph at $r = 0$. The orange diamond marks a leaf in the tree, indicative of a wall nucleation event. The inverted green triangle indicates a merging event between two wall defects, the white circle shows a rare wall annihilation event, characterized by the extinction of a tree. **h)** Profiles of the radial auto-correlation function of the kymographs made at various distances from the wall. The pattern size in the kymographs decreases with r, and stabilizes after r =40 µm.

AN texture with the optical flow method (Chapter 2). Figure 4.6 a shows a $+\frac{1}{2}$ defect navigating towards the right along the boundary. As a result, the $-\frac{1}{2}$ wall defect slides towards the right. The inferred velocity field is non-zero along the wall (Figure 4.6 a) and successive images of the colloids reveals that indeed, near the wall colloids are advected at a speed of roughly $4.4\,\mu m \cdot s^{-1}$. We average over 60 s and along $L_x = 150\,\mu m$ the absolute value of the tangential and orthogonal components of the velocities. The profile of such quantities is shown on figure 4.6 d. They reveal that the tangential velocity decays close to the wall but does not reach 0. The average tangential velocity at the wall is $1.7\,\mu m \cdot s^{-1}$. From the profile of $< |v_y| >$ we can extract an effective slipping length of about $10\,\mu m$. One could nuance this statement by arguing that the motion of defects involves local reorientation of the material and no material transport. The optical flow method would be fooled by this and detects apparent tangential motion. However, the motion of the colloids near the wall indeed weights in favor of slip boundary conditions.

Therefore, we conclude that the grid wall creates slip boundary condition for the AN. Along a PDMS boundary, such as the rim of the chamber containing the entire system (Figure 4.6 e), MT bundles stick to the boundary in certain locations. The change in the boundary condition does not prevent the wall nucleation and the formation of a boundary layer, but affects defects dynamics at the wall. Indeed, negative wall defects are less motile along the boundary and consumed via the wall annihilation mechanism more often, as can be seen on the kymograph 4.6 f). As a side note, nucleation occurs at recurring locations along the boundary, which might indicate that the PDMS boundary does not have translational invariance.

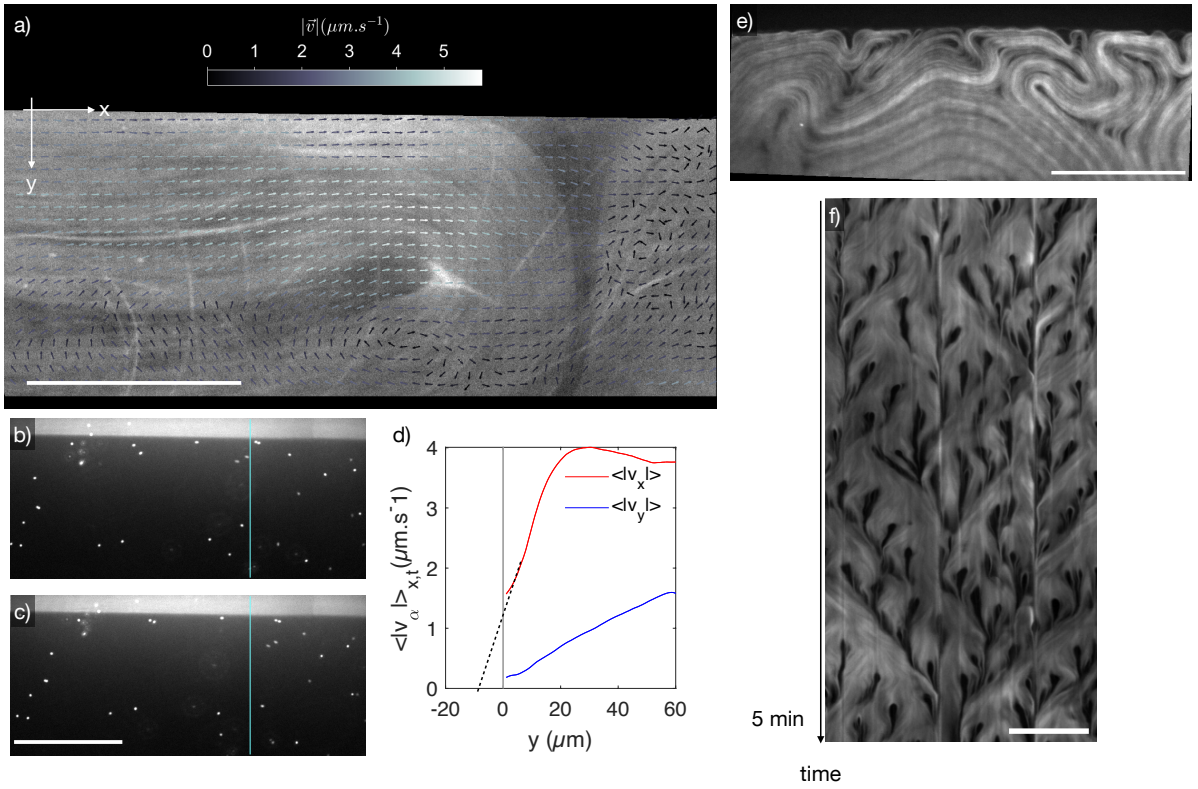

FIGURE 4.6 – **Slip boundary conditions at the wall. a)** high magnification (x60) image of the AN near the wall of the grid. The movie showing only the active nematic texture is accessible here. A $+\frac{1}{2}$ defect is pushing towards the right a negative $-\frac{1}{2}$ wall defect. The instantaneous velocity field computed with the optical flow method is overlaid, the vector length is normalized and the velocity magnitude is encoded by the color. Scale bar 50 µm. **b-c)** Two frames of the colloids seeding the AN separated by Δt =2s, scale bar 50 µm. A cyan line is drawn as a landmark. We clearly see that the colloids near the wall are advected towards the right. **d)** average absolute value of the tangential (red) and normal (blue) component of the velocity at increasing distance y from the wall. **e)** fluorescence micrograph near the rim of the pool made of PDMS at the usual x10 magnification. Scale bar 100 µm. **f)** kymograph along the PDMS wall that displays a higher number of extinguished trees and isolated leaves witnessing wall annihilation events, in comparison to kymographs along the wall of the grid. Scale bar 100 µm.

2 Control of the Active Boundary Layer with geometrical patterning

In this part, we investigate the possibility to control the ABL with geometrically patterned boundaries.

2.1 Curved and triangular walls : defect segregation and organized flows

First, we study the AN next to curved and triangular boundaries. Curved walls are made of a succession of hemicycles of radius R_c with opposite curvature (Figure 4.7 a). Therefore the wavelength of the pattern is $\lambda = 4R_c$. In Figure 4.7 b, the magenta box defines the outer

concavity of the wall, and Figure 4.7 c shows the outer convexity of the wall. Triangular walls are isosceles triangular protrusions of height h and basis $\lambda = 2h$ (Figure 4.7 h).

Defect segregation and pinning Along the curved wall, wall negative defects reside in average at the outer convexity of the wall and avoid the outer concavity of the wall as attested by the fluorescent micrographs displayed in Figure 4.7 a-d. Wall defects slide along the portion of the wall having convex curvature $\frac{1}{R_c}$. In the kymographs corresponding to the wall contour (Figure 4.7 e), the patterns created by wall defects do not intersect the cyan vertical lines that indicate the wall concavity.

Triangular walls have zero curvature, but they have a convex singularity at the tip of the protrusion and a concave singularity at the indentation. A $-\frac{1}{2}$ wall defect is pinned permanently at the tip of the protrusion (Figure 4.7 f, a movie is accessible here). We observe that negative defects can nucleate along the straight portion of the walls, and then migrate towards the

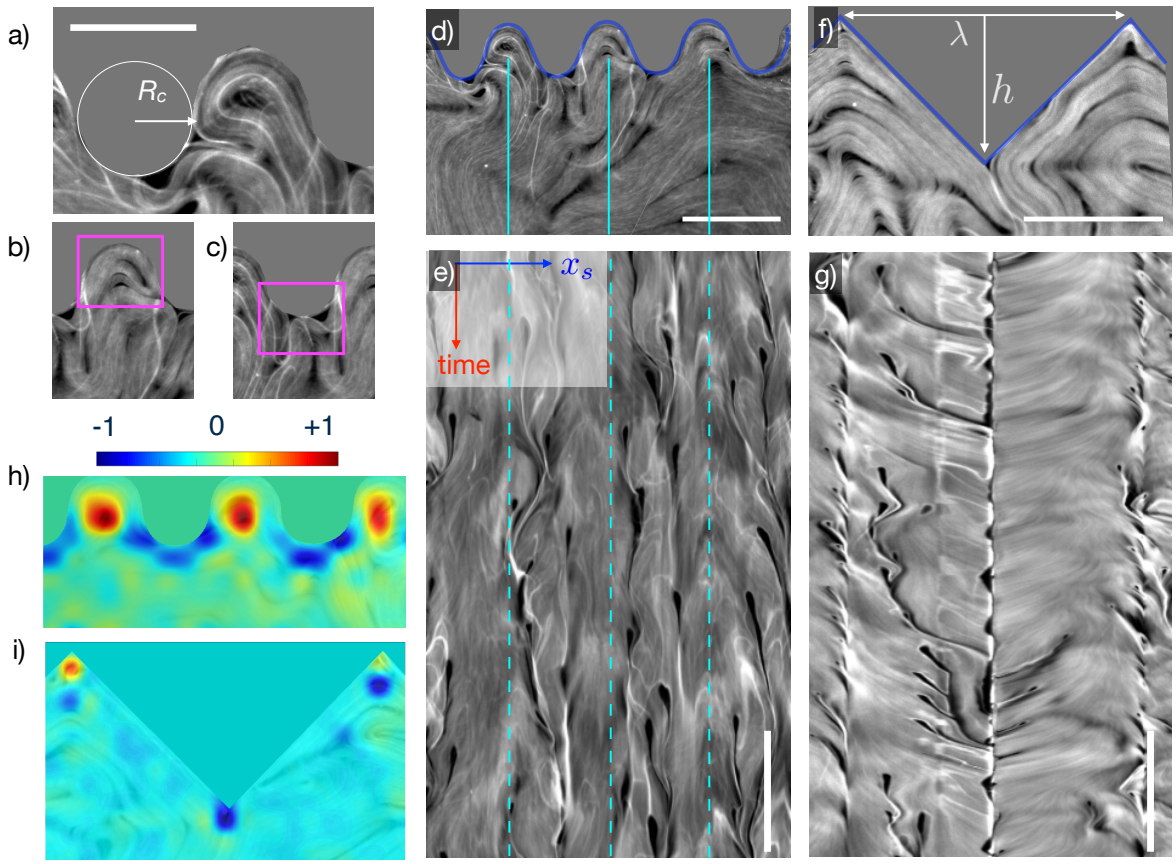

FIGURE 4.7 – **Defects segregation and defect pinning. a)** curved wall made by hemicycles with radius of curvature R_c =50 µm, scale bar 100 µm ; **b)** concavity of the pattern ; **c)** convexity of the pattern. **d)** AN next to the curved wall of radius of curvature R_c =50 µm ; **e)** kymograph along the curved boundary (blue line on d). **f)** AN next to a triangular wall with $h = 200$ µm, the corresponding movie is accessible here ;**g)** kymograph along the triangular wall. Vertical scale bar for e,g 60s. **h)** (respectively i) average topological charge density along the curved wall (respectively, around the triangular wall).

tip and fuse with the pinned $-\frac{1}{2}$ defect. This behavior is clearly captured by the kymograph corresponding to the contour of the triangular wall, which displays tree of branches converging towards the vertical trunk created by the pinned defect (Figure 4.7 g).

We detect topological defects as explained in Chapter 2, and use the collection of their positions $\vec{r_i}$ and topological charges s_i to construct the normalized topological charge density :

$$\rho(\vec{r}) =< \sum_i s_i \delta(\vec{r} - \vec{r_i}) >_t \tag{4.2}$$

In Figure 4.7 h, j, we display the topological charge density re-scaled between [-1,1] by using the following formula

$$\rho_{norm} = \frac{2\rho - \rho_{max} - \rho_{min}}{\rho_{max} - \rho_{min}} \tag{4.3}$$

The normalized topological charge density is overlaid in Figure 4.7 h,i. The negatively charged region is spread along the convex part of the curved wall, while it is very concentrated around the singular convexity of the triangular wall. The outer concavity of the curved wall is visited exclusively by bulk $+\frac{1}{2}$ defects. Next, we use triangular walls of increasing wavelength λ = 50, 100, 200, 400 µm, keeping the aspect ratio of the triangle constant, to probe the effect of the pattern size (Figure 4.8 a-d). We find that patterns whose size is too small in comparison to the active length scale (λ =50 µm) fails to pin systematically negative defects at the protrusion (Figure 4.8 a). Patterns whose wavelength is too big in comparison to the active length scale (λ =400 µm) efficiently pin negative defects at their cusp but do not prevent nucleation of negative defects near the indentation (Figure 4.8 d). Therefore, they do not create regions of important positive charge density. To efficiently modulate the topological charge density along the wall, the optimal pattern size is λ =100, 200 µm, that is to say, close to the active length scale. Such patterns segregate topological charges according to their sign : positive defects are located in the concavity of the pattern, and negative defects along the convex part of the wall.

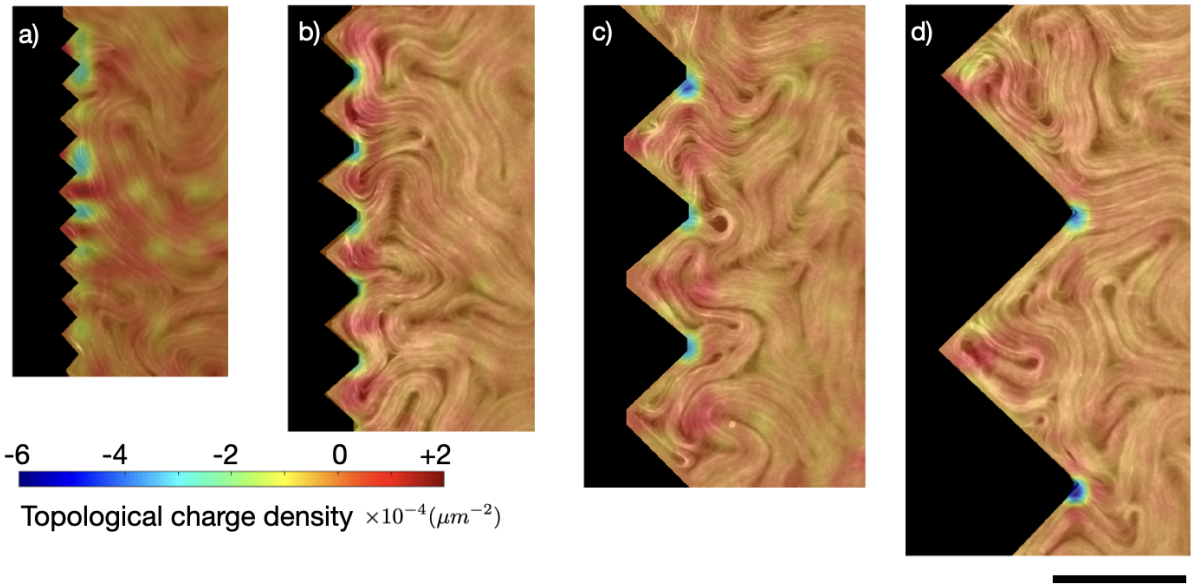

FIGURE 4.8 – **Effect of pattern size.** Average (non normalized) topological charge density along triangular wall of increasing wavelength. **a)** h=25 µm ; **b)** h=50 µm ; **c)** h=100 µm ; **a)** h=200 µm. Scale bar 200 µm.

Control of orthogonal flows We extract the velocity field from a 2 min movie with the optical flow method. Triangular walls create organized flow patterns in their vicinity. While the average flow is zero near a straight wall due to symmetry reasons, the triangular protrusion produces a jet of material directed towards the bulk. Between two protrusions, the currents points towards the indentation (Figure 4.9 a,b). In this regard, the wall acts as if it modulates pressure : high pressure points are at the tip and low-pressure points are at the indentation.

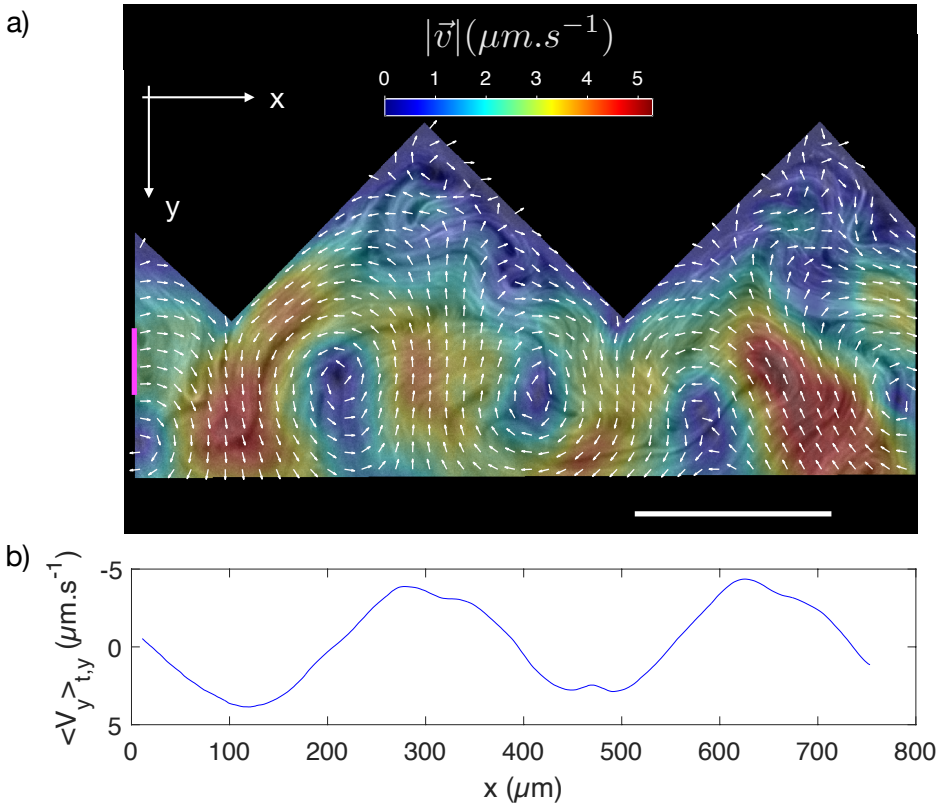

FIGURE 4.9 – **Triangular walls create in-and-out orthogonal currents. a)** Instantaneous velocity field near the triangular wall. Arrows are normalized, the magnitude of the velocity is overlaid in color. Scale bar = 200 µm. **b)** average orthogonal velocity along the boundary at distance $y \leq 70$ µm from the protrusion (this region is materialized by the pink bar to the left). Temporal average is performed over 60 s.

The curved and triangular wall upper-mentioned do not break the symmetry $\boldsymbol{e_x}/-\boldsymbol{e_x}$ and do not create a net current along the x axis parallel to the wall. Next, we pattern the wall with asymmetric triangular protrusions.

2.2 Active nematic ratchet effect

We pattern three of the walls of a square grid with right-angle triangles of length $\lambda = 200$ µm and different amplitudes $h = 50$, 100, 200 µm. The repetition of such units creates a saw-tooth pattern along the wall, that we call "ratchet pattern" (Figure 6.5 a-d). A movie showing the active nematic near a ratchet wall with $h = 100$ µm is accessible here.

Directed currents We measure persistent directed currents parallel to the wall in the direction $+\boldsymbol{e_x}$ (the ratchet "easy" direction) for all the three types of ratchet wall. Figures 6.5 a-c display the average velocity field extracted with the optical flow method from a 2-minutes movie. We consider that the origin of the y axis, perpendicular to the wall, is located at the tip of the protrusion. The average profile of the longitudinal velocity, $V_x(y) =< v_x(x, y, t) >_{x,t}$ is positive at distance $y \leq 200$ µm from the wall, so on a region twice as large as the active length scale

(Figure 6.5 d). The pattern that created the strongest longitudinal current is the one having the smallest ratchet amplitude (h =50 µm). However, it is difficult to compare the influence of different patterns on the velocity given that we observe the AN along the outer walls of a square grid, and the position of the interface with respect to the bottom surface of the observation chamber can vary from one wall to the other creating more or less resistance to the flow.

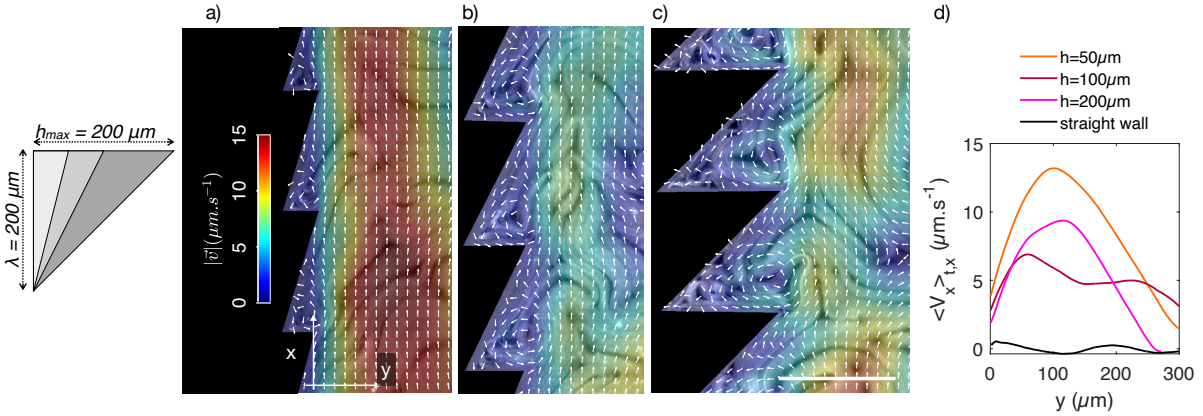

FIGURE 4.10 – **Ratchet walls create directed longitudinal currents. a-c)** velocity field averaged over 2 min, for a fixed wavelength $\lambda = 200\,\mu m$ and different tooth amplitude h. Arrows are normalized, the magnitude of the velocity is overlaid in color. Scale bar = 200 µm. **a)** h = 50 µm ; **b)** $h = 100\,\mu m$, a movie for this tooth aspect ratio is accessible here ; **c)**, $h = 200\,\mu m$; **d)** average velocity profiles along ratchet walls compared to the velocity profile next to a straight wall.

Effective tilted anchoring We detect the orientation $\theta \in [0, \pi]$ of the director field and compare it with the vector $\boldsymbol{\nu}$ tangential to the hypotenuse of the tooth, using the alignment parameter previously defined for the straight wall in Section 1 : $P_w(y) =< 2(\boldsymbol{n}\cdot\boldsymbol{\nu})^2 - 1 >_{x,t}$. Here, the origin of the y axis is positioned at level of the indentation (Figure 4.11 a). The profile of the alignment parameter, as a function of the distance from the wall y, displays a local maximum at y_{max}, roughly equal to the tooth amplitude h (Figure 4.11 b), sign that the director fields adopts an orientation similar to the ratchet angle α. Then, we measure the average angle made by the director field at the distance from the wall for which the alignment with the ratchet hypotenuse is maximal $< \theta >_{x,t,y=y_{max}}$ (Figure 4.11 c). This angle is larger than and increases with the slope of the ratchet α. Therefore, even though the local anchoring of the bundles at the wall is still planar, the ratchet pattern enforces an effective tilted anchoring of the nematic field with respect to the wall direction $\boldsymbol{e_x}$.

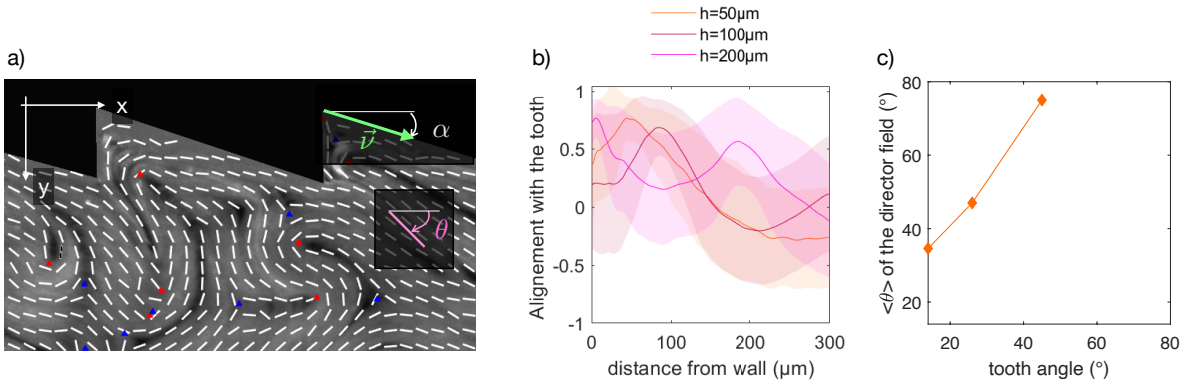

FIGURE 4.11 – **Effective tilted anchoring enforced by ratchet walls. a)** Director field along the ratchet wall with teeth making an angle α. The distance from the wall is measured from the concave corner of the pattern. **b)** Profiles of the alignment parameter with respect to the vector $\boldsymbol{\nu}$ for different ratchet amplitude h. **c)** Average angle of the director field $< \theta >$ where the alignment with the tooth is maximum. The angle of the director field is higher than the angle of the tooth.

Conclusion. We summarize the main results of this chapter. The AN develops an "active boundary layer" (ABL) along lateral boundaries. The ABL is topologically polarized in the sense that it exclusively hosts negative topological defects. Negative wall defects have exotic properties in comparison to bulk negative defects. They have an inherent polar symmetry in average due to the presence of the wall, instead of the three-fold symmetry of bulk negative defects. Active forces around these negative wall defects are unbalanced, resulting in a net force that traps the defect in the near-wall region. Additionally, a lateral asymmetry in the director field surrounding the wall defect generates a net force which, combined to the free-slip boundary condition, pushes the defects laterally. Wall-defect motion is constrained to 1D along the wall. Therefore like-sign wall defects eventually get closer and merge together through a topological transformation that involves an outsider $+\frac{1}{2}$ defect. We call the boundary layer "active" to refer to the persistent nucleation, motion and recombination of defects within the layer. We pointed out the slip boundary condition that the polymeric grid enforces of the AN film, which seems to influence the dynamics of the active nematic in the wall neighborhood. Finally, we demonstrated the possibility to control the ABL using geometrically patterned boundaries. The patterns that we used consist of a succession of curves, symmetric triangular protrusions or ratchet teeth having a size comparable to the active length scale. With curved boundaries, we were able to spatially segregate topological defects with respect to the sign of their topological charges : positive defects migrate towards the wall concavities, while negative wall defects nucleate and move along the wall convexities. A sharp triangular indentation is able to pin a wall negative defect at the cusp, inducing the injection of an orthogonal jet of AN material towards the bulk. Ratchet walls create longitudinal directed currents and enforce an effective tilted anchoring of the nematic field.

Chapter 5

Active nematic channels

In this chapter, we study the behavior of active nematics confined to long and narrow channels with open ends, the building block of an AN-based microfluidic device.

Recent experiments on close annular channels have shown that microtubule-based ANs can spontaneously flow if the channel is sufficiently narrow [50, 51]. We are referring here to a flow state embedding topological defects, with positive topological defects developing polar order in the downstream direction, and that has not been addressed by theoretical work yet. The flow can set up in either direction with equal probability when the walls of the annulus are smooth, however, a small chiral notch along the channel boundary is enough to break this symmetry and set the current direction.

Here, we investigate the possibility of having directional flow in long and straight channels whose open ends are connected to a chaotic external AN bath, as sketched in Figure 5.1 a-c. This geometry is particularly interesting for addressing some fundamental questions, such as assessing the robustness of the directional flowing state against fluctuations, but also for the development of active flow networks, that is, networks of interconnected channels designed to perform a given task. In the first section of this chapter, we focus on channels with straight walls and study the effect of the channel geometry (width and length) on the flow velocity and stability. In the second section, we create a robust self-pumping microfluidic channel by shaping the channel walls with the ratchet pattern developed in the previous chapter. In the last section, we propose and discuss a theoretical model to describe the flow fluctuations in the channel.

1 Straight open channels

We study the effect of the width w and length L of the channel in two separate sets of experiments, with two grid models. The first grid is composed of five 2mm-long channels with different widths w=50, 100, 150, 200 and 300 µm, and the second grid is composed of four 100 µm-wide channels of lengths L=250, 500, 1000 and 2000 µm. The active length scale of the unconfined active nematic film is about L_ζ =100 µm in our experiments, therefore we are exploring channels of width 0.5 to 3 times the active length scale, and channels of length 2 to 20 times the active

length scale. All the channels have open extremities, so the grids were designed with a set of bridges connecting the channels from above to hold all the parts together (Figure 5.1 a, d). The surface of AN film confined within the channels is much smaller than the surface of the surrounding nematic film (Figure 5.1 b, e), therefore we can consider that the channel is coupled to an external active bath that is not significantly affected by the channels. A consequence is that neighbouring channels are independent from each other, their respective in-coming/out-coming currents are absorbed by the surrounding bath. Velocity fields are extracted from the stack of images with PIV measurements, unless it is stated that we use the optical flow method.

1.1 Spontaneous currents in narrow and long channels

Consistently with previous works on annular channels, we find that a persistent spontaneous current sets-up in channels that are narrow enough ($w \leq 200\,\mu m$) and long enough ($L \geq 500\,\mu m$) as attested by the velocity profiles $|V_x(y)| = |< v_x >_{x,t}|$ averaged over 5 minutes in Figure 5.1 f and g. The flow direction is selected by spontaneous symmetry breaking, since in some channels the flow points towards $+\boldsymbol{e_x}$ and in some others towards $-\boldsymbol{e_x}$, and for some channels the current even reversed its direction during the experiment, as we will see later in Figure 5.2 and Figure 5.3. Therefore we can reasonably rule out that an external asymmetry (for instance, the AN film in the channel is not horizontal, but tilted or curved) is necessary for a current to set-up. The averaged velocity profile has a symmetric shape with respect to the center of the channel $y = 0$: the maximum velocity $v_{x\max}$ is reached in the center of the channel, while the velocity at the wall is closed to 0. It is difficult to assess the slip length here due to the low magnification ($\times 10$) used to image the channel. The amplitude of the velocity depends on the channel geometry, both in terms of width and length. If we rescale velocity profiles by their maximum value $v_{\max} = \max|V_x(y)|$, and plot the rescaled profiles as a function of $\frac{y}{h}$, we see that velocity profiles have good agreement in terms of shape across the different geometries (Figure 5.1 i and f).

1.2 Tuning flow amplitude and stability with channel geometry

We define and measure the instantaneous surfacic flow rate as $\phi(t) = w < v_x(x, y, t) >_{x,y}$ where the longitudinal velocity v_x is spatially averaged over a rectangular window as wide as the channel, and 1000 µm long, when we vary the channel width, and only 250 µm long, when we vary the channel length for meaningful comparison. We observe that for channels that are long and narrow enough ($L \geq 500\,\mu m$ and $w \leq 150\,\mu m$), the flow ϕ fluctuates in time around two values $\pm\phi_0$ (Figure 5.2 a-c). For each experiment and each channel c, we plot the distribution $P_c(\phi)$ from the flow fluctuations $\phi(t)$ over 1 hour. If the flow does not reverse during the course of the experiment, the associated distribution displays only one peak located at $\pm\phi_0$. For each channel geometry, we superimpose the distributions obtained in different experiments using different colors, which reveals the two-bumps of the symmetric probability distribution of ϕ. Even though there is some variability between experiments, we can draw some general trends. Increasing the channel width at fixed channel length L=2000 µm makes the flow amplitude ϕ_0

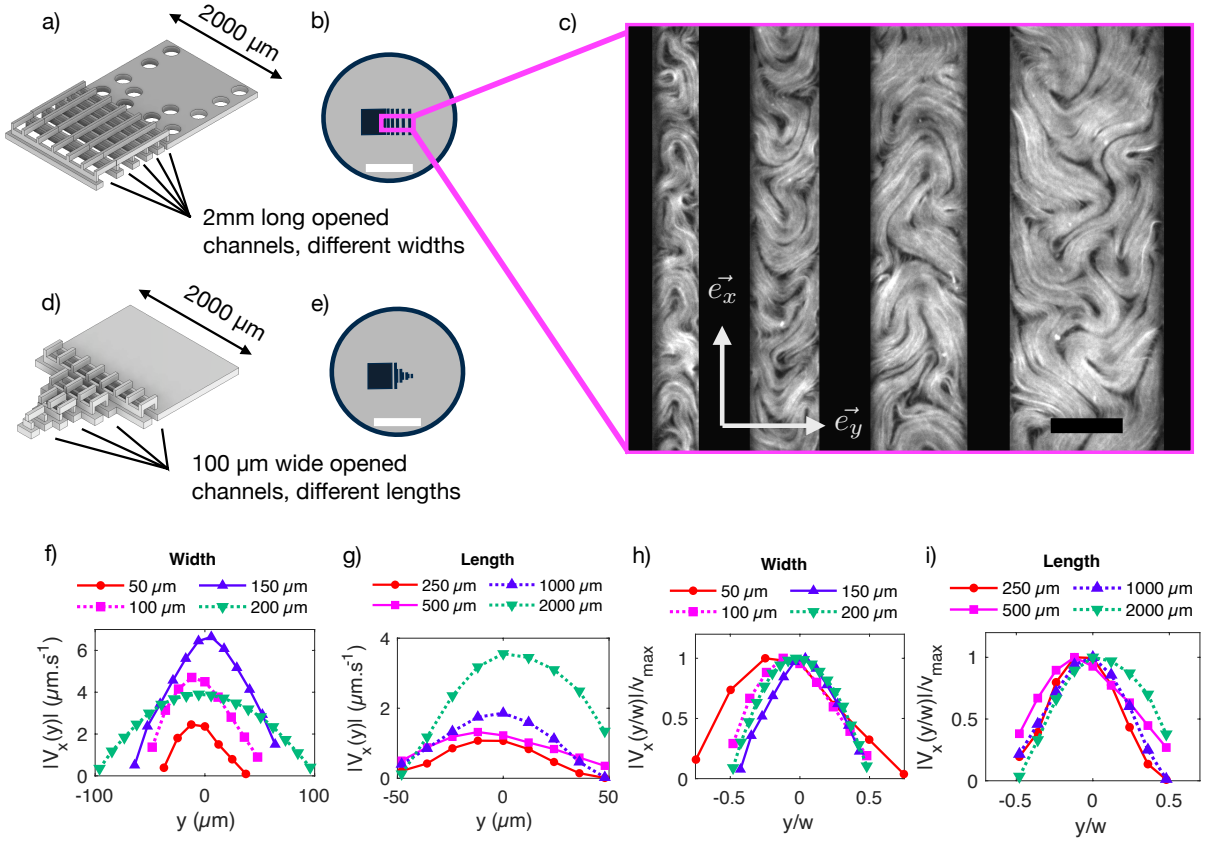

FIGURE 5.1 – **Spontaneous currents in narrow opened channels. a)** illustration of the grid embedding 5 channels of fixed length L=2000 µm and widths w=50, 100, 150, 200, 300 µm ; **d)** illustration of the grid embedding 4 channels of fixed width w=100 µm and lengths L=250, 500, 1000, 2000 µm ; **b)** and **e)** are two sketches representing the grids inside the entire experimental system, scale bar 3mm ; **c)** fluorescence micrograph showing the AN film confined in the microfluidic channels of grid a), scale bar 100 µm ; **f-g)** velocity profiles across channels of different widths (f) and lengths (g), velocity profiles were averaged over 5 minutes and over a spatial window 1000 µm long for grid (b) and 250 µm long only for grid (c). Continuous lines denote a current in $+\boldsymbol{e_x}$ direction, while dashed lines indicate a current in $-\boldsymbol{e_x}$. **h,i)** Velocity profiles rescaled by the channel width w and by $v_{\max}$. Access movies here and here to see the spontaneous flow in channels of length L =2000 µm and different widths.

increase without disrupting its stability, as long as $w \leq 150\,\mu m$ (Figure 5.2 d and e). Indeed, the relative fluctuations, defined as the flow standard deviation $\sigma = \sqrt{\mathrm{Var}(|\phi|)}$ divided by the average absolute value of the flow $\overline{\phi} =< |\phi| >_t$, shoot up when $w >150\,\mu m$. Increasing further the channel width results in lower flow values and larger fluctuations, making flow reversals more likely to happen. Increasing the channel length at fixed width w =100 µm, in contrast, reduces the relative fluctuations, which become less than 20% for L =2000 µm. It also induces an increase in the flow amplitude, which doubles from L =250 µm to L =2000 µm. However, we expect the flow amplitude to reach a maximum value when L is increased above 2000 µm.

These results demonstrate that the channel geometry can be chosen in order to obtain flows with desired amplitude and reversal frequency. Indeed, for some applications, we might want the flow fluctuations to be important so that the system can explore different configurations. For other applications, on the contrary, we might want the flow to be very stable and never able to reverse. To tune the flow stability, the most direct parameter is the channel length : for instance keeping $L \geq$1000 µm ensures that the relative fluctuations are below 50%, and therefore, flow reversal is unlikely. To tune the flow amplitude, the good lever is the channel width, which can be increased from 50 µm up to 150 µm, a value comparable to the active length scale, to obtain volumetric flow rates between 100 $\mu m^2/s$ and 600 $\mu m^2/s$. For channel widths above 150 µm the flow becomes too unstable.

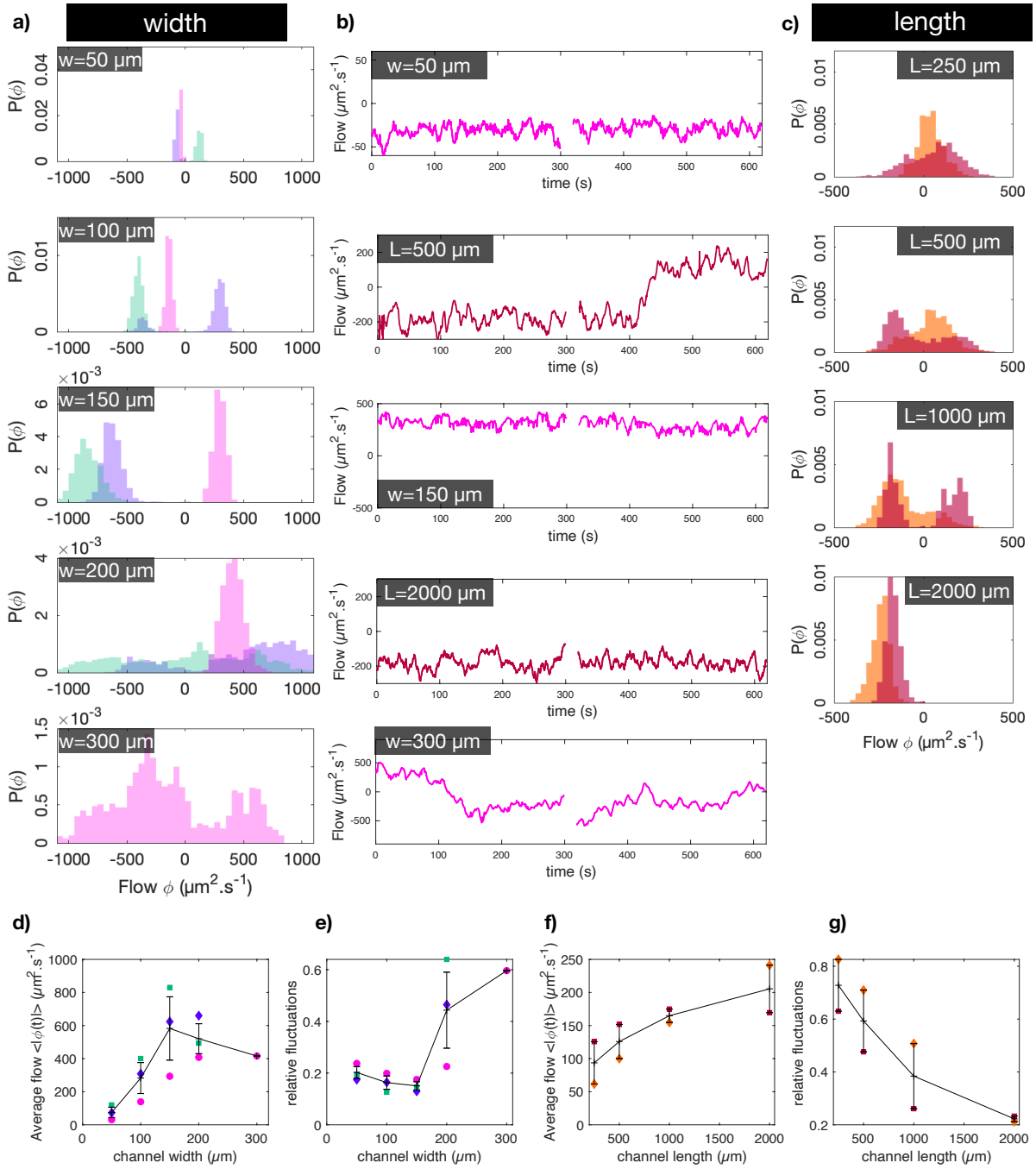

FIGURE 5.2 – **Channel geometry affects the flow.** In this figure, a color (pink, purple, green, dark red and orange) is assigned to the results of each independent experiment, **a)** normalized histograms of the flow rate ϕ for channels of width w=50, 100, 150 200 and 300 µm from 3 independent experiments ; **c)** normalized histograms of the flow rate ϕ for channels of length L=250, 500, 1000 and 2000 µm from 2 independent experiments ; **b)** some extract of the fluctuations of $\phi(t)$ in different channels ; **d)** plot of the average of the absolute value of the flow $< |\phi(t)| >_t$ versus the width of the channel ; **e)** plot of relative fluctuations versus the width of the channel ; **f-g)** the same quantities are displayed for channels of fixed widths and various lengths L=250, 500, 1000 and 2000 µm.

1.3 Flow reversal

We now describe how the velocity field evolves when the current reverses its direction. We use a reversal event observed in a 100 µm wide and 500 µm long channel (Figure 5.3 a-e). In this particular case, the velocity field is calculated with the optical flow method rather than PIV measurement for more precise results. The flow $\phi(t)$ is assessed over the entire channel. We look closely at the shape of the velocity field and the velocity profiles across the channel as $\phi(t)$ changes sign. When the fluid is flowing, the velocity field is unidirectional with some spatial oscillations (Figure 5.3 c, e). When $\phi(t) = 0$, the velocity field stream lines loop on themselves to form vortexes. In Figure 5.3 d, we observe more counter-clockwise (CCW) than clockwise (CW) vortexes. This explains the transient sinusoidal shape of the velocity profile at the time of the reversal (Figure 5.3 a,b). It is interesting to note that this process is asymmetric with respect to the two walls of the channel.

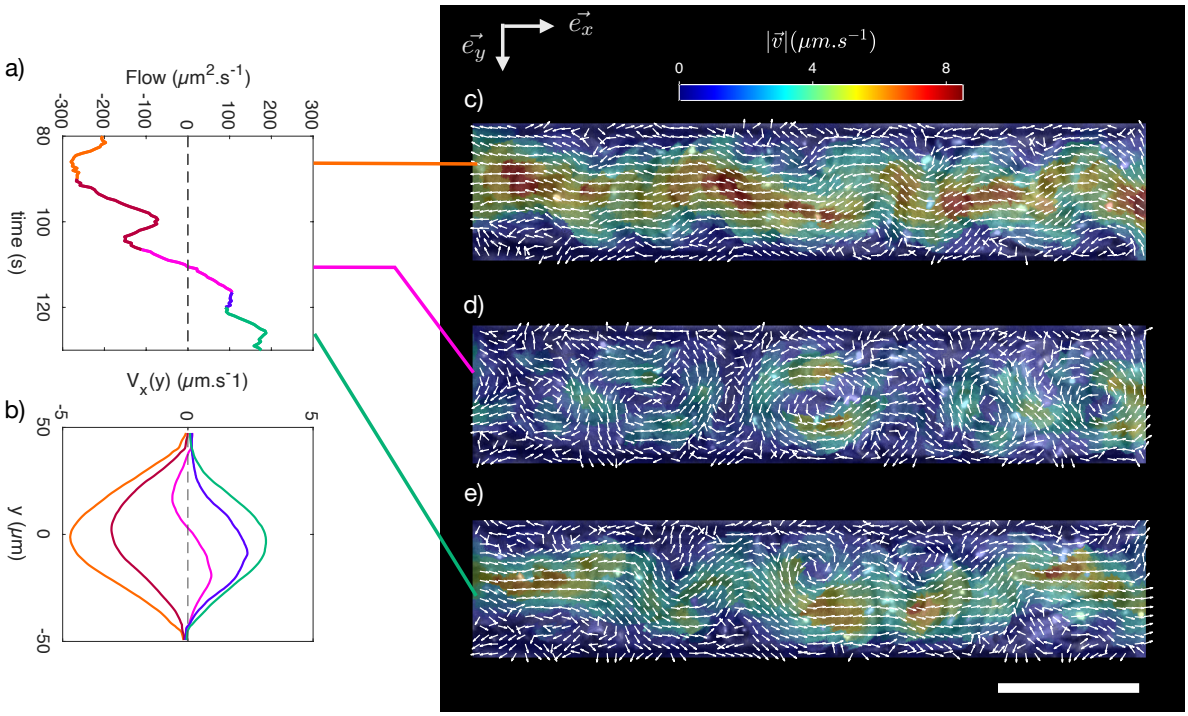

FIGURE 5.3 – **Flow reversal. a)** The averaged volumetric flow $\phi(t)$ changes sign during the experiment. The process is chunked into 5 time intervals, which can be distinguished by different colors. **b)** Velocity profiles $V_x(y)$ in the channel averaged over time for each time interval, which reveal that the initially parabolic velocity profile reverses its shape by going through a transient sinusoidal profile. **c-e)** instantaneous normalized velocity fields and colormaps of the velocity magnitude for the 3 successive states : c) flowing towards $-\boldsymbol{e_x}$, d) 0-flow e) flowing towards $+\boldsymbol{e_x}$.

1.4 Spatio-temporal correlations in the velocity field

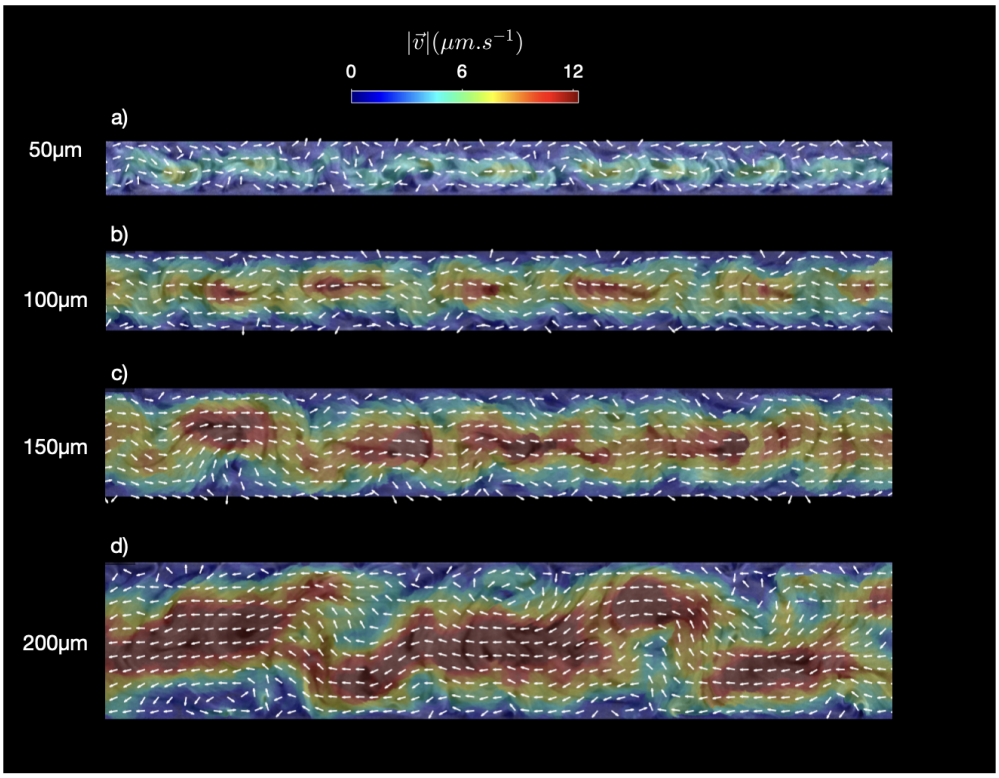

FIGURE 5.4 – **Flow field and channel width.** Instantaneous velocity field, extracted with the optical flow method, in 2000 µm long channels of various width. Arrows have been normalized, the magnitude of the velocity is overlaid in color. **a)** w =50 µm ; **b)** w =100 µm ; **c)** w =150 µm ; **a)** w =200 µm.

In this section, we analyze in more detail how the velocity field is structured and evolves with time. We use an optical flow method to capture the velocity field with pixel resolution (1.54 pixel/µm). We first obtain the instantaneous velocity fields in channels of different width (w=50, 100, 150 and 200) corresponding to the experiment shown in Figure 5.4. Then, we select time intervals where the flow is stable and we look at the spatio-temporal correlations of the two components of the velocity field, $C_y(s,\tau)$ for the transversal velocity, and $C_x(s,\tau)$ for the longitudinal velocity :

$$C_y(s,\tau) = \frac{< v_y(x,y,t)v_y(x+s,y,t+\epsilon\tau) >_{x,y,t}}{\sigma_y^2}$$
$$C_x(s,\tau) = \frac{< (v_x(x,y,t) - \overline{v_x})(v_x(x+s,y,t+\epsilon\tau - \overline{v_x})) >_{x,y,t}}{\sigma_x^2},$$

where $\epsilon = 1$ when the current is in $+\boldsymbol{e_x}$ and $\epsilon = -1$ when the current is in $-\boldsymbol{e_x}$, $\overline{v_x} =< v_x(x,y,t) >_{x,y,t}$ and σ_y and σ_x are the standard deviations of v_y and v_x. The average is performed over a spatial window 1000 µm long, and a temporal window of 5 minutes over which the current does not change direction.

In Figure 5.5, we plot the correlations for the transversal component v_y, $C_y(s,\tau)$, which

capture the undulation of the velocity field along the channel. The position of the first minimum s_{min} of the spatial correlations $C_y(s,0)$ (which is easier to measure than the first maximum), corresponds to the distance after which v_y is anti-correlated, which is half the wavelength of the oscillations. We find that s_{min} increases proportionally to the channel width and is comparable to the typical distance between $+\frac{1}{2}$ defects (Figure 5.5 b). The fact that the distance between topological defects is smaller than the intrinsic active length scale $L_\zeta \propto \sqrt{\frac{K}{\zeta}}$ under strong confinement has already been reported [52]. We expect the inter-defect distance to saturate towards the intrinsic active length scale for large value of the channel width. The spatial correlation between two time points separated by τ, $C_y(s,\tau)$, reveals that the flow patterns are not static but travel in the stream direction (Figure 5.5 c). To measure the speed of the wave, we track the position of the first maximum s_{max} with τ (Figure 5.5 d, e). For all the channels, the wave travels faster than the current speed $< v_x(x,y,t) > x,y,t$ (Figure 5.5 e). As the channel width is increased above $w = 200$ µm, we expect the structure size to reach a plateau, corresponding to the intrinsic active length scale L_ζ of the system, and the speed of the wave and current to decay to 0. The same analysis applied to the longitudinal component v_x shows that the longitudinal component also travels at a similar speed (data not shown).

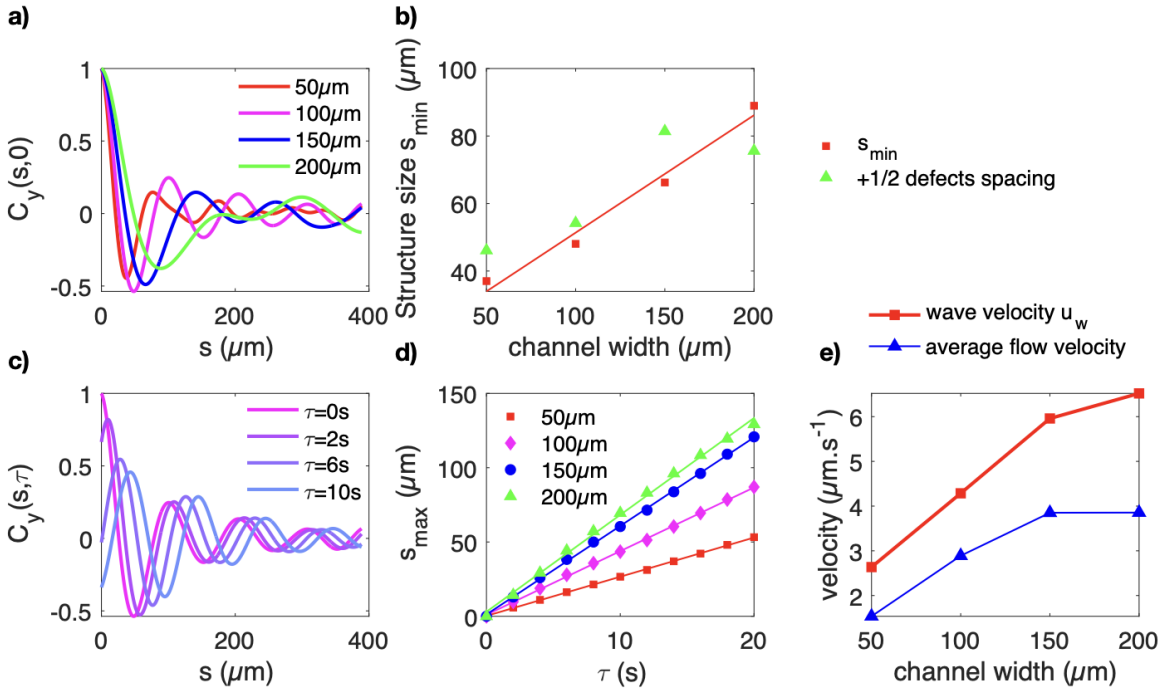

FIGURE 5.5 – **Spatio-temporal correlations in the velocity field. a)** spatial correlations of v_y for different widths. The position of the first minimum s_{min} represents the typical size of the flow structure **b)** and is comparable to the distance between $+\frac{1}{2}$ defects ; **c)** spatio-temporal correlations $C_y(s,\tau)$ for the channel of width w=100 µm ; **d)** the position of first maximum s_{max} of the spatio-temporal correlations curve $C_y(s,\tau)$ is increasing with the delay τ, sign that a wave is propagating in the current direction, **e)** at a velocity that depends on the channel width and that is in average 1.6 times higher that the mean current speed $\overline{v_x}$.

From the point of view of the flow field, we find that this active nematic system displays the

same behavior than some active polar fluids under channel confinement, despite being composed of radically different microscopic units. Wioland et al [19] have confined a dense suspension of flagellated *Bacillus Subtilis* inside a racetrack, and they also report oscillating flow structures that travel faster than the stream. When the confinement width becomes too wide, vortex forms and the travelling waves disappear with the current. Moreover, sound waves, ie propagation of velocity waves together with density waves, have also been reported for polar fluid composed of colloidal rollers [81]. In contrast, the bacterial suspension upper-mentionned and the active nematic film appears spatially homogeneous, except for the presence of topological defects in the latest.

1.5 Topological defects organization

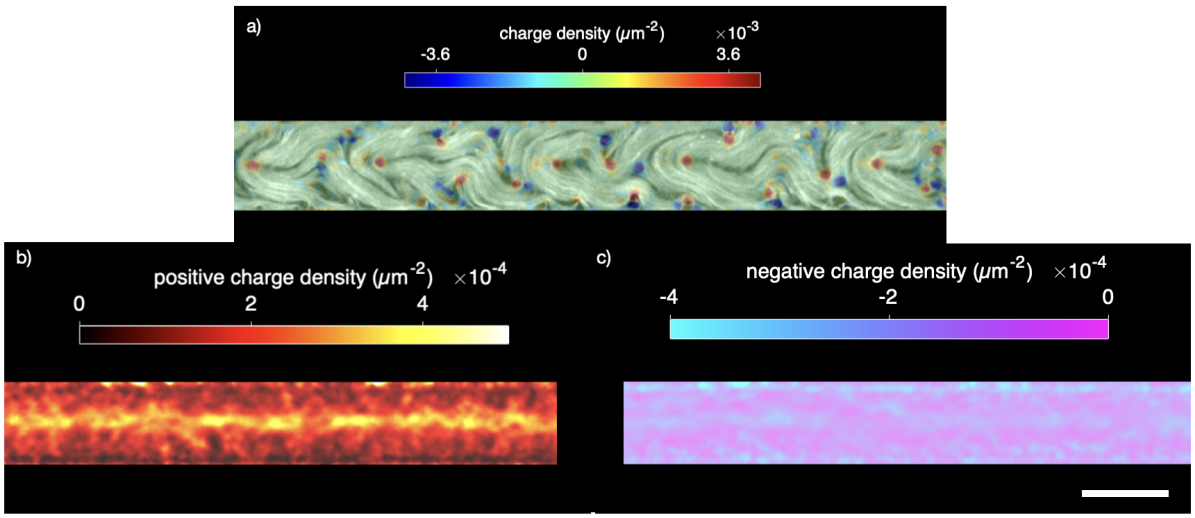

FIGURE 5.6 – **Defects spatial order in straight channels. a)** colormap of the instantaneous charge density q ; **b)** colormap of the time averaged positive charge density $< q_+ >_t$; **c)** colormap of the time averaged negative charge density $< q_- >_t$, scale bar 100 µm, channel width $w =$ 100 µm.

Spatial order. We compute the instantaneous diffuse charge density q as explained in Chapter 2 (Figure 5.6 a). We decompose q into a positive part, $q_+ = \max(q, 0)$, and a negative part, $q_- = \min(q, 0)$, representing respectively the density of positive charges and the density of negative charges such that $q = q_+ + q_-$. The temporal averages of q_+ and $q-$ (Figure 5.6 b and c) show some spatial modulation in the lateral direction y only, due to the invariance by translation along the channel long axis x. Positive defects are twice more likely to be found along the channel center-line than on the side, while negative defects mostly occupy the walls and the center-line.

Orientational order. We investigate if $+\frac{1}{2}$ defects, which are polar singularities in the director field, develop some kind of orientational order under channel confinement. We detect their individual polarity $\boldsymbol{p}_i$ (Figure 5.7 a, upper row on the right), and we average it along the channel

and over a 5 minute time-window to construct the lateral profile of the polar order parameter of positive defects : $P(y) = |< \boldsymbol{p}_i \delta(y_i - y) >_{i,x,t}|$ where i, $\boldsymbol{p}_i$, y_i, represent the index, polarity and y-coordinate of a $+\frac{1}{2}$ topological defect. The average is performed over a 1000 µm space-window and a 5 minute time-window. In Figure 5.7, we display the results for a channel 100 µm wide where the flow has set in the $-\boldsymbol{e_x}$ direction. The profile displays 3 maxima, next to each wall and in the center of the channel, where the polar order parameter is quite high ($P = 0.5$), indicating that defects have a particular orientation (Figure 5.7 b). We inspect the angular distribution of defects in each of the three regions. In the central region, defects point in the current direction, while on the side, defects tend to orient against the current, making a tilt of about 30°with respect to the wall (Figure 5.7 c). The fact that positive defects orient in the direction of the current was also observed in annular channels [51], but the authors report that defects near the walls makes a 90°angle with respect to the boundary, in contrast to our observations.

The orientation of positive defects relative to their like-sign nearest neighbours is compatible with earlier theoretical and experimental work about unconfined AN films [82] . Positive defects along the center line are often separated by a negative defect, which promotes their ferromagnetic orientation, and the same is true for defects orienting against the current along the wall (Figure 5.7 a). A center-line $+\frac{1}{2}$ defect and a near-wall $+\frac{1}{2}$ defect, on the other hand, are not separated by a negative defect, hence their anti-ferromagnetic interaction.

The orientation of $+\frac{1}{2}$ defects at the wall is reminiscent of bacteria swimming in microfluidic channels [19]. Indeed, bacteria accumulate at the walls and collectively orient in the direction opposed to the current. The flows generated by their flagella add up and cause the bulk current. Bulk bacteria, however, swim also against the current, which is in contrast with center-line positive defects that navigate downstream. This is not surprising since defect orientations are coupled via the director field.

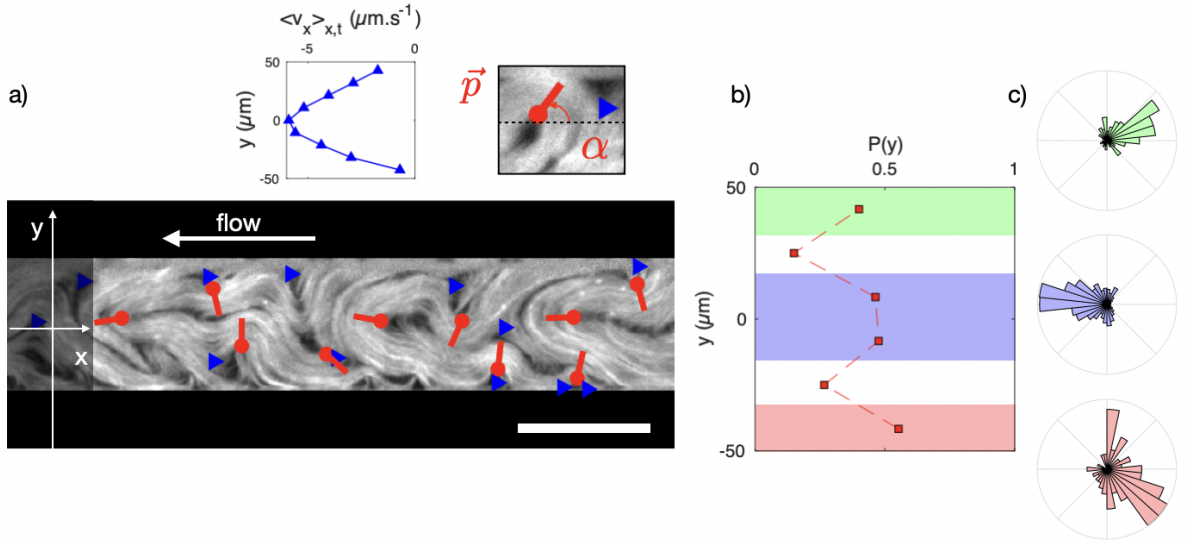

FIGURE 5.7 – **Orientational order of $+\frac{1}{2}$ defects. a)** fluorescent micrograph of the AN in a w=100 µm wide channel flowing in $-\boldsymbol{e_x}$ direction, detected $-\frac{1}{2}$ defects are marked with blue triangles and detected $+\frac{1}{2}$ defects are marked with red dots, in addition their individual polarity $\boldsymbol{p}_i$ is represented with a bar stemming from the defect core and pointing towards the head, scale bar 100 µm ; **b)** the polarity profile $P(y)$ defines three regions with relatively high polar ordering of $+\frac{1}{2}$, at the $y = +\frac{w}{2}$ wall (green), around $y = 0$ (blue), and at the $y = -\frac{w}{2}$ wall (red) ; c) polar histograms representing the orientation of $+\frac{1}{2}$ in each region, the orientation in the histograms represent directly the orientation in the image a).

Active force field. The active force depends on the gradient of the $\boldsymbol{Q}$-tensor and is proportional to $-\boldsymbol{\nabla} \cdot \boldsymbol{Q}$ in the case of extensile AN. Therefore, it is particularly localised around the core of positive defects. In Figure 5.8 b, we show that positive defects along the center-line generate a strong active force pointing in the current direction, and positive defects in the near-wall region exert a force in the opposite direction. However, friction with the boundary reduces velocities near the wall (Figure 5.8 a). As a result, the power of the active force is negligible at the wall, and overall the active force contributes to move the active nematic in the flow direction (Figure 5.8 c). We can speculate that, with free slip boundary conditions, there would be no net current in the channel, in the same way that it is almost impossible to walk on a slippery floor.

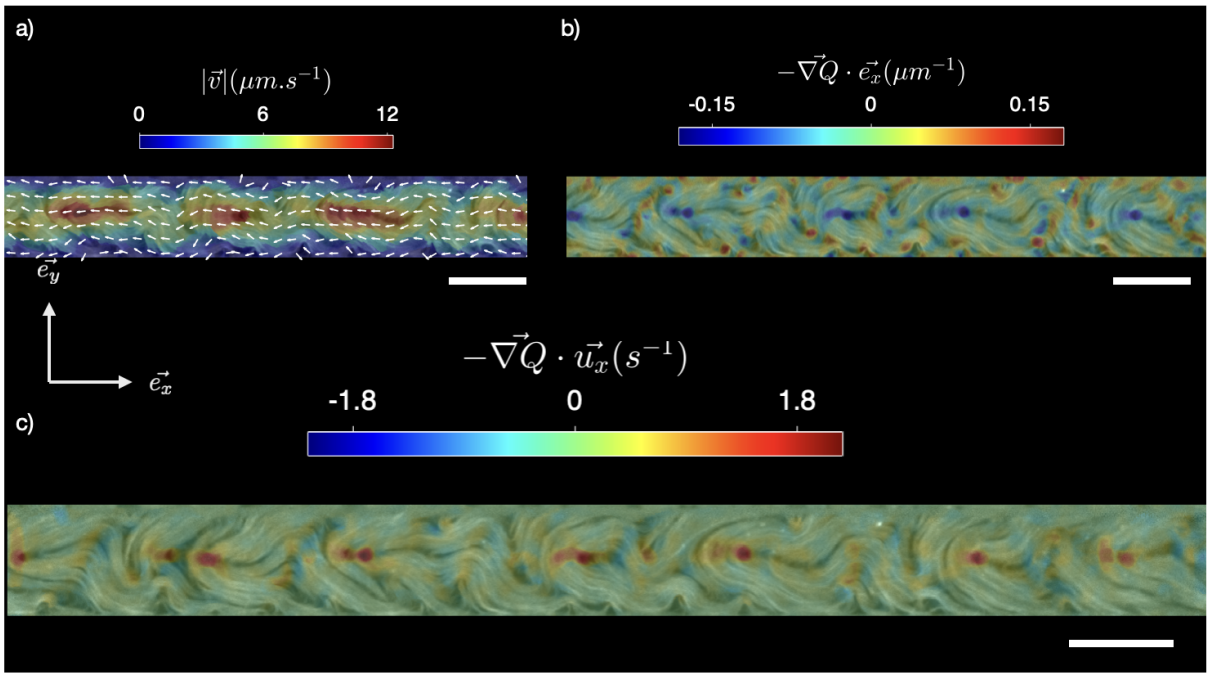

FIGURE 5.8 – **Active force and power.** Channel width is 100 µm, scale bar = 100 µm **a)** instantaneous velocity field ; **b)** projection of the active force along the channel direction ; **c)** longitudinal contribution of the power of the active force.

1.6 Proposed flow mechanism

We propose a self-perpetuating flow mechanism that is based on a bend-instability cycle. These cycles do not occur in a coordinated manner along the channel, but they can be observed locally in some portion of the channel, as we show in Figure 5.9. Initially, the director field is bent in the direction of the current, inducing the nucleation of pairs of $\pm\frac{1}{2}$ defects at the center-line, where the active stress is stronger(Figure 5.9 a, d). In such a configuration, the director becomes more and more aligned along the channel long axis. This aligned state is unstable against bend deformation : the bend- instability grows in the transversal direction and aligns the director orthogonally to the walls (Figure 5.9 b, e). Then, a second bend instability occurs in the longitudinal direction, but, due to the global current in the channel, the bending of the director occurs more likely towards the current direction than against it. Therefore, the instability develops usually in the current direction, and new defect pairs are created, sustaining the flow in the initial direction (Figure 5.9 c, f). The mechanism has performed a full cycle. The flow in the channel is self-substained because bend-instability cycles in different parts of the channel do not occur in phase. When the transversal bend instability occurs globally, that is when the net flow goes through a transitory state of zero flow, the current can take any of the two directions with the same probability. This explanation is in agreement with our earlier observation that, in long channels, the flow is very stable.

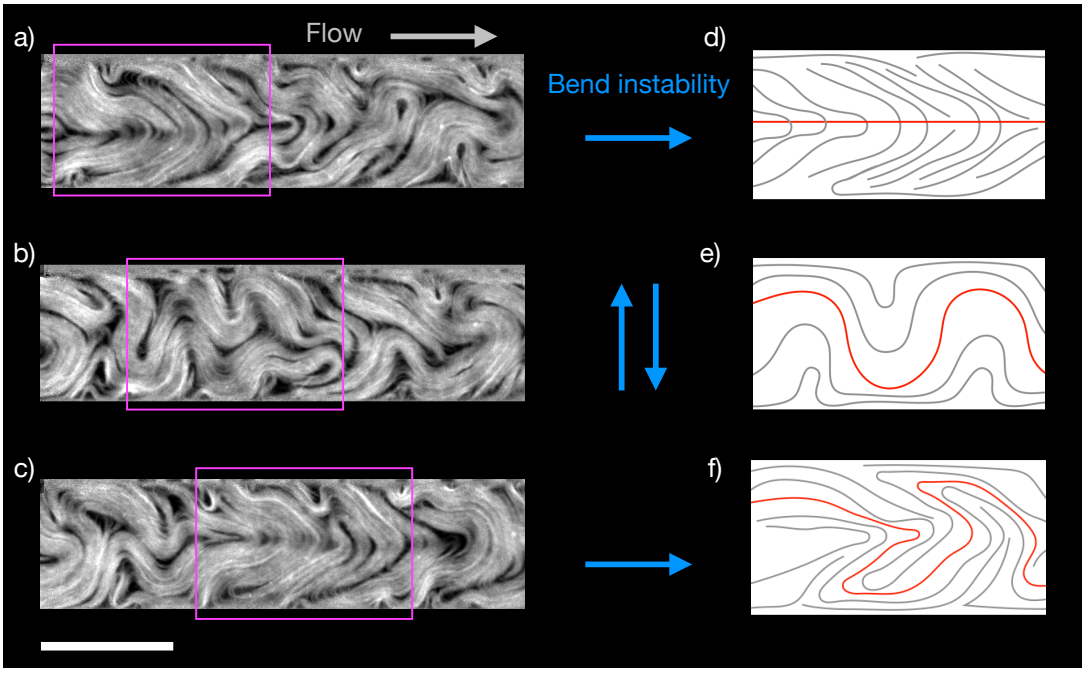

FIGURE 5.9 – **Flow mechanism based on an asymmetric bend instability.** Examples from a channel of width 150 µm. **a-c)** time sequence of 3 fluorescence micrographs, approximately 10 seconds apart, the magenta rectangular frame follows the zone of interest as it drifts ; **d-f)** illustration of the mechanism. Black line represents the director field. A material line is colored in red ; **a and d)** initially, the nematic field is bent in the $+\boldsymbol{e_x}$ direction, which generates a flow towards the right and aligns the director parallel to the channel long axis ; **b and e)** the quasi-aligned director field is prone to bend instability in the transversal direction, aligning the director in the transversal direction ; **c and f)** the nematic is now prone to bend instability in the longitudinal direction, and the global net current in the channel favors the bending in the $+\boldsymbol{e_x}$ again, generating a train of $\pm\frac{1}{2}$ pairs of defects. Scale bar = 150 µm.

In straight channels, the flow direction is set by an initial spontaneous symmetry breaking. In the next section of this chapter, we show how the flow symmetry can be externally broken with ratchet patterns along the walls.

2 Controlled flow in ratchet channels

As mentionned in the introduction of this chapter, previous works showed that, for the two-dimensional AN under study, small chiral notches are enough to break the symmetry and control the current direction in small and closed channels [50, 51]. Here, we propose a new design that strongly stabilises the flow, referred to as the "ratchet channel", made by indenting the walls of a 2000 µm long open channel with the saw tooth periodic pattern presented in the Chapter 4. Teeth are 100 µm long, and protrude by 50 µm (Figure 5.10 a,b), making a 27°angle with the horizontal. The walls are distant by 200 µm at the widest point, and by 100 µm at the narrowest, between two facing teeth. In contrast with [50] and [51], our asymmetric pattern has a size comparable to active length scale. In this way, the pattern controls the flow direction by acting directly on the topological defects all along the channel. This design promises a robust

flow control when the ratchet channel becomes part of a network of connected channels. In this situation, we expect the channel to behave as a diode, by totally preventing the current to go along the uneasy ratchet direction.

2.1 Directed flow

The current systematically sets in the $+\boldsymbol{e_x}$ direction, which is the easy direction of the ratchet pattern (Figure 5.10 c, d, e). We do not observe any current reversal, and the fluctuations are reduced compared to straight channels of comparable width.

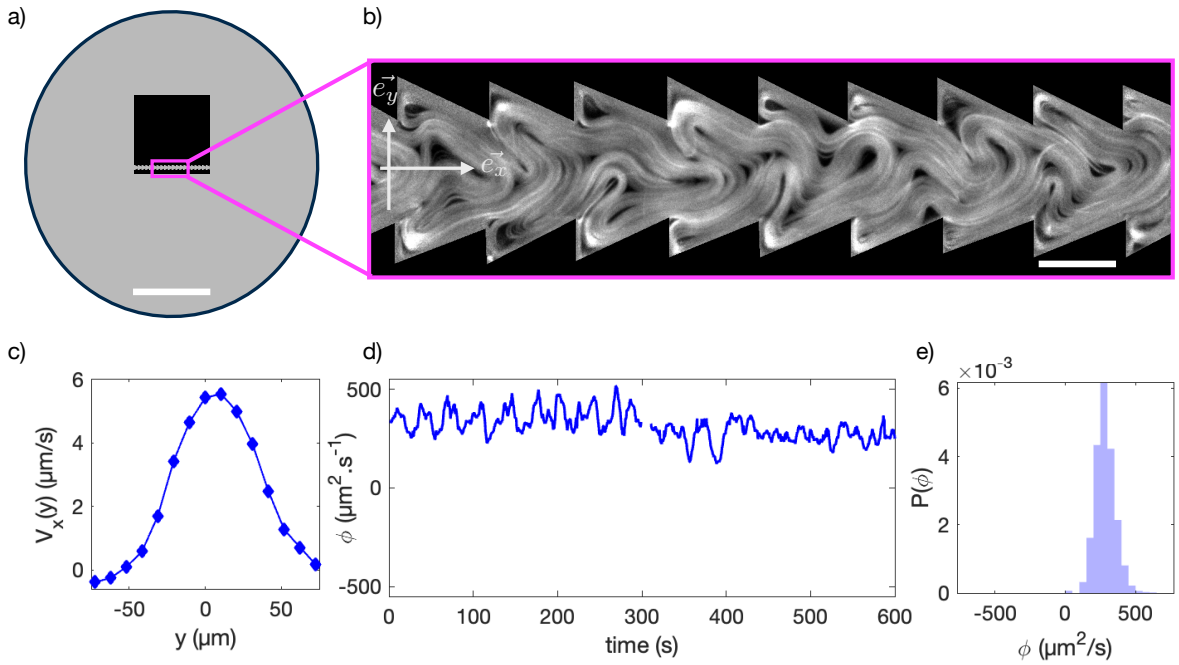

FIGURE 5.10 – **Directed current in ratchet channel a)** sketch of the grid placed in the AN film ; **b)** fluorescence micrograph of the AN confined in the ratchet channel, scale bar = 100 µm ; **c)** average velocity profile $V_x(y)$; **d)** time fluctuations of the volumetric flow ϕ ; **e)** the distribution of the volumetric flow ϕ displays only one peak around $\phi_0 > 0$. A movie is accessible here

2.2 Structure of the velocity field

The spatio-temporal correlations $C_y(s, \tau)$ for the transversal velocity v_y (Figure 5.11 a,b,c) are similar to the straight channel. At fixed time, the wavelength of the transversal oscillation does not correspond to the ratchet wavelength of 100 µm. Indeed, we find that v_y is anticorrelated at $s_{min} = 70$ µm, so a full period would be 140 µm. The transversal oscillations also travel along the channel in the direction of the current, at a speed that is very similar to the case of the straight channel of width $w = 150$µm. However, in contrast to the straight channel, we find that the longitudinal component of the velocity is strongly constrained by the ratchet pattern (Figure 5.11 d, e, f), since the period of oscillation is found to be equal to 100 µm. Moreover, the longitudinal component is static and does not travel along the channel. We attribute this to

the periodic constriction associated to the ratchet pattern combined to the incompressibility of the AN fluid.

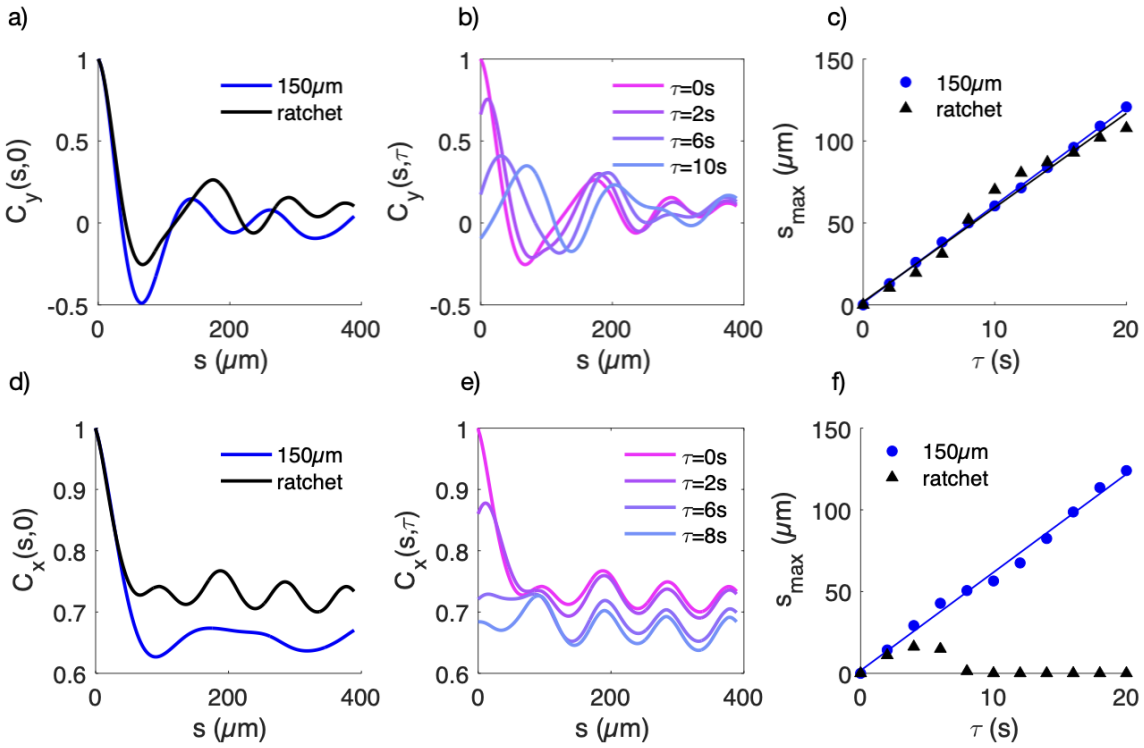

FIGURE 5.11 – **Spatio-temporal correlations in the velocity field in ratchet channels a-c)** correlations $C_y(s,t)$ of the lateral component of the velocity v_y. In a, c, d, and f, the blue curve is for a straight channel of width w=150 µm. **d-f)** correlations $C_x(s,t)$ of the longitudinal component of the velocity v_x. There is no wave propagation for the longitudinal component in the ratchet channel, as opposed to the straight channel.

2.3 Defects organization

We detect topological defects in the ratchet channel. $-\frac{1}{2}$ defects located at the tip of each ratchet tooth are not detected by the algorithm, this is why we circle them manually in Figure 5.13 a. The code also misinterprets the void found in the corner of each ratchet tooth as a negative defect, while, in reality, this should have a 0 boundary charge associated to it.

Spatial order. Temporal averages of diffuse density of charges q_+ and q_- display some periodic patterns imposed by the periodicity of the ratchet walls (Figure 5.13 b,c). This denotes some spatial organization of topological defects, in stark contrast with the case of straight smooth-walled channels. Also, q_+ features some oval rings in the corners of each ratchet tooth, they result from the very consistent looping trajectory followed by positive defects in the corners.

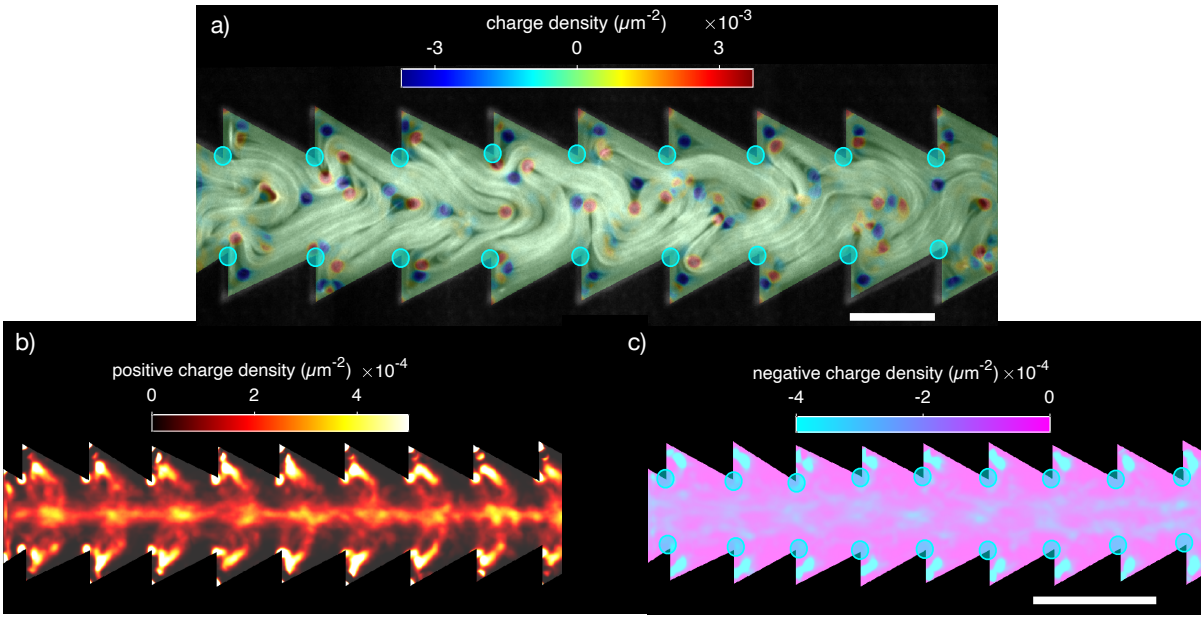

FIGURE 5.12 – **Spatial organization of topological defects in ratchet channels. a)** the instantaneous charge density is concentrated around topological defects. Negative wall defects, pinned at the tip of each ratchet tooth, are not detected by the algorithm but circled in turquoise manually ; **b)** average density of positive defects forms an ear-wheat pattern ; **c)** average charge density of negative defects. Scale bar = 100 µm

Orientational order of $+\frac{1}{2}$. We find that around the center-line positive defects orientation $\boldsymbol{p}$ tends to point in the current direction, which is the "good direction" of the ratchet (Figure 5.13 a). Like for straight channels, we observe the formation of the train of $\pm\frac{1}{2}$ pairs of defect along the center-line . Side positive defects, on the contrary, adopt an opposite orientation, they point in the up-stream direction, at an angle comparable to the indentation slope of 27°(Figure 5.13 c). The orientational order is similar for straight channels. Nevertheless, the degree of polar order is higher in the ratchet channel, in particular in the lateral regions where it reaches 0.9 instead of 0.5 for the straight channels (Figure 5.13 b). The fact that side defects linger in the corners for a while before deflecting their trajectory towards the center of the channel, can explain the stronger polar order at the walls. We can speculate that the strong orientation stems from the wall, whose asymmetric teeth force the positive defects to point in $-\boldsymbol{e_x}$ direction at the wall, and in turn, control the orientation in the center, via the antiferromagnetic alignment of positive defects not separated by a negative charge. One can now wonder how defects orientation is transformed when the two ratchet walls have opposite orientation.

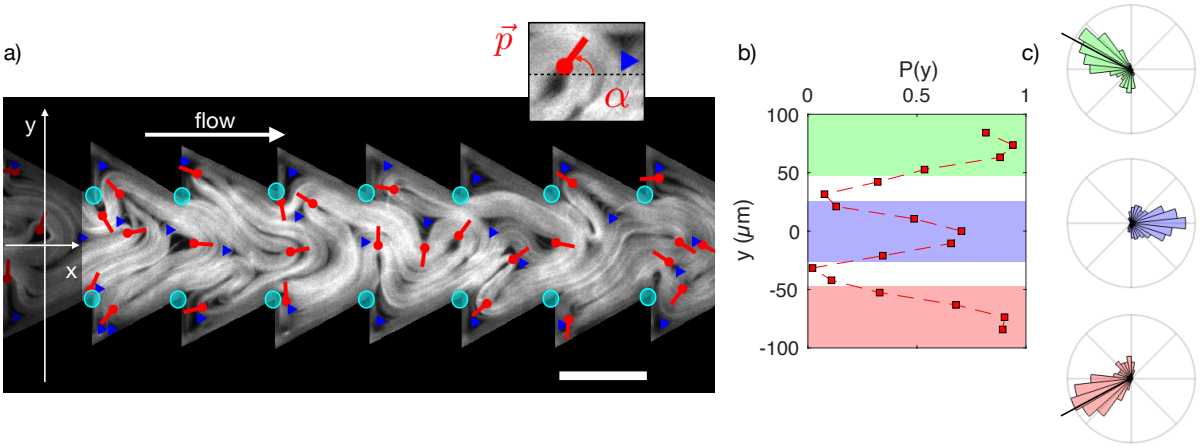

FIGURE 5.13 – **Orientational order of $+\frac{1}{2}$ defects in ratchet channels. a)** fluorescence micrograph with detected negative defects marked with a blue triangle, positive defects with the red dot ; **b)** Polar order parameter across the channel has 3 maxima ; **c)** distribution of $+\frac{1}{2}$ orientation in each polar region. For the 2 histograms representing the orientation in the near wall regions, we have added a black line standing for the angle of the indentation.

2.4 Channels with antagonistic ratchet walls

Ratchet teeth on the lower wall ($y = -100$ µm) are oriented towards $-\boldsymbol{e_x}$, while the upper wall teeth ($y = +100$ µm) points towards $+\boldsymbol{e_x}$, as shown in Figure 5.14 a-c. The velocity field is a combination of two states. It can either be dominated by vortexes, often rotating clockwise, as promoted by the ratchet walls (Figure 5.14 a), or display more apparent bidirectional flows oriented in accordance to each wall easy flow direction (Figure 5.14 b). In average, the velocity field shears the fluid along the channel (Figure 5.14 c), the velocity profile has a sinusoidal shape (Figure 5.14 d) and the net flow ϕ is closed to 0 (Figure 5.14 e). While classic narrow channels favor a net flow state, the ratchet channel with antagonistic walls is a microfluidic element able to stabilize the 0-flow state.

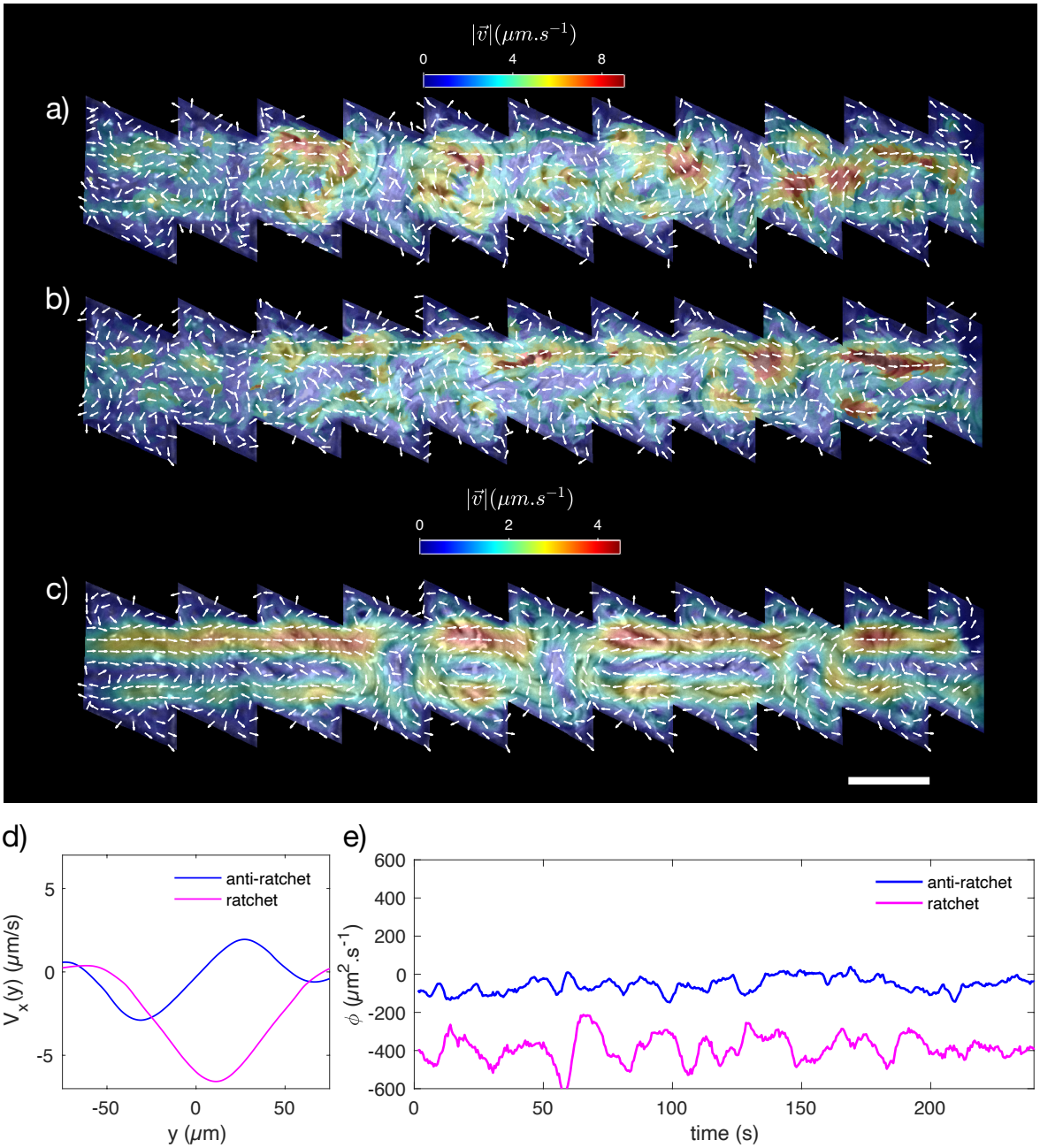

FIGURE 5.14 – **Stabilization of zero-flow state with antagonistic ratchet walls.** a) Instantaneous velocity field in a state dominated by CW vortexes ; b) instantaneous velocity field in a state where bidirectional flux are more apparent ; c) average of the velocity field over 5minutes, shows bidirectional flow. d) 5-minute average of the velocity profile $V_x(y)$ in the anti-ratchet channel (blue) compared to the ratchet channel (magenta). e) Fluctuations of net flow $\phi(t)$. In the anti-ratchet channel, the net flow is close to 0.

3 Discussion and modelling

Several work have used equilibrium models to describe the behavior of active systems. For instance, Wioland et al [83] created a microfluidic square lattice of interconnected circular ca-

vities filled with a microbial solution. In each cavity, bacteria spontaneously generate a circular flow. Therefore, they represent the dynamical state of each cavity by a continuous vortex spin V_i associated to a symmetric double-well potential. In the lattice, spins are coupled to their neighbours through two competitive effects : hydrodynamic interaction at the gap connecting cavities favor antiferromagnetic order, and edge currents of bacteria around the separative pillars favor ferromagnetic order. They modelled the system with a lattice field theory Hamiltonian taking into account cavity spins V_i and pillar circulations P_i. This mathematical model, similar to the 2D-equilibrium Ising model, recovers the ferromagnetic order for strongly interconnected cavities and antiferromagnetic order for small-overlapped cavities.

Inspired by this work, we carry a similar analysis for the AN confined to straight open channels only. We project the complex dynamics of the AN in the channel to only one degree of freedom, the instantaneous net flow $\phi(t)$ along the channel, measured, as explained in Section 1 of this chapter, by averaging over a 1000 µm long section of the channel. We have observed that $\phi(t)$ fluctuates around two opposite values $+\phi_0$ and ϕ_0 and can occasionally transition from one value to the other, especially if the channel is short or wide. Therefore, we choose to model the flow dynamics as Brownian motion in a double-well potential.

3.1 Langevin dynamics in a double-well potential

We choose to model the dynamics of the surfacic flow $\phi(t)$ by an over-damped Langevin equation

$$\frac{d\phi}{dt} = -\frac{dV}{d\phi} + \sqrt{2T}W(t) \tag{5.1}$$

where $V(\phi)$ is a double-well potential $V(\phi) = \frac{a}{4}\phi^4 + \frac{b}{2}\phi^2$ and $W(t)$ is a Gaussian noise with average $< W(t) >= 0$ and correlation function $< W(t)W(t') >= \delta(t - t')$.

The experimental data consist in a discrete set of observations $\{\phi_i = \phi(t_i = i\Delta t)\}$ for $i = 1 : N$, made at regular intervals $\Delta t = 0.5$ s. We discretize the Langevin equation according to the Euler-Maruyama scheme :

$$\phi_{i+1} = (1 - b\Delta t)\phi_i - a\Delta t\phi_i^3 + \sqrt{2T\Delta t}N_i \tag{5.2}$$

Where the N_i are independent Gaussian random variables following $\mathcal{N}(0, 1)$, we note f their probability density function.

3.2 Inferring the model's parameters

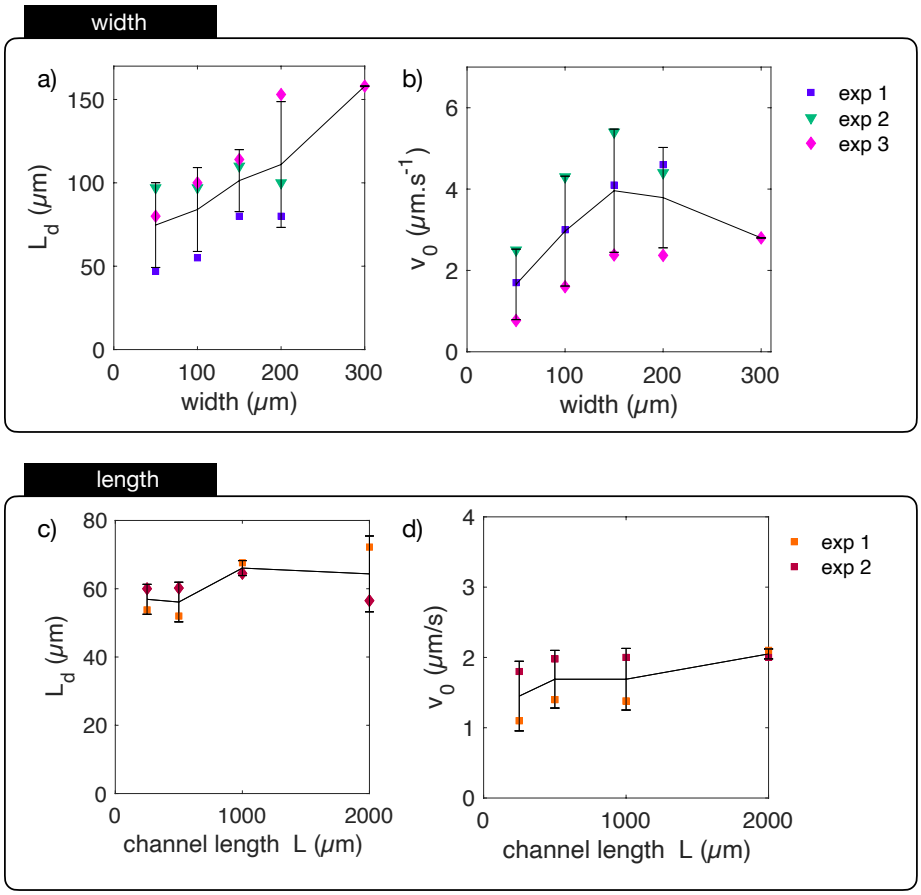

FIGURE 5.15 – **Variability between experiments. a)** Distance between topological defects L_d and **b)** average fluid velocity v_0 increases with the confinement width w before saturating, but have a variability of roughly 50 % from one experiment to another. **c,d)** The same parameters vary less with the length of the channel L but still vary between the two experiments.

Rescaling. Two experiments usually differ in various ways : activity, density of bundles, friction with the substrate... To account for this variability, for each channel of width w, length L from a given experiment, we measure the average norm of the velocity $v_0 =< |\boldsymbol{v}| >_{x,y,t}$ and the average distance between positive topological defects L_d (Figure 5.15 a-d). L_d and v_0 are directly impacted by the width of the channel w, but also, for a given channel geometry they vary from one experiment to the other. This provides us with a characteristic time $\tau = \frac{L_d}{v_0}$. We then rescale the flow as $\tilde{\phi} = \frac{\phi}{v_0 L_d}$ and time as $\delta t = \frac{\Delta t}{\tau}$. Under this rescaling, the equation becomes :

$$\tilde{\phi}_{i+1} = (1 - \tilde{b}\delta t)\tilde{\phi}_i - \tilde{a}\delta t\tilde{\phi}_i^3 + \sqrt{2\tilde{T}\delta t}N_i \tag{5.3}$$

With the dimensionless parameters $\tilde{a} = a\tau v_0^2 L_d^2$, $\tilde{b} = b\tau$, $\tilde{T} = \frac{T\tau}{v_0^2 L_d^2}$. From now on, we will only work with the dimensionless variables and omit the tilde notation.

Log-likelihood maximisation Given a set of parameters a, b, T, the probability to observe the time sequence $\{\phi_1, \phi_2, ..\phi_N\}$ starting from an initial condition ϕ_0 is the probability of the associated noise time sequence : $\{N_0, N_1, ..., N_{N-1}\}$ with :

$$N_i = \frac{1}{\sqrt{2T\delta t}} \left[\phi_{i+1} - (1 - b\delta t)\phi_i + a\delta t\phi_i^3\right] \tag{5.4}$$

We look for the parameters a and b that maximize this probability, or, equivalently, the log likelihood estimator S :

$$\begin{aligned} S(a,b) &= \log(f(N_0, ..., N_{N-1})) = \log(\prod_{i=0}^{N-1} f(N_i)) \\ &= -\frac{1}{2}\log(2\pi) - \frac{1}{2T\delta t}\sum_{i=0}^{N-1}\left[\phi_{i+1} - (1 - b\delta t)\phi_i + a\delta t\phi_i^3\right]^2 \end{aligned}$$

We have used the fact that the N_i are independent and follow the standard normal distribution. For convenience, we minimize the cost function J with respect to a and b :

$$J(a,b) = \frac{1}{N}\sum_{i=0}^{N-1}\left[\phi_{i+1} - (1 - b\delta t)\phi_i + a\delta t\phi_i^3\right]^2 \tag{5.5}$$

We do so using a gradient descent with momentum algorithm.

Once we have found the optimal parameters a and b, we can assess the noise amplitude T by estimating the variance :

$$2T\delta t = \frac{1}{N}\sum_{i=0}^{N-1}\left[\phi_{i+1} - (1 - b\delta t)\phi_i + a\delta t\phi_i^3\right]^2 \tag{5.6}$$

3.3 Results

For narrow and long channels, the inference method finds $a > 0$ and $b < 0$, confirming the hypothesis of the double-well potential (Figure 5.16 a, e). At given width w, the inferred parameter $a_E(w)$ and $b_E(w)$ inferred from experiment E are quite dispersed, and we notice that recasting the results in terms of the effective width $w_{eff} = \frac{w}{L_d}$ reduces a little the dispersion of the points (Figure 5.16 c), indicating that the effective width might be a more relevant geometrical parameter. We find that the noise amplitude T also increases with the channel width (Figure 5.16 b, d), and decays with the channel length (Figure 5.16 f).

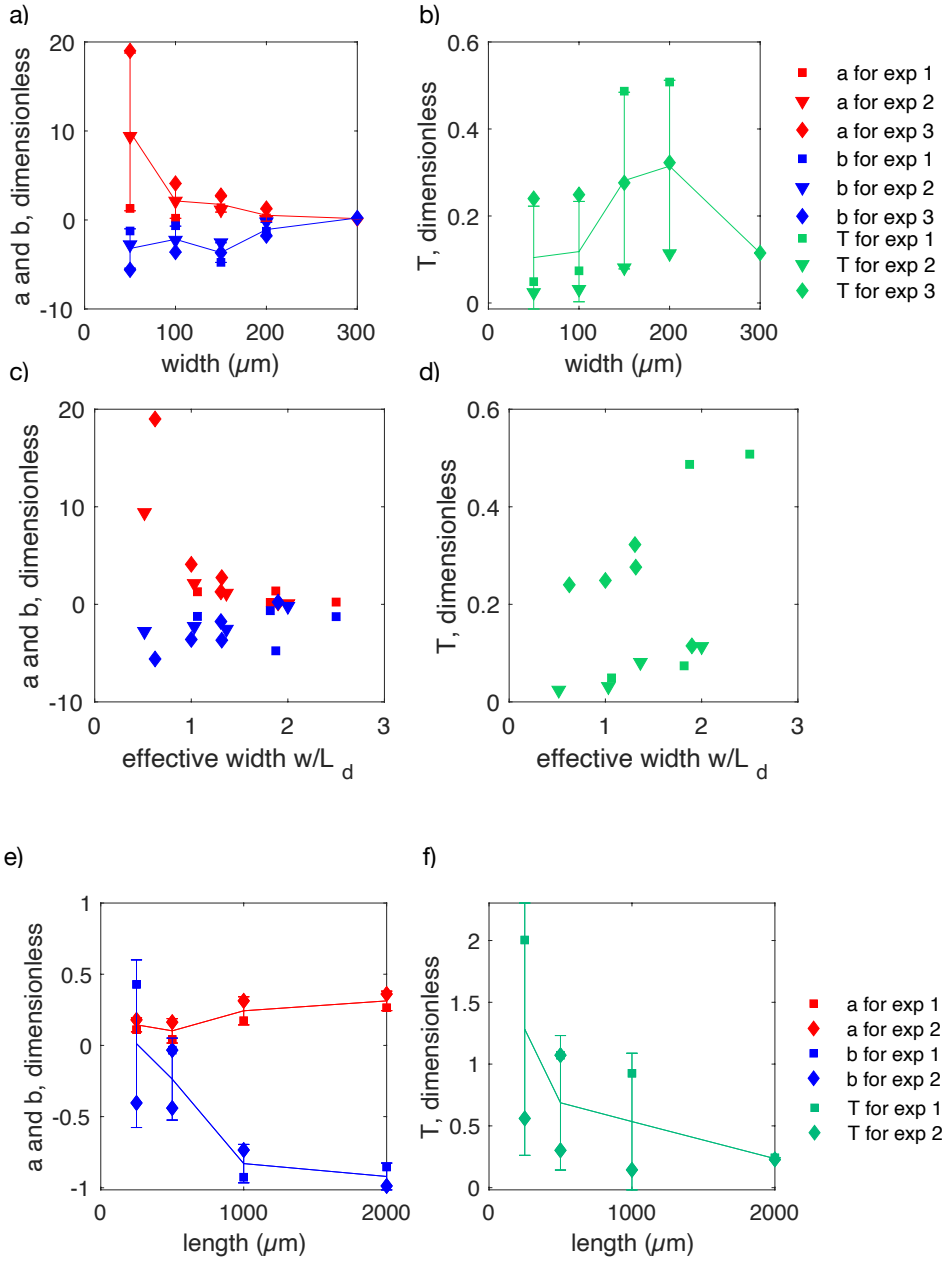

FIGURE 5.16 – **Parameters of the model. a,b,c,d** Dimensionless parameters for channels of different widths from each experiment, a symbol is attributed to each experiment. The lines represent the average value and associated error bar.**a)** Inferred a, b versus the channel width ; **b)** inferred T versus the width ; **c)** a, b versus the effective channel width $\frac{w}{L_d}$ are slightly less dispersed ; **d)** T versus the effective channel width. **e)** Inferred a, b versus the channel length ; **f)** inferred T versus the length.

For a given geometry, we average the inferred parameters over the experiments E : $\overline{a}(w) =< a_E(w) >_{E=1,2,3}$, $\overline{b}(w) =< b_E(w) >_{E=1,2,3}$ for the width, and $\overline{a}(L) =< a_E(L) >_{E=1,2}$, $\overline{b}(L) =< b_E(L) >_{E=1,2}$, for the length. We recover the parameters in their original dimension using the averaged values of L_d and v_0. In Figure 5.17 a and b, we plot the inferred potentials $V(\phi)$.

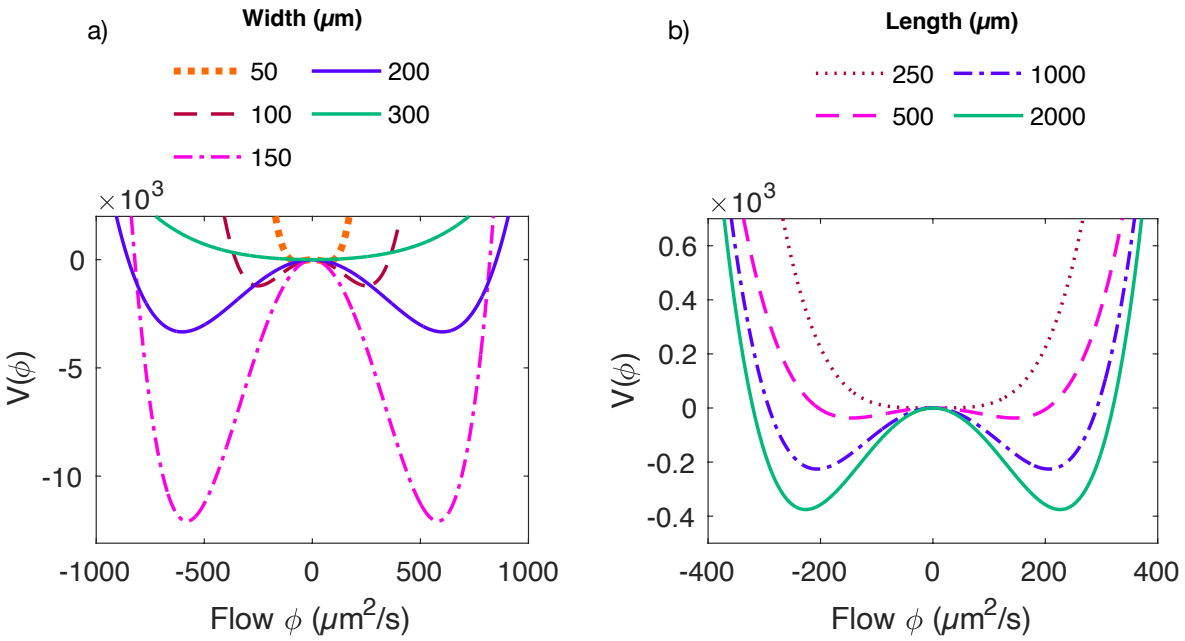

FIGURE 5.17 – **Inferred potentials. a)** Inferred double-well potentials for channels of identical length and different widths. **b)** Inferred double-well potentials for channels of identical width and different lengths.

3.4 Discussion

Assuming the suitability of the model, the inference method proves that the channel geometry (L and w) affects both the potential shape and the noise causing the fluctuations of the flow rate ϕ. The dependence of the potential on the width w was visible from Section 1, by the fact that the flow amplitude ϕ_0 increases with the width, but was less obvious for the dependence on the channel length, where both a small energy barrier between the two minima of the potential and a high noise amplitude could explain the higher reversal rate for short channels.

The channel length has a local stabilizing effect on the flow ϕ by both increasing the energy barrier between the two minima $\pm\phi_0$, and decreasing the noise amplitude T (Figure 5.16 e and f). The dependence of the noise T on the channel geometry, shows that part of the noise is intrinsic to the fluid confined in the channel, it is not only coming from the extremities of the channel. To confirm this point, it would be interesting to measure the flow rate ϕ on different portions of the channel, to see to what extent, if at all, the flow at the extremity of the channel is more disturbed by the surrounding fluid.

However, it is surprising that the inference finds single-well profiles for w =300 µm, and L =250 µm. Moreover, when we assume a potential of order 6 such as : $V(\phi) = \frac{a}{6}\phi^6 + \frac{b}{4}\phi^4 + \frac{b}{4}\phi^4$, the parameters a, b, c inferred are not consistent across geometries and experiments. It is a sign that the model does not fit very well the flow dynamics. The model is probably too simplistic. First, the flow rate ϕ might not be sufficient to describe the system's dynamics. We could include more degrees of freedom, in particular one that is related to the nematic distortions in the system, in link to the flow mechanism involving a cycle of bend instabilities we have proposed in Section

1. In addition to this, here we have assumed a white Gaussian noise for the perturbation. In reality, the noise could depend on the system state, in particular if it is related to the defects configuration. When the flow is low, usually the system is bent in the transversal direction, a situation where positive defects are orthogonal to the walls and more prone to orient in the direction opposite to the current, so we could expect that the noise is more important in this configuration. Furthermore, the over-damped Langevin dynamics is a memory-less process. The cycle of bend instability relies on the non-synchronicity of channels portions, implying that a memory of the flow is kept by neighbouring section of the channel. This could be accounted for by a generalized Langevin equation including an inertial term.

Conclusions. We have experimentally studied the effect of confining the active nematic to long, narrow channels with open ends, and shown that net persistent currents spontaneously emerge in such geometry. In channels with straight walls, the direction of the current is selected by spontaneous symmetry breaking and it can be occasionally reversed if the fluctuations are high enough. The channel geometry affects the flow, for instance the current's amplitude increases with the channel width, up to a certain point where fluctuations become important, and the flow stability increases with the channel length. Ratchet walls dictate the current's direction, with equal orientation they create a self-pumping microfluidic channel, with antagonistic orientation they stabilize the zero-flow state. We found that these flow states are associated to travelling waves in the velocity field and to the ordering of topological defects, particularly enhanced by the ratchet patterns : $+\frac{1}{2}$ defects orient in the direction of the current around the channel center-line, and in the direction opposite to the current in the near-wall region. Finally, we proposed to describe the flow fluctuations in a straight channel with an equilibrium-like model : the overdamped Langevin equation in a double-well potential. Even if the model is a satisfying first-order approximation, more complex models should be considered in the future. Some questions are still open, for instance, does the flow state sets-up in infinitely long channels, or would it be cancelled by an occlusion ? To our knowledge, such flow states embedding topological defects are not explained yet by theoretical models of active liquid crystals. In the next chapter, we will capture with numerical simulations the main features of these experimental results.

Chapter 6

Numerical study of active nematics in channels

There is great interest in reproducing with numerical simulations the main features of experimental active nematics. First, to validate the mathematical models used to describe such AN systems. From there, numerical simulations can provide some insights on which are the key parameters that control the system's dynamics, predict the behavior in original set-ups, and provide guidance for future experimental work.

To our knowledge, numerical simulations have not reproduced the spontaneous flow of active nematics confined to a straight channel reported in the previous chapter, nor have they tackled the topic of channels with ratchet walls yet. In this chapter, we describe our efforts towards this objective, using the mathematical model and numerical methods described in Chapter 3. We run numerical simulations of an AN system confined in a quasi 2D channel with periodic boundary conditions in the channel axis. In the first part, we try to reproduce the flow state embedding topological defects in a channel with straight walls. In the second part, we recover the spontaneous flow in channels with ratchet walls.

1 Straight periodic channels

1.1 Net-flow states might arise from the AN equations

One theoretical work has reported a net-flow state with topological defects in AN channels [84]. Wagner et al, have explored the dynamical phase space of 2D AN in a channel with periodic boundary conditions, with a method different from the numerical simulations of the nematodynamics equations. They look at particular fixed point of the AN equations, called Exact Coherence Structures (ECS). They are of three kinds : stationnary states, periodic orbits (PO) and relative periodic orbits (RPO). Relative periodic orbits are solutions for which, after a relative period T, the velocity field and the director field are the same but translated along the channel axis by l. ECS are not chaotic, and they are landmarks in the infinite dynamical phase space. A system's dynamics might never be exactly one of them, but its trajectory in

phase space meanders between ECS and visit their neighborhood. They study the stability of ECS, and they find that two RPOs are stable solutions of the equations, hence attractors for the dynamics. This relative periodic orbits display topological defects and a net current. Wagner et al indicate that some RPOs cycles between a vortex lattice, where the net current is 0, and an almost unidirectional flow state, where the net current is thus close to 100%. These particular flow states that they find reminds us of the cycle of bend instability that we proposed to explain the net current emerging in the experiments in Chapter 5. Although they use a different set of parameters than what we typically use, and, in particular, they neglect flow alignment setting $\xi = 0$, their results encourage us to explore further that what has already been done with numerical simulations the possible dynamics arising from the AN equations.

1.2 Computational set-up

The channel of active nematic is represented by a 3D-square lattice, with $N_x = 400$ nodes in the channel's long direction x, $N_y = 100$ nodes in the channel lateral direction y, and $N_z = 6$ nodes in the vertical direction z. Periodic boundary conditions are implemented in x and z direction, while the walls in the y direction enforce no-slip for the velocity and finite planar anchoring of strength $W = 1$ for the nematic field.
To solve the coupled AN equations, we employ a hybrid Lattice Boltzmann method, meaning that the Beris–Edwards equations for $\boldsymbol{Q}$ is solved using finite differences while the Navier-Stokes equation is solved with the lattice Boltzmann Method, using the D3Q15 velocity set, a second-order scheme by using the trapezoidal approximation for the collision and force term, and mid-grid bounce back boundary conditions to enforce no-slip at the walls [78, 75].

The system is initialized with a random director in the xy plane, partially, but not fully, relaxed towards equilibrium. During this relaxation phase, it is assumed that the velocity field $\boldsymbol{v} = 0$ everywhere, such that the equation for the $\boldsymbol{Q}$-tensor reduces to Ginzburg–Landau relaxation. We consider the end of the relaxation phase to be the simulation initial state at $t = 0$. From $t = 0$ onwards, the hydrodynamics is turned on, which means that $\boldsymbol{u}$ is allowed to be non-zero, the advection term is introduced in the $\boldsymbol{Q}$-tensor evolution equation, and the Navier-Stokes equation is evolved with the Lattice Boltzmann Method. The initial state has still many topological defects embedded in the director field, and has either a zero velocity field (static initialization), or a uniform velocity field in the $+\boldsymbol{e_x}$ direction (non-static initialization).

Values for the parameters are : $A_0 = 0.1$, $U = 3.0$, $L = 0.1$, $\Gamma = 0.1$, $\xi = 1.$, $\eta = 1/3$, and for the activity, a typical value is $\zeta = 0.01$. $U = 3.0$ sets the value of the order parameter to $S = 0.5$ in a homogeneous system. The nematic coherence length, which determines the size of the core of topological defects, is $\sqrt{\frac{L}{A_0}} = 1$. Since $\frac{W}{L}$=10, the anchoring is strong. The only parameter from this list that varies is the activity ζ. As explained in Chapter 1, for unconfined systems the activity controls the active length scale $L_\zeta = \sqrt{\frac{L}{\zeta}}$, which is the typical distance between defects and also the typical size of the flow structures. When confined in a long channel of

width w, confinement screens interactions at a distance superior than w. The relevant parameter controlling the transition towards active turbulence is therefore the dimensional activity number $A = \sqrt{\frac{\zeta w^2}{L}}$ [23]. In our simulations, we fix the channel width at $w = 100$ in lattice units and we adjust the activity until we find a behavior that looks like the experiments. We chose not to explore the full parameter space, and to use generic values that have been shown to reproduce experimental behavior of the AN [23, 85, 86, 87, 77].

1.3 Static initialization

As a starting point, we present the dynamics following a static initial state. These dynamics and the transition between them as the activity number is increased have been studied in great details in previous works [85, 23], but their simulations differ from ours in several ways. They use homeotropic anchoring and the director field is initially aligned in $\boldsymbol{e_y}$ direction. In addition, their system is represented by a 2D lattice. Despite these differences, we recover most of their results in our own simulations. In this section, we present the three main dynamics emerging in our simulations as the activity number ζ is increased. In particular, after a laminar stationary flow state at moderate activity level, for an intermediate range of activity, the system evolves towards a dancing disclinations (DD) state. At higher activity, the dynamics is chaotic. Once the system has reached the final state, we compute the average velocity $v_0 =< |\boldsymbol{v}>_{x,y,t}|$, and the average velocity along $\boldsymbol{e_x}$ to quantify the net flow in the channel $\psi = \frac{<v_x>_{x,y}}{v_0}$.

Laminar state. For $0.001 \geq \zeta \geq 0.003$, activity is not high enough to maintain and produce topological defects in the channel. The director field adopts a defect-free configuration with strong splay distortion along a central line, and the velocity field is unidirectional. On the example shown on Figure 6.1 a,b, the AN flows in $+\boldsymbol{e_x}$ direction. The flow direction selected depends on the initial director field, which, as we said, is asymmetric after the partial relaxation phase. Since the velocity field is unidirectional, the flow order parameter $\frac{<v_x>_{x,y}}{v_0}$ is 100% (Figure 6.1 h).

Dancing disclinations state ($0.003 \geq \zeta \geq 0.01$). The DD state is the first regime we find where activity is high enough to produce topological defects (Figure 6.1 c). A movie, with $\zeta = 0.005$, is accessible here. Topological defects move periodically along well-defined trajectories. Once the regime is reached, there are no nucleation or annihilation events, defects are eternal. $-\frac{1}{2}$ defects stay at the wall, while $+\frac{1}{2}$ braid in the middle of the channel. Half of the $+\frac{1}{2}$ defects move towards $+\boldsymbol{e_x}$ while the other half moves towards $-\boldsymbol{e_x}$. As they pass each other, they form a transient rotating pair of "dancers". All the pairs rotate with the same handedness almost simultaneously. After a half-rotation, dancers part ways and each defect pairs with their other neighbour, rotating in the opposite handedness. The dance of $+\frac{1}{2}$ defects is reflected in the velocity field, organized as a 1-d lattice of counter-rotating vortices. Defect pairs alternatively rotate around the CCW and the CW vortexes (Figure 6.1 d), hence the sinusoidal shape of the instantaneous velocity profile (Figure 6.1 g). The DD state is symmetric in terms of $\pm\boldsymbol{e_x}$,

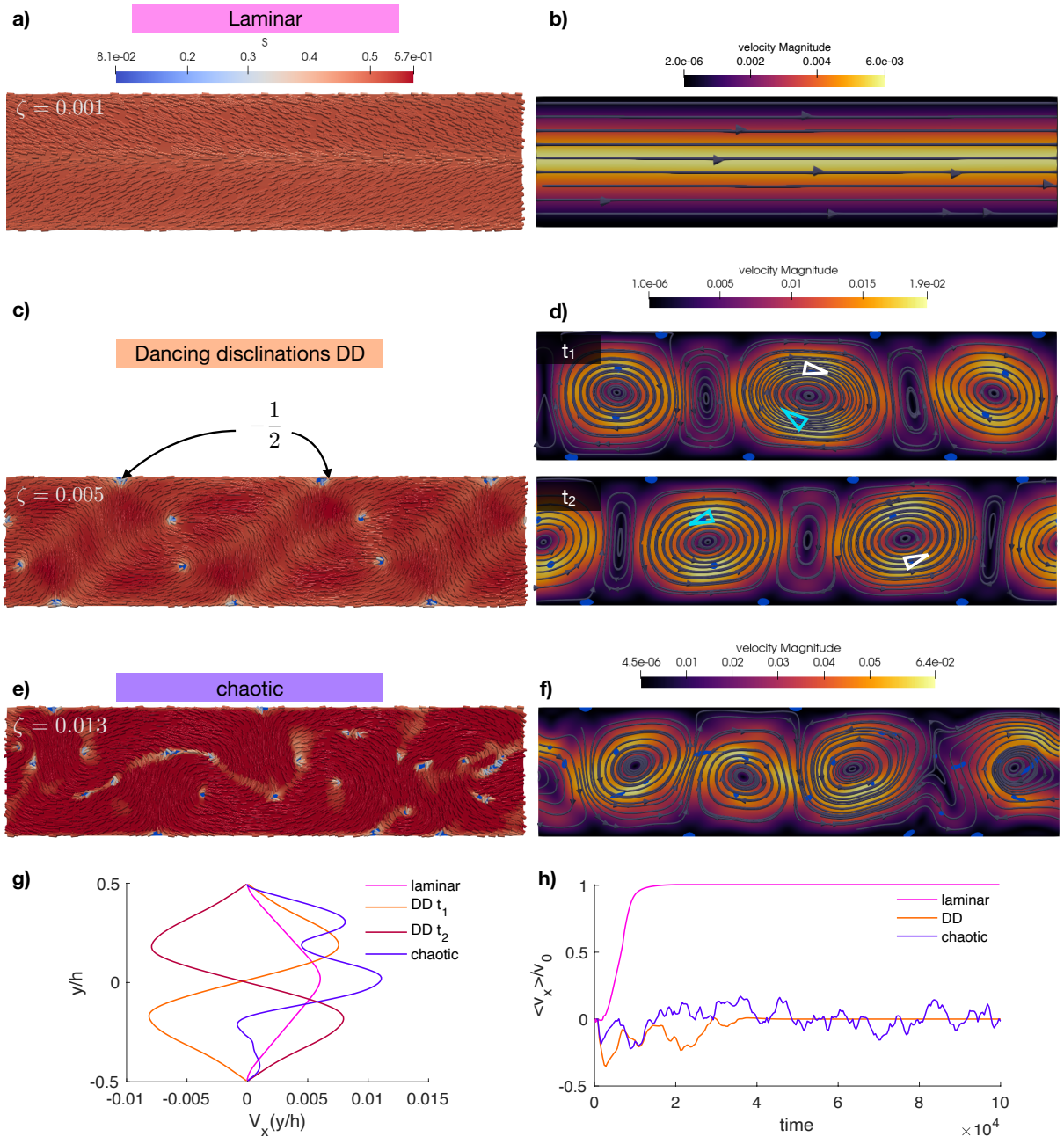

FIGURE 6.1 – **Dynamics following a static initial state. a, c, e)** Instantaneous director field ; **b, d, f)** stream line representation of the instantaneous velocity field. **a, b)** At low activity $\zeta = 0.001$, the system evolves towards a stationary laminar state free of topological defects, and the velocity field is parallel to $\boldsymbol{e}_x$. **c, d, f)** At higher activity $\zeta = 0.005$, the system falls into the periodic dynamical state called "dancing disclinations" (DD). Access movie here. d) At time t_1, the velocity field is a 1D lattice of counter-rotating vortexes, where CW vortexes are dominant, then at $t_2 > t_1$ CCW vortexes are dominant. We tag two $+\frac{1}{2}$ defects with white and blue triangles. **e, f)** At $\zeta = 0.013$, the system stays in a chaotic state for the duration of the simulation ; **f)** the velocity field is dominated by counter-rotating vortexes subject to perturbations ; **g)** instantaneous velocity profiles for the states described above, for the DD regime we plot the velocity profiles at time t_1 and time t_2 ; **h)** flow order parameter evolution with time.

there is not net current along the channel at any time once the regime is reached (Figure 6.1 h). Shendruk et al [85] note that the DD dynamics can sometimes be defective, counting more defects going in one direction than the other, generating a net drift in the system. However, this drift lattice defect state is four times less likely to settle than the DD regime, and the net flow is negligible in comparison to the typical fluid velocity, judging by the published simulation movies. They interpret drifting lattice defects as excited states in which the system is trapped, while the dancing disclination regime would be the fundamental state. On the contrary, in the experiments, the system is systematically in a flow state, the 0-flow state occurs only transiently during a reversal event.

Chaotic state. At high activity $\zeta \geq 0.013$, the dynamics is chaotic. In comparison to the DD state, additional topological defects are nucleated, in particular $-\frac{1}{2}$ can be found in the bulk of the channel, and not only at the walls (Figure 6.1 e). Defects no longer follow the periodic braiding trajectories of the DD. The velocity field also gets perturbated. Although it is still largely dominated by a 1-d chain of vortices, the lattice can deform and a small current can transiently slalom around the vortices (Figure 6.1 f, g, h). Thus, the net current is not strictly zero, but it is less than 10% of the typical velocity in the fluid. Moreover, the net flow oscillates around 0 and not around two distinct value $\pm\phi_0$ like in the experiments. Numerical stability limits the value of activity ζ we can explore.

In conclusion, we do not find in our simulations starting from a static configuration a true flow state, embedding topological defects, similar to our experimental observations. Our strategy is thus to change the initial condition of the simulation : if the fluid is given an initial net current, can the current be maintained at later time ?

1.4 Initial velocity field

We give the AN in the channel an initial uniform velocity $\boldsymbol{v_i} = v_i \boldsymbol{e_x}$. We only vary two parameters, the activity ζ and the initial norm of the velocity v_i. The DD state and the no-net-current chaotic state described before give way to net-current final states if the initial velocity v_i is higher than a threshold v_c that depends on the activity, as is shown in the phase diagram $\{v_i, \zeta\}$ in Figure 6.2 a. We observe that steady state dynamics are reached within 2×10^4 time steps. Therefore, we chose the simulation duration to be 4×10^4 time steps. For $\zeta \leq 0.01$, the system evolves towards the defect-free laminar state described before. For $\zeta \geq 0.01$, the system reaches a net-flow state embedding topological defects, that we call “drifting”. The final velocity $v_f =< v_x >_{x,y}$ depends on the activity ζ but not on v_i as long as $v_i \geq v_c$, in the range of v_i we have explored (Figure 6.2 b). The current speed v_f is almost equal to the mean velocity in the channel v_0, leading to a flow order parameter of nearly 100%. We will now describe in more details the drifting state.

Remarks : in the case of an initial uniform velocity field (plug flow), at $t = 0$ the fluid next to a boundary is suddenly decelerated because of the no-slip boundary condition. This creates a important shear profile perpendicular to the wall. We ran a few simulations where we replaced

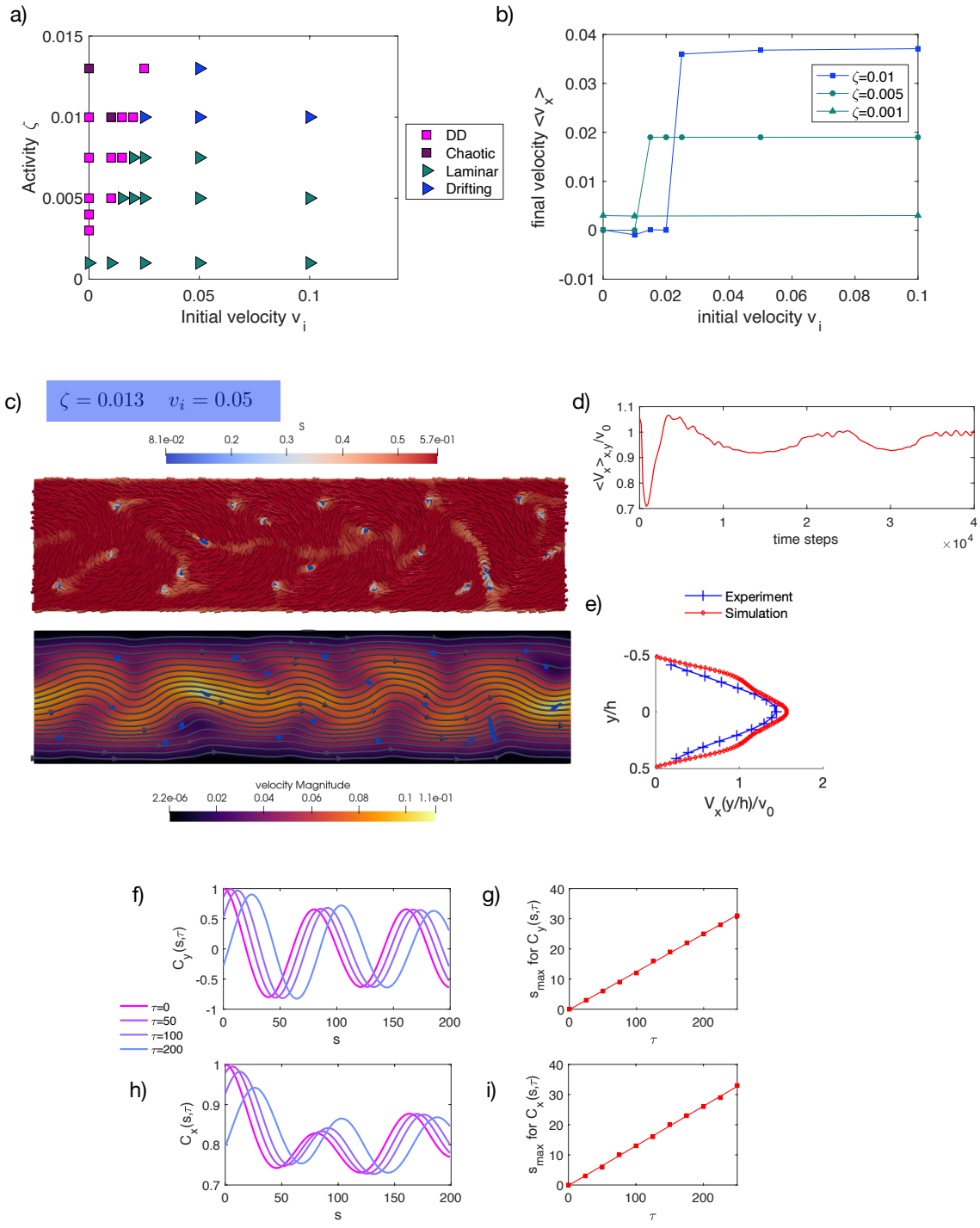

FIGURE 6.2 – **Dynamics following a non-zero velocity initial states. a)** Phase diagram showing the dynamics obtained for activity ζ and initial velocity v_i ; **b)** final average velocity $< v_x >_{x,y,t}$ along the channel long axis $\boldsymbol{e}_x$ versus the initial velocity v_i. All simulations here are 40000 time steps in duration, and start with the same the initial random director field. **c to i)** Numerical results for the simulation with $\zeta = 0.013$ and $v_i = 0.05$, which displays to the "drifting" state. Access movie here ; **c)** director field and velocity field ; **d)** temporal fluctuations of the flow order parameter ; **e)** normalized velocity profile $V_x(y)$ (red) compared to the experimental velocity profile in a channel of width w= 200 µm (blue). **f)** (respectively h) Spatiotemporal correlation function for the transversal velocity v_y (respectively, for the longitudinal velocity v_x ; **g)** (respectively i) drifting of the first maximum of the $C_y(s,\tau)$ (respectively $C_x(s,\tau)$).

the plug flow by an initial Poiseuille velocity field of maximum value $v_{\max} = 0.05$, and we observed the same final state.

1.4.1 The drifting state

This flow state displays topological defects. We give an example of it for $\zeta = 0.013$ in Figure 6.2 c, d, e. A movie showing the director field during the simulation is accessible here. Positive defects in the channel are no longer braiding like in the DD state. First, pairs of $\pm\frac{1}{2}$ nucleate and annihilate, in particular in the regions close to the walls. In contrast with both previous simulations initialized with a static configuration, and the experiments, nucleation does not happen exactly at the wall, but at a distance from the wall $\delta = 15 - 20$ in lattice units, which is not negligible in comparison to the channel width $h = 100$. As the newly nucleated $-\frac{1}{2}$ stays in the nucleation layer and drifts in $+\boldsymbol{e_x}$ direction, its $+\frac{1}{2}$ counterpart crosses the channel and annihilates with a $-\frac{1}{2}$ on the other side. Therefore, the two nucleation layers host a negative charge density. Meanwhile, two or three topological $+\frac{1}{2}$ defects are swimming in the channel in the $+\boldsymbol{e_x}$ direction. If the activity is high enough, a few negative defects can be found in the center of the channel and not only next to the wall, the defect dynamics is then more prone to instabilities. There are as many positive as negative defects, as topology requires. At lower activity $\zeta = 0.010$, there are no negative defects in the center of the channel, and defect dynamics is very regular. The instantaneous velocity field features spatially oscillating streamlines travelling in $+\boldsymbol{e_x}$ direction, very similar to the experimental velocity fields (5 Figure 5.4). The study of spatiotemporal correlation functions for the transversal component of the velocity v_y and the longitudinal v_x reveals that a wave is travelling in the velocity field in the current direction $+\boldsymbol{e_x}$, at a speed $c_\perp = 0.1255$ for v_y and $c_\parallel = 0.1316$ for v_x (Figure 6.2 f-i). The wave velocity is about 2.5 times higher than the current speed. The wave travels faster in the simulation than in the experiments. The velocity profile $V_x(y) =< v_x >_{x,y,t}$ noticeably differs from the experimental one : the slope is steeper in the near-wall region. However, we should keep in mind that the velocities extracted from the experimental images can be misleading, in particular next to walls where bundle alignment causes the algorithm to under-estimate velocities parallel to the wall.

Discrepancies between simulations and experiments. We have already brought up two major differences, one is the steep slope of the velocity profile next to the wall, the other is the nucleation layer detached from the wall by $\delta = 20$. One can notice that between the wall and the negative defects, the director field is not parallel to the wall, instead it adopts a constant and almost homogeneous orientation of approximately 13°angle with the wall (Figure 6.3 a, c). This highly ordered region between the wall and the nucleation layer constitutes a boundary layer. Moreover, we find that positive defects orient differently. The polar order is minimum in the center of the channel (Figure 6.3 b), where defects have an anisotropic orientation (blue histogram), but do not point in the current direction, as opposed to the experiments (chapter 5 Figure 5.7). In the region next to the wall, however, we also find that positive defects orient in the up-stream direction. We speculate that the lack of negative defects in the center of the

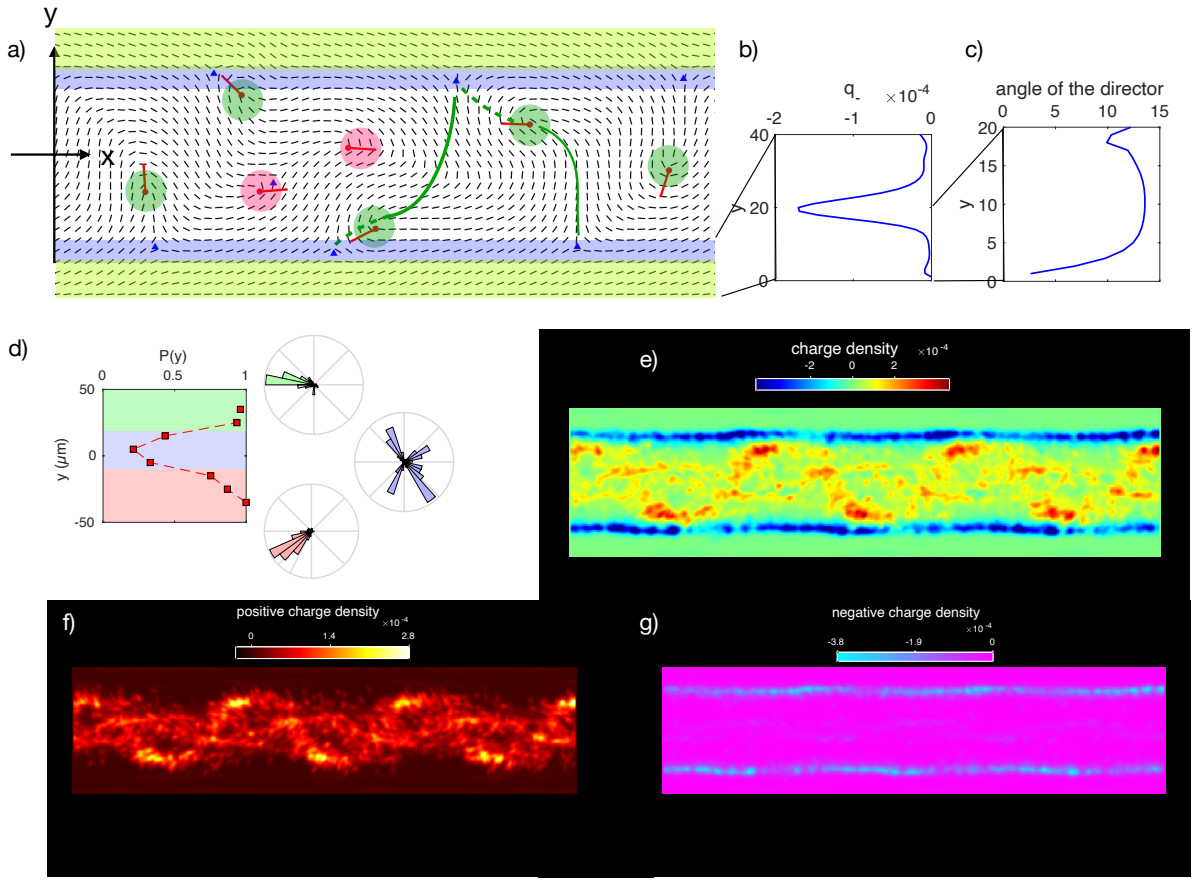

FIGURE 6.3 – **The drifting state.** Detailed analysis of the final drifting state for $\zeta = 0.013$. A movie is accessible here. Warm-up time for the analysis is 2×10^4. **a)** Director field and topological defects. Crossing positive defects are marked with a green disk and their past and future trajectories are materialized with full and dashed lines respectively. Travelling positive defects are marked with a pink disk. The nucleation layer, where negative defects reside, is overlaid in blue, while the boundary layer, with a high degree of orientational order, is overlaid in lime green. **b)** profile of the negative charge density q_- next to the wall; **c)** profile of the average angle of the director in the boundary layer; **d)** Profile of polar order of $+\frac{1}{2}$ defects, and polar histogram of the orientation within the three colored regions; **e-f-g)** colormaps of the average charge density, average positive charge density q_+, and average negative charge density q_-.

channel, revealed by the charge density maps in Figure 6.3 g, i, prevents the polar ordering of positive defects.

The formation of the boundary layer suggests that we should treat boundaries differently. On the one hand, for a polymer solution flowing in a microchannel in response to a pressure gradient, hydrodynamic interactions with the walls can cause the migration of polymers from the wall towards the channel center-line [88, 89]. As a result, the polymeric concentration is lower in the near-wall region, and wall depletion leads to the apparent free-slip motion of the polymers. On the other hand, for active swimmers such as *Escherichia coli*, hydrodynamic interactions with the wall lead to an increased density of swimmers next to the boundaries [90]. These arguments motivate us to modify the boundary condition in our next simulations. Since our AN model is not lyotropic, we impose an activity profile across the channel that accounts for either for depletion or accumulation of microtubules near the walls.

1.4.2 Activity boundary layer

An non-uniform activity field creates a new active force term : $\nabla(\zeta \boldsymbol{Q}) = \zeta \boldsymbol{\nabla} \cdot \boldsymbol{Q} + \boldsymbol{Q}(\boldsymbol{\nabla}\zeta)$. The role of this new force has not been systematically studied so far. We now impose a hyperbolic activity profile next to each wall :

$$\zeta(y) = \zeta_0 \left[1 + \epsilon(\tanh\left[\alpha(y-\delta)\right] + \tanh\left[\alpha(N_y - \delta - y)\right] - 2)\right] \tag{6.1}$$

where ζ_0 is the activity far from the walls, δ is the distance between the wall and the inflexion point of the profile, α the sharpness of the profile, and ϵ controls $\zeta_0 - \zeta_w$, with ζ_w the activity level at the walls . We choose $\delta = 20$ so that the step of activity matches the position of the boundary layer we characterized previously, $\alpha = 1$, $\zeta_0 = 0.013$ and vary only ϵ between -0.25 (more active boundaries) to +0.25 (less active boundaries). Activity profiles are displayed in Figure 6.4 a. The system initial velocity is $v_i = 0.05$.

We find that for $\epsilon \leq 0.1$, the slope of the velocity profile is affected only next to the walls, which affects the net flow (Figure 6.4 b, c) while the boundary layer keeps a constant thickness and the director adopts the same angle (Figure 6.4 d, e, f). The fact that the gradient of velocity increases with the activity in the boundary layer is not surprising, since the active stress is $-\zeta \boldsymbol{Q}$.

Flow extinction for low activity boundaries. At $\epsilon = 0.25$, the profile of activity drops sharply by 50% from its central value ζ_0 (Figure 6.4 b, c). The system final state is a chaotic state with no net current, with negative defects at the wall and no longer detached from the wall (Figure 6.4 e, f).

The angle made by the director field and the position of negative defects, defining the limit of the boundary layer, seems to be independent from from the activity value within the boundary layer. However, the boundary layer needs a minimum activity to be stable, indicating that there is an active phenomenon at play here. When the boundary layer disappears, a flow state cannot be sustained. In conclusion, the hyperbolic activity profile used to decrease the activity near the walls, and thereby to account for potential depletion of microtubules near the walls, does

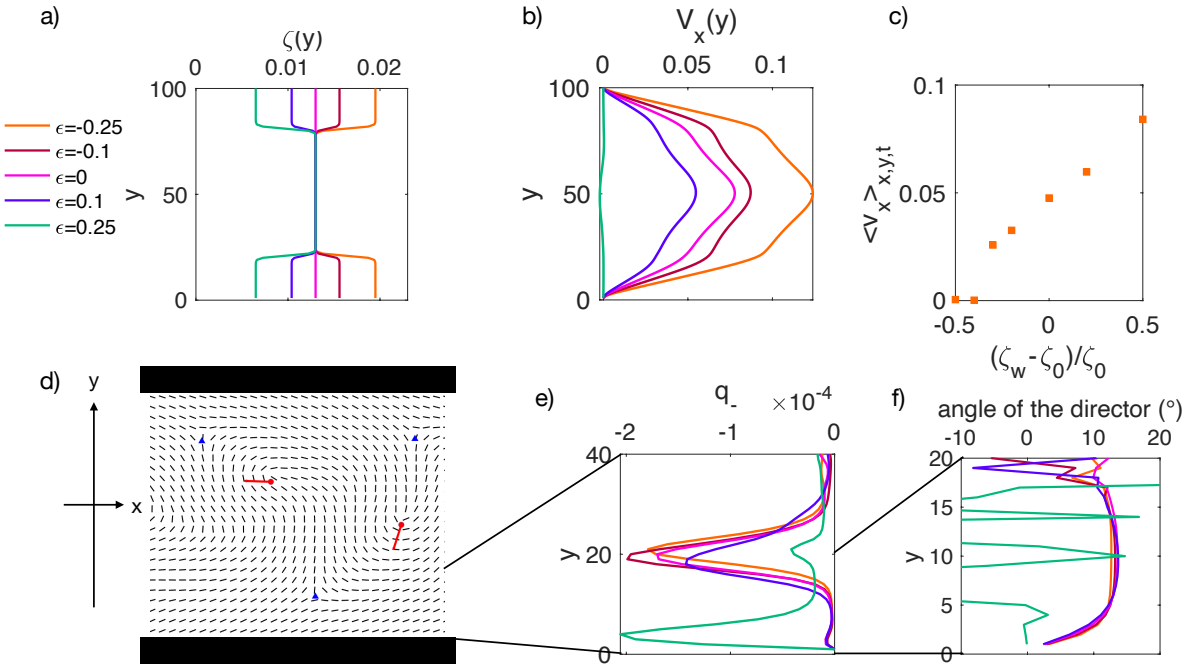

FIGURE 6.4 – **Activity boundary layers. a)** Hyperbolic activity profiles with different values of ϵ ; **b)** velocity profiles $V_x(y)$.**c)** Average flow velocity $< v_x >_{x,y,t}$ is dependant on the activity in the boundary layer ; **d)** reminder that the boundary layer is the layer between the negative defects and the wall ; **e)** negative charge density has a peak located at $\delta = 20$ for all the flow states, while for $\epsilon = 0.25$ (no flow) negative defects are located at the wall ; **f)** angle made by the director field profile shows that for all the flow state the director tilts by 13°with respect to the wall in the boundary layer. For $\epsilon = 0.25$ (no flow) the director has no particular orientation hence the randomness of the curve.

not produce a net flow state without the boundary layer. We showed that, by initializing the system with a plug flow of high enough amplitude, the dynamics evolves towards a net flow state with topological defects embedded. Although the numerical dynamics shares some similarities with the experiment, we did not manage to resolve all the discrepancies in the time frame of this thesis. We did not systematically explore the full parameter space. In particular, we used a unique value of $\xi = 1.0$ for the alignment parameter. In the future, we also plan to study the effect of free-slip boundary conditions. Additionally, the mathematical model could be too simple to produce spontaneous flow transition in channels with straight walls at high activity. The flow observed in the experiments could rely on some details not accounted for in our model. However, ratchet patterns on the walls of the channel might induce spontaneous, robust flow states not relying on such details.

2 Ratchet periodic channels

We now study the effect of patterning the channel walls with ratchets. First, we aim at numerically reproducing the experimental dynamics of the standard ratchet channel, generating a net current in the easy direction of the ratchet. We quantitatively compare the dynamics in terms of velocity field, spatial and orientational organization of topological defects. The good agreement between simulations and experiments leads us, in the second part, to make a series of predictions regarding how the design of the channel can be used to modify the active nematic dynamics.

2.1 Standard ratchet channel

2.1.1 Computational set-up

Just as the straight channels, the ratchet channel is represented by a 3D square lattice $Nx = 400$ nodes in the channel's long direction x, $Ny = 100$ nodes in the channel lateral direction y, and $Nz = 6$ nodes in the vertical direction z. Each wall bounding the y direction is patterned with 8 ratchet teeth, introduced as particles as explained in Chapter 3. Teeth have a length $L = 50$ and an amplitude $H = 25$, such as the distance between the two walls is 50 at its shortest point and 100 at its widest point. These dimensions replicate the experimental aspect ratio. Periodic boundary conditions are implemented in x and z direction. Ratchet walls enforce no-slip for the velocity and finite planar anchoring of strength $W = 1$ for the nematic field, unless stated otherwise. The system is initialized with a partially relaxed director field and no initial velocity.

2.1.2 Spontaneous current

Even in the absence of an initial current, the presence of a ratchet pattern induces a spontaneous current in the $+\boldsymbol{e_x}$ direction for all activity values in the range [0.005, 0.015] (Figure 6.5 a). The critical activity ζ_c above which the laminar state disappears is significantly higher than

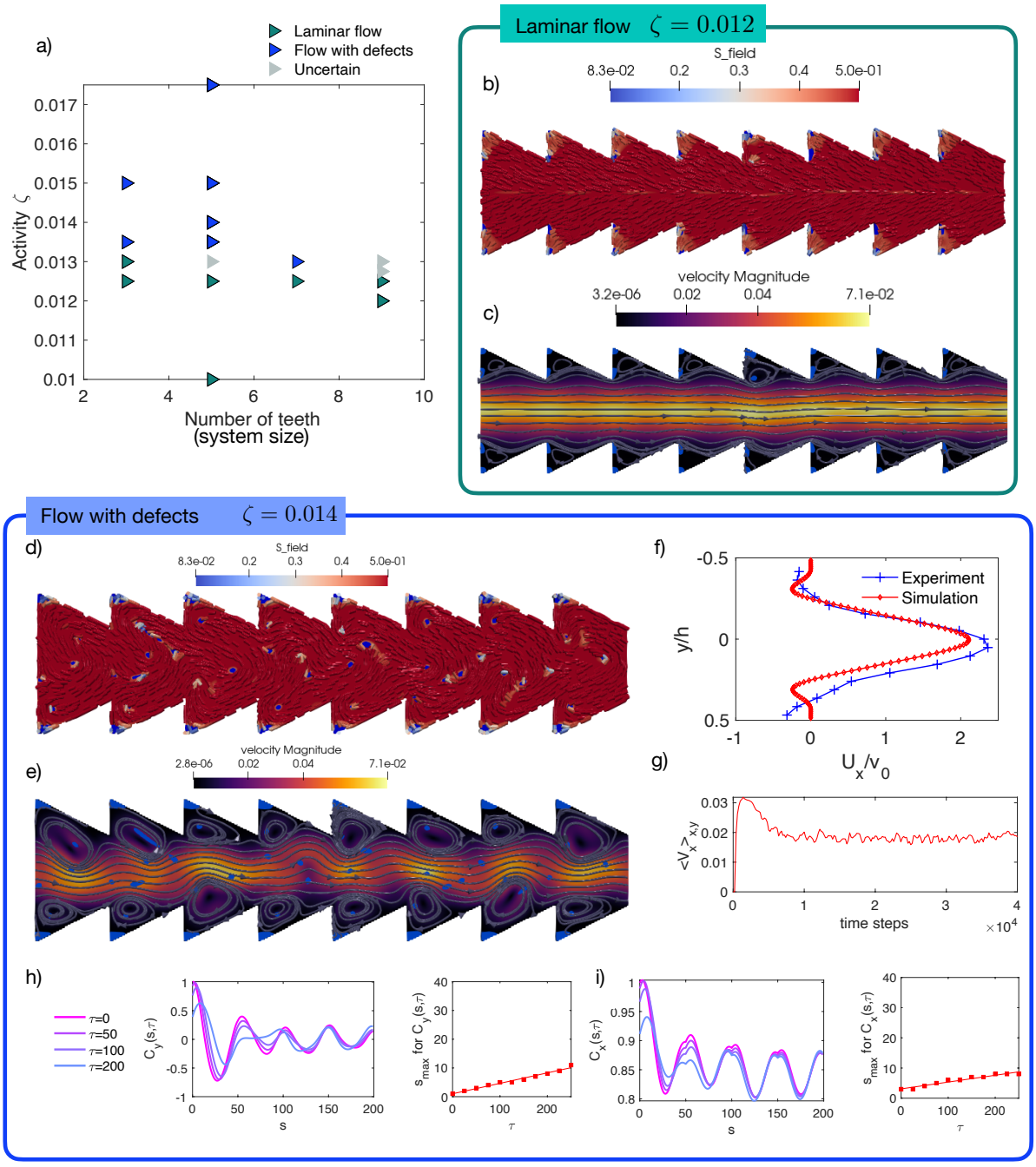

FIGURE 6.5 – **Spontaneous flow in ratchet channels.** a) phase diagram showing that the final flow state (defect-less laminar flow, or flow with defects) does not depend on the channel length but on the activity ; **b, c** director and velocity field for the laminar flow state ; **d-g** the flow state embedding topological defects for $\zeta = 0.014$ **d)** director field ; **e)** velocity field ; **f)** velocity profile $V_x(y)$; **g)** net flow fluctuates weakly with time ; **h)** (respectively i) spatiotemporal correlation function for the transversal velocity v_y (respectively, for the longitudinal velocity v_x and the position of the first maximum shows that there is no wave travelling in the velocity field. A movie is accessible here

for the straight channels of width 100. The laminar state that spontaneously appears for $\zeta \leq \zeta_c$ is also associated to splay center-line configuration (Figure 6.5 b, c). We can relate this result to the work of Rorai et al [91] : for a system invariant along the x direction, they show that hybrid anchoring at the channel walls causes a net flow. The ratchet walls impose an effective hybrid anchoring. For $\zeta \geq \zeta_c$ we find a flow state embedding topological defects subject to a new kind of dynamics (Figure 6.5 d, e). A movie for $\zeta = 0.014$ is accessible here. The velocity field features oscillating stream lines sided by vortexes in the ratchet corners. We find that there is no wave propagation in the velocity field (Figure 6.5 h, i), probably because of the strong constriction imposed by the ratchet.

2.1.3 Defect organization in the flow with defect state

Here we present the results of the simulation that was looking the most like the experiments with $\zeta = 0.014$. Each ratchet protrusion is systematically hosting an eternal boundary $-\frac{1}{2}$ defects (not detected by our defect detection algorithm) and this induces an excess amount of positive defects in the bulk of the channel. However, pairs of defects nucleate and annihilate, as opposed to the dancing disclinations regime. Nucleation happens in the bulk of the channel, leaving in the center of the channel negative defects that are advected by the current. The newly nucleated $+\frac{1}{2}$ unbinds in the upstream direction and is trapped for a while in the corner of the ratchet indentation (Figure 6.6 a, b). Then, it is deflected towards the center of the channel and reoriented in the downstream direction by flow alignment. Bulk negative defects allow the formation of a train of $+\frac{1}{2}/-\frac{1}{2}$ defects along the center-line, also observed in the experiments, along with polar ordering of positive defects in the downstream direction (Figure 6.6 b). The looping trajectories in the corners of positive defects is clearly visible on the charge density map, where they create this ear-wheat pattern similar to the experiments (Figure 6.6 c, d).

2.2 Predictions

Numerical simulations of the AN equations reproduce the experimental results in terms of spontaneous flow, polar ordering of positive defects and defect trajectories for the ratchet channel configuration. Comforted by this success, we now make a series of predictions regarding how the ratchet design can produce different behaviors.

2.2.1 Flow states are controlled by the tooth aspect ratio

We first vary the ratchet amplitude H from 0 to 40 at fixed ratchet length $L = 50$ and activity $\zeta = 0.014$ (Figure 6.7 a, b). For very flat ratchet, the system ends up in a flow state looking very much like the straight channel with velocity initialization. We call this regime "drifting dancing disclinations" (DDD) because topological defects reproduce the dancing disclinations trajectories with a drift in $+\boldsymbol{e_x}$. Negative defects cannot be maintained at the tip of the ratchet because the corners are too short to accommodate the distorsions, hence the formation of a negative layer detached from the wall (Figure 6.7 d). As opposed to the drifting state in the straight channel, here positive defects do not annihilate with negative defects. For higher ratchet

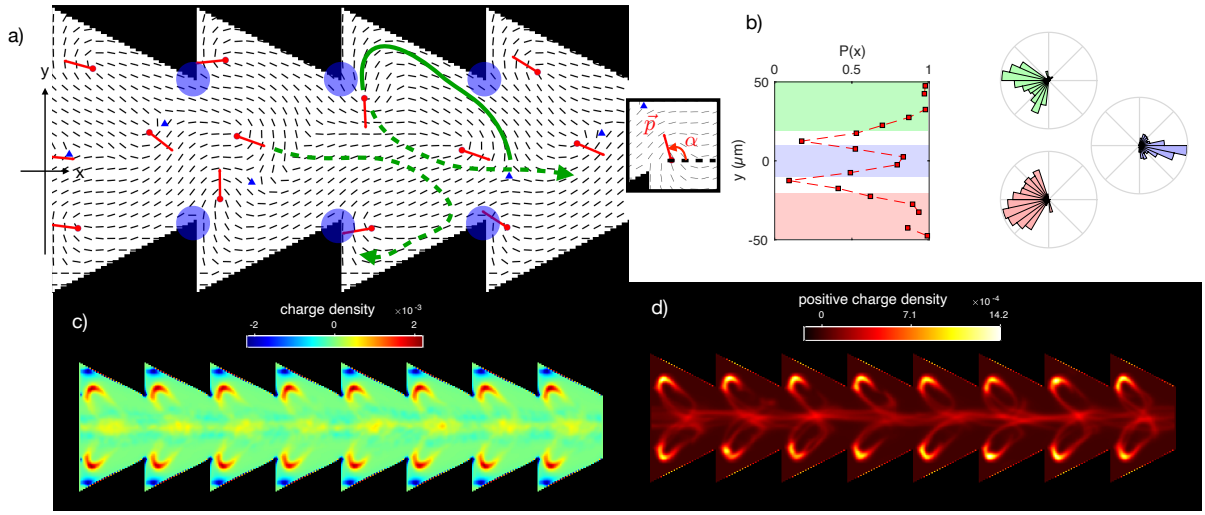

FIGURE 6.6 – **Defects organization in ratchet channel a)** director field and topological defects. Boundary $-\frac{1}{2}$ are marked with a blue disk. We have represented the past and future trajectories of two positive defects with a full and dashed green line ; **b)** polar ordering of positive defects ; **c)** charge density ; **d)** positive defects charge density displays an ear-wheat pattern.

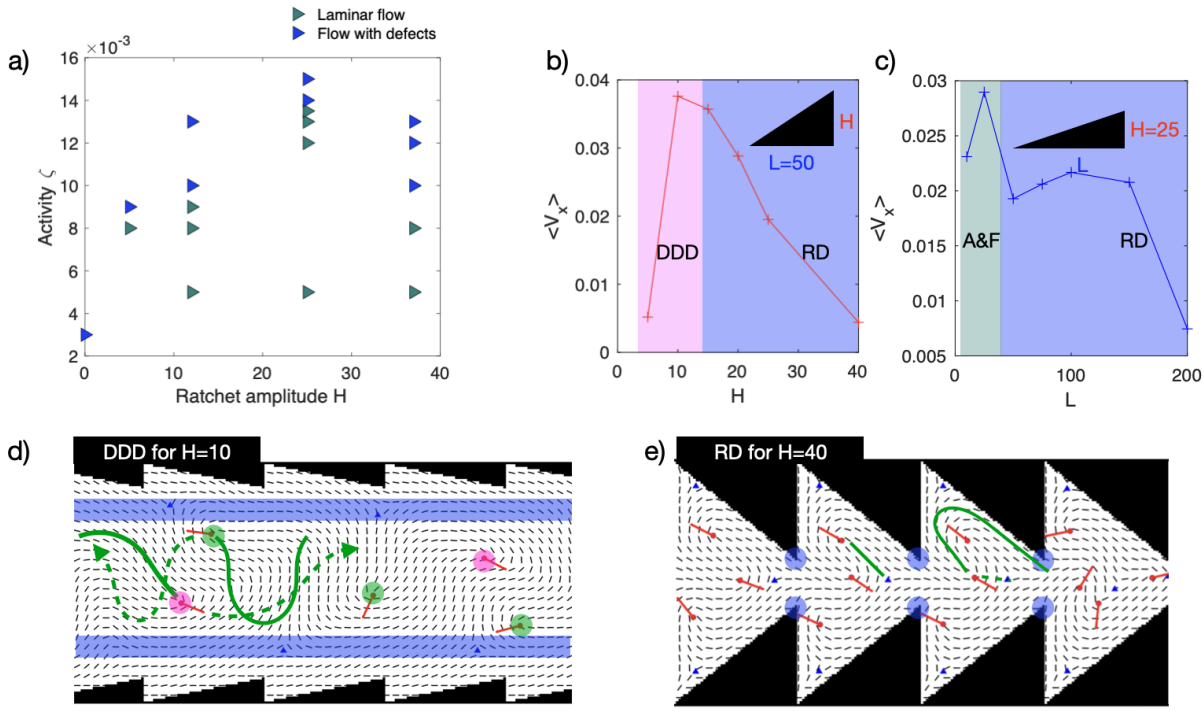

FIGURE 6.7 – **Ratchet aspect ratio.** For all the subfigures besides a), $\zeta = 0.014$. **a)** phase diagram ζ/H reveals that the stabilization of topological defects depends both on the activity and on the tooth amplitude ; **b)** average velocity $< v_x >$ depends on the tooth amplitude and **c)** on the tooth length ; **d)** the drifting dancing disclinations (DDD) regime, with the detached negative defects layer in blue, downstream-directed positive defects marked with a pink disk, and upstream-directed negative defects marked with a green disk. **e)** the ratchet dynamics reappears when negative defects are pinned at the tip of the ratchet teeth.

amplitude, negative defects are located at the tip and the system flow state transitions to the "ratchet dynamics" (RD) described before (Figure 6.7 e). Positive defects trajectories create an ear-wheat pattern. The more the teeth protrude, the more regular the defects dynamics becomes : at $H = 40$, for instance, there are (almost) systematically 3 positive defects for one ratchet unit.

Second, we vary the ratchet wavelength L at fixed amplitude $H = 25$ (Figure 6.7 c). For small L, the inclination of the tooth is high and the director field is subject to a strong distortion from one wall to the other. The system ends up in the laminar flow state associated to the splay center-line configuration (A&F). For longer ratchet wavelengths, we recover the ratchet dynamics.

We note that the ratchet dynamics, for a given activity, is not the dynamics associated to the strongest flow. Our interpretation is that vortexes in the corners of the teeth in the ratchet dynamics dissipate energy without contributing to the net flow.

2.2.2 Reversing ratchet effect with homeotropic anchoring

Norton et al [92] have done simulations of AN confined inside a disk and they note that in this particular case, the dynamics is not affected by anchoring boundary conditions. However, we find strikingly different results when the anchoring constrain is combined to a geometrically patterned wall such as the ratchet. With planar anchoring, the AN flows in the $+\boldsymbol{e_x}$ direction, which is the easy direction of the ratchet. In contrast, when the anchoring is homeotropic, it flows in the opposite direction (Figure 6.8 f, g). This phenomenon provides an additional proof that channels currents, weather they are stabilized in the straight channels or they spontaneously emerge in the ratchet channel, are coming from the orientation of the director field next to the walls. Unfortunately, this prediction cannot be tested in experiments with the microtubule-based AN because we are not able to control the anchoring that is planar due to hydrodynamic interactions with the boundary, and does not originate from thermodynamics or chemical interactions.

2.2.3 Channel with antogonistic ratchet walls

We give an opposite orientation to the two ratchet walls : the pattern on the bottom wall is oriented towards $+\boldsymbol{e_x}$ whereas the pattern on the top wall points towards $-\boldsymbol{e_x}$. In the absence of any frictional forces $f_{\text{friction}} = -f\boldsymbol{v}$ (which has always been the case so far in our simulations), hydrodynamics interactions are dominant and the flow state that appears is a lattice of counter rotating vortexes, despite the fact that the patterns should favor CCW rotation (Figure 6.8 a, b). To obtain a velocity field more similar to the experiments, where usually the averaged velocity profile has a sinusoidal shape and several co-rotating vortexes can connect, we have to introduce a frictional force of coefficient $f = 0.03$, that screens hydrodynamics interactions (Figure 6.8 c, d). With added friction, CCW vortexes occupy most of the channel, as a result, the velocity profile is sinusoidal (Figure 6.8 e).

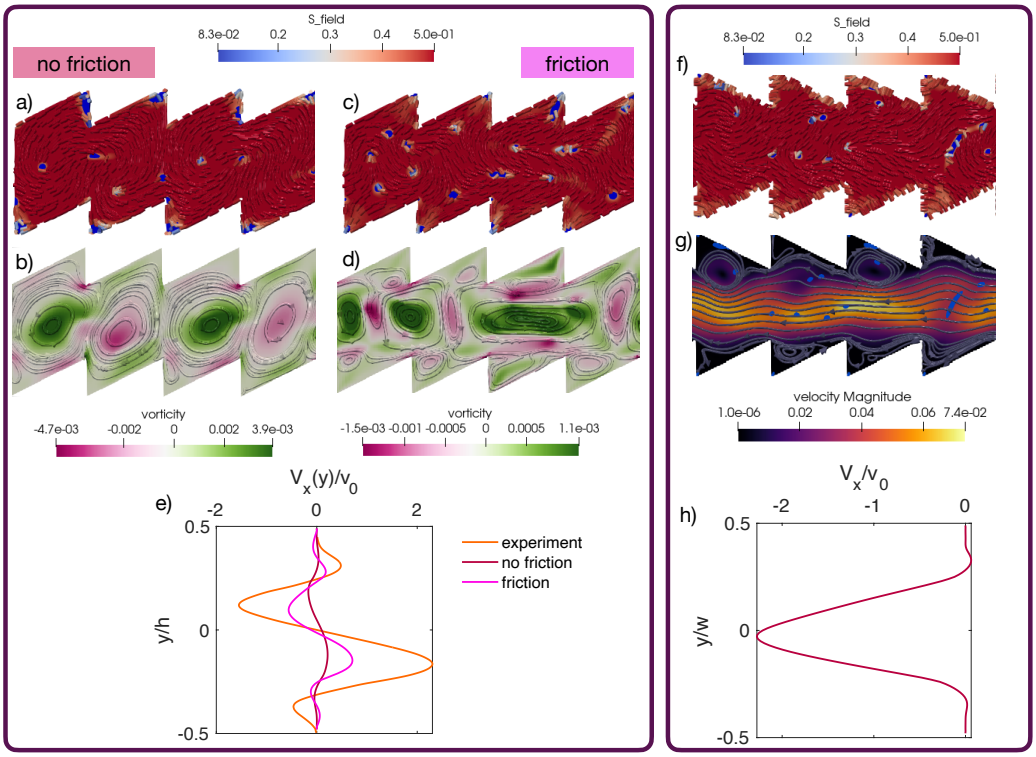

FIGURE 6.8 – **Antagonistic ratchet walls and reverse current with homeotropic anchoring. a, b)** opposite ratchet channel without friction, **a)** director field ; **b)** norm of the vorticity field and stream lines show a lattice of counter-rotating vortexes ;**c, d)** a frictional force of coefficient $f = 0.03$ is added ; **c)** director field **d)** vorticity field and the stream lines dominated by CCW vortexes ; **e)** comparison of the velocity profiles from the experiment and the simulation, with and without friction ; **f, g, h)** ratchet channel with homeotropic anchoring ; **f)** director field ; **g)** velocity field and stream lines associated to a current in $-\boldsymbol{e_x}$ direction ; **h)** velocity profile.

2.2.4 Positive defects perform specific braid

We now comment on the different positive defects trajectories that we observed : Drifting Dancing Disclinations (DDD) (Figure 4.5 a), the ear-wheat pattern (RD) obtained in ratchet channels (Figure 4.5 b), and the bow-tie (BT) observed in the opposite ratchet channel with no friction (Figure 4.5 c). Why do defects follow such particular trajectories ? This question was addressed by Tan et al [93], who analyzed unconfined AN dynamics in terms of chaotic mixing. Chaotic mixing is a process by which a fluid is mixed, and particles of fluid stretch and deform, creating fractal patterns in the fluid with time. Chaotic mixing can occur in 2D when the flow field is time-dependant, a typical way to achieve this is to stir the fluid with 3 or more rods following a particular pattern of permutation. The motion of the stirring rod stretch the material lines exponentially with time, at a rate called topological entropy, and two neighbouring particles of fluid will separate exponentially with time, at a rate called Lyapunov exponent. Tan et al have shown that, for the unconfined 2 dimensional AN system, the fact that bundles stretch under the action of molecular motors results in the creation of topological entropy and of a Lyapunov exponent, and this strongly constraints the motion of the positive defects that play the role of stirring rods. Positive defects must move in such a way that they generate the good amount of topological entropy.

For AN confined in channel in sub-turbulent regime, the dynamics in term of velocity field and nematic field is not chaotic in a strict meaning, since it is periodic, or relatively periodic in time. But there is chaotic mixing in the system, because the trajectory of a particle of fluid is chaotic, it does not coincide with the instantaneous streamlines. In the DD regime for instance, defects are indeed not trapped on the streamline of one vortex.

The positions of $+\frac{1}{2}$ defects in the plane (x,y), reported along a third axis representing time, define a braid. Tan et al noticed that in the DD regime, defects perform a particular braid called silver braid [94], in reference to the topological entropy per braid generator that is related to the silver number. Defect trajectories in the DDD regime are topologically identical to that of the Dancing Disclination regime, so we can claim that they also perform the silver braid. For the RD, all the positive defects, that are eternal, take part in the same braid, but it is less clear for us what type of braid it is. For the BT dynamics, groups of either 3 or 4 defects braid together in the golden braid pattern, generating 3 bow-tie trajectories. The topological entropy per braid generator is related to the golden ratio. According to [94], the different amount of topological entropy generated depends on periodic boundary conditions of the domain in which the stirring rods are living.

Conclusions We have performed numerical simulations using the active nematodynamics equation in rectangular channels with periodic boundary conditions and a hybrid Lattice Boltzmann method. For channels with straight walls, we were able to send the system towards a net flow state embedding topological defects by initializing the velocity field with a current in the channel's long direction. In contrast, when starting from a static configuration, the system evolves either towards a chaotic attractor or the DD attractor, neither of them featuring a net flow, at least not important enough in comparison to the experiments. For simulations of chan-

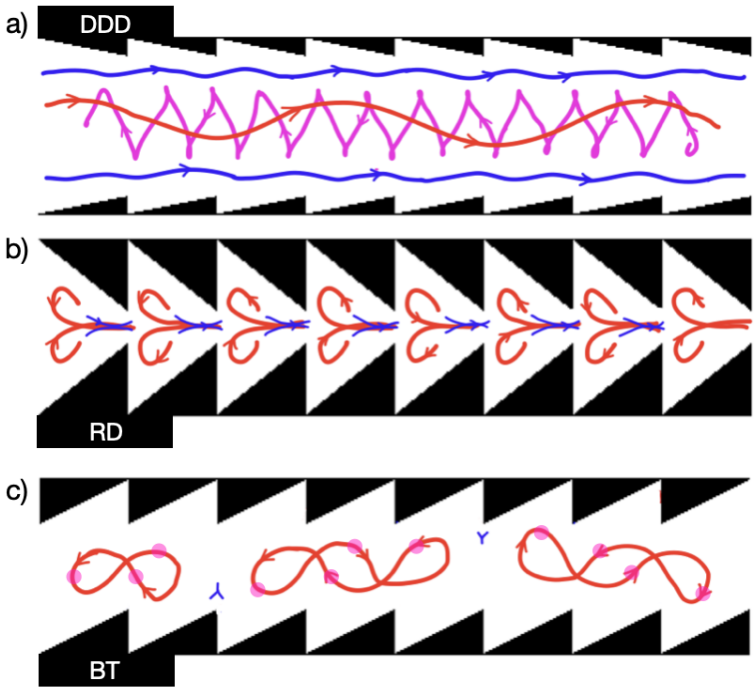

FIGURE 6.9 – **Defects trajectories.** Blue lines represents the trajectory of negative defects, red a,d pink lines the trajectories of positive defects, we have marked the position of some positive defects with a pink disk ; **a)** the drifting dancing disclination state obtained for small amplitude ratchet walls. Negative defects drift along the walls in $+\boldsymbol{e_x}$. The trajectory of positive defects navigating downstream (red line), presents long oscillations, while the trajectory of positive defects navigating upstream present short oscillations ; **b)** The ratchet dynamics, with the ear-wheat pattern ; **c)** the bow-tie (BT) trajectories are obtained for a channel with antagonistic ratchet walls, without frictional forces. Bow-tie consists in 2 or 3 loops depending on how many positive defects are involved (3 or 4), and can have both handedness. A negative defects is found between each bow-tie trajectory, creating an elastic energy barrier in the channel that prevent the exchange of defects between bow-ties.

nels with ratchet walls, a net flow state emerge spontaneously, in which the orientations and trajectories of the topological defects are very similar to those found in the experiments. For a given activity, the amplitude, wavelength and orientation of the saw-tooth pattern can be adjusted in order to obtain a defect-free flow state, or different defects dynamics. Defects in the channel produce chaotic mixing, therefore such ratchet channels could be used as self-pumping and self-mixing devices.

A fundamental ingredient that is missing in the mathematical model is a source of noise. In the experiments, fluctuations are an important aspect of the flow in open channels (Chapter 5), which occasionally reverses its direction. Therefore, in the future, we would like to introduce fluctuations in the model in order to maintain the system away from the chaotic and dancing disclination state, without having to use an initial velocity field. This could be first introduced as a Gaussian random field perturbation to the field of activity ζ, independent from the nematic $\boldsymbol{Q}$ field and the velocity field $\boldsymbol{v}$. Spatio-temporal fluctuations in the activity could account for density fluctuation in our model, in which the density field does not evolve. However, it would probably be more interesting to couple the activity fluctuations to $\boldsymbol{Q}$ and $\boldsymbol{v}$, for instance via a continuous lyotropic model, or mesoscopic model of AN [95].

Chapter 7

Active nematic flow networks

To transport fluid, nutrients or information, living organisms often rely on networks. If some of these networks are mostly passive, like the blood vasculature that relies on a central pumping system (the heart), in others local active processes ensure the transport of the fluid. In the respiratory track, for example, the bronchial epithelium is carpeted by millions of cilia beating in a coordinate manner in order to propel the mucus towards the exit [96, 97]. Other fluid networks rely on peristalsis, like the lymphatic system or the *Physarum Polycephalum* organism in its vegetative phase, which generates cytoplasmic flows by contracting the membranes of the tubular network and has the capacity to reshape to adjust to changing external conditions [98, 99]. This chapter touches on a particular category of active networks, for which the network boundaries are fixed and the fluid itself is active and has the capacity to spontaneously flow under channel confinement. They are called "active flow networks" (AFN). What principles govern the flow state statistics of active flow networks, which are inherently out-of-equilibrium ? Here, we experimentally study the behavior of the active nematic when confined inside a microfluidic network, and compare our results with lattice field theoretical models of AFN.

1 Active Flow Networks : framework

Here, we present the theoretical framework developed by Woodhouse et al [35] to describe active flow networks.

1.1 Closed active flow networks

To describe active flow networks, Woodhouse et al propose to represent the network with a graph, that is a set of vertices $v \in \mathcal{V}$ connected by a set of edges $e \in \mathcal{E}$. Edges allow transport of fluid in any of the two directions. To indicate the current direction, an arbitrary direction is given to the edge e so that $\phi_e > 0$ denotes a current with the same orientation than e and $\phi_e < 0$ a current with the opposite direction.

They propose to capture the state of the system solely via the flow configuration vector, $\boldsymbol{\phi}$, whose e-th component is the flow ϕ_e along the edge e. Each flux is constrained by a double-well

channel potential V, for instance of order 6th $V_6(\phi_e) = \frac{1}{6}\phi^6 - \frac{1}{4}\phi^4$, that favors flow states at a specific rate $\phi_e = \pm 1$ over the non-flowing state $\phi_e = 0$, as it is typically observed for active matter confined in narrow channels. The choice of having a potential of order 6 instead of 4 will be justified later. The incompressibility of the fluid implies that vertex cannot accumulate matter, therefore the net incoming flux at the vertex should be 0. This is Kirchhoff's current law, and can be strictly imposed for all the nodes in the graph through the vectorial constraint $\mathbf{D}\boldsymbol{\phi} = \mathbf{0}$, where $\mathbf{D}$ is the V × E incidence matrix of the graph : D_{ve} is 0 if edge e is not linked to node v, +1 if it is directed into v and -1 if it is directed out of v. However, to allow some small fluctuations, a soft rather than a strict incompressibility constraint is imposed via a quadratic compression cost. The AFN has a total energy $H(\boldsymbol{\phi})$:

$$H(\boldsymbol{\phi}) = \lambda \sum_e V(\phi_e) + \frac{\mu}{2} \sum_v (D_{ve}\phi_e)^2 \tag{7.1}$$

with λ and μ are the coupling constants quantifying respectively the strength of the channel potential and of the incompressibility, and we apply Einstein summation rule on repeated indices. We only consider the case where incompressibility prevails over spontaneous channel flow ($\mu >> \lambda$).

Ground states They find that the minima of this energy are discrete and have all their edge flux ϕ_e in the set $\{-1, 0, 1\}$. To see this, let us consider two nodes connected by three edges (Figure 7.1 a). In the incompressible limit $\mu \to \infty$, we have $\phi_3 = -\phi_1 - \phi_2$ and so the potential energy can be expressed only as a function of ϕ_1 and ϕ_2 : $H(\boldsymbol{\phi}) = V_6(\phi_1) + V_6(\phi_2) + V_6(\phi_1 + \phi_2)$. H has 6 local minima, all of ground-state energy. In any of these ground-states, there is one channel where the flux is 0 while in the other channels the flow is ± 1. We can qualify these ground states of polarized flow state because the distribution of the value taken by ϕ_e is peaked around 0 and around ± 1. However, if the double-well potential is of order 4 instead of order 6, $V_4 = \frac{1}{4}\phi_e^4 - \frac{1}{2}\phi_e^2$, minima are not a discrete set but a continuous set, that, in the plane (ϕ_1, ϕ_2) is an ellipse. The flow ϕ_e in any channel can take any value in $[-1, 1]$ with equal probability, therefore the quadratic potential does not lead to polarized flow states. Woodhouse et al choose a potential of order 6 to obtain the discrete minima. The properties of polarized stable flow state remains true for bigger networks like the hexagonal network depicted in Figure 7.1 d, where flow states are composed of unit cycles (flow in ± 1 all along the cycle) separated by non-flowing edges comprising no-cycles (because for the hexagonal network, bulk nodes have degree 3). The more edges have $\phi_e = \pm 1$, the lower the energy of the configuration.

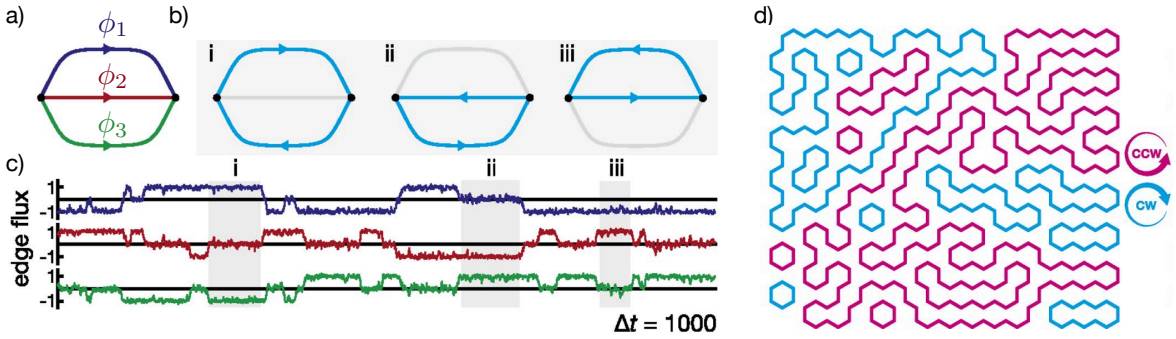

FIGURE 7.1 – **Cycle selection in AFN.** Adapted from [35] ; **a)** 3 equal-length channels connecting 2 nodes, with flow ϕ_1, ϕ_2, ϕ_3 ; **b)** 3 of the 6 degenerate ground-states ; **c)** flow fluctuations allow the system to visit all the ground-states if given enough time ; **d)** one of the ground-states arising in an hexagonal AFN, the flow configuration consists in disjointed CW and CCW cycles.

Network dynamics They assume that the network dynamics follows the overdamped Langevin equation :

$$d\boldsymbol{\phi} = -\frac{\partial H}{\partial \boldsymbol{\phi}} dt + \sqrt{2T} d\boldsymbol{W_t} \tag{7.2}$$

with $\boldsymbol{W_t}$ a vector of independent Wiener processes and T an effective temperature controlling the amplitude of the fluctuations (of intrinsic and external origins). A Wiener process is a continuous 1-d Brownian trajectory, current increment $dW_t = W_{t+dt} - W(t)$ is independent from past increments and current position, and is normally distributed around 0 with variance dt. Thermal noise enables the system to occasionally escape from a local minimum and transition towards another minimum. We consider situations where the noise is low, so that the system is found near its ground-state with a very high probability.

1.2 Networks with inlet-outlet

Let us consider now AFNs that have the capacity to exchange material with outside, and compare them with their passive counter-parts. A subset of the vertices $v \in \mathrm{I} \in \mathrm{V}$ receives an input currents $I_v \in \{0, 1\}$, for them mass conservation writes $D_{ve}\phi_e = -I_v$. Another subset of vertices $v \in \mathrm{O} \subset \mathrm{V}$ release output currents O_v that writes $O_v = (D_{ve}\phi_e)$.

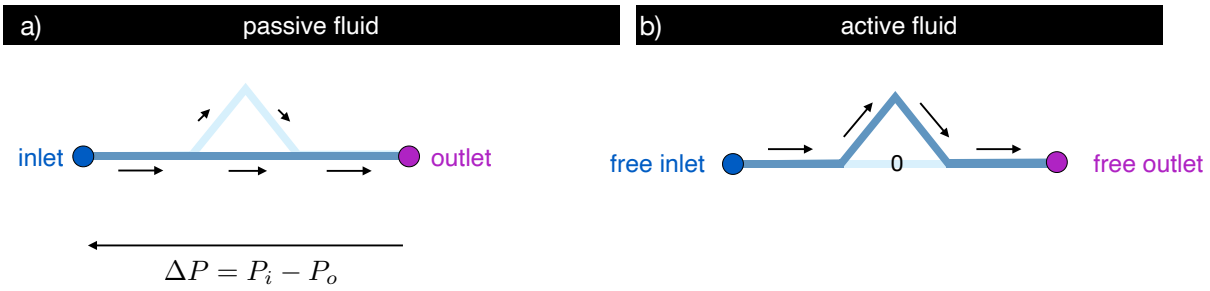

FIGURE 7.2 – **Passive versus active flow networks. a)** for a passive fluid, a pressure difference ΔP is applied between the inlet and the outlet in order to put the fluid into motion. The fluid flows in the two branches, but more importantly in the shortest of the two ; **b)** for the active fluid, a flow sets spontaneously from the inlet to the outlet (or the other way) along the longest path, while the flow is 0 in the other path.

In a pressure-driven *passive* flow network, a Newtonian fluid flows in all the paths connecting the inlet to the outlet, but at different rates [100]. The flow rate is higher along the path of least resistance. Resistance is caused by viscous dissipation. If all the channels have the same width, the path of least resistance is the shortest path. A particle travelling along this path will arrive faster at destination than along the other paths. The flow state minimize the total viscous dissipation.

Active flow networks behave much differently. First, there is no need to apply an external pressure difference for some current to emerge. Second, the flow state selected is not the path of least resistance from the viscous dissipation view point. Instead, according to the cost function we wrote, the flow sets in one of the paths at a time, and in the ground state, it sets in the longest path connecting the inlet to the outlet. Therefore, in the ground-state, a particle travelling from the inlet to the outlet takes more time than in any of the other stable states.

1.3 Applications to logical devices

Taking advantage of the discrete flow values adopted by active flow networks, Woodhouse et al [34] propose to design circuits that compute logical operations upon fluidic currents : $\phi = 1$ codes for a bit of value 1, and $\phi = 0$ stands for a bit of value 0. All the vertices in the network have degree 2 or 3, this particular network topology imposes stronger constraints on flow states, therefore outputs are very responsive to a change in the input currents. A subset of the vertices $v \in \mathrm{I} \in \mathrm{V}$ receives input currents $I_v \in \{0, 1\}$, for them mass conservation writes $D_{ve}\phi_e = -I_v$. Another subset of vertices $v \in \mathrm{O} \subset \mathrm{V}$ release output currents O_v, on which no constraint is applied, they simply write $O_v = D_{ve}\phi_e$. In addition to the input constraint, they introduce in the network a few non linear compounds, diode edges $e \in \mathrm{E}_+ \subset \mathrm{E}$. Diodes only permit flows in their positive direction. To impose $\phi_e > 0$, a diode energy is added to the double-well energy : the energy associated to one diode is $H_d(\phi_e) = V_6(\phi_e) + H_+(\phi_e)$ with $H_+(\phi \geq 0) = 0$ and $H_+(\phi_e < 0) = -\infty$. The energy associated to the whole AFN is therefore :

$$H(\phi) = \lambda \sum_{e\in \mathrm{E}} V_6(\phi_e) + \frac{\mu}{2} \sum_{v\in \mathrm{V}\setminus(\mathrm{I}\cup\mathrm{O})} (D_{ve}\phi_e)^2 + \frac{\mu}{2}\sum_{v\in \mathrm{I}}(D_{ve}\phi_e + I_v)^2 + \sum_{e\in \mathrm{E}_+} H_+(\phi_e). \qquad (7.3)$$

Circuits are appropriately designed so that the outputs released by the network correspond to the results of the targeted logical operations. In figure 7.3 a and b, we show the AND-OR logical gate designed by Woodhouse et al, composed of 7 edges including 4 diodes, assembled into an asymmetric H junction. The two inputs X and Y are the currents injected on the two vertices on the left, and the outputs OR $(X \vee Y)$ and AND $(X \wedge Y)$ are the currents exiting the network at the end of the two legs on the right. Diode edges are placed at the input and output levels to prevent them from taking the value -1. The branch leading to the OR gate is longer so that this path is selected when $X = 1$ and $Y = 0$. For the AND/OR logical circuit, there is a unique ground-state for each input configuration, but the circuit designed to store 1 bit of information (Figure 7.3 c and d) relies on the contrary on degenerate ground-states. The operator can act on one of the two inputs, R and S, at a time. Whatever the initial flow state is, when the operator wants to store "1", they inject an input current of 1 at the S node. This will change the flow configuration and the node Q starts to receive a current of 1, that persists even after we stop injecting the current at S (hence memory). To erase the information, the operator injects a current of "1" at the R node (R for reset). The current received by Q is set to 0 when the operator stops injecting current at R.

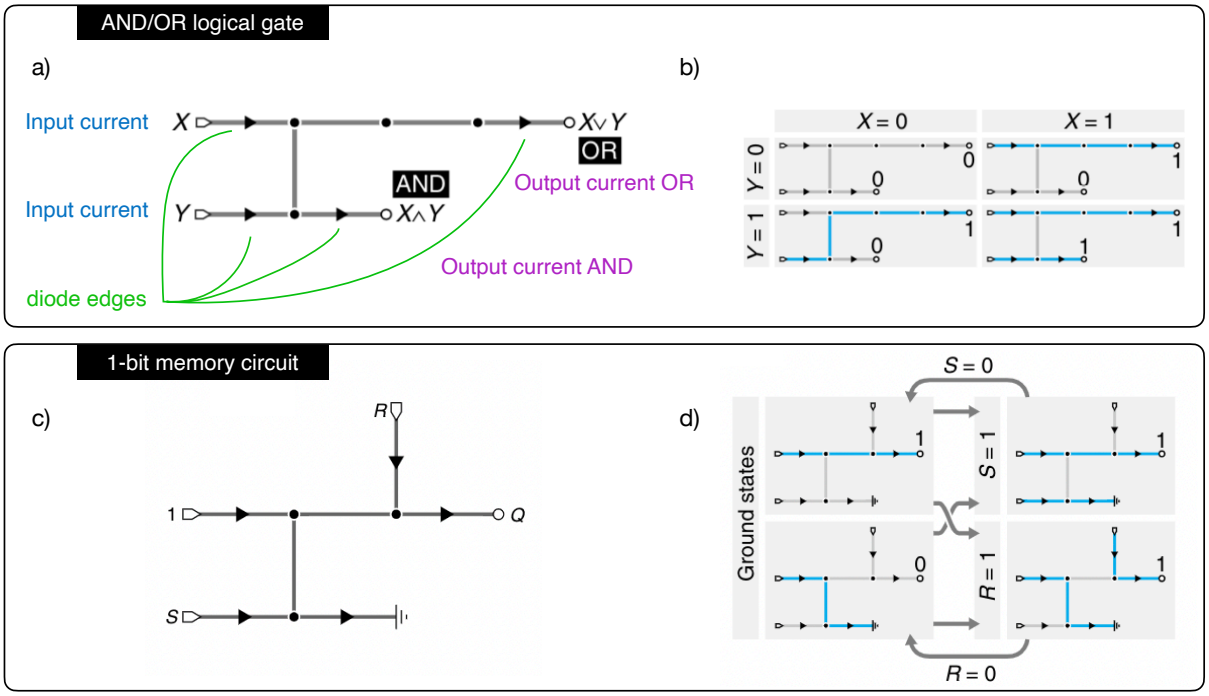

FIGURE 7.3 – **Logical gates.** Adapted from [34]. Oriented channels are diode edges. **a-b)** Logical circuit performing the operation AND and OR on two input currents X and Y ; **b)** flow states for the 4 input configurations. **c and d)** Circuit storing 1-bit of information. The bit value is the flow received by the node Q ; **d)** flow states.

In the rest of this chapter, we present our experimental realizations of active flow networks, and we discuss if the AFN theoretical framework is adapted to describe networks filled with the active nematic liquid crystal. Do polarized flow states spontaneously emerge in the network ? Does the flow set along the longest path ? We first investigate the behavior in an elementary AFN compound : a bifurcation. Next, we make the AND/OR logical gate to illustrate the potential of network design to produce controlled flow states.

2 Bifurcations

First, we want to check the rules governing the behavior of the AN in a microfluidic network using an elementary circuit. The 2D AN system limits us to planar networks, therefore we cannot test the elementary closed network consisting of 2 nodes connected with 3 links of equal length. Instead, our test network is a bifurcation : three symmetric channels A, B, C connected together by a single node (Figure 7.4). Each channel A, B, C can have a flow ϕ_A, ϕ_B, ϕ_C. They are coupled to the surrounding AN at their other extremity. The energy associated to the bifurcation is in theory the same as for the closed elementary network.

2.1 Model's predictions

We assume a strict incompressibility constraint, so that ϕ_A can be deduced from ϕ_B and ϕ_C and the potential energy of the system expressed only in terms of ϕ_B and ϕ_C. We assume a Langevin dynamics, which implies that the probability of observing a configuration (ϕ_B, ϕ_C) is related to the configuration energy via the Boltzmann distribution $P(\phi_B, \phi_C) \propto \exp -\frac{H(\phi_B,\phi_C)}{2T}$. We compare the effect of the potential V_6 of order 6 versus the potential V_4 of order 4 in various bifurcation geometries.

We predict flow states emerging in a *symmetric* bifurcation where the three channels have the same length ($L_A = L_B = L_C$). First, we study an *unconstrained* bifurcation : A, B and C have straight walls so that they do not favor flows in one direction. In Figure 7.4 a and b, we plot the resulting energies $H(\phi_B, \phi_C)$. When the channel potential is V_4, the total energy admits a continuous set of minima in the shape of an ellipse (Figure 7.4 a). In contrast, for V_6, the total energy landscape has 6 discrete minima that are all polarized flow states (flow is 0 in one channel while it is ± 1 in the other two). We then replace channel A with a diode, to constrain ϕ_A to be positive. This can be achieved by patterning the walls of channel A with ratchet indentations. We assume that the energy associated to ϕ_A is $\frac{w}{2}(1 - \phi_A)^2$, so that the strength of the diode can be modulated with the parameter w. When the diode is weak ($w = 1$), V_4 for ϕ_B and ϕ_C yield an energy landscape with 3 local minima, with the global minimum being a mixed flow state : the input flow ϕ_A splits equally in the branches B and C (Figure 7.4 c). In contrast, V_6 produces 2 polarized ground-states : $\phi_B = 0, \phi_C = 1$ and $\phi_B = 1, \phi_C = 0$. However, increasing the strength of the diode channel ($w = 10$) leads to polarized ground-states for both V_6 and V_4 (Figure 7.4 e and f).

In conclusion, for a symmetric bifurcation with order 6 channel potential, polarized flow

states always emerge. A potential of order 4 leads to an infinity of mixed flow states if no constraint is applied on the bifurcation, however imposing an input current somewhere leads to two polarized ground-states.

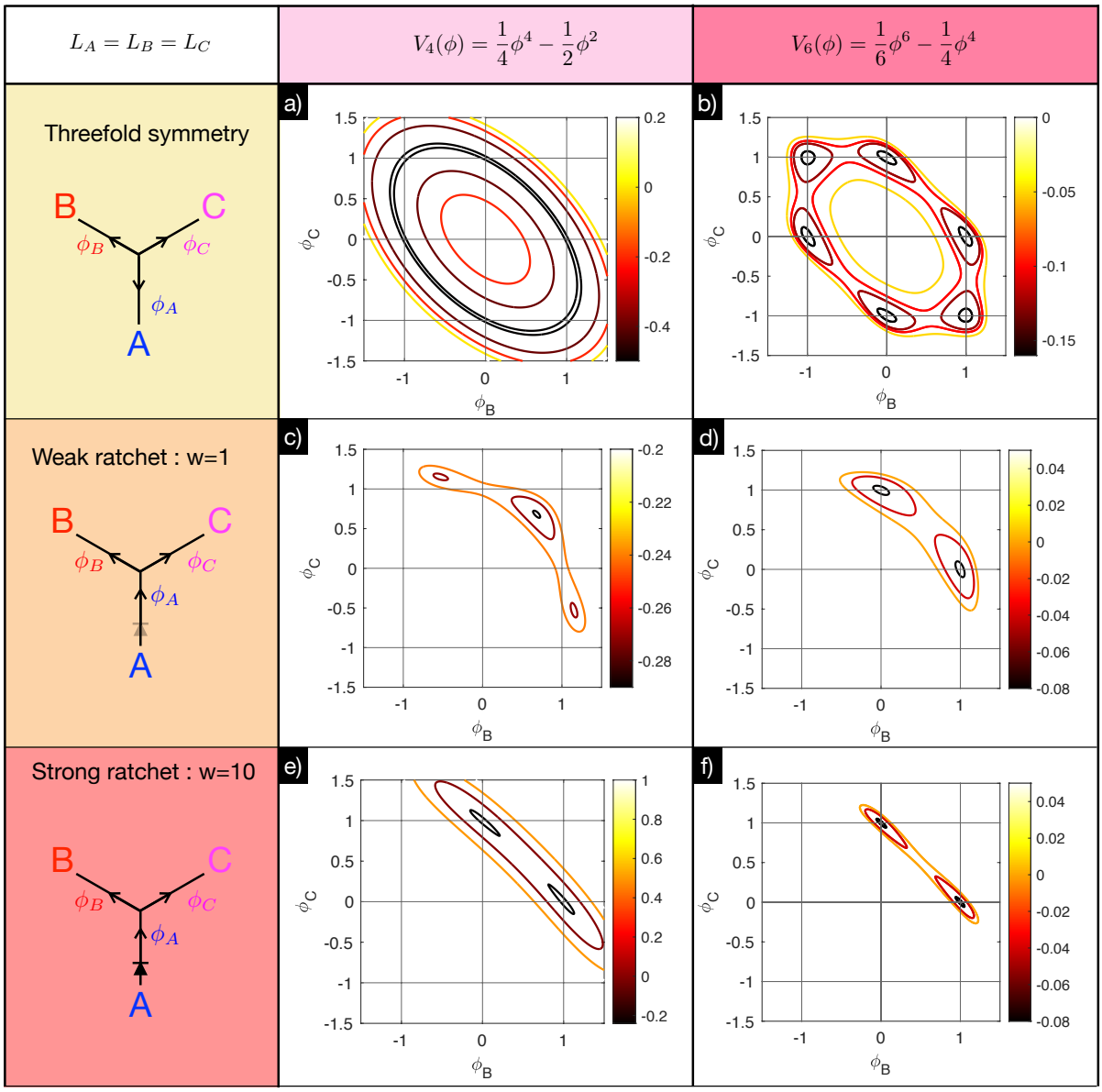

FIGURE 7.4 – **Potentials $H(\phi_B, \phi_C)$ for a symmetric bifurcation.** We plot a few iso-lines to represent the energy landscape. **a,c,e)** Channel potential is V_4 ; **b,d,f)** channel potential is V_6 ; **a,b)** no input is imposed in channel A, the three channels A, B, C are identical ; **c,d)** channel A weakly imposes $\phi_A \approx 1$; **e,f)** channel A strongly imposes $\phi_A \approx 1$

Next, we predict the behavior of the active flow in an *asymmetric* bifurcation : channel C is shortened by half so that $L_A = L_B = 2L_C$. As already implied by the summation of individual channel potentials, we assume that the potential exerted by a channel is proportional to its length. When no input is imposed to the bifurcation, both potentials admit discrete minima. The energy landscape produced with V_6 has the same polarized local minima as before, but

only ($\phi_C = 0, \phi_B = \pm 1$) are ground states (Figure 7.5 b). The energy landscape produced by V_4 admits the 2 polarized ground-states ($\phi_C = 0, \phi_B = \pm 1$) and two mixed excited states (Figure 7.5 a). When channel A acts as a weak diode, only two local minima survive, with ($\phi_C = 0, \phi_B = +1$) as the ground state (Figure 7.5 c and d). When the strength of the diode is stronger, only the polarized ground-state is maintained for V_4 (Figure 7.5 e), whereas for V_6, the system still admits a stable excited state at ($\phi_B = 0, \phi_C = +1$) (Figure 7.5 f).

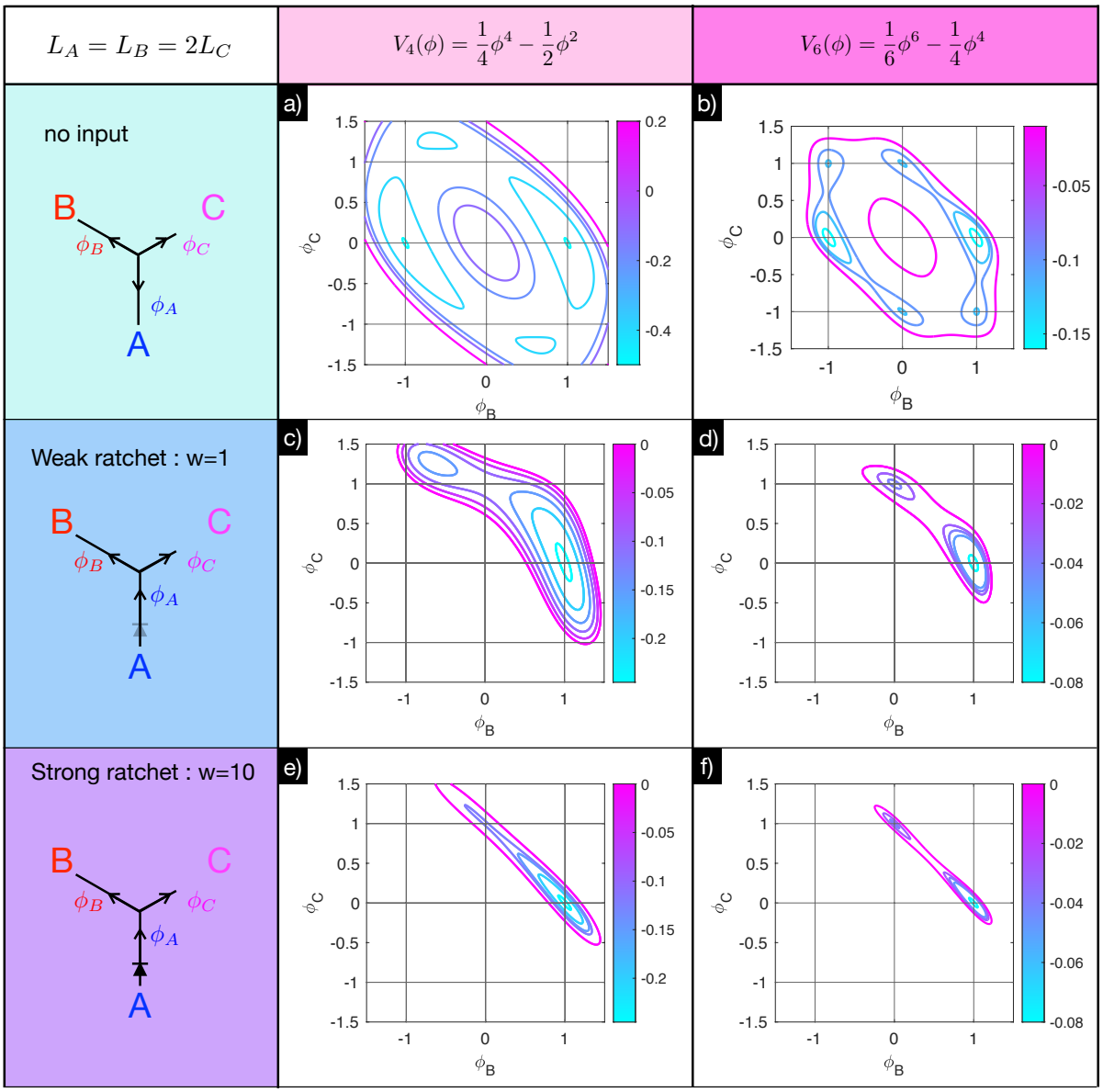

FIGURE 7.5 – **Potentials $H(\phi_B, \phi_C)$ for an asymmetric bifurcation.** Branch C is half the length of branches A and B. We plot a few iso-lines to represent the energy landscape. **a,c,e)** Channel potential is V_4 ; **b,d,f)** channel potential is V_6 ; **a,b)** no input is imposed in channel A ; **c,d)** channel A weakly imposes $\phi_A \approx 1$; **e,f)** channel A strongly imposes $\phi_A \approx 1$

To conclude, an asymmetry in the lengths of the two daughter branches B and C leads to a polarized ground-state where the flow follows the longest of the daughter branches.

2.2 Experimental results for symmetric bifurcations

First, we experimentally test symmetric bifurcations where the three channels have the same length of 1000 µm and the same width of 100 µm, a geometry for which stable flows set-up in individual channels (Chapter 5).

Unconstrained bifurcation. The bifurcation is totally symmetric (Figure 7.6 a and b). We observe the bifurcation for 2 hours, recording 5 minutes movies spaced in time. The AN layer in channel B in this experiment is not in focus, preventing us from measuring the flow in this branch. The histogram representing the joint probability $P(\phi_A, \phi_C)$ (Figure 7.6 c) displays what looks like the south-west part of the elliptic valley of the potentials in Figure 7.4 a and b, with certain configurations more visited than others. In Figure 7.6 d, we plot the fluctuations of ϕ_A and ϕ_C for 5 successive movies. The system tends to be in a polarized state, first, the fluid flows from C to A, then from C to B, and then from A to B. From the full observations, we deduce that the system has transitioned at least 4 times. Each transition sees the flow in one branch getting activated $0 \to \pm 1$, and we never observe the full direct transition $\pm 1 \to \mp 1$ in one branch. The results of this experiment are thus compatible with the system hoping from a local minimum to a neighbouring local minimum along the elliptic valley depicted on Figure 7.4 b. However, our experimental ellipse is skewed (flows are smaller in C than in A), denoting an unwanted asymmetry in the bifurcation, likely coming from the position of the interface under the grid bridges. This asymmetry could also explain why the system never visited the superior part of the ellipse corresponding to $\phi_B < 0$.
We note that, in any branch of the bifurcation, we observe more ϕ reversals $\pm 1 \to 0 \to \mp 1$ than in an isolated individual channel of the same length 1000 µm. The zero flow state is unstable for the individual channel (chapter 5). In contrast, in the bifurcation, the $\phi = 0$ state in a branch is stabilized by the presence of flux in the other two branches. In a branch, the flow can thus reverse more easily by passing through an intermediate metastable state that lowers the energy barrier between the initial state and the final state, in a way that is analogous to catalysis in chemistry. This means that, in order to obtain stable flows in networks, channels should be longer than in the case where they are isolated.

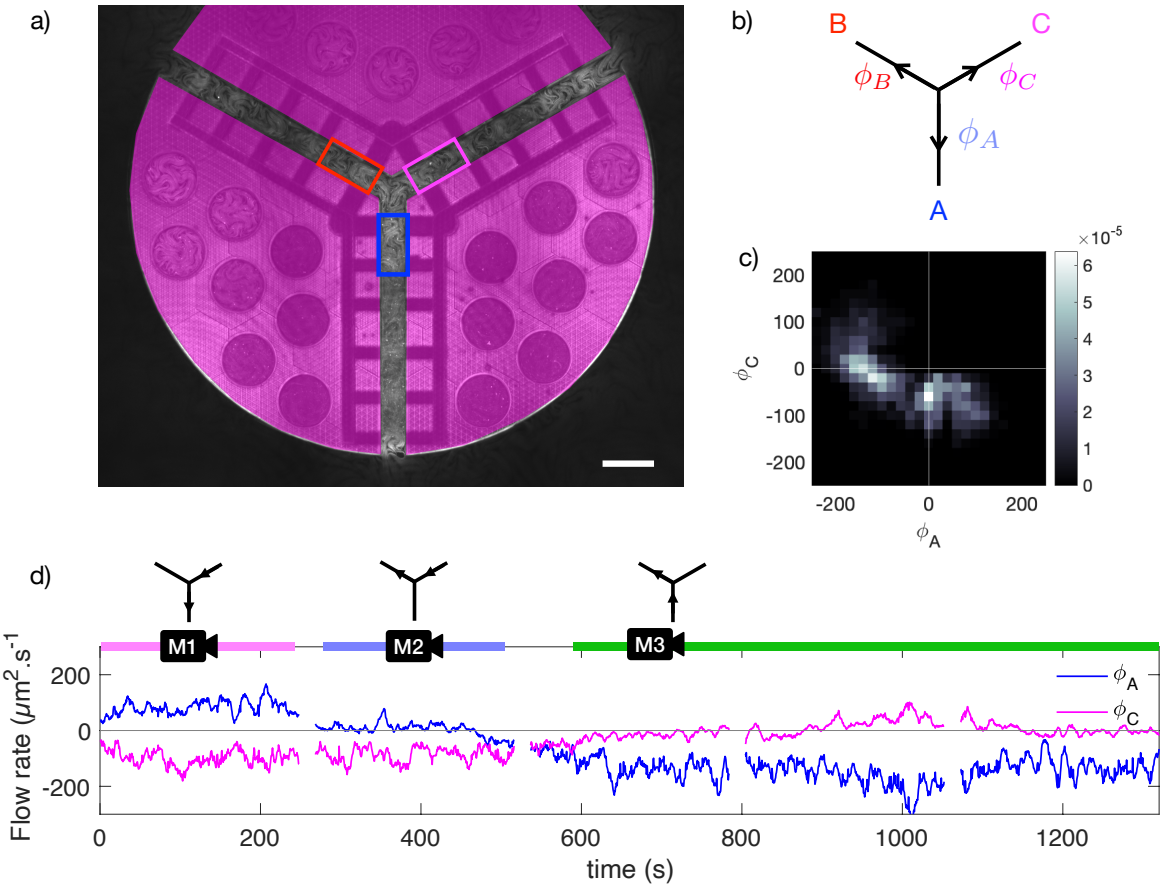

FIGURE 7.6 – **Unconstrained symmetric bifurcation. a)** Large fluorescence image of the AN confined in the three-fold symmetric bifurcation. The grid is overlaid in magenta. ϕ_A, ϕ_B, ϕ_C are measured in their respective 200 µm-long window, scale bar = 200 µm ; **b)** sketch showing the orientation we attribute to each edge ; **c)** bivariate histogram representing the joint probability $P(\phi_A, \phi_C)$ computed from all the movies (about 90 minutes in total) ; **d)** extract of the fluctuations of ϕ_A and ϕ_C. Access corresponding movies by clicking on these links : M1, M2 and M3.

Bifurcation with an input. The input channel A is indented with a 3-ratchet pattern in order to fix the current $\phi_A \approx +\phi_0$ (Figure 7.7 a). Having only 3 ratchet indentations might create a weak diode. We made this choice so that the flow along channel A is positive but adapts its amplitude to the straight portion of the channel and matches the minimum ϕ_0 of the double-well potential associated to B and C.

The flow ϕ_A in the A-branch is indeed always positive, confirming the efficiency of the ratchet pattern to control the flow direction in networks (Figure 7.7 d). The joint probability $P(\phi_B, \phi_C)$ displays a peak corresponding to a mixed flow state where the input flow ϕ_A splits into the two daughter branches B and C (Figure 7.7 c). However, $\phi_B > \phi_C$ on average. This is a sign that there could be a bias in the set-up. It is difficult to reconcile this result with our previous conclusion, drawn from the unconstrained bifurcation, unless the diode is weak and the channel potential is V_4 of order 4 (figure 7.4 c), or the ratchet channel A promotes $\phi_A > \phi_0$, an input flow of too high amplitude to yield polarized flow states. As a result, the input flow would have

to split in B and C.

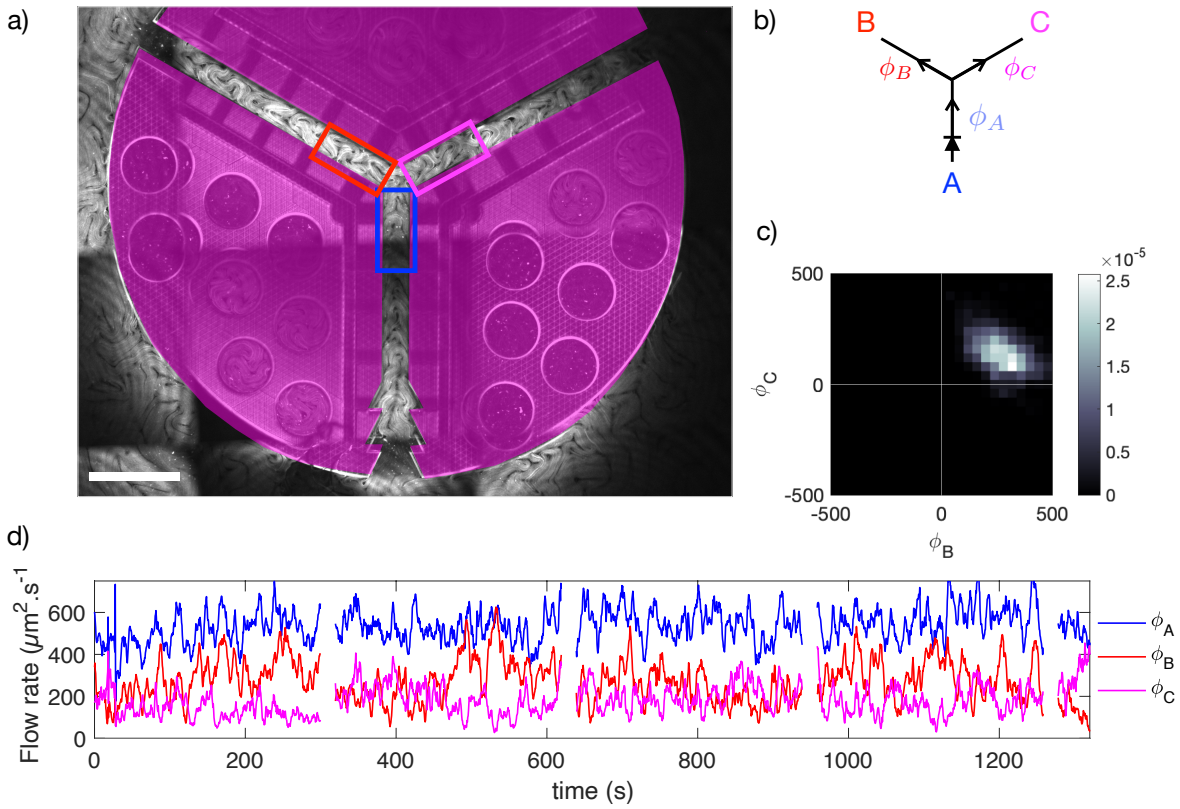

FIGURE 7.7 – **Input-fed symmetric bifurcation. a)** Large fluorescence image of the AN confined in the bifurcation. The grid is overlaid in magenta, scale bar = 200 µm ; **b)** sketch showing the orientation we attribute to each edge ; **c)** bivariate histogram representing the joint probability $P(\phi_B, \phi_C)$; **d)** extract of the fluctuations of ϕ_A, ϕ_B and ϕ_C.

2.3 Experimental results for asymmetric bifurcations

We now test asymmetric bifurcations, where the channel C is only 500 µm long while A and B are still 1000 µm long. In this case as well, channel A is indented with 3 ratchet teeth in order to act as a diode.

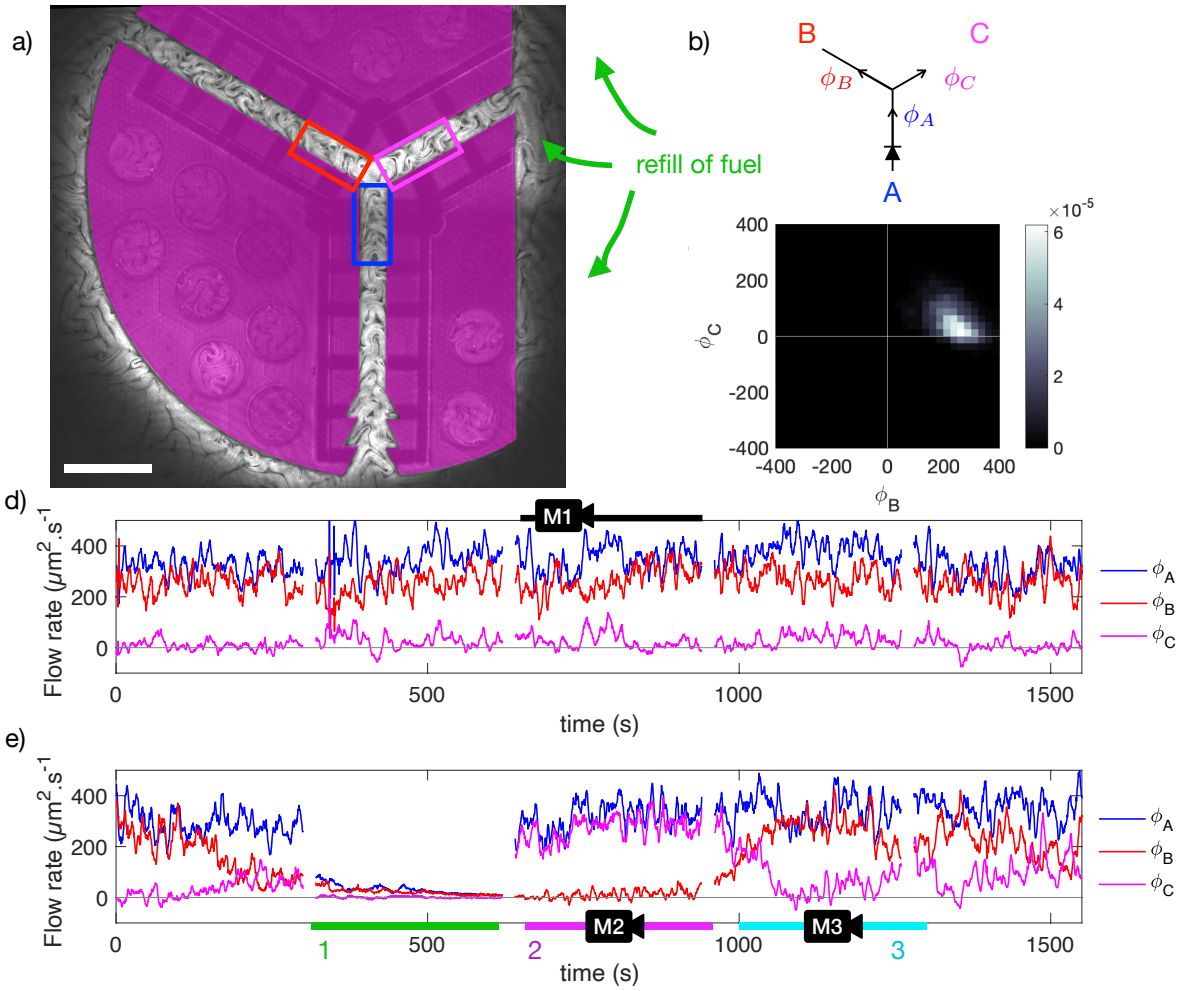

FIGURE 7.8 – **Input-fed asymmetric bifurcation. a)** Large fluorescence image of the AN confined in the bifurcation. The grid is overlaid in magenta,branches A and B are 1000 µm long, and branch C 500 µm long. scale bar = 300 µm ; **b)** sketch showing the orientation we attribute to each edge ; **c)** bivariate histogram representing the joint probability $P(\phi_B, \phi_C)$; **d)** extract of the fluctuations of ϕ_A, ϕ_B and ϕ_C. Access movie here. **e)** extract of flow fluctuations at later time, during time window 1 activity is depleted, and we inject with a syringe far from the grid PEP to restore the activity. During time window 2, as PEP diffuses from the right, the activity and the flow are restored in channel A and C first, while the nematic is still partially static in channel B (access movie here). In time window 3, the entire channel B recovers normal activity levels, and the flow ϕ_B starts again in this channel (access movie here).

In the experiment whose results are shown in Figure 7.8, the flow clearly sets in the branch B, twice longer than branch C. However, for three other experiments that we made, the flow was less biased towards B. In one experiment, the flow was even slightly more important in the short branch. The issue is that the position of the interface in the grid channels is difficult to control. If the interface is very curved at the extremity of one of the channels, we can imagine that it affects the flow, either by favoring it, or preventing it. Also, even if we follow the same protocol to prepare the samples, differences exist between them. These differences are often enhanced after confinement in the channels. We measure differences in term of density of topological defects,

different flow amplitude, and different amplitude of fluctuations. All of these parameters might affect the flow state in the bifurcation greatly. To confirm if really the flow follows the longest path, a statistical study is necessary, as well as increasing the length of channel B up to 2000 µm to increase the effective energy difference between the two paths.

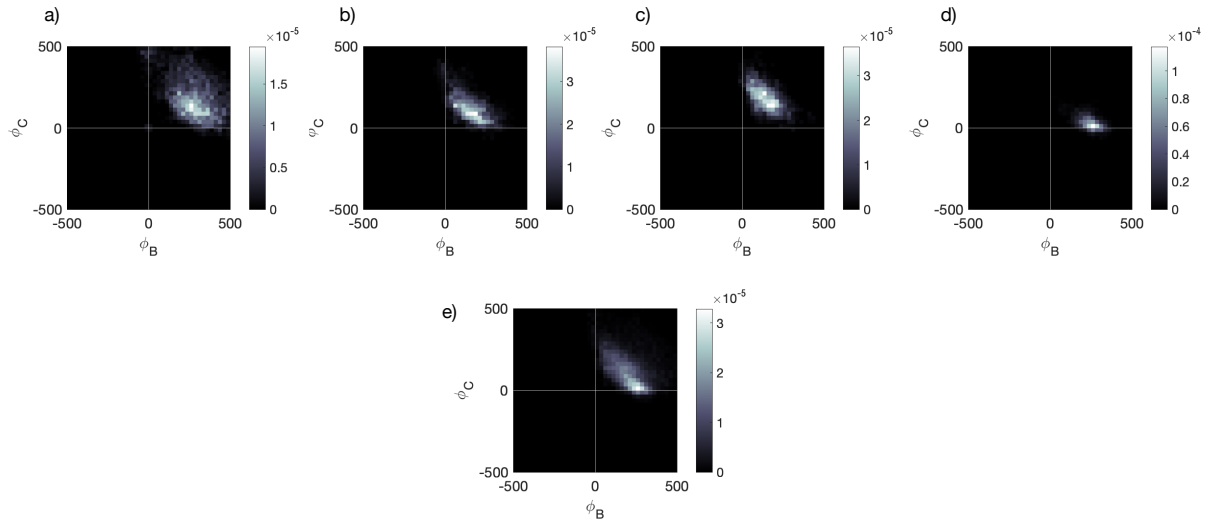

FIGURE 7.9 – **Flow state probability for input-fed asymmetric bifurcation : the flow is more likely to set in the longest branch. a,b,c,d)** histograms representing $P(\phi_B, \phi_C)$ for 4 experiments, observed for 50 minutes. **e)** histogram gathering the four experiments contributions.

2.4 Discussion

Geometry of the bifurcation. The AFN model discussed here assumes an effective energy that only depends on flows along edges, nodes are involved only through the compression cost. This assumption is legitimate for networks where channels have a very high aspect ratio $\frac{L}{w}$. However, the channels in our experiments are 1000 µm long and 100 µm wide, giving an aspect ratio of 10 only. Therefore, the respective orientation of the channels at the junction might affect the flow state. For instance, a positive topological defect arriving at the junction from the input channel A faces a triangular protrusion of 120°, that deforms the defect and induces the nucleation of a new pair of defects. A time sequence illustrating this type of event is shown in Figure 7.10. Each one of the positive defects then enters into one of the daughter branches, splitting the input current in the two output branches. Furthermore, orientating one output channel in the axis of the input, while placing the other output channel perpendicularly, should direct the input current preferentially towards the first channel.

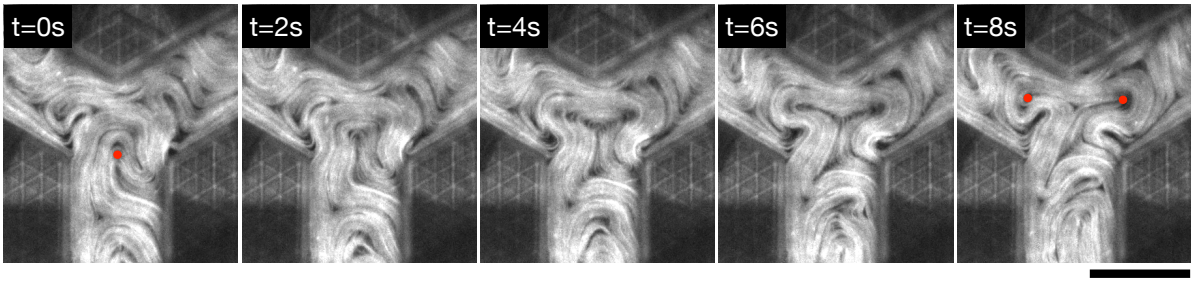

FIGURE 7.10 – **Defect branching at the junction.** Time sequence showing a $+\frac{1}{2}$ defect arriving at the junction from channel A. The defect faces the triangular protrusion, its head flattens and two new positive defects nucleate, one directed towards branch B and the other directed towards branch C. Scale bar = 100 µm.

Low noise regime. We do not always observe a clearly polarized flow state. This can be the result of fluctuations of too high amplitude in comparison to the energy barrier between the local minima. Reducing the system activity (ATP concentration) could reduce the noise and stabilize the flow states.

3 AND/OR logical gate

We now want to apply these design rules to create functional AFN with the active nematic material. As a proof of concept, we build an AND/OR logical gate, the smallest of all the circuits proposed by Woodhouse et al.

3.1 Logical gate design

We reproduced almost identically the design shown in Figure 7.3. Our logical gate is composed of 7 unit channels of 500 µm length assembled into an asymmetric H-junction. Two input currents X and Y and two output currents OR and AND respectively enter and exit the circuit through a diode channel to prevent back flow. A current of $+\phi_0 > 0$ codes for "1" and the absence of current codes for "0". Diode channels are the ratchet channels presented in Chapter 5. Various widths for the straight channels are tried : $w = 100$ (Figure 7.11) and $w = 150, 200$ µm (Figure 7.12).

Also, a triangular tip is added on the right side of the H junction to redirect the input flow Y towards the OR gate in the case where X=0 (Figure 7.11, and 7.12 a). In chapter 4, we explained that triangular protrusions pin negative defects and create continuous jet of material perpendicularly to the wall. It is the only modification we add to the conceptual design. Indeed, if the experiments in the asymmetric bifurcation have shown a tendency for the flow to set along the longest path, we judged this tendency not robust enough against unwanted external asymmetry and the 90° angle that the flow Y has to take to reach the OR gate.

Because we currently do not have the experimental technique to switch an input current to 0 or 1, we test the 4 input pairs in 4 replica of the circuit embedded in the same grid (Figure 7.11 b). A closed input channel sets the input to 0, while an opened input channel spontaneously

leads to an input of 1. A movie showing the active nematic confined to the logical-gate circuit is accessible here.

3.2 Results

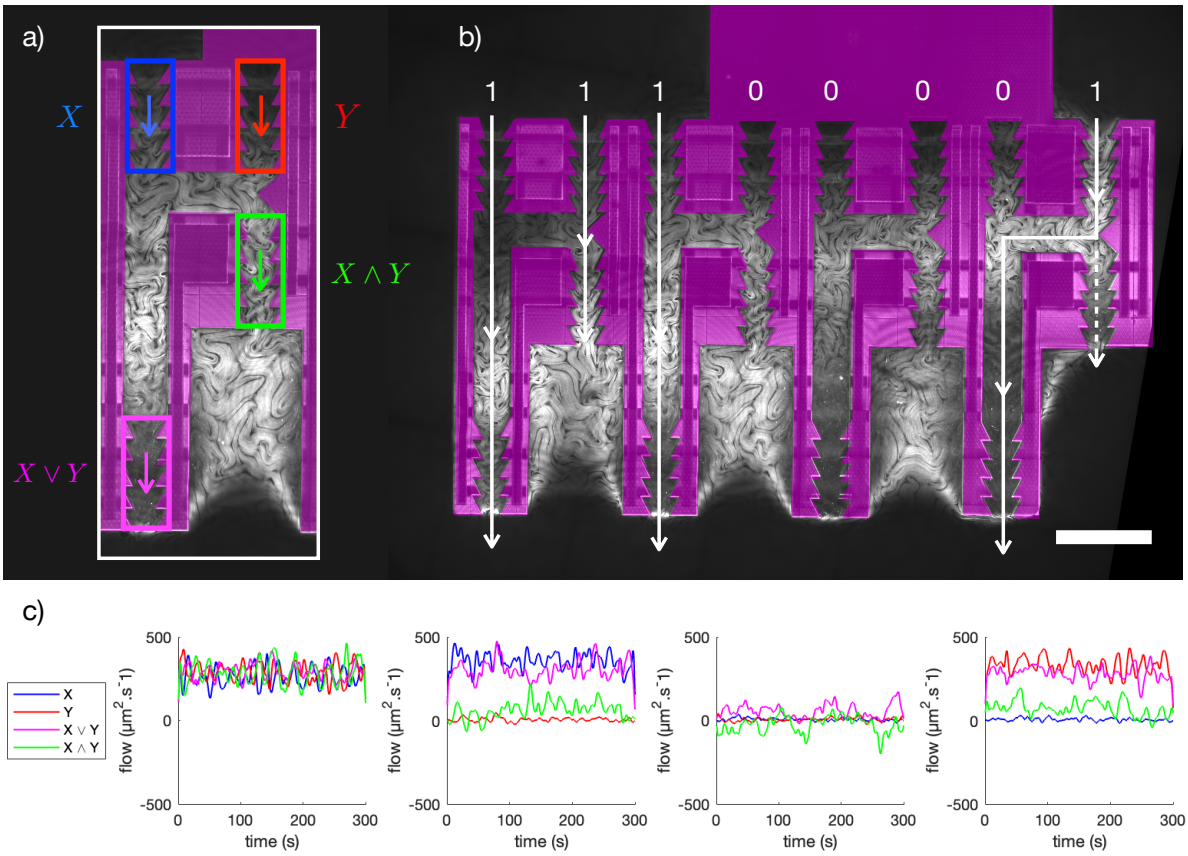

FIGURE 7.11 – **AND/OR logical gate.** All the areas overlaid in magenta in fluorescence micrographs a and b represent the walls of the grid. **a)** The AND/OR logical gate is an asymmetric H-junction that takes two input currents X (in blue) and Y (in red) and releases the output current OR ($X \vee Y$, in magenta) at the end of the long leg and the output current AND ($X \wedge Y$, in green) at the end of the short leg. The flat portions of the channels are 200 µm wide and diodes edges prevent back flows at the inputs and outputs. Input and output currents are measured in the arrows direction and averaged spatially over rectangular windows ; **b)** Fluorescence micrograph of the active nematic layer confined within the logical circuits of the entire grid (overlaid in magenta). The grid encompasses 4 logical circuits corresponding to the 4 pairs of inputs. To obtain an input current of 1, the diode channel is open on the rest of the system. To set it to 0, the diode channel entrance is closed (hence the magenta rectangular area upstream of all the ratchet channels set to 0, this part of the grid is also where the capillary is attached). Flow states that we typically observe during the experiments are drawn in white. Scale bar = 500 µm ; **c)** Input and output flows versus time for each pair of inputs.

We measure the 4 volumetric flow rates X, Y, $X \vee Y$ and $X \wedge Y$ over 500 µm long rectangular windows as shown in Figure 7.11 a. The field of view of the microscope is not large enough to allow us to film the 4 flow rates within one circuit at the same time. For each circuit, we film

for 5 minutes the input X and Y, then the output AND, and then the output OR. We assume that each circuit has reached a steady-state. Evaluating the current in the horizontal channel of the H junction confirms the steady-state hypothesis.

The first observation to make is that, although we do not strictly impose the inputs X=1 and Y=1, the open ratchet channel spontaneously generates an input of 1. Only in the case where channels are too narrow (w=150 µm in Figure 7.12 f and g), the high resistance of the circuit restrains the amplitude of X and Y when both are activated. We find that the circuit with large straight channels (w=200 µm) releases the outputs the most compatible to the operations $X \vee Y$ and $X \wedge Y$. With this design, the input current $Y = 1$ is almost entirely directed towards the OR gate (Figure 7.11 c). For the input pair (X=0, Y=0), a back flow occurred transiently, going from the AND gate towards the OR gate. When the width of the straight channels are narrower (w=150 µm, we find that when only one of the input is activated, the flow tends to split, the most part is directed towards the OR output, but the AND output receives a residual current (Figure 7.12 c and e). When the width is too narrow (w=100 µm in Figure 7.12 f), then when X=0, the input flow Y=1 goes mostly towards the AND gate, while approximately 25% is directed towards the OR gate. When the straight channels are not wide enough to accommodate the input flow created by the ratchet channel, flow states are not polarized anymore and the input current splits into the two outputs.

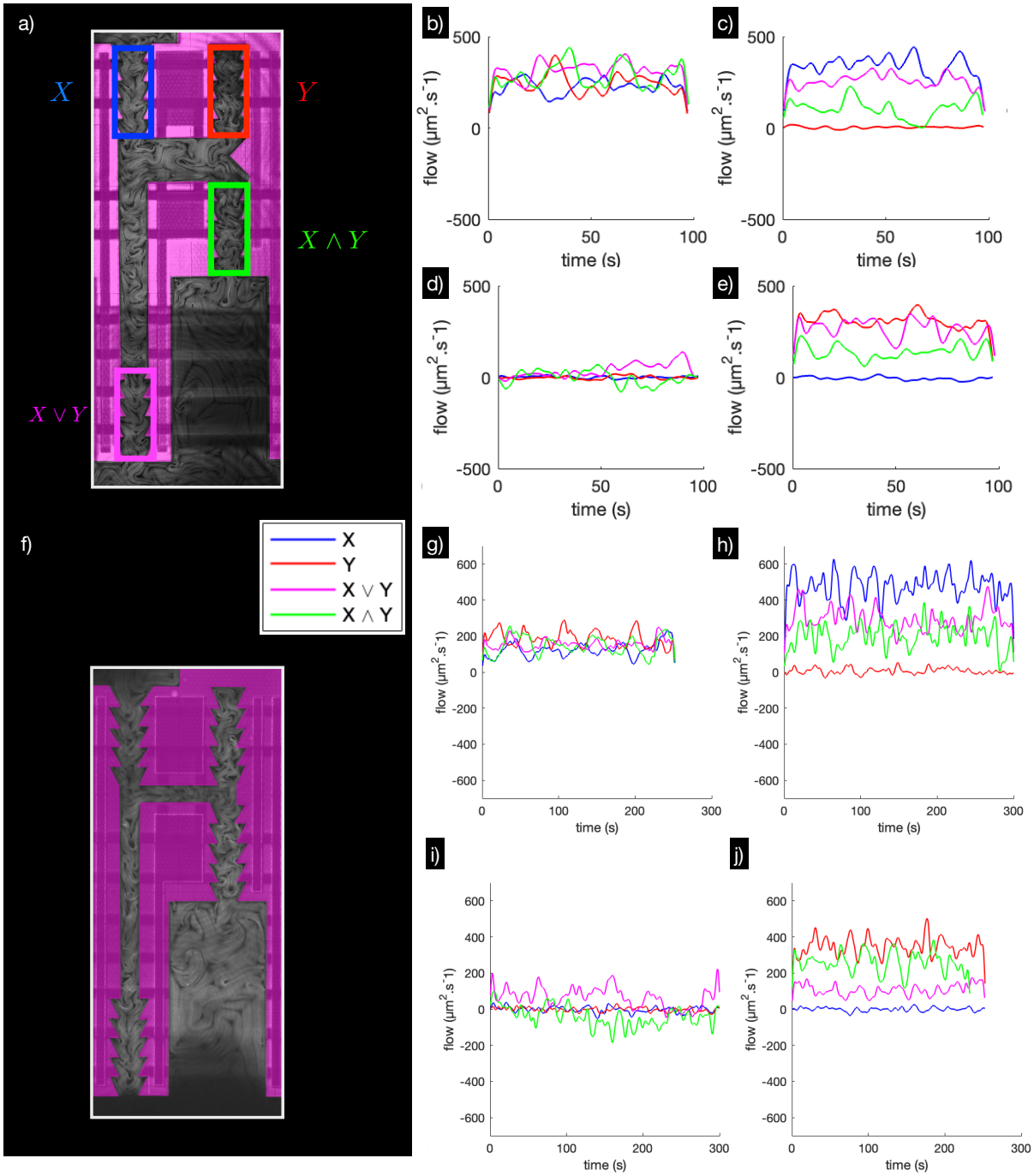

FIGURE 7.12 – **Design variations : increasing network resistance.** The width w of the straight channels is reduced to 150 µm for design displayed on **a)**, associated flow states are plotted in **b,c,d,e** ; the width w of the straight channels is reduced to 100 µm for design displayed on **f)**, also, there is no triangular tips on the right of the H-junction, associated flow states are plotted in **g,h,i,j**.

Design improvements. Many design modifications could improve the logical gate accuracy. First, we can make the OR branch longer, to lower even more the energy of this flow path. However, this could increase the likelihood of the back flow we observed in the case (X=0,Y=0).

This back flow shows that the cost of flowing against a ratchet can sometimes be overcome by flowing in the second ratchet in the easy direction and along the 1500 µm of straight channel. Second, we could reduce the input amplitude by reducing the width of the input channels. Third, the 90°angle on the path from Y to the OR gate does not help the input flow to be directed towards the OR gate when (X=0, Y=1). Instead, the Y input could be rotated to be perpendicular to the AND output.

This type of active matter logical gates are already strongly geometrically constrained : the selection of a path depends on the length of this path. If, on top of that, we constrain the bifurcation angles, branching logical circuit in cascade starts to be a complex task. Also, the strategy of lengthening a path to lower its effective energy, increase the device accuracy at the expense of compactness and of the response time, that is the time it takes for the outputs to respond to a change of the inputs.

3.3 Alternative experimental set-ups

We briefly present other experimental set-ups that were tried prior to the logical device presented before. Grids manually placed at the interface are convenient to confine the active nematic film in relatively small networks. However, for bigger networks, the probability that the grid is broken or that the active nematic film is not well confined in some part of the device is high. Moreover, it seems hardly compatible with the insertion of microfluidic pumps and valves, to control the input. Therefore, we first considered to create closed chambers (as opposed to the open pool in which we dip the grid) and to confine the AN in microfluidic channels directly attached on the glass substrate.

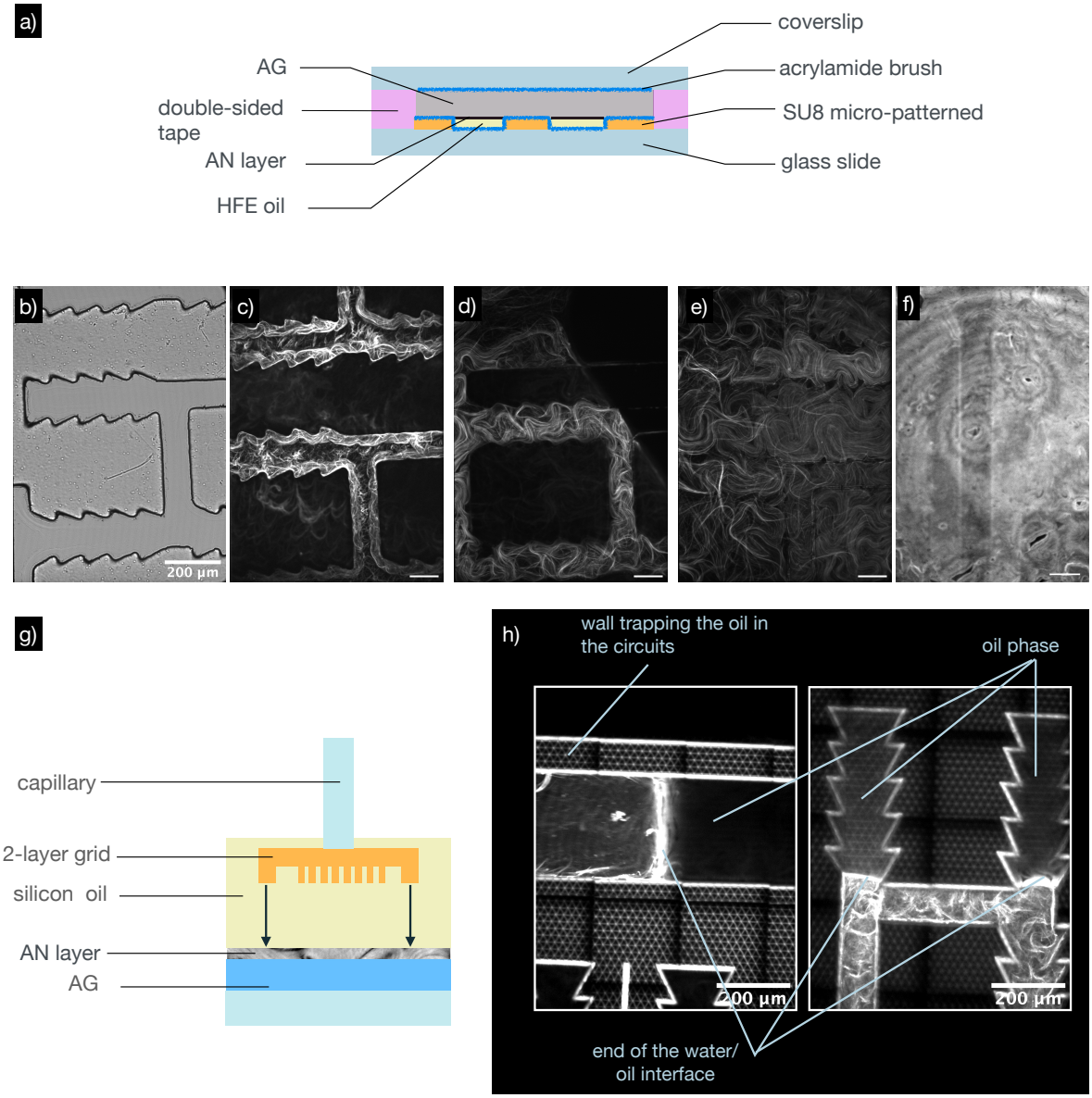

FIGURE 7.13 – **Alternative experimental set-ups. a)** sketch representing the observation chamber with the circuits lithographed on the glass slide, with the SU8 photo-resist. Ideally, the oil would be trapped in the channels only ; **b)** bright field image of the lithographed channels ; **c)** circuits were lithographed on glass treated with omnicoat, then the micro-patterned glass slide was plasma-etched and coated with acrylamide. The chamber was assembled, filled with HFE oil, then filled with the AG. Bundles accumulate near the walls ; **d)** glass slide was sinalized (instead of ominicoat), no surface treatment was applied to the lithographed glass slide. The active gel does not fill all the channels ; **e)** same as d, except that the HFE oil was dropped over the lithographed glass slide before covering the chamber with the coverslip. The oil submerges the micro-patterns, AN film covers everything ; **f)** circuits were 3D printed on the glass slide treated with ITO, with the nanoscribe, then treated with aquapel. The oil submerged the circuits. Scale bar for b,c,d,e,f 100 µm ; **g)** sketch representing the 2-layer grid dipped in the open pool chamber ; **h)** fluorescence images showing that the AG phase pushes back the oil phase in the corners.

Photolithography on glass. This confinement protocol is directly inspired from Opathalage et al [50]. We create micro patterns directly on a glass slide using a classic photo-lithography protocol. First, we treat the glass slide in order to increase the adherence of the photo-resist, either with "omnicoat" or we silanize the glass slide. Micro-patterns are made of SU-8 82035, a bio compatible negative-tone photo-resist (the polymer reticulates under light exposure) whose viscosity creates patterns of 35 µm of height [101]. A photomask is placed in direct contact with the photo-resist layer (the direct contact is important to obtain our 50 µm-sized patterns with good resolution) then the photo-resist is exposed to UV-light. After a post-exposure-baking step, the micro-pattern glass slide is developed in propylene glycol monomethyl ether acetate (PGMEA) to dissolve the un-reticulated photoresist (filling the channels), and hard baked for 5min at 200°C.

2-photon polymerisation on glass. The same technique used to print the grid is used to print the circuit directly on a glass slide coated with indium tin oxide (ITO). This allows to have a very good pattern resolution, and to control the height of the pattern very precisely.

Whatever technique is used to print the network on the glass slide, the protocol afterwards is as follow (Figure 7.13 a). First, the micro-patterned glass slide is plasma-etched and made hydrophilic with acrylamide-silane surface treatment (see Chapter 2). We found that acrylamide surface treatment destroyed the network printed with 2-photon polymerisation. Then, we create the chamber by sandwiching double-sided tape between the glass slide and an acrylamide-coated cover-slip. We fill the chamber with HFE7500 oil, containing 5% 008-FluoroSurfactant (RAN Biotechnologies). Next, the active gel (without pluronic, the surfactant we use with the silicon oil) is injected in the chamber. Because the chamber is hydrophilic, the oil is mostly replaced by the AG, but a fraction is trapped in the channels. The chamber is sealed with UV-curable glue (NOA), and centrifuged for a few minutes to deplete the bundles at the oil/water interface.

We find that this confinement technique does not work well for networks. Opathalage et al managed to confine the AN inside circular pool that were at most 800 µm in diameter, and 20% of the patterned disks retained some oil and successfully enclosed the AN. For the network of channels, the AG phase can flush away easily most of the oil, leaving only a very thin lubricating film in some areas (Figure 7.13 c). This results in the lack of oil/water interface in some areas, and heterogeneous friction with the substrate resulting from the uneven height of the oil film. Also, the hydrophilic character of the chamber hinders the oil phase progression by capillarity. We often find air bubbles in the chamber. When, instead of the acrylamide surface treatment, we apply aquapel (hydrophobic coating) on the lithographed glass slide, the oil submerges the micro-patterned structures, failing the confinement inside the network's channels (Figure 7.13 f). We (rarely) find a few areas where the AN layer is confined in the channel. The ratchet pattern created by classic photo-lithography are imprecise and rounded (Figure 7.13 b).

Undoubtedly, more advanced surface treatment and patterning deserve to be considered and tested to retain the oil in the network, however for the sake of this thesis we give up photo-lithographed networks on glass to turn towards a confinement method that we mastered well :

the grid. We first design a grid made of two layers : the network layer and a supportive layer (Figure 7.13 g). The 4 circuits are surrounded by a wall whose role is to prevent the oil from escaping from under the grid. The grid is positioned as usual at the interface. At first, the active nematic layer is well confined within the channels, but this situation is meta-stable. Soon, the interface touches the supportive plate, and, since the water/oil interface has an surface energy cost, the water phase pushes the oil in the network dead-ends and corners (Figure 7.13 h). After this attempt, we designed the logical gate with the bridges shown in Figure 7.11 and 7.12, and found that the bridges were solid enough.

3.4 Future improvements

Besides optimizing the network design, a next important step is to implement input control. One option is spatio-temporal activity patterning relying on light-responsive molecular motors [54].

Implementing input control with patterns of light. Redford et al [54] have demonstrated experimentally that actin/myosin based 2D active nematics can be optically controlled. They used engineered tetrameric myosin molecular motors, whose lever arm contains the light sensitive LOV2 domain [102]. Under UV-light stimulation, motors walk along actin filaments at high velocity, while their velocity is drastically reduced in the absence of stimulation. Patterns of light of any shape can be applied to the sample, thereby modulating the activity field. Topological defects are confined within high activity regions, and their trajectory can be guided along virtual channels (no physical boundary, just a path of light). Then, Zhang et al confirm the experimental observation with numerical simulations. They predict that a triangular patch of light induces the nucleation of a pair of $\pm\frac{1}{2}$ defects, and that pathways of light can control the trajectory of positive defects confined within a hard-walled H-junction.

Next, we plan to use light-sensitive kinesin molecular motors [103] to power microtubule-based AN. This will allow us to switch on and off the input currents within a logical circuit, and to assess the response time of the device. If we use kinesins that are activated under light illumination (the opposite version exists as well), we could illuminate the whole sample but apply a mask over the input channel to set the current to 0. The incidental observation we reported for the asymmetric bifurcation (Figure 7.8) is indeed a good indication that the flow stops when a portion of the channel is inactive. More generally, combining hard-walls boundaries, geometrical patterning and activity patterns is a promising method to achieve greater control over ANs.

3-D active fluid. Confining laterally an interface is difficult. It is simpler to fill a network with a 3D active fluid, for instance a microtubule-based active gel. Wu et al have shown that an isotropic suspension of active microtubule bundles confined inside microfluidic channels can spontaneously develop coherent flows in set-ups as long as 1 m [104]. However, the authors suggest that the current stems from the strong orientational order of bundles at the channels boundaries, similarly to the bacterial suspension confined in channels [19, 83]. Boundary layers could lead to different network behaviors from those we observed with the 2D AN. Recently, Duclos et

al assembled a 3D active nematic with microtubule bundles, clusters of kinesins and a passive nematic liquid crystal of filamentous viruses [9]. The behavior of 3D AN under confinement is yet largely unexplored experimentally in channels, however, numerical simulations recover net flow state (without disclinations) when the aspect ratio of the channel cross section is close to isotropic [105, 106].

3.5 Discussion

Previously, in chapter 5 and chapter 6, we have studied the behavior of individual channels of active nematic. We found that the active nematic spontaneously flows at a preferred speed controlled by the channel geometry. In the present chapter, we have experimentally addressed the topic of active nematic flow networks, in which several channels are coupled together. We studied network topologies where nodes have degree 2 or 3, and started with an elementary bifurcation network. We found that the competition between of activity and incompressibility of the active nematic, leads, for the specific network topologies explored here, to polarized flow states. The flow is often more important along particular paths of the network, while the other channels are in a frustrated state where the flow is close to 0. Our preliminary results indicate that the flow is more likely to set-up in the longest path available. In the second part of this chapter, we built a logical gate circuit, specifically designed to compute the AND/OR logical operations. Additional experiments are needed to confirm the preliminary results, and optimize the conditions leading to polarized flow states. Beyond logical operations, our experiments demonstrate the possibility to engineer active microfluidic networks with specific functions.

Conclusion and perspectives

We now summarize the main results obtained during this Ph.D, and provide some perspectives that are closely related to the work presented in this manuscript. The objective was to study how lateral confinement transforms the chaotic dynamics of unconfined active nematics into more stable, organized flow patterns.

To address this question, we mostly relied on experiments with a model experimental system based on microtubules and kinesin molecular motors. The 2-dimensional active nematic film formed at the interface between water and oil was laterally confined by means of a polymeric grid embedding various types of microfluidic channels (chapter 2). The experiments were complemented with numerical simulations using a continuous hydrodynamic model for liquid crystals, namely the Beris-Edwards equations, generalized to active nematics by the addition of an active stress tensor. The coupled partial differential equations were solved with a hybrid lattice Boltzmann method (chapter 3).

1 Active nematics near walls

We have experimentally investigated the **behavior of the active nematic near a wall** (chapter 4). The polymeric walls of the grid placed at the interface impose planar alignment and slip boundary conditions to the microtubule bundles. We showed that, under these conditions, the AN develops an "active boundary layer" (ABL) near the wall, which exclusively hosts negative topological defects with unusual properties. These defects nucleate along the wall, and due to their inherent polar symmetry, remain trapped in the near-wall region. Due to a lateral asymmetry in the force field surrounding the wall defect, wall defects can be subject to a net force that makes them laterally move along the wall. This lateral motility of wall defects within the ABL is facilitated by the slip boundary condition. Since wall defects motion is constrained to 1-dimension along the wall, they eventually get closer and merge together, involving an outsider $+\frac{1}{2}$ defect. This type of recombination event, involving three defects and the fusion of two like-sign defects, is wall-specific, as in the bulk, like-sign topological charges repel each other. The persistent nucleation, motion and recombination of defects at the wall are a manifestation of the active character of these boundary layers. Finally, we demonstrated the possibility to control the ABL with geometrically patterned boundaries. We used geometrical patterns whose sizes were comparable to the active length scale, in order to act directly on the defects. With curved

boundaries, we were able to spatially segregate topological defects with respect to the sign of their topological charges : positive defects migrate towards the wall concavities while negative wall defects nucleate and move along the wall convexities. A sharp triangular indentation is able to pin a wall negative defect at the tip of the protrusion. The pinned negative defect creates a rather stable flow pattern, in which an orthogonal jet of active nematic material is injected from the tip towards the bulk. Finally, we showed that ratchet walls, made of a repetition of asymmetric triangular protrusions, create longitudinal directed currents and enforce an effective tilted anchoring of the nematic field.

2 Active nematics in channels

We have studied **the new dynamics emerging when the active nematic is confined to a channel** (chapters 5 and 6). Experimentally, this was done by confining the AN in long, narrow channels with open ends, which were connected to the surrounding unconfined AN bath, playing the role of a thermal bath. In the simulations, the channels had periodic boundary conditions instead. The channels had either straight walls, or ratchet patterned walls. In the experiments, first of all, we found that net persistent currents spontaneously emerge in the straight channels that are sufficiently narrow ($w \leq 200\,\mu m$) and long ($L \geq 2000\,\mu m$). The direction of the current is selected by spontaneous symmetry breaking and it can be occasionally reversed if the fluctuations are high enough. The channel geometry affects the flow, for instance, the current's amplitude increases with the channel width until the confinement-induced order is lost, and the flow stability increases with the channel length. Numerical simulations using the Beris-Edwards equations initialized with a static configuration did not recover a net flow state embedding topological defects. However, the system dynamics converged towards a net flow state with defects when a net current was initially enforced. For such flow states, negative defects are separated from the wall by a a layer of well-defined thickness, in which the director field adopts a tilted orientation with respect to the wall. The stability of such boundary layer together with the net flow were destroyed by reducing the activity coefficient in the near-wall region below a threshold value.

Next, we created robust self-pumping channels by shaping the channel walls with ratchet patterns pointing in the same direction. The direction of the current that emerges is not selected by spontaneous symmetry breaking anymore but fixed by the ratchet direction. In the numerical simulations, the net flow state was reached starting from a static configuration and we showed that, for a given activity, the amplitude and wavelength of the saw-tooth pattern can be adjusted in order to obtain a defect-free flow state, or different types of defects dynamics. We showed that the zero-flow state was stabilized in the experiments when the ratchet walls have antagonistic orientations.

Both in the experiments and in the simulations of channels with either straight or ratchet walls, we found that these net flow states are associated to **travelling waves** in the velocity field

and to the **ordering of topological defects**, particularly enhanced by the ratchet patterns : $+\frac{1}{2}$ defects orient in the direction of the current around the channel center-line, and in the direction opposite to the current in the near-wall region of the channel. In the case of the ratchet channels, positive topological defects follow specific trajectories which, all together, form an ear-wheat pattern along the channel.

Finally, we proposed to describe the flow fluctuations in a straight channel with an equilibrium-like model : the over-damped Langevin equation in a double-well potential. We used the experimental data to infer the parameters of the model. Even if the model is a satisfying first-order approximation, more complex models should be considered in the future. In particular, it would be interesting to investigate to what degree the noise depends on the system state, and if we need to include extra degrees of freedom besides the volumetric flow rate $\phi(t)$ in the model.

Some questions concerning active nematics confined to channels are still open, for instance, does the flow state sets-up in infinitely long channels, or would it be cancelled by an occlusion ? Additionally, it would be interesting to analyze the flow state in terms of topological entropy and braiding associated to the motion of topological defects. Moreover, a theoretical explanation for the flow state embedding topological defects in straight channel is still missing.

The theoretical model used to describe the active nematic could be improved in several ways in order to comply better with the experimental system. First, we should consider different boundary conditions. So far, we enforced no-slip for the velocity and planar anchoring for the $\boldsymbol{Q}$-tensor as we would do for a passive liquid crystal : with a surface free energy term accounting for the anchoring of the mesogens at the boundary. Nevertheless, in active nematics, the effective planar anchoring seem to arise from hydrodynamic interactions. Experimentally, defects can nucleate and slide along the wall. Moreover, a fundamental ingredient that is missing in the mathematical model is a source of noise. In the experiments, fluctuations are an important aspect of the flow in open channels (chapter 5), which occasionally reverses its direction. Therefore, in the future, we would like to introduce fluctuations in the model in order to maintain the system away from the chaotic and dancing disclination state, without having to use an initial velocity field. This could be first introduced as a Gaussian random field perturbation to the field of activity ζ, independent from the nematic $\boldsymbol{Q}$-tensor field and the velocity field $\vec{v}$. Spatio-temporal fluctuations in the activity could account for density fluctuations in our model. However, it would probably be more interesting to couple the activity fluctuations to $\boldsymbol{Q}$ and $\vec{v}$, for instance via a continuous lyotropic model, or mesoscopic model of AN [95].

3 Active nematic flow networks

In the last part of this thesis, we increased the degree of complexity in terms of geometry and topology of the confining environment. We studied experimentally the flow dynamics arising when the active nematic is confined to microfluidic networks. Previously published theoretical models suggested that the coupling between fluid activity and incompressibility leads to polarized flow states for some network topologies. First, we started with an elementary network, consisting in three identical channels A, B, C connected together through a central junction node, forming

a bifurcation of threefold symmetry. We found that the flow state $\{\phi_A, \phi_B, \phi_C\}$ was unstable for such experimental conditions, although the flows were slightly polarized : the flow was often more important in two of the channels and weaker in the third one, however, transitions between different polarized flow states were frequent. Next, we introduced asymmetry in the bifurcation by reducing the length of the branch C, and by adding a few ratchet patterns to the channel A in order to generate an input current in A. In this case, the flow state was polarized and more stable : the input current coming from A is directed towards the longest of the two daughter branches, B. These results are in agreement with theoretical works modelling active flow networks, upon which logical gate designs were proposed. Therefore, we built microfluidic circuits whose function is to compute the AND and OR logical operations upon X and Y input flows : an incoming current codes for 1, while the absence of current codes for 0. The circuit is composed of seven unit channels, assembled into an asymmetric H-junction : the branch leading to the OR gate is the longest in order to be more likely to capture an input flow than the path leading towards the AND gate. We used ratchet channels as diode elements preventing back-flows at the level of the inputs and the outputs. The experimental results we obtained are encouraging and compatible with theoretical predictions, however the design could be improved in multiple ways. In the near future, we plan to implement input control with light-activatable molecular motors. This would enable us to explore the time response of the device, but also to build memory circuits. Besides input-control, light-control opens up fascinating perspectives, such as the capacity to make reconfigurable circuits, and thereby to increase the number of operations that can be computed by the device (Figure 7.14 a and b). We also plan to develop new methods to confine the active nematic film to networks that are directly attached to a substrate, analogously to integrated circuits.

4 Perspectives

We now provide a list of experimental ideas more remotely related to what has already been achieved in this thesis, and that would be worth trying :

Active nematic carrier. We propose to deposit at the interface where the active nematic forms particles with a broken symmetry, for instance a ratchet raft, a boomerang, or Pac-Man shaped particles (Figure 7.14 c). Such particles could be printed with the nano-scribe, and receive proper surface treatment in order to favor their positioning at the interface between water and oil. Since active fluids can create uneven pressure around boundaries, we anticipate that, with a suitable design, such particle could be propelled by the surrounding active flows. The transport direction with respect to reference frame attached to the laboratory could be controlled by orienting the particle with a magnetic field, or guiding it along microfluidic channels. These are ideas that we will implement in collaboration with the group of Tyler Shendruk, from the University of Edinburgh.

Topological defect protection. Conversely, Pac-Man and boomerang-shaped particles could also be used to protect and guide topological defects. In chapter 4, we showed that positive defects tend to linger in the concavities of the wall patterns (concave curves, concave corners of the ratchet, etc.). However, since the boundaries were fixed, positive defects eventually escaped from the concavity. The situation could be different if the boundary (particle) is free to move in the AN film. The positive defect, herewith capped by the particle, could not annihilate with negative defects and would be protected (Figure 7.14 d). The particles could be manipulated externally, for instance by mean of an optical tweezer, in order to guide the defect.

Logical operations with topological defects. In chapter 7, information in flow network was encoded in flows. Alternatively, we could build logical and memory circuits where information is encoded by a topological defect [107]. Topological defects have the advantage to be topologically protected, and thus robust against noise. Active topological defects, in addition, can be transported without the need of an external force [108].

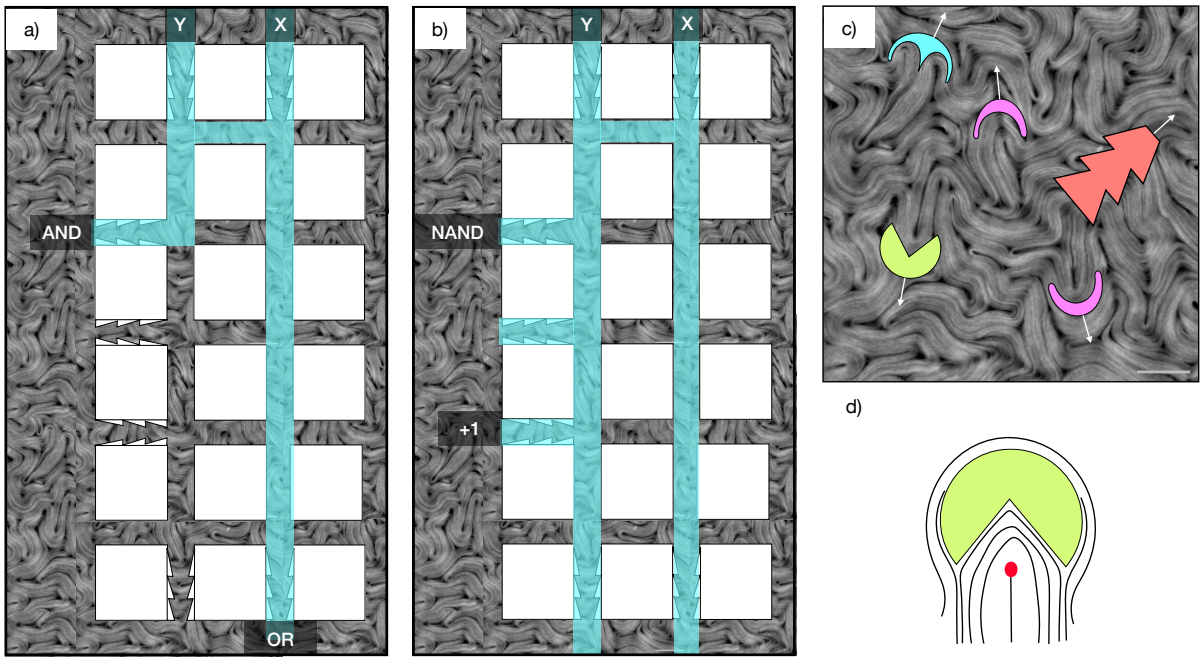

FIGURE 7.14 – **Perspectives.** The same uniform square mesh network (with a few diode elements) can be reconfigured with patterns of light into **a)** a AND/OR logical circuit or **b)** a NAND logical circuit. **c)** Particles with broken symmetry being transported by the active nematic. **d)** $+\frac{1}{2}$ topological defect protected by a Pac-Man shaped particle.

List of publications

Published articles

Jérôme Hardoüin, Claire Doré, Justine Laurent, Teresa Lopez-Leon, Jordi Ignés-Mullol, Francesc Sagués. "*Active boundary layers in confined active nematics*". Nature Communications. DOI: https://doi.org/10.1038/s41467-022-34336-z

Articles in preparation

Claire Doré, Jérôme Hardoüin, Justine Laurent, Jordi Ignés-Mullol, Francesc Sagués, Teresa Lopez-Leon. "*Autonomous microfluidics and logical circuits with active nematics*".

Claire Doré, Noe Atzin Canas, Ali Mozaffari, Rui Zhang, Teresa Lopez-Leon and Juan de Pablo. "*Control of active topological defects in geometrical channels*".

Presentations in international conferences

C. Doré, J. Hardoüin, J. Laurent, J. Ignés-Mullol, F.Sagués, T. Lopez-Leon. "*2-dimensional active nematics in the vicinity of a geometrical boundary*". Eutopia, virtual, 2021

C. Doré, J. Hardoüin, J. Laurent, J. Ignés-Mullol, F.Sagués, T. Lopez-Leon. " *Active nematics near walls*". APS March Meeting, virtual, 2021

C. Doré, J. Hardoüin, J. Laurent, J. Ignés-Mullol, F.Sagués, T. Lopez-Leon. "*Autonomous microfluidics and active flow networks in active nematics*". APS March Meeting, Chicago, 2022

Bibliography

[1] Antoine Bricard, Jean Baptiste Caussin, Nicolas Desreumaux, Olivier Dauchot et Denis Bartolo. « Emergence of macroscopic directed motion in populations of motile colloids ». *Nature* 503 (7474 2013), p. 95-98 (cf. p. 2, 3).

[2] Andreas Walther et Axel H. E. Müller. « Janus Particles : Synthesis, Self-Assembly, Physical Properties, and Applications ». *Chemical Reviews* 113.7 (2013), p. 5194-5261 (cf. p. 2).

[3] Jing Yan, Ming Han, Jie Zhang, Cong Xu, Erik Luijten et Steve Granick. « Reconfiguring active particles by electrostatic imbalance ». *Nature Materials* 15 (10 2016), p. 1095-1099 (cf. p. 2, 3).

[4] Mojtaba Rajabi, Hend Baza, Taras Turiv et Oleg D. Lavrentovich. « Directional self-locomotion of active droplets enabled by nematic environment ». *Nature Physics* 17.2 (2021), p. 260-266 (cf. p. 2).

[5] Corinna C. Maass, Carsten Krüger, Stephan Herminghaus et Christian Bahr. « Swimming Droplets ». *Annual Review of Condensed Matter Physics* 7.1 (2016), p. 171-193 (cf. p. 2).

[6] Charlotte de Blois, Vincent Bertin, Saori Suda, Masatoshi Ichikawa, Mathilde Reyssat et Olivier Dauchot. « Swimming droplets in 1D geometries : an active Bretherton problem ». *Soft Matter* 17 (2021), p. 6646-6660 (cf. p. 2).

[7] Volker Schaller, Christoph Weber, Christine Semmrich, Erwin Frey et Andreas R. Bausch. « Polar patterns of driven filaments ». *Nature* 467 (7311 2010), p. 73-77 (cf. p. 2).

[8] L Huber, R Suzuki, T Krüger, E Frey et A R Bausch. *Emergence of coexisting ordered states in active matter systems*. 2018, p. 255-258 (cf. p. 2, 3).

[9] Guillaume Duclos, Raymond Adkins, Debarghya Banerjee, Matthew S.E. Peterson, Minu Varghese, Itamar Kolvin et al. « Topological structure and dynamics of three-dimensional active nematics ». *Science* 367 (6482 2020), p. 1120-1124 (cf. p. 4, 25, 132).

[10] Tim Sanchez, Daniel T N Chen, Stephen J DeCamp, Michael Heymann et Zvonimir Dogic. « Spontaneous motion in hierarchically assembled active matter ». *Nature* 491.7424 (2012), p. 431-434 (cf. p. 4, 5, 13, 20, 25).

[11] Stephen J. DeCamp, Gabriel S. Redner, Aparna Baskaran, Michael F. Hagan et Zvonimir Dogic. « Orientational order of motile defects in active nematics ». *Nature Materials* 14.11 (2015), p. 1110-1115 (cf. p. 4).

[12] P. Baconnier, D. Shohat, C. Hernández López, C. Coulais, V. Démery, G. Düring et al. « Selective and collective actuation in active solids ». *Nature Physics* 18.10 (2022), p. 1234-1239 (cf. p. 4).

[13] Julien Deseigne, Olivier Dauchot et Hugues Chaté. « Collective motion of vibrated polar disks ». *Physical Review Letters* 105 (9 2010) (cf. p. 4).

[14] Manuele Brambilla, Eliseo Ferrante, Mauro Birattari et Marco Dorigo. « Swarm robotics : a review from the swarm engineering perspective ». *Swarm Intelligence* 7.1 (2013), p. 1-41 (cf. p. 5).

[15] Jeremie Palacci, Stefano Sacanna, Asher Preska Steinberg, David J. Pine et Paul M. Chaikin. « Living Crystals of Light-Activated Colloidal Surfers ». *Science* 339.6122 (2013), p. 936-940. eprint : https://www.science.org/doi/pdf/10.1126/science.1230020 (cf. p. 5).

[16] Christopher Dombrowski, Luis Cisneros, Sunita Chatkaew, Raymond E. Goldstein et John O. Kessler. « Self-Concentration and Large-Scale Coherence in Bacterial Dynamics ». *Physical Review Letters* 93 (9 2004), p. 098103 (cf. p. 5).

[17] Henricus H. Wensink, Jörn Dunkel, Sebastian Heidenreich, Knut Drescher, Raymond E. Goldstein, Hartmut Löwen et al. « Meso-scale turbulence in living fluids ». *Proceedings of the National Academy of Sciences* 109.36 (2012), p. 14308-14313 (cf. p. 5).

[18] Andrey Sokolov et Igor S. Aranson. « Physical Properties of Collective Motion in Suspensions of Bacteria ». *Physical Review Letters* 109 (24 2012), p. 248109 (cf. p. 5).

[19] Hugo Wioland, Enkeleida Lushi et Raymond E Goldstein. « Directed collective motion of bacteria under channel confinement ». *New Journal of Physics* 18.7 (2016), p. 075002 (cf. p. 5, 76, 77, 131).

[20] Sri Ram Krishna Vedula, Man Chun Leong, Tan Lei Lai, Pascal Hersen, Alexandre J. Kabla, Chwee Teck Lim et al. « Emerging modes of collective cell migration induced by geometrical constraints ». *Proceedings of the National Academy of Sciences* 109.32 (2012), p. 12974-12979 (cf. p. 5).

[21] Kyogo Kawaguchi, Ryoichiro Kageyama et Masaki Sano. « Topological defects control collective dynamics in neural progenitor cell cultures ». *Nature* 545.7654 (2017), p. 327-331 (cf. p. 5, 17).

[22] Pau Guillamat, Jordi Ignés-Mullol et Francesc Sagués. « Control of active liquid crystals with a magnetic field ». *Proceedings of the National Academy of Sciences of the United States of America* 113 (20 2016), p. 5498-5502 (cf. p. 5, 16, 17).

[23] Amin Doostmohammadi, Tyler N. Shendruk, Kristian Thijssen et Julia M. Yeomans. « Onset of meso-scale turbulence in active nematics ». *Nature Communications* 8 (2017) (cf. p. 5, 94).

[24] Vasil Bratanov, Frank Jenko et Erwin Frey. « New class of turbulence in active fluids ». *Proceedings of the National Academy of Sciences* 112.49 (2015), p. 15048-15053 (cf. p. 5).

[25] Jörn Dunkel, Sebastian Heidenreich, Knut Drescher, Henricus H. Wensink, Markus Bär et Raymond E. Goldstein. « Fluid Dynamics of Bacterial Turbulence ». *Physical Review Letters* 110 (22 2013), p. 228102 (cf. p. 5, 6).

[26] P. Guillamat, J. Ignés-Mullol et F. Sagués. « Taming active turbulence with patterned soft interfaces ». *Nature Communications* 8 (1 2017), p. 1-8 (cf. p. 6, 16, 17).

[27] M. C. Marchetti, J. F. Joanny, S. Ramaswamy, T. B. Liverpool, J. Prost, Madan Rao et al. « Hydrodynamics of soft active matter ». *Reviews of Modern Physics* 85 (3 2013), p. 1143-1189 (cf. p. 6).

[28] « The 2020 motile active matter roadmap ». *Journal of Physics Condensed Matter* 32 (19 2020) (cf. p. 6).

[29] Christopher Battle, Chase P. Broedersz, Nikta Fakhri, Veikko F. Geyer, Jonathon Howard, Christoph F. Schmidt et al. « Broken detailed balance at mesoscopic scales in active biological systems ». *Science* 352.6285 (2016), p. 604-607 (cf. p. 6).

[30] David A. Egolf. « Equilibrium Regained : From Nonequilibrium Chaos to Statistical Mechanics ». *Science* 287.5450 (2000), p. 101-104 (cf. p. 7).

[31] « Confined Flow : Consequences and Implications for Bacteria and Biofilms ». *Annu. Rev. Chem. Biomol. Eng* 9 (2018), p. 175-200 (cf. p. 7).

[32] R. Di Leonardo, L. Angelani, D. Dell'Arciprete, G. Ruocco, V. Iebba, S. Schippa et al. « Bacterial ratchet motors ». *Proceedings of the National Academy of Sciences of the United States of America* 107 (21 2010), p. 9541-9545 (cf. p. 7, 8).

[33] Andreas Kaiser, Anton Peshkov, Andrey Sokolov, Borge Ten Hagen, Hartmut Löwen et Igor S. Aranson. « Transport powered by bacterial turbulence ». *Physical Review Letters* 112 (15 2014), p. 1-5 (cf. p. 7, 8).

[34] Francis G. Woodhouse et Jörn Dunkel. « Active matter logic for autonomous microfluidics ». *Nature Communications* 8.1 (2017), p. 15169 (cf. p. 7, 114, 115).

[35] Francis G. Woodhouse, Aden Forrow, Joanna B. Fawcett et Jörn Dunkel. « Stochastic cycle selection in active flow networks ». *Proceedings of the National Academy of Sciences* 113.29 (2016), p. 8200-8205 (cf. p. 7, 111, 113).

[36] Andrew G. Clark et Danijela Matic Vignjevic. *Modes of cancer cell invasion and the role of the microenvironment*. 2015 (cf. p. 8).

[37] Clemens Bechinger, Roberto Di Leonardo, Hartmut Löwen, Charles Reichhardt, Giorgio Volpe et Giovanni Volpe. « Active particles in complex and crowded environments ». *Reviews of Modern Physics* 88 (4 2016) (cf. p. 8).

[38] Nikolai Nikola, Alexandre P. Solon, Yariv Kafri, Mehran Kardar, Julien Tailleur et Raphaël Voituriez. « Active Particles with Soft and Curved Walls : Equation of State, Ratchets, and Instabilities ». *Physical Review Letters* 117 (9 2016), p. 1-5 (cf. p. 8).

[39] Peter Galajda, Juan Keymer, Paul Chaikin et Robert Austin. « A Wall of Funnels Concentrates Swimming Bacteria ». *Journal of Bacteriology* 189.23 (2007), p. 8704-8707 (cf. p. 9).

[40] Sang Yub Kim, Eun Se Lee, Ho Jae Lee, Se Yeon Lee, Sung Kuk Lee et Taesung Kim. « Microfabricated ratchet structures for concentrating and patterning motile bacterial cells ». *Journal of Micromechanics and Microengineering* 20.9 (2010), p. 095006 (cf. p. 9).

[41] Ivan Berdakin, Y Jeyaram, VV Moshchalkov, Lyn Venken, Seppe Dierckx, SJ Vanderleyden et al. « Influence of swimming strategy on microorganism separation by asymmetric obstacles ». *Physical Review E* 87.5 (2013), p. 052702 (cf. p. 9).

[42] C J Olson Reichhardt et C Reichhardt. « Ratchet Effects in Active Matter Systems ». *arXiv* (2016), p. 1-26 (cf. p. 9).

[43] Peter Reimann. « Brownian motors : noisy transport far from equilibrium ». *Physics Reports* 361.2 (2002), p. 57-265 (cf. p. 9).

[44] Tristan Maquart. « Disk-sphere field duality theorem » (2018) (cf. p. 12).

[45] Amin Doostmohammadi, Jordi Ignés-Mullol, Julia M. Yeomans et Francesc Sagués. « Active nematics ». *Nature Communications* 9.1 (2018), p. 3246 (cf. p. 13).

[46] Berta Martínez-Prat, Jordi Ignés-Mullol, Jaume Casademunt et Francesc Sagués. « Selection mechanism at the onset of active turbulence ». *Nature Physics* 15.4 (2019), p. 362-366 (cf. p. 14).

[47] Felix C. Keber, Etienne Loiseau, Tim Sanchez, Stephen J. DeCamp, Luca Giomi, Mark J. Bowick et al. « Topology and dynamics of active nematic vesicles ». *Science* 345 (6201 2014), p. 1135-1139 (cf. p. 14, 15).

[48] Perry W. Ellis, Daniel J. G. Pearce, Ya-Wen Chang, Guillermo Goldsztein, Luca Giomi et Alberto Fernandez-Nieves. « Curvature-induced defect unbinding and dynamics in active nematic toroids ». *Nature Physics* 14.1 (2018), p. 85-90 (cf. p. 15).

[49] Martina Clairand. *Dynamic coupling between passive and active complex fluids in curved geometries* PhD thesis, Université Paris sciences et lettres (2021) (cf. p. 15).

[50] Achini Opathalage, Michael M Norton, Michael P N Juniper, Blake Langeslay, S Ali Aghvami, Seth Fraden et al. « Self-organized dynamics and the transition to turbulence of confined active nematics. » *Proc Natl Acad Sci U S A* 116.11 (2019), p. 4788-4797 (cf. p. 15, 16, 51, 55, 68, 80, 130).

[51] Jérôme Hardoüin, Justine Laurent, Teresa Lopez-Leon, Jordi Ignés-Mullol et Francesc Sagués. « Active microfluidic transport in two-dimensional handlebodies ». *Soft Matter* 16.40 (2020), p. 9230-9241 (cf. p. 15, 16, 58, 68, 77, 80).

[52] Jérôme Hardoüin, Rian Hughes, Amin Doostmohammadi, Justine Laurent, Teresa Lopez-Leon, Julia M. Yeomans et al. « Reconfigurable flows and defect landscape of confined active nematics ». *Communications Physics* 2.1 (2019), p. 121 (cf. p. 15, 51, 75).

[53] Kristian Thijssen, Dimitrius A. Khaladj, S. Ali Aghvami, Mohamed Amine Gharbi, Seth Fraden, Julia M. Yeomans et al. « Submersed micropatterned structures control active nematic flow, topology, and concentration ». *Proceedings of the National Academy of Sciences* 118.38 (2021), e2106038118 (cf. p. 16, 17).

[54] Rui Zhang, Steven A. Redford, Paul V. Ruijgrok, Nitin Kumar, Ali Mozaffari, Sasha Zemsky et al. « Spatiotemporal control of liquid crystal structure and dynamics through activity patterning ». *Nature Materials* 20.6 (2021), p. 875-882 (cf. p. 16, 17, 48, 131).

[55] Tobias Bonhoeffer et Amiram Grinvald. « Iso-orientation domains in cat visual cortex are arranged in pinwheel-like patterns ». *Nature* 353.6343 (1991), p. 429-431 (cf. p. 17).

[56] R. Kemkemer, D. Kling, D. Kaufmann et H. Gruler. « Elastic properties of nematoid arrangements formed by amoeboid cells ». *The European Physical Journal E* 1.2 (2000), p. 215-225 (cf. p. 17).

[57] G. Duclos, S. Garcia, H. G. Yevick et P. Silberzan. « Perfect nematic order in confined monolayers of spindle-shaped cells ». *Soft Matter* 10 (2014), p. 2346-2353 (cf. p. 17).

[58] Thuan Beng Saw, Amin Doostmohammadi, Vincent Nier, Leyla Kocgozlu, Sumesh Thampi, Yusuke Toyama et al. « Topological defects in epithelia govern cell death and extrusion ». *Nature* 544.7649 (2017), p. 212-216 (cf. p. 17, 18).

[59] Yonit Maroudas-Sacks, Liora Garion, Lital Shani-Zerbib, Anton Livshits, Erez Braun et Kinneret Keren. « Topological defects in the nematic order of actin fibres as organization centres of Hydra morphogenesis ». *Nature Physics* 17 (2 2021), p. 251-259 (cf. p. 17, 18).

[60] Amin Doostmohammadi, Sumesh P. Thampi et Julia M. Yeomans. « Defect-Mediated Morphologies in Growing Cell Colonies ». *Physical Review Letters* 117 (4 2016), p. 048102 (cf. p. 18).

[61] Eckhard Mandelkow et Eva-Maria Mandelkow. « Microtubule structure ». *Current Opinion in Structural Biology* 4.2 (1994), p. 171-179 (cf. p. 21).

[62] F Gittes, B Mickey, J Nettleton et J Howard. « Flexural rigidity of microtubules and actin filaments measured from thermal fluctuations in shape. » *J Cell Biol* 120.4 (1993), p. 923-934 (cf. p. 21).

[63] K Svoboda et S M Block. « Force and velocity measured for single kinesin molecules. » *Cell* 77.5 (1994), p. 773-784 (cf. p. 21).

[64] A A Hyman, S Salser, D N Drechsel, N Unwin4 et T J Mitchison. *Role of GTP Hydrolysis in Microtubule Dynamics : Information from a Slowly Hydrolyzable Analogue, GMPCPP*. 1992, p. 1155-1167 (cf. p. 22).

[65] Qingzong Tseng, Eve Duchemin-Pelletier, Alexandre Deshiere, Martial Balland, Hervé Guillou, Odile Filhol et al. « Spatial organization of the extracellular matrix regulates cell–cell junction positioning ». *Proceedings of the National Academy of Sciences* 109.5 (2012), p. 1506-1511 (cf. p. 30).

[66] Deqing Sun, Stefan Roth et Michael J. Black. « Secrets of optical flow estimation and their principles » (2010), p. 2432-2439 (cf. p. 30).

[67] Perry W. Ellis. *Nematic Materials in Curved Spaces* PhD thesis, Georgia Institute of Technology (2018) (cf. p. 31).

[68] Joachim Weickert. « Coherence-Enhancing Diffusion Filtering ». *International Journal of Computer Vision* 31.2 (1999), p. 111-127 (cf. p. 32).

[69] Matthew L Blow, Sumesh P Thampi et Julia M Yeomans. « Biphasic, lyotropic, active nematics ». *Physical review letters* 113.24 (2014), p. 248303 (cf. p. 32).

[70] John Crocker et David Grier. « Methods of Digital Video Microscopy for Colloidal Studies ». *Journal of Colloid and Interface Science - J COLLOID INTERFACE SCI* 179 (1996), p. 298-310 (cf. p. 33).

[71] Antony N. Beris et Brian J. Edwards. « Thermodynamics of flowing systems : with internal microstructure ». 1994 (cf. p. 34).

[72] Yashodhan Hatwalne, Sriram Ramaswamy, Madan Rao et R. Aditi Simha. « Rheology of Active-Particle Suspensions ». *Physical Review Letters* 92 (11 2004), p. 118101 (cf. p. 40).

[73] Complex Systems. *The Lattice Boltzmann Method (continued)*. 2004, p. 1-7 (cf. p. 40, 42).

[74] Colin Denniston, Enzo Orlandini et J. M. Yeomans. « Lattice Boltzmann simulations of liquid crystal hydrodynamics ». *Physical Review E - Statistical Physics, Plasmas, Fluids, and Related Interdisciplinary Topics* 63 (5 2001) (cf. p. 40).

[75] C. Denniston, D. Marenduzzo, E. Orlandini et J. M. Yeomans. « Lattice Boltzmann algorithm for three-dimensional liquid-crystal hydrodynamics ». T. 362. Royal Society, 2004, p. 1745-1754 (cf. p. 40, 93).

[76] « Steady-state hydrodynamic instabilities of active liquid crystals : Hybrid lattice Boltzmann simulations ». *Physical Review E - Statistical, Nonlinear, and Soft Matter Physics* 76 (3 2007) (cf. p. 40).

[77] Rui Zhang, Nitin Kumar, Jennifer L. Ross, Margaret L. Gardel et Juan J. De Pablo. « Interplay of structure, elasticity, and dynamics in actin-based nematic materials ». *Proceedings of the National Academy of Sciences of the United States of America* 115 (2 2017), E124-E133 (cf. p. 48, 94).

[78] Rui Zhang, Tyler Roberts, Igor S. Aranson et Juan J. De Pablo. « Lattice Boltzmann simulation of asymmetric flow in nematic liquid crystals with finite anchoring ». *Journal of Chemical Physics* 144 (8 2016) (cf. p. 48, 93).

[79] Jerôme Hardoüin, Claire Doré, Justine Laurent, Teresa Lopez-Leon, Jordi Ignés-Mullol et Francesc Sagués. « Active boundary layers in confined active nematics ». *Nature Communications* 13.1 (2022), p. 6675 (cf. p. 51).

[80] Benoît Jubin. « A generalized Poincaré-Hopf index theorem » (2009) (cf. p. 56).

[81] Delphine Geyer, Alexandre Morin et Denis Bartolo. « Sounds and hydrodynamics of polar active fluids ». *Nature materials* 17.9 (2018), p. 789-793 (cf. p. 76).

[82] D. J. G. Pearce, J. Nambisan, P. W. Ellis, A. Fernandez-Nieves et L. Giomi. « Orientational Correlations in Active and Passive Nematic Defects ». *Physical Review Letters* 127 (19 2021), p. 197801 (cf. p. 77).

[83] Hugo Wioland, Francis G. Woodhouse, Jörn Dunkel et Raymond E. Goldstein. « Ferromagnetic and antiferromagnetic order in bacterial vortex lattices ». *Nature Physics* 12.4 (2016), p. 341-345 (cf. p. 85, 131).

[84] Caleb G. Wagner, Michael M. Norton, Jae Sung Park et Piyush Grover. « Exact Coherent Structures and Phase Space Geometry of Preturbulent 2D Active Nematic Channel Flow ». *Physical Review Letters* 128 (2 2022), p. 028003 (cf. p. 92).

[85] Tyler N Shendruk, Amin Doostmohammadi, Kristian Thijssen et Julia M Yeomans. « Dancing disclinations in confined active nematics ». *Soft Matter* 13.21 (2017), p. 3853-3862 (cf. p. 94, 96).

[86] Ali Mozaffari, Rui Zhang, Noe Atzin et Juan J. De Pablo. « Defect Spirograph : Dynamical Behavior of Defects in Spatially Patterned Active Nematics ». *Physical Review Letters* 126 (22 2021) (cf. p. 94).

[87] Nitin Kumar, Rui Zhang, Juan J. De Pablo et Margaret L. Gardel. « Tunable structure and dynamics of active liquid crystals ». *Science Advances* 4 (10 2018), p. 1-13 (cf. p. 94).

[88] Howard A. Barnes. « A review of the slip (wall depletion) of polymer solutions, emulsions and particle suspensions in viscometers : its cause, character, and cure ». *Journal of Non-Newtonian Fluid Mechanics* 56.3 (1995), p. 221-251 (cf. p. 100).

[89] Richard M. Jendrejack, David C. Schwartz, Juan J. de Pablo et Michael D. Graham. « Shear-induced migration in flowing polymer solutions : Simulation of long-chain DNA in microchannels ». *The Journal of Chemical Physics* 120.5 (2004), p. 2513-2529 (cf. p. 100).

[90] Allison P. Berke, Linda Turner, Howard C. Berg et Eric Lauga. « Hydrodynamic Attraction of Swimming Microorganisms by Surfaces ». *Physical Review Letters* 101 (3 2008), p. 038102 (cf. p. 100).

[91] C. Rorai, F. Toschi et I. Pagonabarraga. « Active nematic flows confined in a two-dimensional channel with hybrid alignment at the walls : A unified picture ». *Phys. Rev. Fluids* 6 (11 2021), p. 113302 (cf. p. 104).

[92] Michael M. Norton, Arvind Baskaran, Achini Opathalage, Blake Langeslay, Seth Fraden, Aparna Baskaran et al. « Insensitivity of active nematic liquid crystal dynamics to topological constraints ». *Phys. Rev. E* 97 (1 2018), p. 012702 (cf. p. 106).

[93] Amanda J. Tan, Eric Roberts, Spencer A. Smith, Ulyses Alvarado Olvera, Jorge Arteaga, Sam Fortini et al. « Topological chaos in active nematics ». *Nature Physics* 15 (10 2019), p. 1033-1039 (cf. p. 108).

[94] Jean Luc Thiffeault et Matthew D. Finn. « Topology, braids and mixing in fluids ». *Philosophical Transactions of the Royal Society A : Mathematical, Physical and Engineering Sciences* 364 (1849 2006), p. 3251-3266 (cf. p. 108).

[95] Timofey Kozhukhov et Tyler N. Shendruk. « Mesoscopic simulations of active nematics ». *Science Advances* 8.34 (2022), eabo5788 (cf. p. 110, 135).

[96] Mustapha-Kamel Khelloufi, Etienne Loiseau, Marc Jaeger, Nicolas Molinari, Pascal Chanez, Delphine Gras et al. « Spatiotemporal organization of cilia drives multiscale mucus swirls in model human bronchial epithelium ». *Scientific Reports* 8.1 (2018), p. 2447 (cf. p. 111).

[97] Etienne Loiseau, Simon Gsell, Aude Nommick, Charline Jomard, Delphine Gras, Pascal Chanez et al. « Active mucus–cilia hydrodynamic coupling drives self-organization of human bronchial epithelium ». *Nature Physics* 16.11 (2020), p. 1158-1164 (cf. p. 111).

[98] A Grebecki et M Cieślawska. « Plasmodium of Physarum polycephalum as a synchronous contractile system. » *Cytobiologie* 17.2 (1978), p. 335-342 (cf. p. 111).

[99] Karen Alim, Gabriel Amselem, François Peaudecerf, Michael P. Brenner et Anne Pringle. « Random network peristalsis in Physarum polycephalum organizes fluid flows across an individual ». *Proceedings of the National Academy of Sciences of the United States of America* 110 (33 2013), p. 13306-13311 (cf. p. 111).

[100] Michael J. Fuerstman, Pascal Deschatelets, Ravi Kane, Alexander Schwartz, Paul J. A. Kenis, John M. Deutch et al. « Solving Mazes Using Microfluidic Networks ». *Langmuir* 19.11 (2003), p. 4714-4722 (cf. p. 114).

[101] Krishnamurthy V. Nemani, Karen L. Moodie, Jeoffry B. Brennick, Alison Su et Barjor Gimi. « In vitro and in vivo evaluation of SU-8 biocompatibility ». *Materials Science and Engineering : C* 33.7 (2013), p. 4453-4459 (cf. p. 130).

[102] Paul V. Ruijgrok, Rajarshi P. Ghosh, Sasha Zemsky, Muneaki Nakamura, Rui Gong, Lin Ning et al. « Optical control of fast and processive engineered myosins in vitro and in living cells ». *Nature Chemical Biology* 17.5 (2021), p. 540-548 (cf. p. 131).

[103] Muneaki Nakamura, Lu Chen, Stuart C Howes, Tony D Schindler, Eva Nogales et Zev Bryant. « Remote control of myosin and kinesin motors using light-activated gearshifting. » *Nat Nanotechnol* 9.9 (2014), p. 693-697 (cf. p. 131).

[104] Kun Ta Wu, Jean Bernard Hishamunda, Daniel T.N. Chen, Stephen J. DeCamp, Ya Wen Chang, Alberto Fernández-Nieves et al. « Transition from turbulent to coherent flows in confined three-dimensional active fluids ». *Science* 355 (6331 2017) (cf. p. 131).

[105] Santhan Chandragiri, Amin Doostmohammadi, Julia M. Yeomans et Sumesh P. Thampi. « Flow States and Transitions of an Active Nematic in a Three-Dimensional Channel ». *Physical Review Letters* 125 (14 2020) (cf. p. 132).

[106] Miha Ravnik et Julia M. Yeomans. « Confined active nematic flow in cylindrical capillaries ». *Physical Review Letters* 110 (2 2013), p. 1-5 (cf. p. 132).

[107] Žiga Kos et Jörn Dunkel. « Nematic bits and universal logic gates » (2020) (cf. p. 137).

[108] Rui Zhang, Ali Mozaffari et Juan J De Pablo. *Logic operations with active topological defects*. 2022, p. 9060 (cf. p. 137).

RÉSUMÉ

Les systèmes vivants se composent d'un grand nombre d'unités convertissant l'énergie chimique environnante en mouvement. Par conséquent, ces systèmes sont intrinsèquement hors d'équilibre. Dans cette thèse, nous étudions un matériau actif synthétique inventé par le groupe de Zvonimir Dogic, appelé "nématique actif", fait à partir de constituants du cytosquelette. L'unité active est un faisceau de microtubules, qui s'étire sous l'action des kinésines, moteurs moléculaires consommateurs d'adénosine triphosphate. Les faisceaux de microtubules s'auto-assemblent à l'interface d'une huile, où ils forment un film dense présentant un ordre nématique sur une distance bien plus grande que le faisceau de microtubules. A la différence des cristaux liquides à l'équilibre, l'ordre nématique est interrompu par la présence de défauts topologiques auto-propulsés, qui conduisent la dynamique vers un état de chaos spatio-temporel. Dans cette thèse, nous explorons l'émergence de structures spatio-temporelles ordonnées dans les systèmes nématiques actifs confinés latéralement. En nous appuyant à la fois sur des expériences et des simulations numériques, nous montrons que l'on peut utiliser les parois latérales pour contrôler les flux actifs. Dans la première partie, nous étudions expérimentalement les films nématiques actifs à proximité d'une paroi latérale. La paroi est exclusivement habitée par des défauts topologiques de charge négative qui présentent une forme et une dynamique insolite. Nous montrons que des parois aux contours géométriques sont capables d'influencer les lieux de nucléation des défauts et d'induire des écoulement dirigés. Dans la partie principale, nous confinons le nématique actif dans des canaux étroits et ouverts à leur deux extrémités. Nous constatons l'émergence d'un écoulement dans l'une des directions, sélectionnée par brisure de symétrie spontanée. Lorsque les fluctuations sont importantes, la direction de l'écoulement peut s'inverser. Nous montrons que l'amplitude et la stabilité du flux sont contrôlées par la géométrie du canal. Par exemple, des parois en dents de scie permettent d'obtenir soit un flux unidirectionnel dans une direction choisie, soit un flux de cisaillement. Les contours géométriques des parois induisent l'ordre spatial et orientationnel des défauts topologiques. Nous réalisons également des simulations numériques des équations nématodynamiques généralisées aux systèmes actifs, utilisant une version hybride de la méthode de Boltzmann sur réseau et nous reproduisons numériquement les caractéristiques principales du système expérimental. Enfin, nous fabriquons expérimentalement des réseaux de canaux remplis du fluide nématique actif, ce qui nous permet de tester un modèle théorique précédemment publié. Partant d'une configuration relativement simple de bifurcation, nous terminons par l'élaboration d'une porte logique ET/OU, démontrant le potentiel des cristaux liquides actifs et des fluides actifs en général pour alimenter des réseaux microfluidiques autonomes et reconfigurables.

MOTS CLÉS

cristaux liquides, matière active, défauts topologiques, confinement géométrique, microfluidique autonome, matériaux bio-inspirés

ABSTRACT

Living systems rely on a large number of agents converting local chemical energy into motion. Therefore they are inherently out-of-equilibrium. In this thesis, we study a model synthetic active material created by the group of Zvonimir Dogic using cytoskeleton elements, which is typically referred to as « active nematic ». Here, the active unit is an extensile bundle of microtubules driven by kinesin clusters fueled by adenosine triphosphate. At an oil interface, the bundles self-assemble into a dense film that displays nematic order on a scale much larger than the microtubule or the bundle itself. However, unlike passive liquid crystals, here nematic order is disrupted by the presence of motile topological defects that drive the system dynamics into spatio-temporal chaos. In this thesis, we investigate the emergence of ordered spatio-temporal patterns in laterally confined active nematics using both experiments and numerical simulations, and we show that lateral boundaries can be used to control active flows. In the first part, we experimentally study semi-confined active nematics in the vicinity of a lateral boundary. We find that the lateral wall is exclusively populated by negative defects, which exhibit exotic structure and dynamics. We show that geometrical patterning of the lateral boundary can allow for control over defect nucleation and induce directional flows. In the main part, we confine the active nematic to individual, narrow, open channels, and observe the emergence of directional flows along one direction, selected by spontaneous symmetry breaking. When fluctuations are important, the system can reverse the flow direction. We show that the flow amplitude and its stability can be geometrically controlled. For instance, we are able to effectively enforce either shear or directed flow states by shaping the confining wall with a ratchet pattern. Geometrical patterning of the channel wall induces spatial and orientational ordering of the motile topological defects. We perform numerical simulations using nematodynamics equations and a hybrid Lattice Boltzmann method, capturing some main features of our experimental results. Finally, we experimentally build active nematic flow networks where we test a previously published theoretical model. We start with a simple configuration of three channels connected in a bifurcation, and we conclude with the realization of an AND/OR logical gate, demonstrating the potential of active nematics to power autonomous microfluidic networks.

KEYWORDS

liquid crystals, active matter, topological defects, geometrical confinement, autonomous microfluidics, bio-inspired materials